UNIVERSITY OF SOUTHAMPTON

Novel Devices in Periodically Poled Lithium Niobate

Joyce Anne Abernethy

Submitted for the degree of Doctor of Philosophy

Optoelectronic Research Centre
Faculty of Engineering and Applied Science

September 2002

UNIVERSITY OF SOUTHAMPTON

ABSTRACT

FACULTY OF ENGINEERING AND APPLIED SCIENCE
OPTOELECTRONICS RESEARCH CENTRE

Doctor of Philosophy

NOVEL DEVICES IN PERIODICALLY POLED LITHIUM NIOBATE

by Joyce Anne Abernethy

This thesis describes the research carried out to develop several novel periodically poled lithium niobate (PPLN) devices. These devices exploit the ability to invert micro-domains of spontaneous polarisation in ferroelectrics such as lithium niobate.

The fabrication of PPLN devices is described and extensive studies into factors influencing the poling quality are presented. In particular a comparison of material properties of unprocessed lithium niobate material from a range of different suppliers is carried out. Several novel PPLN devices are reviewed and two main devices are investigated - an electro-optically controlled Bragg grating modulator for laser beam switching and modulation and a titanium indiffused waveguide in PPLN for frequency conversion.

The design, fabrication and operation of the electro-optic Bragg modulators is described and results for the first infrared operation at 1064nm of such a device are presented. Several discrepancies are seen between experimental results, both in this thesis and previously published results, and a theoretical model based on Kogelnick's coupled wave analysis. These anomalies are further investigated at visible operation (633nm and 488nm) and solutions and methods for alleviating the discrepancies are presented.

Work on titanium indiffused channel waveguides in PPLN is reported, including a study into fabrication issues and the demonstration of second harmonic generation of 416nm in such a device.

Contents

Chapter 1 : Introduction 1

1.1 Thesis synopsis 2

1.2 History of ferroelectrics and domain reversal 5

1.3 References 9

Chapter 2 : Properties of lithium niobate 15

2.1 Crystal growth 16

2.2 Crystallographic properties 18

2.3 Physical properties 20

2.4 Linear optical properties 20

2.5 Nonlinear optical properties 22

2.5.1 Introduction to nonlinear optics 22

2.5.2 Nonlinear susceptibility tensor 23

2.5.3 Nonlinear wave propagation 25

2.5.4 Phasematching 27

2.5.4.1 Birefringent phasematching 30

2.5.4.2 Beam walk-off and 90° phasematching 32

2.5.4.3 Quasi-phasematching 33

2.6 Ferroelectric properties 35

2.7 Pyroelectric effect 36

2.8 Piezoelectric effect 37

2.9 Electro-optic effect 38

2.10 Photorefractive effect 39

2.11 Chapter conclusions 40

2.12 References 40

Chapter 3 : Periodically poled lithium niobate 43

3.1 Fabrication of PPLN using an electric field poling technique 45
3.1.1 Fabrication process 45
3.1.2 Alternative methods of poling 51
3.1.2.1 Reverse poling method 53
3.1.3 Assessment of PPLN gratings 57
3.2 Material and fabrication issues 60
3.2.1 Material discrepancies 60
3.2.1.1 Thickness variations 62
3.2.1.2 Refractive index variations 64
3.2.1.3 Domain wall deviations 66
3.2.1.4 Surface defects 68
3.2.1.5 Conclusions to material discrepancies 71
3.2.2 Defects arising from the fabrication process 71
3.2.2.1 Poling dots 71
3.2.2.2 Stitching errors 74
3.2.2.3 Photolithography issues 77
3.2.2.4 Conclusions to fabrication issues 78
3.2.3 Conclusions to material and fabrication investigations 78
3.3 Effect of periodic poling on lithium niobate properties 80
3.3.1 Periodic domain inversion and the photorefractive effect 80
3.3.2 Periodic domain inversion and the electro-optic coefficient 82
3.3.3 Periodic domain inversion and the nonlinear coefficient 83
3.3.4 Periodic domain inversion and acid etching 83
3.4 Novel PPLN devices 83
3.4.1 Modulation and switching devices 84
3.4.1.1 Bragg grating modulators 84
3.4.1.2 Total internal reflection switches 85
3.4.2 Nonlinear frequency generations devices 85
3.4.2.1 Titanium waveguides and PPLN 86
3.4.2.2 HexLN 87

3.4.3 Microstructuring of lithium niobate using differential acid etching 88
3.4.3.1 Surface relief gratings 90
3.4.4 Novel PPLN devices summary 94
3.5 Chapter summary 94
3.6 References 95

Chapter 4 : Electro-optic Bragg modulator in periodically poled lithium niobate 104

4.1 Introduction to laser modulation devices 104
4.1.1 Acousto-optic devices 105
4.1.2 Electro-optics devices 107
4.1.3 Summary 108
4.2 Electro-optic Bragg modulators in PPLN 109
4.2.1 Previous work 111
4.3 Theoretical model 116
4.3.1 Assumptions for coupled wave analysis 117
4.3.2 Derivation of the coupled wave equations 118
4.3.3 Solutions of the coupled wave equations 121
4.3.4 Diffraction efficiency of a grating 122
4.3.5 Diffraction efficiency of an unslanted, lossless dielectric transmission grating 123
4.3.6 O-polarised incident light 123
4.3.7 Deviations in incident angle and wavelength 124
4.3.8 Analysis of Kogelnick theory 125
4.3.9 Comparison to bulk electro-optic lithium niobate modulators 127
4.4 Design and fabrication of Bragg modulators 128
4.4.1 Design considerations 128
4.4.2 Fabrication procedure 129
4.4.3 Fabrication issues due to design 129

4.5 Set up and testing of modulator devices 132
4.5.1 Set up considerations 133
4.6 Bragg grating modulator operating at 1064nm 134
4.6.1 Device specifications 134
4.6.2 Results 134
4.6.3 Discussion 138
4.7 Chapter conclusions 139
4.8 References 140

Chapter 5 : Further investigations into Electro-optic Bragg modulator in PPLN 143

5.1 Visible operation of Bragg grating modulators 144
5.1.1 On / off drive voltage with wavelength 144
5.1.2 Effect of wavelength and grating period of Bragg angle 145
5.1.3 Operation at 633nm 145
5.1.4 Operation at 488nm 147
5.2 Investigation into discrepancies 149
5.2.1 Offset in effective zero field point 151
5.2.2 Increased on / off voltages at higher applied voltages 153
5.2.3 Reduced diffraction efficiency 154
5.2.3.1 Grating quality 154
5.2.3.2 Wavelength and angular sensitivity 154
5.2.3.3 Parasitic higher diffraction orders 155
5.2.3.4 Field induced scattering 156
5.2.3.5 Grating profile assumption 159
5.3 Alternative theoretical analyses 159
5.3.1 Background theory 160
5.3.2 Simulations 163
5.3.3 Analysis 163
5.3.4 Conclusions 166
5.4 Chapter conclusions 167
5.5 References 168

Chapter 6 : Titanium indiffused waveguides in periodically poled lithium niobate 170

6.1 Nonlinear optical waveguides 171

6.2 Diffusion of titanium into lithium niobate 173

6.3 Channel waveguide diffusion model 176

6.3.1 Initial variables in the diffusion model 176

6.3.2 Activation energy 177

6.3.3 Diffusion coefficient 177

6.3.4 Diffusion depth 179

6.3.5 Possible modelling extension 179

6.4 Waveguide fabrication 181

6.4.1 Channel waveguides 182

6.4.2 Planar waveguides 183

6.4.3 Furnace diffusion 184

6.4.4 Investigation into diffusion parameters 185

6.4.5 Fabrication issues 188

6.5 Waveguide characterisation 192

6.5.1 Mode profiles 192

6.5.2 Transmission spectra 193

6.6 Titanium waveguides and periodically poled lithium niobate 194

6.6.1 Issues involved in combining the two fabrication processes 194

6.6.1.1 Surface defects 195

6.6.1.2 Spontaneous poling 195

6.6.1.3 Thermal shock limit 197

6.6.1.4 Curie temperature 197

6.6.1.5 Lithium outdiffusion 198

6.6.1.6 Domain inversion due to titanium indiffusion 199

6.6.1.7 Crystal impurities 199

6.6.1.8 Compatibility conclusions 200

6.6.2 Fabrication order 200

6.6.2.1 Method one: PPLN gratings poled first 200

6.6.2.2 Method two: titanium waveguides diffused first 202

6.6.3 Fabrication conclusions 205
6.7 Second harmonic generation in a Ti:PPLN waveguide 205
6.7.1 Optical set up 206
6.7.1.1 Oven design 207
6.7.2 Experimental results 208
6.7.3 Conclusions 212
6.8 Chapter conclusions 213
6.9 References 213

Chapter 7 : Conclusions and future work 218
7.1 Material quality 218
7.2 Electro-optic Bragg grating modulators 220
7.3 Ti:PPLN waveguides 221
7.4 Other periodically poled lithium niobate devices 225
7.5 References 226

Appendix I : Theoretical model of titanium indiffused waveguides 229

Appendix II : MATLAB code 234

Appendix III : Journal and conference papers 239

Acknowledgements

My greatest thanks to my supervisor, Peter Smith, without his constant encouragement, patience and guidance I could never have completed this research and would never have gained as much as I did from it.

Thank you also to Anne Tropper who gave me the freedom and flexibility during the Light Express Roadshow to simultaneously write up.

Thank you to EPSRC, DERA and the ORC for their financial support.

My thanks to the many people I have worked with in the ORC for their help; whether through encouragement, action or taking the mik !! Specifically, thanks to Dave Sager for his help, encouragement and endless ideas, and also to the workshop crew who are solely responsible for my aversion to hacksaws.

In particular I would like to thank my closest friends who have kept me sane both in and out of work – to Steve for his cups of tea, mountain biking and generally being such a cool bloke, to Gates for his totally madness, out-of-date food and electronics knowledge, to Corin for the fun in the cleanroom and at conferences, for voluntarily reading my whole thesis, answering endless questions, and for being my PPLN buddy, and to Catherine for the gossip and support. I'll miss you guys, particularly the lunch-time traditions and the trips to the Crown, but know we'll keep in touch and if I ever get a break from marking and lesson planning, I hope to see you soon !!

To my family, who despite never really understanding what my research was about, were always encouraging and supportive.

And finally to Chris - my best friend, and now husband - for understanding, listening and always being there through both the good and the bad. Words will never express my thanks and respect for you...

"Research ! A mere excuse for idleness;
it has never achieved,
and will never achieve any results of the slightest value."
Benjamin Jowett (1817-1893), British theologian.

"If we knew what it was we were doing,
it would not be called research, would it ?"
Albert Einstein.

"Physics is like sex:
sure, it may give some practical results,
but that's not why we do it."
Richard Feynman.

"If it's green or wriggles, it's biology.
If it stinks, it's chemistry.
If it doesn't work, it's physics..."
anon.

"Very strange people, physicists
- in my experience the ones who aren't
dead are in some way very ill"
Mr Standish "The Long Dark Tea-Time Of The Soul"
by Douglas Adams

Chapter 1

Introduction

Without light no living thing would survive, it is essential to our very existence. Man has always had a great fascination with light, worship of the sun became part of early civilisation and great ancient philosophers such as Pythagoras, Plato and Aristotle began the study of what we now know as photonics – the science of light. Man also learned very quickly to use light, around 400,000 BC early man used fire to light caves and around 1,500 BC light from the sun was first used to tell the time. The Greeks and the Romans were the first to use matter to manipulate light by making lenses from glass spheres filled with water. Today applications of light surround us in everyday life from lasers in CD players to holograms on credit cards. Light is also the driving force behind modern telecommunications and the recent telecommunications revolution was fuelled by the invention of the LASER (Light Amplification by Stimulated Emission of Radiation) in the 1960's [1,2].

This thesis looks at the integration of light and matter and how materials can be engineered to manipulate light. The research carried out is in the specific area of integrated optics which deals with the creation, transmission, switching, guiding and detection of guided optical beams in a plane, and the integration of all these functions on a single substrate in a compact device. The concept of integrated optics was introduced in 1969 by S.E. Miller [3]. Borrowing from the concept of the integrated electronic circuit, Miller proposed an optical integrated circuit (OIC) in which various components could be combined on a single, small, substrate. In recent years, the explosive growth of the optical fibre telecommunications industry has spurred increased interest in optical integrated circuits. In these circuits, light is controlled by

electro-optic, acousto-optic, or thermo-optic effects. Over the past few years, research in the area of integrated optics has focussed on new materials which present ideal properties for nonlinear optical applications such as laser beam modulation, second harmonic generation and optical detection [4]. Overall trends are toward higher levels of integration and more functionality on a single chip while decreasing component size and cost, enabling new commercial opportunities for this technology.

So far, the most commonly used substrate materials for integrated optical devices include III-V compound semiconductors such as gallium arsenide [5,6], the ferroelectric materials lithium niobate [7,8], lithium tantalate [9] and potassium titanyl phosphate (KTP) [10,11], polymers [12,13], and natural materials such as quartz or glass [14,15]. Out of all of these, lithium niobate continues to be the dominant material for integrated optics due to its wide availability, relatively low manufacturing costs, low losses, good stability, and its excellent electro-optical, acousto-optical and nonlinear optical properties [7,16]. Moreover, mature technologies for the fabrication of optical waveguides in this material exist, namely titanium indiffusion and proton exchange [17].

1.1 Thesis synopsis

This thesis consists of seven Chapters including this first introductory Chapter which gives an overview of the thesis content and a historical background to ferroelectrics and domain reversal.

Chapter 2 introduces the material lithium niobate. Several works describe extensively the physics of lithium niobate [18,19,20,21], however this Chapter highlights the main physical and optical properties which influence the fabrication and performance of the periodically poled lithium niobate (PPLN) based optical devices in the following Chapters. Crystal growth techniques are outlined, the crystallographic properties described and a table of commonly used physical properties is presented. The wealth of linear, nonlinear and ferroelectric properties, which make lithium niobate such a unique material, are described. In particular the ability to invert the spontaneous

polarisation is introduced, this forms the basis of all the PPLN devices described in the following Chapters.

Chapter 3 begins by outlining the fabrication procedure for periodically poled lithium niobate (PPLN) using an electric field poling technique with liquid gel electrodes [71,22]. Alternative methods of domain inversion in lithium niobate are then discussed and methods of grating quality assessment presented. The middle part of the Chapter presents an extensive investigation into possible explanations for the significant difference seen in poled grating quality between material sourced from different suppliers, and an investigation into the causes of grating defects arising from fabrication procedures. The Chapter finishes by presenting several novel PPLN devices researched as part of this thesis and in collaboration with other research group members in the ORC which exploit the effect of periodic poling on several lithium niobate properties, such as the electro-optic coefficient, nonlinear coefficient, differential acid etching and the photorefractive effect. These devices include electro-optic Bragg grating modulators [80], frequency conversion devices, for example, 2-dimensional photonic crystals (HexLN) [23], titanium indiffused PPLN channel waveguides [75] and direct bonded PPLN buried waveguides [24], and devices created by differential etching of PPLN including ridge waveguides [85], micro-cantilevers [86] and surface relief gratings [25].

Chapters 4 and 5 describe the work done to investigate and develop an electro-optic Bragg grating modulator in periodically poled lithium niobate [80]. In Chapter 4 a review of currently available electro-optic and acousto-optic modulators, and previous work on electro-optic Bragg modulators by other authors [79,81,82] is presented. A theoretical analysis based on Kogelnik's coupled wave theory [26] is developed and analysed. The design considerations and fabrication process for such modulators is outlined and the first infrared demonstration of a Bragg modulator at 1064nm is reported [27,28]. It is shown that from the results in Chapter 4, and from the review of previous work by Yamada [79,81] and Gnewuch [82] several discrepancies and anomalies exist between the experimental results and the theoretical predictions. To investigate these further an experimental investigation into operation at visible wavelengths is carried out and the results presented in Chapter 5. The second part of Chapter 5 looks at several of the discrepancies in turn and offers explanations and

solutions for each. In particular, the effect on device performance of residual gratings after domain inversion, imperfections in the poled gratings, non-sinusoidal refractive index gratings, multiple reflections from the end faces, photorefractive effects and a new field induced light scattering effect at higher drive voltages due to poling are discussed. Finally, in the concluding part of Chapter 5, an alternative theoretical model is developed which overcomes some of the limiting assumptions of the Kogelnik theory, such as the sinusoidal refractive index grating assumption. This shows a more genuine picture of the diffraction, particularly of higher order diffraction orders and background scatter not covered by the Kogelnik model.

Chapter 6 describes the work carried out to integrate titanium indiffused waveguides and PPLN for use in harmonic frequency conversion [75]. Different types of nonlinear PPLN waveguides are reviewed with titanium indiffusion shown to exhibit several advantages over other methods such as proton exchange [29,30] and direct bonding [24]. The mechanisms of titanium diffusion in lithium niobate are discussed, and a theoretical model developed to enable the mode profile of a diffused waveguide to be calculated for any set of initial diffusion variables. Titanium waveguide fabrication and characterisation is described and investigations into fabrication issues such as spontaneous poling and lithium outdiffusion are included. The research carried out to investigate the integration of titanium indiffused waveguides and periodically poled lithium niobate is described. Although fundamental steps in the fabrication procedures suggest that these two techniques are incompatible, experimental work is presented which endeavours to overcome these problems by adapting or altering the fabrication processes. The final Section in this Chapter presents results achieved in a successful Ti:PPLN device for third order second harmonic generation of 416nm light in a 12μm wide titanium waveguide running through an 8.7μm period PPLN grating.

Finally, Chapter 7 presents conclusions and future work arising from the research presented in this thesis.

1.2 History of ferroelectrics and domain reversal

All the devices researched in this thesis are based on the defining property of ferroelectrics – the ability to reverse the direction of the spontaneous polarisation. This Section looks at the history of ferroelectrics and the development of domain reversal in them.

A ferroelectric crystal is defined as a crystal which belongs to the pyroelectric family and of which the direction of the spontaneous polarisation can be reversed by an electric field. This phenomenon was first recognised over 80 years ago in the 1920's by Valasek in Rochelle salt [31,32], but for over 20 years the phenomenon was thought to be an accident in nature as Rochelle salt remained the only known example. Sodium potassium tartrate tetrahydrate ($NaKC_4H_4O_6.4H_2O$), better known as Rochelle salt, was first synthesized in 1655 by the pharmacist Pierre Seignette in La Rochelle (France) for medical purposes [33]. In 1920, Valasek discovered that the polarisation of Rochelle salt could be reversed by the application of an external field. He recognised ferroelectricity by experiments which showed that the dielectric properties of this crystal were in many respects similar in nature to the ferromagnetic properties of iron in that there was a hysteresis effect in the field–polarisation curve, a Curie temperature, t_c, and an extremely large dielectric and piezoelectric response in and near the ferroelectric region.

It was not until the discovery of a whole series of ferroelectric crystals in the late 1930's by a group in Zurich that term ferroelectricity became more commonly used [34]. The crystals in question were the phosphates and arsenates, in particular the crystal potassium dihydrogen phosphate (KDP). In 1941 Slater presented the first model of a ferroelectric which stimulated interest in ferroelectricity for many physicists [35].

After the discovery of the KDP series another decade passed without further experimental breakthrough, and there was growing conviction that ferroelectrics were comparative rarities in nature. In 1945 barium titanate was independently found to possess ferroelectric properties by groups in Japan, USA and Russia [36,37], and

although it was not realised at the time this material was the predecessor of what is now the largest single class of ferroelectrics – the oxygen octrahedral ferroelectrics. After this discovery considerable effort was spent on a search for new ferroelectrics and slowly they were found; $KNbO_3$ and $KTaO_3$ in 1949 [38], $LiNbO_3$ and $LiTaO_3$ in 1949 [39], and $PbTiO_3$ in 1950 [40]. In the late fifties the breakthrough came and the list of known ferroelectrics ran into the hundreds, as illustrated in Figure 1.1. In the 1960's the modern era of theoretical understanding of ferroelectrics really began with the articles of Anderson [41] and Cochran [42].

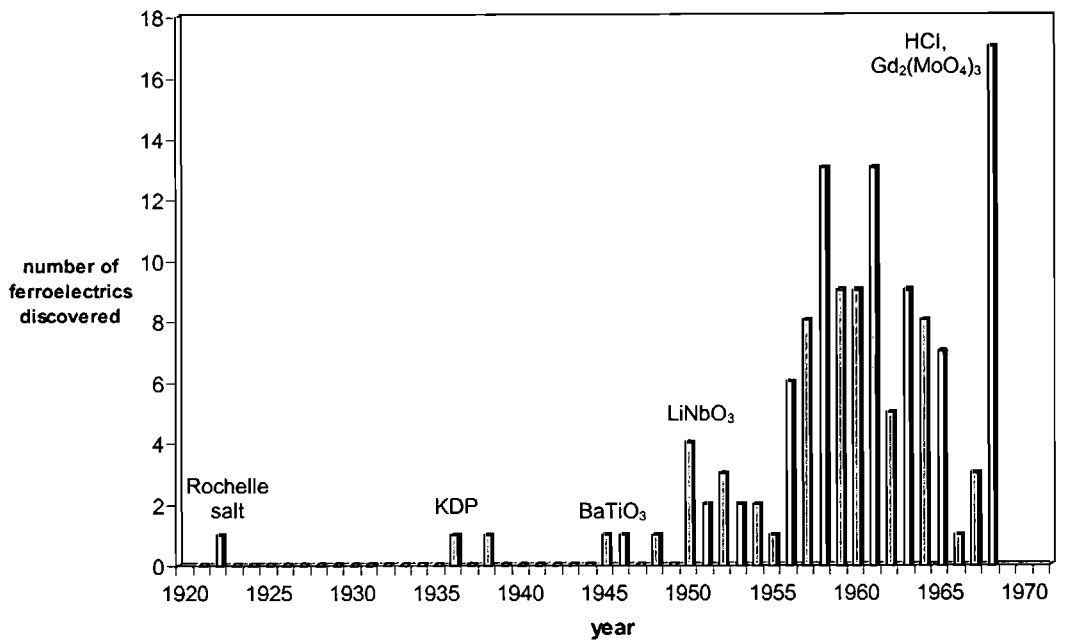

Figure 1.1 The number of ferroelectrics discovered in each year [18]

Although the understanding of the fundamental nature of ferroelectrics was fairly slow in progressing, the number of applications was not. The large dielectric and piezoelectric constants of these materials made them attractive for a variety of applications such as sonar detectors (used in World War II), infrared detection and phonograph pickups. However these early applications did not directly use the ferroelectric nature of the material, namely the large reversible spontaneous polarisation.

It was the advent of the laser in the 1960's [1,2] that brought the need for materials with large nonlinear polarisability at optical frequencies for applications such as

second harmonic generation and electro-optic modulation. As early as 1962 Armstrong et al. proposed a scheme for quasi-phasematching for second harmonic generation of laser light by periodically inverting the polarisation by 180° [43]. These ideas were developed by Miller in 1964, who gave a theoretical treatment of poling and experimented with electric field poling in $BaTiO_3$ [44]. Original fabrication techniques involved raising the ferroelectric material above its Curie temperature and applying a small electric field whilst cooling the crystal through the Curie temperature. This approach is useful for poling bulk crystals, either during or after growth, however it does not provide adequate control for micrometer scale periodic restructuring of the domains and required for frequency conversion, etc.

It was not for a further 20 years that fabrication techniques improved sufficiently to make small scale periodic poling possible. The first controllable micro-scale domain inversion techniques involved heat treatments at, or around, the Curie temperature. In 1985, Thaniyavarn et al. presented results of domain inversion of 4μm wide channels in lithium niobate using titanium indiffusion [45,46]. This idea was first reported by Miyazawa [47] who saw a partial domain switch on the positive z face under the influence of the titanium diffusion process. In 1987, Nakamura et al. reported another heat treatment, LiO_2 outdiffusion, which induced domain inversion in lithium niobate. This was preferred over the titanium indiffusion for some applications as it did not result in the degradation in device performance due to the titanium 'impurities'. Both these treatments resulted in domain inversion only on the positive z face. The presence of titanium or the Li deficiency in the lithium niobate crystal is thought to lower the Curie temperature in that portion [48] and enables the pyroelectrically induced field to reverse the spontaneous polarisation [49]. More recently heat treatments have been used in materials other that lithium niobate. Domain inversion has been reported in KTP by cooling through the Curie temperature [50,51], and in MgO doped $LiNbO_3$ by lithium out diffusion [52].

Periodically poled materials were also produced using a modified growth process which involved the application of a periodically alternating electric field during growth. In the late eighties both periodically poled $LiTaO_3$ [53] and $LiNbO_3$ [54]

devices were realised, however these devices could only be grown for short lengths of a few millimetres.

The next technique developed for domain inversion involved proton exchange in benzoic or pyrophosphoric acid followed by a heat treatment at a temperature just below the Curie temperature [55,56]. By the early 1990's fabrication techniques had developed sufficiently to allow a device of inversion period less than 4μm to be fabricated for first order second harmonic generation of blue light in lithium tantalate [57,58,59] and in lithium niobate [60,61,62].

Periodic domain inversion in KTP for harmonic generation was discovered by Van der Poel et al. during a known waveguide fabrication process [63]. They noticed that ion exchange in a rubidium-nitrate bath also resulted in domain inversion. Shortly after this discovery devices were fabricated using this method for harmonic generation of blue light [64].

All the processes mentioned so far required high temperature treatments which could degrade the samples for certain applications. The first demonstration of room temperature domain inversion was reported in 1991 by Yamada and Kishima in lithium niobate [65]. They discovered that electron bombardment at 25keV on the negative z face of lithium niobate caused domain inversion. This technique was immediately applied to $LiTaO_3$ [66] and $MgO:LiNbO_3$ [67] and developed for harmonic generation [68]. Domain inverted grating periods as fine as 3μm were achieved using this method [68,69].

Although the first discovery of ferroelectricity by Valasek was using an electric field, it was not until 1993 that the fabrication process had been developed sufficiently to produce fine period devices using electric fields at room temperature [70]. This technique was developed shortly after by other groups [71,72] and in other materials, including $LiTaO_3$ [73], $MgO:LiNbO_3$ [74], $Ti:LiNbO_3$ [75], $RbTiOAsO_4$ [76] and $KTiOAsO_4$ (KTA) [77] for use in frequency generation.

Fabrication techniques are continually being developed and improved and although the main driving force behind domain inversion fabrication was for parametric processes such as second harmonic generation, other applications are appearing such as electro-optically controlled lensing [78,79] and deflection [80,81,82], piezoelectric devices such as acoustic wave resonators and reflectors [83,84], and microstructured devices such as ridge waveguides [85] and micro-cantilevers [86].

1.3 References

[1] T H Maiman *'Stimulated optical radiation in ruby'* *Nature* **187** p493 (1960)

[2] P A Franken, A E Hill, C W Peters and G Weinreich *'Generation of optical harmonics'* *Phys. Rev. Lett.* **7** p118 (1961)

[3] S E Miller *'Integrated optics: An Introduction'* *Bell Syst. Tech. J.* **48** p2059-2069 (1969)

[4] J-P Huignard and P Gunter *'Photorefractive Materials and Their Applications: I. Fundamental Phenomena & II. Applications'* Springer-Verlag, New York, (1988, 1989)

[5] L A Knauss, K S Harshavardhan, H M Christen, H Y Zhang, X H He, Y H Shih, K S Grabowski and D L Knies *'Growth of nonlinear optical thin films of $KTa1-_xNb_xO3$ on GaAs by pulsed laser deposition for integrated optics'* *Appl. Phys. Lett.* **73** (26) p3806-3808 (1998)

[6] R J Deri and E Kapon *'Low-Loss III-V Semiconductor Optical Waveguides'* *IEEE J. Quantum Electron.* **27** p626-640 (1991)

[7] M Lawrence *'Lithium niobate integrated optics'* *Rep. Prog. Phys.* **56** (3) p363-429 (1993)

[8] J Schrofel and J Hradilova *'Basic principles and materials on integrated-optics'* *Chemicke. Listy.* **88** (11) p686-695 (1994)

[9] K T Gahagan, V Gopalan, J M Robinson, Q X Jia and T E Mitchell *'Integrated Electro-optic lens/scanner in LiTaO3 single crystal'* *Appl. Opt.* **38** p1186 (1999).

[10] Castech crystals inc. *'Introduction of KTP'* – Data Sheet www.castech.com

[11] J P Ruske, M Rottschalk, B Zeitner, V Grober and A Rasch *'Integrated-optical three-colour-mixing device'* *Elec. Letts.* **34** (4) p363-364 (1998)

[12] S M Garner, S-S Lee, V Chuyanov, A Chen, A Yacoubian, W H Steier and L R Dalton *'Three-dimensional integrated optics using polymers'* *IEEE J. Quantum Elec.* **35** (8) p1146 (1999)

[13] L A Hornak (Editor) *'Polymers for lightwave and integrated optics'* ISBN: 0824786971 Marcel Dekker (1992)

[14] B Poumellec, A Traverse, S Artigaud and J Hervo *'Germanium implantation into substrates for integrated-optics'* *Nucl. Instrum. Meth. B* **86** (3-4) p279-287 (1994)

[15] N A Hall and F L Degertekin *'Integrated optical interferometric detection method for micromachined capacitive acoustic transducers' Appl. Phys. Lett.* **80** (20) p3859-3861 (2002)

[16] *'Properties of lithium niobate' INSPEC data sheet* The institution of electrical engineers (1989)

[17] C Canali, A Carnera, P Mazzoldi and R M De La Rue *'$LiNbO_3$ optical waveguide fabrication by Ti indiffusion and proton exchange: process, performance and stability' SPIE Proc. Int. Opt. Circuit Eng.* **517** p119 (1984)

[18] M E Lines and A M Glass *'Principles and applications of ferroelectrics and relates materials'* Claredon Press Oxford (1977)

[19] R S Weis and T K Gaylord *'Lithium niobate: summary of physical properties and crystal structure' Appl Phys* A37 p191 (1985)

[20] A M Prokhorov and Y S Kuz'minov *'Physics and chemistry of crystalline lithium niobate'* Adam Hilger Bristol (1990)

[21] A Rauber *'Chemistry and physics of lithium niobate'* Current topics in material science 1 E Kaldis, North-Holland (1978)

[22] M Sato, P G R Smith and D C Hanna *'Contact electrode method for fabricating bulk periodically poled LiNbO3' Electron. Lett.* **34** (7) p660-661 (1998)

[23] N G R Broderick, G W Ross, H L Offerhaus, D J Richardson and D C Hanna *'Hexagonally poled lithium niobate: a two-dimensional nonlinear photonic crystal' Phys. Rev. Lett.* **84** p4345-4348 (2000)

[24] C B E Gawith, D P Shepherd, J A Abernethy, D C Hanna, G W Ross and P G R Smith *'Second-harmonic generation in a direct-bonded periodically poled $LiNbO_3$ buried waveguide' Opt. Letts.* **24** (7) p481-483 (1999)

[25] S Mailis, G W Ross, L Reekie, J A Abernethy and R W Eason *'Fabrication of surface relief gratings on lithium niobate by combined UV laser and wet etching' Electronics Letters* **36** (21) p1801-1803 (2000)

[26] H Kogelnik *'Coupled wave theory for thick hologram gratings' The Bell System Technical Journal* **48** (9) p2909-2947 (1969)

[27] J A Abernethy, C B E Gawith, R W Eason and P G R Smith *'First demonstration and optical characteristics of electro-optic Bragg modulators in periodically poled lithium niobate in the near infrared'* Submitted to *App. Phys. Lett.* May (2002)

[28] J A Abernethy, R W Eason and P G R Smith *'Bulk optical Bragg deflectors at 1.064μm based on an electro-optically induced grating in periodically poled lithium niobate' CLEO/Pacific Rim* Chiba **ME2-3** p102-103 15-19th Jul (2001)

[29] M H Chou, K R Parameswaran, M M Fejer and I Brener *'Multiple-channel wavelength conversion by use of engineered quasi-phase-matching structures in $LiNbO_3$ waveguides' Optics Letters* **24** p1157 (1999) and *CLEO'99 CTuW7*

[30] P Baldi, M P De Micheli, K El Hadi, S Nouh, A C Cino, P Aschieri and D B Ostrowsky *'Proton exchange waveguides in $LiNbO_3$ and $LiTaO_3$ for integrated lasers and nonlinear frequency converters' Opt. Eng.* **37** (4) p1193 (1998)

[31] J Valasek *Phys. Rev.* **15** p537 (1920)

[32] J Valasek *Phys. Rev.* **17** p475 (1921)

[33] P J Macquer *Dictionnaire de chymie* **3** p122 (1777)

[34] G Busch and P Scherrer *Naturwiss* **23** p737 (1935)

[35] J C Slater *'Theory of the transition in KH_2PO_4' J. Chem. Phys.* **9** p16 (1941)

[36] B Wul and I M Goldman *C. R. Acad. Sci. URSS* **46** p139 and **49** p177 (1945)

[37] H D Megaw *'Crystal Structure of Barium Titanate' Nature* **155** p184 (1945).

[38] B T Matthias *Phys. Rev.* **75** p1771 (1949)

[39] B T Matthias and J P Remeika *Phys. Rev.* **76** p1886 (1949)

[40] G Shirane, S Hoshino and K Suzuki *'X-ray study of the phase transition in lead titanate' Phys. Rev.* **80** p1105 (1950)

[41] P W Anderson *Fizika Dielektrikov* Akad. Nauk. SSSR, Moscow (1960)

[42] W Cochran *Adv. Phys* **9** p387 (1960)

[43] J A Armstrong, N Bloembergen, J Ducuing and P S Pershan *'Interactions between light waves in a nonlinear dielectric' Phys. Rev.* **127** p1918 (1962)

[44] R C Miller *Phys. Rev.* **A134** p313 (1964)

[45] S Thaniyavarn, T Findakly, D Booher and J Moen *'Domain inversion effects in Ti-$LiNbO_3$ integrated optical devices' Appl. Phys. Letts.* **46** (10) p933 (1985)

[46] J C Peuzin *'Comment on "Domain inversion effects in Ti-$LiNbO_3$ integrated optical devices"' Appl. Phys. Lett.* **48** (16) p1104 (1986)

[47] S Miyazawa *'Ferroelectric domain inversion in Ti-diffused $LiNbO_3$ optical waveguide' J Appl Phys* **50** p4599 (1979)

[48] J R Carruthers, G E Peterson and M Grasso *J. Appl. Phys.* **42** p1846 (1971)

[49] L Huang and N A F Jaeger *'Discussion of domain inversion in $LiNbO_3$' Appl. Phys. Lett.* **65** (14) p1763 (1994)

[50] V D Kugel, G Roseman, N Angert, E Yaschin and M Roth *'Domain inversion in $KTiOPO_4$ crystal near the Curie Point' J. Appl. Phys.* **76** (8) p4823 (1994)

[51] N Angert, M Tseitlin, L Kaplun, E Yashchin and M Roth *'Growth and domain structure of potassium titanyl phosphate crystals pulled from high temperature solutions' J. Cryst. Growth* **137** p116 (1994)

[52] W Y Hsu and M C Gupta *'Domain inversion in MgO-diffused $LiNbO_3$' Appl. Opt.* **32** (12) p2049-2052 (1993)

[53] W S Wang, Q Zou, Z Geng and D Feng *'Study of $LiTaO_3$ crystals grown with a modulated structure: I second harmonic generation in $LiTaO_3$ crystals with periodic laminar ferroelectric domains' J. Cryst. Growth* **79** p706-709 (1986)

[54] A Feisst and P Koidl *'Current induced periodic ferroelectric domain structures in $LiNbO_3$ applied for efficienct nonlinear optical frequency mixing' Appl. Phys. Lett.* **47** p1125-1127 (1985)

[55] K Nakamura, M Hosoya and H Shimizu *'Estimation of thickness of ferroelectric inversion layers in $LiTaO_3$ plates by measuring piezoelectric responses' Japanese J. Appl. Phys.* **29** p95-97 (1990)

[56] H Ahlfeldt, J Webjorn and G Arvidsson *'Periodic domain inversion and generation of blue-light in lithium tantalate waveguides' IEEE Photon. Tech. Lett.* **3** (7) p638-639 (1991)

[57] K Mizuuchi, K Yamamoto and T Taniuchi *'Fabrication of first-order periodically domain inverted structure in $LiTaO_3$' Appl. Phys. Lett.* **59** (13) p1538 (1991)

[58] K Mizuuchi and K Yamamoto *'Characteristics of periodically domain-inverted $LiTaO_3$' J. Appl. Phys.* **72** (11) p5061 (1992)

[59] K Mizuuchi and K Yamamoto *'Domain inversion in $LiTaO_3$ using proton exchange followed by heat treatment' J. Appl. Phys.* **75** (3) p1311 (1994)

[60] E J Lim, M M Fejer, R L Byer and W J Kozlovsky *'Blue light generation by frequency doubling in periodically poled lithium niobate channel waveguide' Electron. Lett.* **25** p731 (1989)

[61] J Webjorn, F Laurell and G Arvidsson *'Blue light generated by frequency doubling of laser diode light in a lithium niobate channel waveguide' IEEE Photon. Tech. Lett.* **1** p316 (1989)

[62] X Cao, R Srivastava and R V Ramaswamy *'Simultaneous blue and green second harmonic generation in quasi-phasematched $LiNbO_3$ waveguide' Appl. Phys. Lett.* **60** (26) p3280 (1992)

[63] C J van der Poel, J D Bierlein, JB Brown and S Colak *'Efficient type I blue 2^{nd} harmonic generation in a periodically segmented $KTiOPO_4$ waveguide' Appl. Phys. Lett.* **57** p2074 (1990)

[64] M J Jongerius, R J Bolt and N A Sweep *'Blue second-harmonic generation in waveguides fabricated in undoped and scandium-doped $KTiOPO_4$' J. Appl. Phys.* **75** (7) p3316 (1994)

[65] M Yamada and K Kishima *'Fabrication of periodically reversed domain structure for SHG in $LiNbO_3$ by direct electron beam lithography at room temperature' Electron. Lett.* **26** p188 (1991)

[66] W-Y Hsu and M C Gupta *'Domain inversion in $LiTaO_3$ by electron beam' Appl. Phys. Lett.* **60** (1) p1 (1992)

[67] S Kurimura, I Shimoya and Y Uesu *'Domain inversion by an electron-beam-induced electric field in $MgO:LiNbO_3$, $LiNbO_3$ and $LiTaO_3$' Japanses J. Appl. Phys. II – Letts.* **35** (1A) pL31-L33 (1996)

[68] M Fujimura, K Kintaka, T Suhara and H Nishihara *'Blue-light generation in $LiNbO_3$ waveguide SHG device with 1^{st} order domain inverted grating formed by EB scanning' Electron. Lette.* **28** (20) p1868-1869 (1992)

[69] A C G Nutt, V Gopalan and M C Gupta *'Domain inversion in $LiNbO_3$ using direct electron beam writing' Appl. Phys. Lett.* **60** (23) p2828 (1992)

[70] M Yamada, N Nada, M Saitoh and K Watanabe *'First-order quasi-phase matched $LiNbO_3$ waveguide periodically poled by applying an external field for efficient blue second-harmonic generation' Appl. Phys. Lett.* **62** (5) p435 (1993)

[71] J Webjorn, V Pruneri, P St J Russell, J R M Barr and D C Hanna *'Quasi-phasematched blue light generation in bulk lithium niobate, electrically poled via periodic liquid electrodes' Electron. Letts.* **30** (11) p894 (1994)

[72] K Kintaka, M Fujimura, T Suhara and H Nishihara *'Fabrication of ferroelectric domain inverted grating for $LiNbO_3$ second harmonic generation devices by voltage application' Electron. Comms. Japan Part II-Electronics* **78** (9) p24-33 (1995)

[73] S Zhu, Y Zhu, Z Zhang, H Shu, H Wang, J Hong and C Ge *'$LiTaO_3$ crystal periodically poled by applying an external pulse field' J. Appl. Phys.* **77** (10) p 5481 (1995)

[74] A Kuroda, S Kurimura and Y Uesu *'Domain inversion in ferroelectric $MgO:LiNbO_3$ by applying electric fields' Appl. Phys. Lett.* **69** (11) p1565 (1996)

[75] J Amin, V Pruneri, J Webjorn, P St J Russell, D C Hanna and J S Wilkinson *'Blue light generation in a periodically poled $Ti:LiNbO_3$ channel waveguide' Opt. Comms.* **135** (1-3) p41-44 (1996)

[76] ZW Hu, P A Thomas, J Webjorn and G M Lioacono *'Domain inversion in $RbTiOAsO_4$ using electric field poling' J. Phys. D: Appl. Phys.* **29** (6) p1681-1684 (1994)

[77] G Rosenman, A Skliar, Y Findling, P Urenski, A Englander, P A Thomas and Z W Hu *'Periodically poled $KTiOAsO_4$ crystals for optical parametric oscillation' J. Phys. D: Appl. Phys.* **32** (14) pL49-L52 (1999)

[78] V Gopalan, K T Gahagan, M Kawas, QX Jia, J M Robinson, T E Mitchell, T E Schlesinger and D D Stancil *'Integration of electro-optic lenses and scanners on ferroelectric $LiTaO_3$' Int. Ferroelectrics* **25** (1-4) p371-376 (1999)

[79] M Yamada, M Saitoh and H Ooki *'Electric-field induced cylindrical lens, switching and deflection devices composed of the inverted domains in $LiNbO_3$ crystals' Appl Phys Lett* **69** p3659-3661 (1996)

[80] J A Abernethy, R W Eason and P G R Smith *'Investigation into bulk optical Bragg deflectors based on an electro-optically induced grating in periodically poled lithium niobate' International Workshop on Periodically Microstructured Nonlinear Optical Materials* Madrid 10-13th Jun (2001)

[81] M Yamada *'Electrically induced Bragg-diffraction grating composed of periodically inverted domains in lithium niobate crystals and its application devices' Rev. Sci. Inst.* **71** no.11 p4010-4016 (2000)

[82] H Gnewuch, C N Pannell, G W Ross, P G R Smith and H Geiger *'Nonosecond response of Bragg deflectors in periodically poled $LiNbO_3$' IEEE Photonics Tech Lett* **10** p1730-1732 (1998)

[83] K Nakamura and H Shimizu *'Ferroelectric inversion layers formed by heat treatment of proton-exchange $LiTaO_3$' Appl. Phys. Lett.* **56** (16) p1535-1536 (1990)

[84] K Nakamura and H Shimizu *IEEE Ultrasonic Symposium* p527 (1983)

[85] I E Barry, G W Ross, P G R Smith and R W Eason *'Ridge waveguides in lithium niobate fabricated by differential etching following spatially selective domain inversion' Appl Phys Lett* **74** p1487 (1999)

[86] C Sones, S Mailis, V Apostolopoulos, I E Barry, C B E Gawith, P G R Smith and R W Eason *'Fabrication of piezoelectric micro-cantilevers in domain engineered $LiNbO_3$ single crystals' J. Micromech. Microeng.* **12** (1) p53-57 (2002)

Chapter 2

Properties of lithium niobate

In this Chapter we briefly describe the main physical and optical properties which influence the fabrication process and which affect the performance of the periodically poled lithium niobate (PPLN) based optical devices described in the following Chapters.

Being an established material, several good reviews describe the physics of lithium niobate. The work by Lines and Glass [1] provides a good general overview of the properties and applications of ferroelectrics with sections on lithium niobate. The book by Prokhorov and Kuz'minov [2], the chapter by Rauber [3], and the paper by Weis and Gaylord [4] all look specifically at lithium niobate, detailing more in depth information about the crystal structure, and the physical and optical properties of lithium niobate. A review of growth techniques is also given in [2].

Its unique physical properties make lithium niobate an important material for applications in a wide range of fields, such as radar, microwave communications, telecommunications, frequency conversion and holographic data storage. It is a man-made, naturally birefringent, ferroelectric material with large pyroelectric, piezoelectric, acousto-optic, electro-optic and photo-elastic coefficients. It also exhibits very strong bulk photovoltaic and photorefractive effects. Worldwide production exceeds five tonnes per annum making it the second largest volume man-made crystal after silicon [5].

2.1 Crystal Growth

Crystals of lithium niobate were first obtained in 1949 by Matthias and Remeika [6], who grew them from a melt solution. Nassau and Ballman [7] subsequently studied the growth conditions, the crystal structure and the electrophysical properties. As soon as it became obvious that lithium niobate was a highly promising material for acoustical [8] and optical applications [9], interest in producing perfect single-crystal lithium niobate and the need for developing industrial technologies to ensure the fabrication of high quality crystals with reproducible characteristics have both greatly increased.

At present, single-crystal lithium niobate is mainly grown in air by the Czochralski technique [2,10]. A cylindrical crystal is pulled vertically from a melt, growth having been initiated by a small seed crystal. The crystal and melt are rotated in opposite directions to aid homogeneity of the melt and to prevent thermal gradients at the crystal-melt interface. After growth the boule is cooled before it is cut into the shapes and orientations required. As a rule, Czochralski grown lithium niobate single crystals are multi-domain, to produce single domain material the crystal is grown in an electric field. The growth conditions are highly critical during growth and any thermal gradients or shocks can affect the result greatly. Conditions necessary for the production of perfect crystals are suggested by Prokhorov and Kuz'minov [2]. These conditions can be finely tuned so that more complex structures can be produced. This has demonstrated recently by Bermudez [11] where the Czochralski technique was used to pull a periodically poled crystal. The first fabrication of periodically poled lithium niobate using a growth technique was in 1985 by Feisst and Koidl [12]. They fabricated periodic laminar ferroelectric domains of width 8μm in chromium doped lithium niobate by modulating the bias current during Czochralski growth.

The composition of the growth product is determined by the composition of the melt or solution it is drawn from, allowing the addition of dopants and control of the elemental ratios in the crystal. Mostly all commercially available lithium niobate material is congruently grown, ie. the melt is lithium deficient (the ratio of lithium to niobate is 0.94). Conversely, stoichiometric lithium niobate has an almost ideal 50:50

ratio resulting in much improved performance characteristics. It can be seen from the phase diagram of the Li_2O–Nb_2O_5 system [Figure 2.1,2,13], when growing lithium niobate crystals using the Czochralski technique, there is a unique point where compositions of melt and the grown crystal are identical throughout the growing process. This point corresponds to the congruent composition (48.6 mol.% of Li_2O) which has the highest melting temperature with respect to other compositions in the solid solution range. Due to these features, there are no difficulties for the growing of large congruent lithium niobate crystals with good homogeneity. In contrast, the stoichiometric composition one has no similar characteristic feature, it is only one of many possible compositions of the solid solution. The stoichiometric crystals can be grown from a melt containing 58.0 mol.% of Li_2O to produce a near 50:50 ratio. Such a difference in the composition of the melt and of the growing crystal results in cooling problems and variations in the crystal composition at different stages of the process.

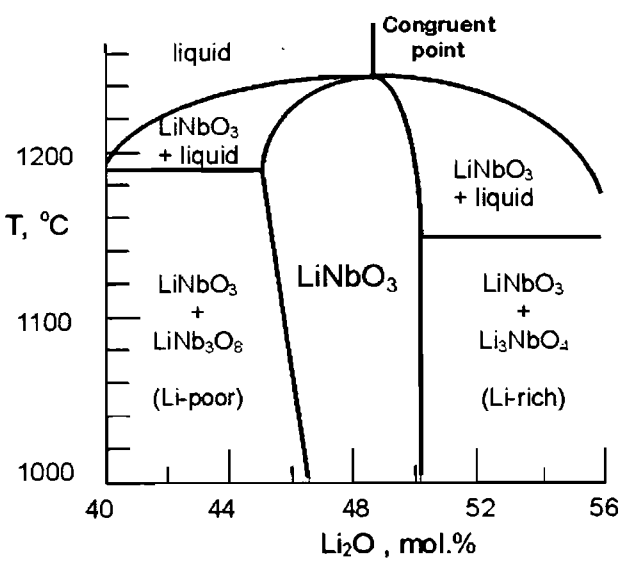

Figure 2.1 Phase diagram of the Li_2O-Nb_2O_5 system [13]

Other methods of crystal growth include the edge-defined film-fed growth (EFG) method, which allows the production of non cylindrical boule shapes, and top seeded growth from solution, which has been investigated as a route to producing crystals with stoichiometric composition [14]

The samples used for the research presented in this thesis have originated entirely from z-cut wafers of varying thickness, from 200μm to 1mm from several suppliers including Crystal Technology, Yamaju Ceramics and Castech Wafers. The material was congruent in composition, ie. 48.4% LiO by molar ratio [15]. The sample faces had an optical finish, achieved by a combination of mechanical and chemical polishing.

2.2 Crystallographic properties

At temperatures below the Curie temperature of 1210°C, lithium niobate is ferroelectric, exhibiting spontaneous crystal polarisation due to charge separation of the lithium and niobate ions. In this ferroelectric phase, lithium niobate possesses trigonal crystal symmetry with 3m point group symmetry about the optic or c axis. It consists of planar sheets of oxygen atoms in a distorted hexagonal close-packed configuration. In between these layers are the Li and Nb ions as shown in Figure 2.2(a). Above the Curie temperature, lithium niobate ceases to be ferroelectric and becomes paraelectric and nonpolar. This is due to the movement of the Li and Nb ions into a centrosymmetric position with the Nb ion lying in the plane of one of the oxygen layers and the Li ion lying exactly half way between the layers, Figure 2.2(b).

Crystallographic planes or particular directions within a 3-dimensional crystal are described by Miller indices. For hexagonal crystal such as lithium niobate a set of four Miller indices is used to describe the crystal planes, defined by $[a_1,a_2,a_3,c]$ as shown in Figure 2.3.

Lithium niobate cleaves naturally along the $[01\bar{1}2]$ plane, but due to its 3 fold rotational symmetry there are two other cleavage planes - $[10\bar{1}2]$ and $[1\bar{1}02]$. The natural cleavage planes are due to the vacant sites in the oxygen structure which lie in these planes. It will be seen in Chapter 3 that the inverted domain walls in a periodically poled structure also follow the directions of these planes.

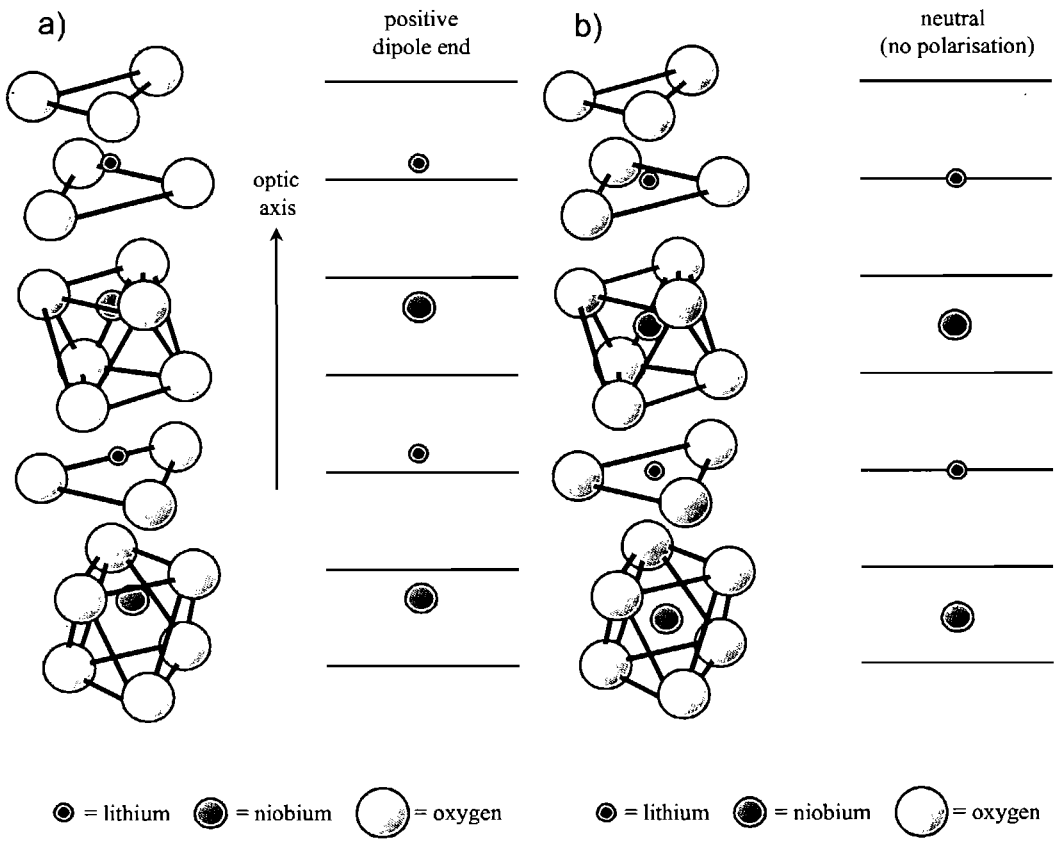

Figure 2.2 *Diagram of lithium niobate crystal structure in a) ferroelectric phase and b) paraelectric phase [4]*

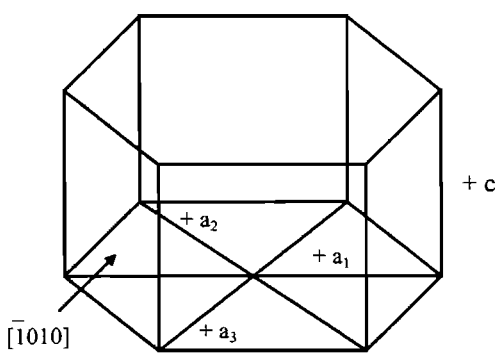

Figure 2.3 *Miller indices of lithium niobate*

A Cartesian co-ordinate system (x,y,z) is used to describe the physical tensor properties of lithium niobate, and these relate to crystal hexagonal axes. The z axis is chosen to be parallel to the c axis, also known as the optic axis. The x axis is chosen to coincide with any of the axes a_1, a_2 or a_3. Then the y-axis is chosen such that the system is right handed, hence the y-axis lies along one of the mirror symmetry planes. The sense of the y and z planes can be determined either by compression along that

axis or cooling of the crystal, however as the x axis is perpendicular to a mirror plane, its sense cannot be determined in this way, but can be found once y and z are known by using the right hand rule.

2.3 Physical properties

Table 2-1 lists some of the more common physical properties of lithium niobate.

Characteristic	Value
Chemical formula	$LiNbO_3$
Density	4.612 g cm^{-3}
Melting point	1260 °C
Curie point	1210 °C
Thermal expansion coefficients @25°C	
a axis	16.7×10^{-6} / °C
c axis	2.0×10^{-6} / °C
Mechanical hardness	5 Mohs
Specific heat @25 °C	0.15 cal / g / °C
Thermal conductivity @25 °C	10^{-2} cal / cm sec °C
Molecular weight	147.9
Solubility	Insoluble in H_2O

Table 2-1 Physical properties of lithium niobate [2]

2.4 Linear optical properties

Lithium niobate is a uniaxial birefringent crystal with ordinary refractive index, n_o (electric field polarised normal to the c axis), and extraordinary refractive index, n_e (electric field polarised along the c axis). These refractive indices are dependent on the wavelength of the incident electromagnetic wave and the crystal temperature. The Sellmeier equation [16] used to describe this dependence within the transparency range of lithium niobate, 340 to 4600 nm, is given by ;

Equation 2-1

$$n_{e,o}(\lambda, T) = \sqrt{A_1 + \frac{A_2 + B_1 F}{\lambda^2 - (A_3 + B_2 F)^2} + B_3 F - A_4 \lambda^2}$$

where λ is the wavelength of the incident light in μm and $F = (T - T_o)(T + T_o + 546)$ is a function of the crystal temperature T in degrees centigrade, with T_o= 24.5°C as a reference temperature. The other coefficients can be found in ref. 16 for ordinary and extraordinary refractive indices. Figure 2.3 shows this equation graphically for the ordinary and extraordinary refractive index at T = T_o = 24.5°C.

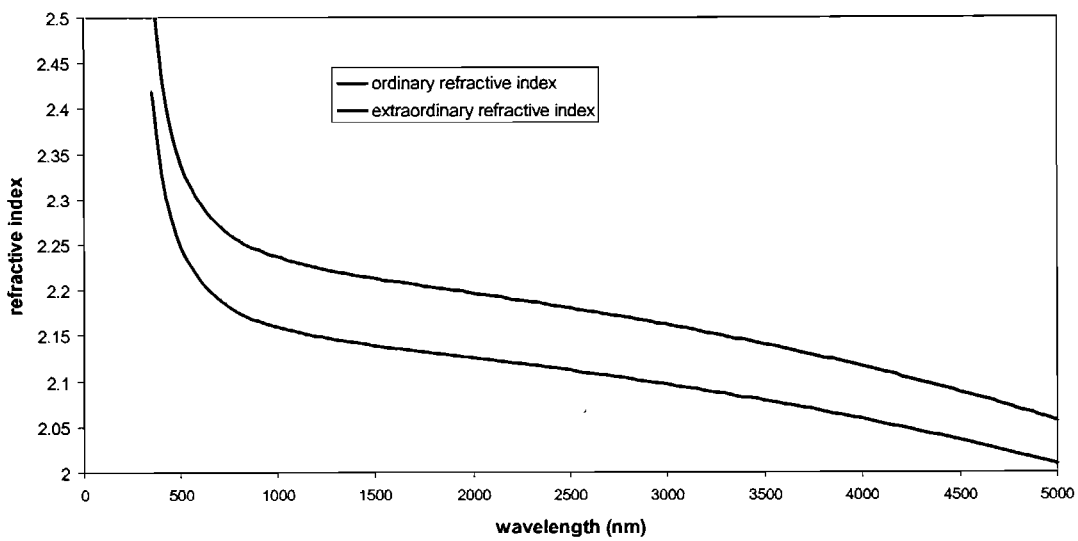

Figure 2.4 Graph showing ordinary and extraordinary refractive index of lithium niobate with wavelength within its optical transmission range

More recently, a revised Sellmeier equation for the extraordinary refractive index has been reported [17]. This is more accurate for predicting refractive indices at long wavelengths, as has been used with PPLN [18,19], and is given by ;

Equation 2-2
$$n_e(\lambda, T) = \sqrt{A_1 + B_1 F + \frac{A_2 + B_2 F}{\lambda^2 - (A_3 + B_3 F)^2} + \frac{A_4 + B_4 F}{\lambda^2 - A_5^2} - A_6 \lambda^2}$$

where as above λ is the wavelength in μm, $F = (T - T_o)(T + T_o + 546)$ with T_o= 24.5°C and the other coefficients can be found in ref. 17. Figure 2.5 shows a plot of the difference in calculated extraordinary refractive index using the old and new

formulae with T=150°C. It can be seen that the greatest difference occurs at wavelengths above 5μm.

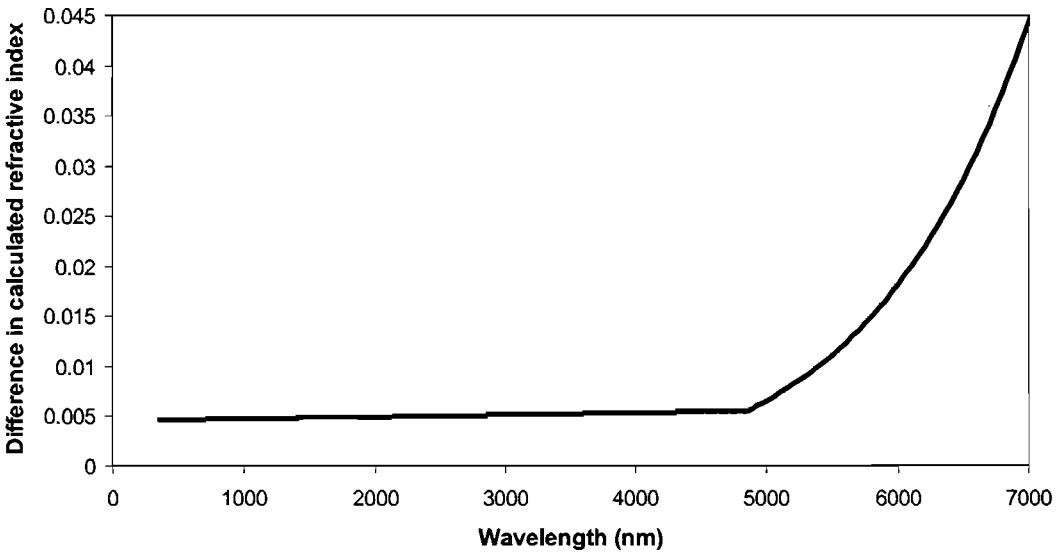

Figure 2.5 *Graph showing the difference in the calculated extraordinary refractive index using the old and new formulae with wavelength*

2.5 Nonlinear optical properties

This Section reviews the area of nonlinear optics in general and discusses the properties of lithium niobate which make it suitable for phasematching for nonlinear processes such as harmonic frequency conversion. In particular the ability to alter the spontaneous polarisation of lithium niobate and hence alternate the sign of the nonlinear susceptibility makes lithium niobate suitable for quasi-phasematching.

2.5.1 Introduction to nonlinear optics

In 1961, shortly after the demonstration of the laser, Franken et al. [20] generated the second harmonic of a ruby laser in a quartz crystal. The success of this experiment relied directly on the enormous increase of power density made available by a laser source compared to incoherent sources. It was the invention of the laser which has enabled several nonlinear phenomena, which previously were regarded as theoretical

curiosities, to be observed and exploited. A laser source provides power densities greater than 10^9 Wcm^{-2}, corresponding to electric field strengths of 10^6 Vcm^{-1}. This field strength is comparable to atomic field strengths and therefore it was not too surprising that materials responded in a nonlinear manner to the applied field.

The early work in nonlinear optics concentrated on second harmonic generation. Harmonic generation in the optical region is similar to the more familiar harmonic generation at radio frequencies, with one exception. In optical harmonic generation, the nonlinear process takes part over a distance much larger than the radiation wavelength. This leads to consideration of propagation effects since the incident electromagnetic radiation interacts over an extended distance with the generated nonlinear polarisation. If this interaction it to be efficient, the phase of the propagating wave and the generated polarisation must be correct. This is known as phasematching. For second harmonic generation, phasematching implies that the phase velocity of the fundamental and second harmonic waves are equal in the nonlinear material. Since all optical materials are dispersive, it is not possible to achieve equal phase velocities in isotropic materials. Shortly after Franken's first relatively inefficient non-phasematched second harmonic generation experiment, Kleinman [21], Giordmaine [22], and Maker et al [23], showed that the phase velocity matching could be achieved in birefringent crystals by using the crystal birefringence to offset the dispersion.

2.5.2 Nonlinear susceptibility tensor

Based on the treatment in Davis [24], the following Section introduces polarisation in nonlinear media. The polarisation of an isotropic linear dielectric medium is given by

Equation 2-3 $$\underline{P} = \varepsilon_0 \chi \underline{E}$$

where χ is the linear susceptibility, ε_o is the permittivity of free space and $\underline{E}$ is the electric field. The resulting electric displacement is given by

Equation 2-4 $$\underline{D} = \varepsilon_0 \underline{E} + \underline{P} = \varepsilon_0 \varepsilon_r \underline{E}$$

where ε_r is the relative permittivity $(1+\chi)$, or the dielectric constant. In an anisotropic medium, the induced polarisation is not necessarily parallel to the electric field direction and the electric displacement is now given by ;

Equation 2-5
$$D_k = \varepsilon_o \sum_l \varepsilon_{kl} E_l \quad \text{or} \quad \frac{1}{\varepsilon_0}\begin{pmatrix} D_x \\ D_y \\ D_z \end{pmatrix} = \begin{pmatrix} \varepsilon_{xx} & \varepsilon_{xy} & \varepsilon_{xz} \\ \varepsilon_{yx} & \varepsilon_{yy} & \varepsilon_{yz} \\ \varepsilon_{zx} & \varepsilon_{zy} & \varepsilon_{zz} \end{pmatrix}\begin{pmatrix} E_x \\ E_y \\ E_x \end{pmatrix}$$

where the dielectric constant, ε_{kl}, is a symmetric tensor.

In a nonlinear dielectric medium the polarisation becomes nonlinear and for spectral regions away from any absorption resonances, is given by;

Equation 2-6
$$\underline{P} = \varepsilon_0 \chi_1 \underline{E} + \chi_2 \underline{E}^2 + \chi_3 \underline{E}^3 + \ldots$$

Therefore the resultant electric displacement is given by;

Equation 2-7
$$\underline{D} = \varepsilon_0 \underline{E} + \underline{P} = \varepsilon_0 \varepsilon_r \underline{E} + P_{NL}$$

The nonlinear polarisation is defined as;

Equation 2-8
$$P_{NL_i} = 2 d_{ijk} E_j E_k$$

where E_j and E_k are the complex field amplitudes and d_{ijk} is the nonlinear susceptibility tensor. Using Kleinman's symmetry conjecture [21], which states that in a lossless medium d_{ijk} is symmetric under any permutation of its indices, d_{ijk} can be reduced to a 3×6 matrix. Therefore the nonlinear polarisation can be written as ;

Equation 2-9
$$\begin{pmatrix} P_1 \\ P_2 \\ P_3 \end{pmatrix} = 2 \times \begin{pmatrix} d_{11} & d_{12} & d_{13} & d_{14} & d_{15} & d_{16} \\ d_{21} & d_{22} & d_{23} & d_{24} & d_{25} & d_{26} \\ d_{31} & d_{32} & d_{33} & d_{34} & d_{35} & d_{36} \end{pmatrix} \begin{pmatrix} E_x^2 \\ E_y^2 \\ E_z^2 \\ 2E_xE_y \\ 2E_yE_z \\ 2E_xE_z \end{pmatrix}$$

where the notation used for d_{ijk} is

i : x = 1, y = 2, z = 3

j k : xx = 1, yy = 2, zz = 3,

zy = yz = 4, xz = zx = 5,

xy = yx = 6

It is the nonlinear susceptibility tensor, d_{ijk}, which determines the strength of nonlinear interactions within a crystal. In centrosymmetric crystals d_{ijk} is zero, which explains why nonlinear effects such as harmonic generation and frequency mixing only occur in non-centrosymmetric crystals such as lithium niobate.

2.5.3 Nonlinear wave propagation

This Section takes a more in-depth look at nonlinear processes using Maxwell's equations, as defined in Davis [24];

Equation 2-10
$$\nabla \times \underline{H} = \underline{j} + \frac{\partial \underline{D}}{\partial t} = \underline{j} + \frac{\partial}{\partial t}(\varepsilon_0 \underline{E} + \underline{P})$$

and $P = \varepsilon_0 \chi_L E + P_{NL}$ where $\underline{j} = \sigma \underline{E}$

Therefore substitution gives ;

Equation 2-11
$$\nabla \times \underline{H} = \sigma \underline{E} + \frac{\partial}{\partial t} \varepsilon \underline{E} + \frac{\partial P_{NL}}{\partial t}$$

Now consider;

Equation 2-12
$$\nabla \times \underline{E} = -\frac{\partial}{\partial t} \mu_0 \underline{H}$$

$$\underline{\nabla} \times \underline{\nabla} \times \underline{E} = -\frac{\partial}{\partial t}(\mu_0 \underline{\nabla} \times \underline{H}) = \underline{\nabla}(\underline{\nabla}.\underline{E}) - \nabla^2 \underline{E}$$

Neglecting anisotropy in the medium and assuming ε_r is scalar, this gives the Nonlinear Wave Equation :

Equation 2-13
$$\nabla^2 E = \mu_0 \sigma \frac{\partial E}{\partial t} + \mu_0 \varepsilon \frac{\partial^2 E}{\partial t^2} + \mu_0 \frac{\partial^2 P_{NL}}{\partial t^2}$$

We now consider the specific problem in one dimension, propagating along z, where $\delta/\delta y = \delta/\delta x = 0$. We also consider the electric fields to be travelling plane waves of frequencies ω_1, ω_2 and ω_3, given by;

$$E_i^{\omega_1}(z,t) = \tfrac{1}{2}\left(E_{1i}(z)e^{i(\omega_1 t - k_1 z)} + c.c\right)$$

Equation 2-14

$$E_k^{\omega_2}(z,t) = \tfrac{1}{2}\left(E_{2k}(z)e^{i(\omega_2 t - k_2 z)} + c.c\right)$$

$$E_j^{\omega_3}(z,t) = \tfrac{1}{2}\left(E_{3j}(z)e^{i(\omega_3 t - k_3 z)} + c.c\right)$$

where i, j, k are x, y or z and $\omega_3 = \omega_1 + \omega_2$.

We are interested in how these three waves relate to each other according to the nonlinear wave equation. Consider the three cases : $\omega_1 = \omega_3 - \omega_2$, $\omega_2 = \omega_3 - \omega_1$, $\omega_3 = \omega_1 + \omega_2$.

Firstly $\omega_1 = \omega_3 - \omega_2$, we have $P_{NL}^{\omega_1} = 2d_{ijk}E_k^{\omega_2}E_j^{\omega_3}$ and substituting in from above ;

Equation 2-15

$$P_{NL} = \frac{d_{ijk}}{2}\left[E_{2k}^{*}E_{3j}e^{i[(\omega_3-\omega_2)t-(k_3-k_2)z]}\right] + c.c. = \frac{d_{ijk}}{2}\left[E_{2k}^{*}E_{3j}e^{i[\omega_1 t - k_3 z - k_2 z]}\right] + c.c$$

Substituting this into the nonlinear wave equation ;

Equation 2-16

$$\nabla^2 E_{1i}(z,t) = \frac{\partial^2}{\partial z^2}E_{1i}(z,t) = \tfrac{1}{2}\frac{\partial^2}{\partial z^2}\left[E_{1i}(z)e^{i(\omega_1 t - k_1 z)}\right] + c.c.$$

$$= -\tfrac{1}{2}\left[k_1^2 E_{1i}(z) + 2ik_1\frac{dE_{1i}(z)}{dz}\right]e^{i(\omega_1 t - k_1 z)} + c.c.$$

Assuming the slow varying amplitude approximation ;

Equation 2-17

$$\frac{dE_{1i}}{dz}k_1 >> \frac{d^2E_{1i}}{dz^2}$$

Using the one dimensional wave equation for E_{1i}, we can write ;

Equation 2-18

$$\tfrac{1}{2}\left[k_1^2 E_{1i}(z) + 2ik_1\frac{dE_{1i}(z)}{dz}\right]e^{i(\omega_1 t - k_1 z)} + c.c.$$

$$= -\mu_r\mu_0\varepsilon_r\varepsilon_0\left[\omega_1^2 E_{1i}e^{i(\omega_1 t - k_1 z)} + c.c.\right] - \mu\mu_0\frac{\partial^2}{\partial t^2}\left[P_{NL_i}^{\omega_1}(z,t)\right]$$

By substituting in for P_{NL} and recognising $k_1^2 = \omega_1^2\mu_o\varepsilon$ gives ;

Equation 2-19

$$\frac{1}{2}\left[k_1^2 E_{1i}(z) + 2ik_1 \frac{dE_{1i}(z)}{dz}\right] e^{i(\omega_1 t - k_1 z)} = -k_1^2 E_{1i} e^{i(\omega_1 t - k_1 z)} - \mu_0 d_{ijk}\left[E_{3j} E_{2k}^* \omega_1^2 e^{i(\omega_1 t + k_2 z - k_3 z)}\right]$$

Tidying up gives :

Equation 2-20

$$\frac{dE_{1i}(z)}{dz} = -\frac{i\omega_1}{2}\sqrt{\frac{\mu_0}{\varepsilon_1}} d_{ijk} E_{3j} E_{2k}^* e^{-i(k_3 - k_2 - k_1)z}$$

Similarly for $\omega_2 = \omega_3 - \omega_1$ and $\omega_3 = \omega_1 + \omega_2$ we get :

Equation 2-21

$$\frac{dE_{2k}(z)}{dz} = -\frac{i\omega_2}{2}\sqrt{\frac{\mu_0}{\varepsilon_2}} d_{ijk} E_{1i}^* E_{3j} e^{-i(k_3 - k_2 - k_1)z}$$

Equation 2-22

$$\frac{dE_{3j}(z)}{dz} = -\frac{i\omega_3}{2}\sqrt{\frac{\mu_0}{\varepsilon_3}} d_{ijk} E_{1i} E_{2k} e^{-i(k_1 + k_2 - k_3)z}$$

These equations can be combined to give ;

Equation 2-23

$$\frac{dE_{1i}(z)}{dz} = \frac{dE_{2k}(z)}{dz} = -\frac{dE_{3j}(z)}{dz}$$

This is known as the Manley-Rowe relation [25] and is essentially a statement of the principle of energy conservation. It holds for any nonlinear interaction involving three frequencies.

These equations are fundamental nonlinear equations and describe all possible interactions between collinear plane electromagnetic waves of frequencies ω_1, ω_2 and ω_3. For example $\omega_1 + \omega_2 = \omega_3$, $\omega_3 - \omega_1 = \omega_2$, $\omega_3 - \omega_2 = \omega_1$, $\omega_3 = \omega_1 + \omega_2$, etc. All these interactions can occur simultaneously in a medium, however which process dominates depends on the relative irradiance levels of the three waves, absorption and the phasematching conditions.

2.5.4 Phasematching

A good nonlinear material provides an efficient energy exchange between the interacting incident and harmonic waves over its entire length. However the

difference in phase velocities of fields oscillating at different frequencies can produce a cumulative phase mismatch which can seriously limit the effective useful length of the nonlinear device. Phasematching is a method of compensating for this phase difference and thus optimising the conversion efficiency in a nonlinear process.

Consider a sum generation process in a nonlinear crystal where two input beams of frequency ω_1 and ω_2 combine to give a third frequency beam : $\omega_1 + \omega_2 = \omega_3$, shown in Figure 2.6.

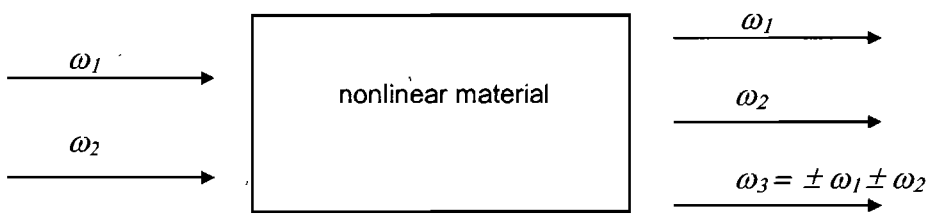

Figure 2.6 Nonlinear crystal mixing process

First consider a very low efficiency generation of ω_3, then very little power is transformed from ω_1 and ω_2. It could therefore be assumed ;

Equation 2-24
$$\frac{dE_1}{dz} \approx \frac{dE_2}{dz} \approx 0$$

From earlier this leaves only one equation ;

Equation 2-25
$$\frac{dE_3(z)}{dz} = -\frac{i\omega_3}{2}\sqrt{\frac{\mu_0}{\varepsilon_3}}d_{eff}E_1E_2e^{-i(k_1+k_2-k_3)z}$$

where $k_1 + k_2 - k_3 = \Delta k$.

Consider a length of crystal, L, we can integrate the above equation to find the magnitude of ω_3 as it emerges from the crystal ;

Equation 2-26
$$E_3(L) = -\frac{i\omega_3}{2}\sqrt{\frac{\mu_0}{\varepsilon_3}}d_{eff}E_1E_2\int_0^L e^{-i\Delta kz}dz = \frac{\omega_3}{2}\sqrt{\frac{\mu_0}{\varepsilon_3}}d_{eff}E_1E_2\left(\frac{-i\Delta kL-1}{\Delta k}\right)$$

$$\frac{e^{-i\Delta kL}-1}{\Delta k}$$

To find the irradiance of ω_3 in Wm^{-2} we use ;

Equation 2-27
$$I_3 = \tfrac{1}{2}\sqrt{\frac{\varepsilon}{\mu_0}}E_3E_3^*$$

Therefore :

Equation 2-28
$$I_3 = \sqrt{\frac{\varepsilon_3}{\mu_0}}\frac{\omega_3^2}{8}d_{eff}^2E_1E_1^*E_2E_2^*\frac{\left(e^{-i\Delta kL}-1\right)\left(e^{i\Delta kL}-1\right)}{\Delta k^2}$$

Substituting in for I_1 and I_2 gives ;

Equation 2-29
$$I_3 = \frac{\omega_3^2}{2}\left(\frac{\mu_0}{\varepsilon_3}\right)^{\frac{3}{2}}d_{eff}^2I_1I_2\frac{2-e^{-i\Delta kL}-e^{i\Delta kL}}{\Delta k^2}$$

$$= \frac{\omega_3^2L^2}{2}\left(\frac{\mu_0}{\varepsilon_3}\right)^{\frac{3}{2}}d_{eff}^2I_1I_2\left(\frac{\sin\frac{\Delta kL}{2}}{\Delta kL/2}\right)^2$$

We can see that the irradiance of ω_3 is proportional to three main terms ;

Equation 2-30
$$I_1I_2,\qquad \frac{d_{eff}^2}{\varepsilon^{\frac{3}{2}}} = \frac{d_{eff}^2}{n^3},\qquad \text{and}\qquad \left(\frac{\sin\frac{\Delta kL}{2}}{\frac{\Delta kL}{2}}\right)^2L^2 = \operatorname{sinc}^2\left(\frac{\Delta kL}{2}\right)L^2.$$

Therefore to increase the conversion efficiency to ω_3, these terms must be maximised. First consider the last term, which has maximum value, *sinc = 1*, when $\Delta k = 0 = k_1 + k_2 - k_3$. Therefore we want $k_3 = k_1 + k_2$, which is known as 'phasematching' and is also a wavevector conservation requirement. As $kc = \omega n$, then it follows that $\omega_3 n_3 = \omega_1 n_1 + \omega_2 n_2$ and therefore to satisfy phasematching, $n_1 = n_2 = n_3$. However normal dispersion in the crystal gives $n_3 > n_2 > n_1$, which would mean $\omega_3 n_3 > \omega_1 n_1 + \omega_2 n_2$, and imply $\Delta k \neq 0$, as shown in Figure 2.7.

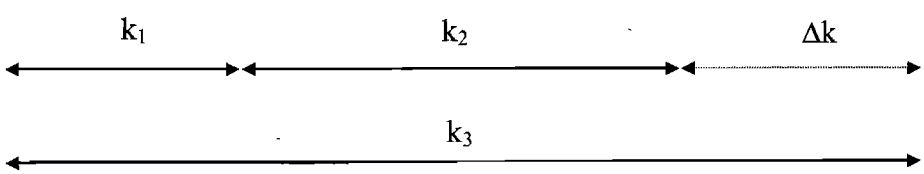

Figure 2.7 Phasematching

There are different methods of overcoming this problem including birefringent phasematching (BPM), and quasi-phasematching (QPM), which are discussed in the following sections.

It can also be seen from the second term, that to increase the efficiency of the nonlinear conversion, the nonlinear susceptibility tensor, d_{eff}, should be as large as possible. The nonlinear susceptibility tensor for lithium niobate is given by ;

Equation 2-31

$$\begin{pmatrix} P_x \\ P_y \\ P_z \end{pmatrix} = 2 \times \begin{pmatrix} 0 & 0 & 0 & 0 & d_{31} & -d_{22} \\ -d_{22} & d_{22} & 0 & d_{31} & 0 & 0 \\ d_{31} & d_{31} & d_{33} & 0 & 0 & 0 \end{pmatrix} \begin{pmatrix} E_x^2 \\ E_y^2 \\ E_z^2 \\ 2E_zE_y \\ 2E_zE_x \\ 2E_xE_y \end{pmatrix}$$

where $d_{22} = 3$ pm V^{-1}, $d_{31} = 5$ pm V^{-1} and $d_{33} = 33$ pm V^{-1} [26]

It can be seen that the greatest response would be given by $P_z = 2\, d_{33}\, E_z^2$. However BPM cannot be used where the input and output have the same polarisation direction. Therefore the largest nonlinear response for orthogonally polarised interactions in lithium niobate using BPM is given by d_{31} which is over six times smaller than d_{33}.

2.5.4.1 Birefringent phasematching

In birefringent media such as lithium niobate an electromagnetic wave propagating in any direction can travel with either the ordinary or extraordinary polarisation. These axes have different refractive indices, n_o and n_e, which are wavelength and temperature dependent. By controlling these dependencies we can find values where $n_1 = n_2 = n_3$.

For wave propagation in a uniaxial crystal the ordinary wave propagates with an index of refraction, n^o, which is independent of propagation direction. The extraordinary wave has an index of refraction, n^e, which is direction dependent given by ;

Equation 2-32

$$\frac{1}{n^e(\theta)} = \left(\frac{\sin^2\theta}{n_e^{\,2}} + \frac{\cos^2\theta}{n_o^{\,2}} \right)^{\frac{1}{2}}$$

The extraordinary index may be either greater than or less than the ordinary index, known as positive or negative birefringence, and equals the ordinary index at $\theta = 0$ (propagation along the optic axis).

In biaxial crystals the situation is more complex since there are more that two indices of refraction. A complete description can be found in Hobden [27].

Unless a crystal birefringence is exactly correct the propagation direction in the crystal must be chosen at a phasematching angle, θ, such that $n^e_{\omega_3}(\theta) = n^o_{\omega_1+\omega_2}$ for a negative birefringent crystal or $n^o_{\omega_3} = n^e_{\omega_1+\omega_2}(\theta)$ for a positive birefringent crystal. This is referred to as Type I phasematching, Figure 2.8.

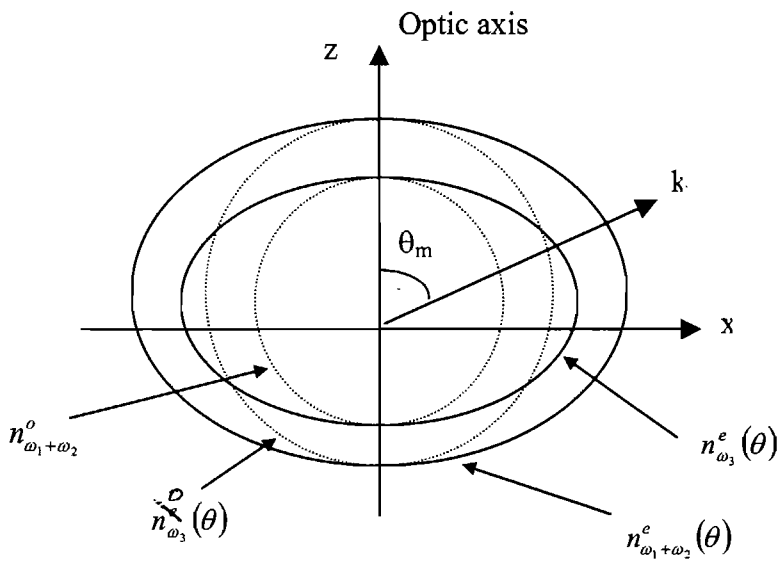

Figure 2.8 *The indicatrix for Type I phasematching in a positive uniaxial crystal*

Phasematching can also be achieved by averaging the birefringence, this is known at Type II phasematching. For negative birefringent crystals obeys the relation ;

Equation 2-33

$$n^{e}_{\omega_3}(\theta) = \tfrac{1}{2}\left[n_{\omega_1+\omega_2}(\theta) + n^{o}_{\omega_1+\omega_2}\right]$$

and for positive birefringent crystals the ordinary and extraordinary waves are reversed.

2.5.4.2 *Beam walk-off and 90° phasematching*

It was seen in Section 2.3 that the refractive index of lithium niobate is temperature dependent, this means the phasematching angle can be temperature tuned. A highly desirable geometry results if the phasematching angle can be tuned to 90^0 in a uniaxial crystal, thus eliminating beam walk-off caused by double refraction. This beam walk-off results because in either Type I or Type II phasematching both ordinary and extraordinary waves are participating in the nonlinear interactions. For collinear phasematching all the wave vectors, *k*, point in the same direction, but the ray directions or Poynting vectors, *S*, do not. Nonlinear generation usually involves narrow focussed laser beams. Along the path of such a beam in the crystal, which follows the Poynting vector, a nonlinearly generated wave of orthogonal polarisation will travel at a different angle, known as 'walk-off', Figure 2.9.

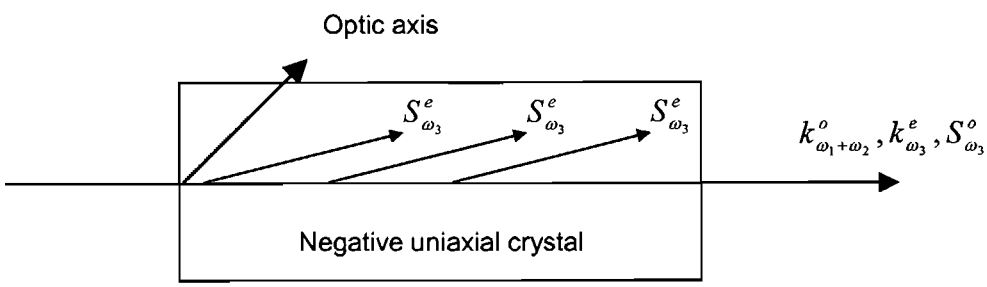

Figure 2.9 *Poynting walk off*

However, if the phasematching occurs at 90^o to the optic axis then no beam walk-off occurs. 90^0 phasematching can be achieved for specific wavelengths in several crystals including lithium niobate, potassium dihydrogen phosphate (KDP) and proustite (Ag_3AsS_3).

2.5.4.3 *Quasi-phasematching*

BPM takes advantage of naturally occurring crystal properties, whereas QPM is accomplished by artificially engineering the structure of the crystal to maintain the required phase relationship. QPM was first demonstrated in 1964, before the development of BPM [28], by Miller using quartz plates [29]. However, QPM has only recently been developed due to the technical problems encountered in fabricating patterned material down to micron scale with good geometrical quality.

As described earlier, when light is incident on any nonlinear material polarisations are set up in the material. If the incident power is high enough, this gives rise to harmonics which constructively and destructively interfere with the incident or fundamental frequency, along the length of the crystal, as shown in Figure 2.10.

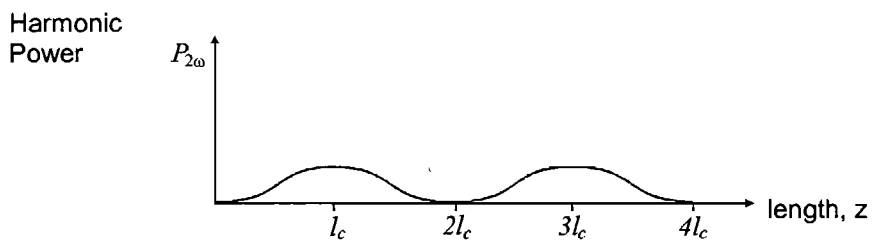

Figure 2.10 Harmonic generation in a nonlinear crystal

It can be seen that for z < coherence length, l_c, the harmonic power is built up from the fundamental wave to a maximum at l_c, corresponding to a phase shift of π. When $z > l_c$ the power couples back to the fundamental wave. To prevent this, the sign of the polarisation could be reversed by changing the sign of d_{eff} every coherence length, l_c, thus inducing a reverse phase shift, and allowing continuous constructive interference between the incident and harmonic waves, resulting in a build up of the harmonic.

This can be done by either building up slices of nonlinear material of thickness l_c, rotated by 180°, or by poling the material periodically. This creates a sequence of nonlinear segments of opposite optical domain direction and thus a change in the sense of polarisation vector by π, by changing the sign of the d_{ijk} coefficient. If every odd multiple of l_c sees a reversal destructive interference of the harmonic is avoided, Figure 2.11.

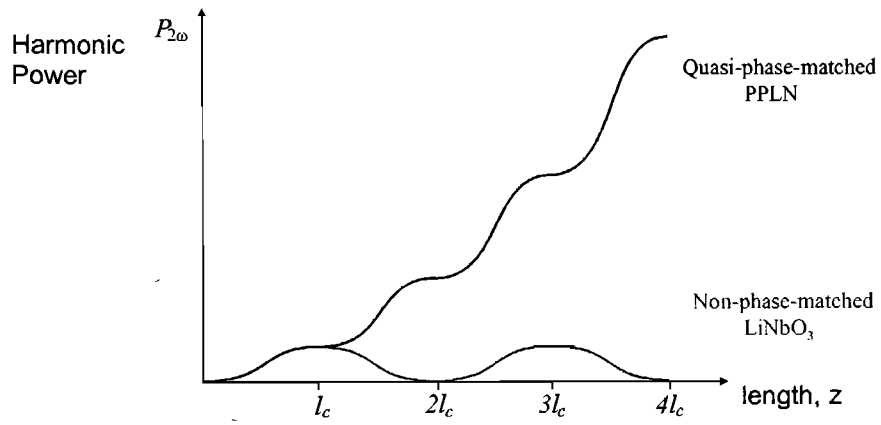

Figure 2.11 Quasi phasematching

The QPM period is given by ;

Equation 2-34
$$\Lambda_n = 2ml_c = \frac{m\lambda_f}{2(n_{h\omega} - n_{\omega})}$$

where m is the QPM order, n_{ω} is the refractive index of the fundamental wave, $n_{h\omega}$ is the refractive index of the harmonic wave and λ_f is the fundamental wavelength.

In general first order QPM is used;

Equation 2-35
$$\Lambda = 2l_c = \frac{\lambda_f}{2(n_{h\omega} - n_{\omega})} \quad \text{with} \quad l_c = \frac{\lambda_f}{4(n_{h\omega} - n_w)}$$

The intrinsic efficiency of QPM compared to BPM is $4 / m^2\pi^2$, therefore first order QPM is only $4 / \pi^2$ times the intrinsic efficiency of BPM. Although QPM is less intrinsically efficient, it does overcome some of the major problems associated with BPM, including low effective nonlinear coefficient, inconvenient phasematching temperatures and angles, photorefractive damage and Poynting vector walk-off. QPM is also a noncritical phasematching technique, allowing the polarisation and direction of the input and output rays to lie in the same plane, for example along one of the crystal axes. Therefore for lithium niobate, the d_{33} nonlinear coefficient can be used, increasing the conversion efficiency by over 20 times that possible with BPM which accesses d_{31}. This also means that we can accomplish phasematching which would

otherwise be impossible, for example in isotropic materials, or materials with too much or too little birefringence at the required wavelength. Another advantage of QPM is tuneability, by changing one of crystal temperature, wavelength or QPM period, a change in the other variables is caused thus we can produce tuneable devices.

2.6 Ferroelectric properties

A brief historical review of the discovery and development of ferroelectrics was presented in Chapter 1. Ferroelectrics are non-metallic solids that possess a spontaneous electric polarisation, P_s. This is defined as the dipole moment per unit volume, or surface charge per unit area.

A ferroelectric domain is a macroscopic, homogeneous region in the ferroelectric crystal in which the direction of the spontaneous polarisation differs from that in adjacent domains. The domain wall separating domains can move within each crystal so that the domains shrink or grow [30]. Domain walls and their movement do not affect the crystal lattice, apart from applying some stress at the boundary between 'up' and 'down' domains, however they do have a considerable effect on switching hysteresis or poling as described in Chapter 3.

The polarisation of lithium niobate can be inverted if the Li ion in the crystal lattice can be induced to move through the triangular plane of oxygen atoms. At the Curie temperature the Li ions move into the oxygen plane such that there is no net polarisation. However, at temperatures lower than the Curie temperature, external electric fields as large as 10^6 Vcm^{-1}, can force the Li ions through the oxygen triangles, thus reversing the spontaneous polarisation. The resultant crystal polarisation when a coercive electric field is applied follows a hysteresis loop as shown in Figure 2.5.

The polarisation inversion is thought to be a two-step process [31]. First, nucleation of the domains occurs at special positions or nucleation sites where some local

irregularity such as a crystal defect encourages it, usually at the face of the crystal. Secondly, the inverted domains grow sideways through domain wall movement.

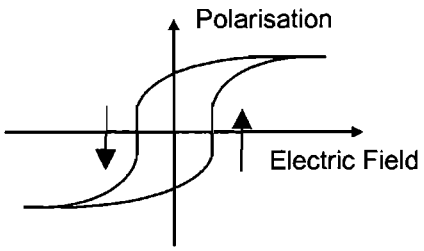

Figure 2.12 Ideal hysteresis behaviour of poling process

The nucleation and domain growth process is still not fully understood but it is thought that the existence of space charge layers near the surface of the crystal induce electric fields within the crystal. The strength of these fields is probably not high enough to generate the inversion process directly, but may contribute to polarisation reversal and nucleation when an external field is applied. The initial nucleations are randomly distributed in both space and time, making it difficult to monitor and calculate the rate of polarisation reversal and domain wall growth and movement.

There are some problems affecting the poling of lithium niobate which should be mentioned. These include material dissociation at high temperatures, even below the Curie point, phase transitions in the material, decomposition of the surface layers and impurities or dopant ions that cause ionic motion and electrical breakdown of the applied field. The poling process and associated problems are described in greater depth in Chapter 3.

2.7 Pyroelectric effect

Pyroelectric materials possess a temperature dependent spontaneous polarisation. Ferroelectric materials, such as lithium niobate, are pyroelectric below the Curie temperature, above this temperature they do not exhibit spontaneous polarisation, therefore do not exhibit pyroelectricity.

As lithium niobate is heated, the crystal lattice expands resulting in a change in the spontaneous polarisation due to the movement of the lithium and niobium ions relative to the oxygen planes. This change in polarisation causes a build up of charges on the positive and negative z faces of the crystal, in particular the positive z face becomes more strongly charged during cooling. The spontaneous polarisation change is linear with temperature change and for lithium niobate the pyroelectric coefficient is $4 \times 10^{-5} C\ cm^{-2} K^{-1}$ [32]

2.8 Piezoelectric effect

Lithium niobate also exhibits piezoelectric properties. Piezoelectricity is the phenomenon where application of a force to a crystal produces a voltage between its faces. This is due to polarisation separation of the positive and negative charges within the medium. The polarisation produced, P, by an applied stress, σ, is described by the equation;

Equation 2-36

$$\begin{pmatrix} P_x \\ P_y \\ P_z \end{pmatrix} = \begin{pmatrix} d_{11} & d_{12} & d_{13} & d_{14} & d_{15} & d_{16} \\ d_{21} & d_{22} & d_{23} & d_{24} & d_{25} & d_{26} \\ d_{31} & d_{32} & d_{33} & d_{34} & d_{35} & d_{36} \end{pmatrix} \begin{pmatrix} \sigma_{11} \\ \sigma_{12} \\ \sigma_{13} \\ \sigma_{14} \\ \sigma_{15} \\ \sigma_{16} \end{pmatrix}$$

where the notation used for d_{ijk} and σ_{ijk} is;

i : x = 1, y = 2, z = 3

j k : xx = 1, yy = 2, zz = 3, zy = yz = 4, xz = zx = 5, xy = yx = 6

and x, y, z are the crystal axes.

For lithium niobate the piezoelectric strain coefficients at 25°C are given as [26];

$d_{15} = 69.2$ $d_{31} = -0.85$ $d_{22} = 20.8$ $d_{33} = 6.0$ $\times 10^{-12}\ C\ N^{-1}$

2.9 Electro-optic properties

The application of an electric field to some crystals, such as lithium niobate, can cause changes in the refractive indices. Non-centrosymmetric crystals produce changes that are proportional to the applied field, known as the linear electro-optic effect, or Pockel's effect, whereas crystals which posses a centre of symmetry can exhibit a quadratic electro-optic, or Kerr effect. Both the linear and quadratic electro-optic effects can be used effectively in various optical devices, but for lithium niobate, and our work, the linear electro-optic effect is of particular interest.

When an electric field, E_k, is applied to the crystal, the refractive index changes according to :

Equation 2-37

$$\Delta\left(\frac{1}{n^2}\right)_{ij} = \sum r_{ijk} E_k \qquad \Delta n = -\frac{n_o^3}{2} r_{ij} E_j$$

where r_{ijk} is the electro-optic tensor and i, j, k can all be x, y or z, the crystal axes. The form of the matrix describing r_{ijk} depends on the crystal symmetry and is closely related to the piezoelectric tensor d_{ijk}, which relates the polarisation produced in a medium due to stress σ_{ijk}.

The value of r_{ijk} is obtained experimentally and a large range of values have been quoted for congruently grown lithium niobate taken at a range of different wavelengths. For example Weis & Gaylord [4] report values from 28 to 34×10^{-12} mV^{-1} for r_{33} and from 6.5 to 10×10^{-12} mV^{-1} for r_{13}. One set of low frequency electro-optic tensor elements, given in reduced notation, are:

$r_{13} = 8.6$ $r_{22} = 3.4$ $r_{33} = 30.8$ $r_{51} = 28$ pm V^{-1} at 633nm [33]

The electro-optic coefficients are also dependent on composition and are larger for stoichiometric lithium niobate, for example Kitamura quotes values of 10.4 pmV^{-1} for r_{13} and 38.3 pmV^{-1} for r_{33} [34].

2.10 Photorefractive effect

The photorefractive effect is an optically induced change in refractive index first observed over thirty years ago [35]. Although the photorefractive effect is exploited in some applications [36,37], for nonlinear optical devices presented in this thesis it is an unwelcome effect as preserving good beam quality is vital, and the photorefractive effect can cause beam distortion and scattering, leading to deterioration in optical performance.

In the case of lithium niobate, when a light beam propagates in the crystal, an optically induced space charge field is generated. The incident light then induces a migration of charge along the optic axis, in which Fe^{2+} and Fe^{3+} ion impurities can be photoexcited to produce electrons and holes respectively ;

Equation 2-38 $$Fe^{2+} + h\nu \Rightarrow Fe^{3+} + e^{-} \qquad Fe^{3+} + h\nu \Rightarrow Fe^{2+} + h^{+}$$

Across the illuminated region electrons and holes are excited and migrate until they are re-trapped by Fe^{3+} ions away from the light beam. This movement of charge results in an electric field, and via the electro-optic effect, a change in the refractive index around the beam of light. Since both electrons and holes can contribute to this, the photorefractive susceptibility of the material is therefore controlled by the oxidation state ratio Fe^{2+} / Fe^{3+}.

There are methods of controlling and reducing the problems of photorefraction. In lithium niobate, the photorefractive effect was found to be self-annealing for crystal temperatures above approximately 180°C for visible radiation and 100°C for near infrared. Therefore by choosing operating temperatures above these values we can minimise or eliminate photorefractive effects. Other ways of reducing the photorefractive effect are by increasing the dark conductivity of the material by using dopants, such as magnesium eg. Mg:$LiNbO_3$, and by optimising the ratio Fe^{2+} / Fe^{3+} by oxidisation or reduction. As the photorefractive effect is generated by photoexcited charge carriers, it is stronger at shorter wavelengths, i.e. visible light, and for lithium niobate has negligible effect above 1μm.

2.11 Chapter conclusions

This Chapter has reviewed some of the material properties of lithium niobate, in particular those which influence the fabrication and operation of novel PPLN devices.

2.12 References

[1] M E Lines and A M Glass *'Principles and applications of ferroelectrics and relates materials'* Claredon Press Oxford (1977)

[2] A M Prokhorov and Y S Kuz'minov *'Physics and chemistry of crystalline lithium niobate'* Adam Hilger Bristol (1990)

[3] A Rauber *'Chemistry and physics of lithium niobate'* in Current topics in material science, vol. 1. Editor E Kaldis (North-Holland, Amsterdam 1978) p481-601

[4] R S Weis and T K Gaylord *'Lithium niobate: summary of physical properties and crystal structure' Appl Phys* A37 p191 (1985)

[5] D H Jundt *(from Crystal Technology)* Private conversation

[6] B T Matthias and J P Remeika *Phys Rev* **76** p1886 (1949)

[7] A A Ballman *J American Ceramic Soc* **48** p112 (1965)

[8] C K Campbell *'Surface Acoustic Wave Devices for Mobile and Wireless Communications'* ISBN 0121573400 *Academic Press: Boston* (1998)

[9] J A Giordmaine and R C Miller *'Tunable coherent parametric oscillation in $LiNbO_3$ at optical frequencies' Phys Rev Lett* 14 p973 (1965)

[10] T Tsukada, K Kakinoki,M Hozawa, N Imaishi, K Shimamura and T Fukada *'Numerical and experimental studies on crack formation in $LiNbO_3$ single crystal' J. Crystal Growth* **180** p543-550 (1997)

[11] V Bermudez, M D Serrano and E J Dieguez *'Bulk periodic poled lithium niobate crystals doped with Er and Yb' J Crystal Growth* **200** p185 (1999)

[12] A Feisst and P Koidl *'Current induced periodic ferroelectric domain structures in $LiNbO_3$ applied for efficient nonlinear optical frequency mixing' Appl. Phys. Lett.* **47** p1125-1127 (1985)

[13] G Malovichko, V Grachev, E Kokanyan and O Schirmer *'Optimization of lithium niobate for advanced applications by variation of extrinsic and intrinsic defect subsystems' Ferroelectrics* **258** p131-140 (2001)

[14] K Polgar, A Peter, L Kovacs, G Corradi and Z Szaller *'Growth of stoichiometric LiNbO3 single crystals by top seeded solution growth method' J Crystal Growth* **177** p211 (1997)

[15] EMIS Datareview Series No5 *'Properties of lithium niobate'* INSPEC London p26 (1989)

[16] G J Edwards and M Lawrence *'A temperature dependant dispersion equation for congruently grown lithium niobate' Opt. Quant. Electron.* **16** p373-375 (1984)

[17] D H Jundt *'Temerature-dependant Sellmeier equation for the index of refraction, n_e, in congruent lithium niobate' Optic Letters* **22** 20 p1553 (1997)

[18] M A Watson, M V O'Connor, P S Lloyd, O Balachninaite, D P Shepherd and D C Hanna *'Long-wavelength operation of synchronously pumped optical parametric oscillators based on periodically poled $LiNbO_3$' CLEO* **CWA11** Long Beach, California May 2002

[19] H Ito, T Hatanaka, S Haidar, K Nakamura, K Kawase and T Taniuchi *'Periodically Poled LiNbO3 OPO for generating mid IR to terahertz waves' Ferroelectrics* **253** p95-104 (2001)

[20] P A Franken, A E Hill, C W Peters and G Weinreich *'Generation of optical harmonics' Phys Rev Letts* **7** p118 (1961)

[21] D A Kleinman *'Nonlinear dielectric polarisation in optical media' Phys Review* **126** p1977 (1962)

[22] J A Giordmaine *'Mixing of light beams in crystals' Phys Rev Letts* **8** p19 (1962)

[23] P D Maker, et al *'Effects of dispersive and focussing on the production of optical harmonics' Phys. Rev. Lett.* **8** p21 (1962)

[24] C C Davis *'Lasers and electro-optics' Cambridge Press* (1996)

[25] J M Manley and H E Rowe *'General energy conservation in nonlinear resistances' Proc. IRE* **47** p2115 (1959)

[26] Crystal Technology, Inc. *'Physical and optical properties of lithium niobate' Data Sheet*

[27] M V Hobden *J. Applied Physics* **38** p4365 (1967)

[28] J A Armstrong, N Bloembergen, J Ducuing and P S Pershan *'Interactions between light waves in a nonlinear dielectric' Phys. Rev.* **127** p1918 (1962)

[29] R C Miller *'Optical second harmonic generation in piezoelectric crystals' Appl Phys Lett* **5** p17 (1964)

[30] Z W Hu, P A Thomas, A Snigirev, I Snigrireva, A Souvorov, P G R Smith, G W Ross and S Teat *'Phase-mapping of periodically domain inverted $LiNbO_3$ with coherent X-rays' Nature* **392** p690-693 (1998)

[31] V Y Shur, E L Rumyantsev et al. *'Regular ferroelectric domain array in lithium niobate crystals for nonlinear optic applications' Ferroelectrics* **236** p129-144 (2000)

[32] A Savage *J. Appl. Phys.* **37** p3071 (1990)

[33] E H Turner *Appl. Phys. Lett* 8 p303-304 (1966)

[34] K Kitamura, S Takekawa, M Nakamura and Y Furukawa *'Commercialisation of stoichiometric $LiNbO_3$ and $LiTaO_3$ for optical devices' CLEO/PR July 2001* WH2-1

[35] A Ashkin, G D Boyd, J M Dziedzic, R G Smith, A A Ballman, J J Levinstein and K Nassau *'Optically-induced refractive index inhomogeneities in $LiNbO_3$ and $LiTaO_3$' Appl. Phys. Lett.* **9** p72-74 (1966)

[36] K Buse, I Nee, M Muller and E Kratzig *'Development of thermally fixed holograms in photorefractive lithium niobare crystals without light' Opt. Mat.* **18** (1) p17-18 (2001)

[37] H Gao, J S Zhang, S Yoshikado and T Aruga *'Photorefractive low-pass temporal filter' Opt. Comms.* **203** (3-6) p363-369 (2002)

Chapter 3

Periodically poled lithium niobate

Ferroelectrics have emerged as an important class of materials due to their incredibly rich range of useful optical phenomena including; piezoelectricity, pyroelectricity, high dielectric constants, optical waveguiding, frequency generation, electro-optics, acousto-optics, photorefraction, phase conjugation, four wave mixing, etc. A number of technological applications exploiting these effects such as piezoelectric transducers [1], pyroelectric detectors [2], ferroelectric memory [3], surface acoustic wave (SAW) devices [4], quasi-phasematched frequency doublers [5], electro-optic scanners [6], two-wave mixing [7], and lenses [8] are all critically dependent on the ability to micro-engineer domains of inverted spontaneous polarisation. Hence the understanding of domain formation, domain wall motion, stabilisation mechanisms, and structure of domain walls becomes very important.

The recent development and improvements of fabrication techniques have made ferroelectric domain inversion much more accessible [9,10,11]. Today a variety of methods exist for periodic poling, including the application of external electric fields, heat treatments, metal indiffusion, and proton exchange [12].

Lithium niobate is a very attractive ferroelectric material for periodically poled applications and has many advantages over other materials such as KTP [13], KTA [14], SBN [15] and BBO [16] - it can be easily periodically poled for a given grating period or domain inverted structure, its large non-linear coefficient, d_{33}, can be accessed for more efficient nonlinear optical interactions, it possesses large electro-

optic, pyroelectric and piezoelectric coefficients, is highly photorefractive and demonstrates low scattering and absorption losses.

In this Chapter we outline the fabrication procedure for periodically poled lithium niobate (PPLN) using a room temperature electric field poling technique using liquid gel electrodes. Alternative methods of domain inversion in lithium niobate are discussed and methods of grating quality assessment presented. The significant difference in grating quality between material sourced from different suppliers is investigated and poling defects caused by procedures in the fabrication process are described.

The combination of periodic poling and different properties of lithium niobate, such as the electro-optic coefficient, nonlinear coefficient, differential acid etching and the photorefractive effect can be exploited to produce novel PPLN devices. This Chapter describes several pieces of work carried out in association with other members of the Nonlinear and Microstructured Optical Materials group in the ORC, including direct bonded PPLN devices for second harmonic generation, microstructuring of lithium niobate using differential acid etching techniques to produce devices such as ridge waveguides, optical fibre alignment guides and micro-cantilevers. Also, an investigation into the combination of differential etching and titanium indiffused waveguides to produce surface relief grating waveguides for use in wavelength filtering, wavelength division multiplexing and distributed feedback is presented. Finally, two-dimensional nonlinear photonic crystals, known as HexLN, which allow quasi-phasematching along several different paths and for several different harmonics simultaneously are described and images of samples fabricated are presented.

In particular, two types of periodically poled lithium niobate devices were studied in greater depth as part of the research for this thesis. Chapters 4 and 5 describe work done specifically for this thesis to further investigate electro-optically controlled Bragg grating modulation devices and in Chapter 6 the combination of PPLN with titanium indiffused channel waveguides for frequency generation is more extensively investigated.

3.1 Fabrication of PPLN using an electric field poling technique

'Periodic poling' of lithium niobate is the process of altering the single domain structure of the material to a structure with periodic 180° reversals of the d_{33} nonlinear coefficient along the axis perpendicular to the optic axis of the crystal, Figure 3.2. This periodic domain inversion in a lithium niobate crystal has been performed using a number of techniques involving the application of heat, external electric fields, Li_2O outdiffusion, metal indiffusion, proton exchange or a combination of these [12,17, Section 3.1.2]. The devices described in this thesis were fabricated using a room temperature electric field poling technique based on photolithographically defined liquid gel electrodes [18,19,20,21]. The main steps in the fabrication of PPLN using this method are described in the following Section and Section 3.1.3 discusses the methods used to assess the quality of resulting PPLN gratings.

3.1.1 Fabrication process

Standard 3 inch diameter, 500μm thick, optical grade lithium niobate wafers were obtained from suppliers such as Crystal Technology [22], Yamaju Ceramics Co. Inc. [23] or Castech [24]. These wafers were diced in-house to the required device size before processing, typically the samples were 3cm by 1.5cm. All samples were thoroughly cleaned before processing according to the multiple solvent procedure outlined in Table 3-1 to produce a uniform surface for the photoresist and to remove surface particles which could cause contamination of the sample surface (resulting in possible defects after poling) or breakdown of the crystal structure during the application of high voltage as part of the poling process. This process was carried out in a class 1000 clean room at a class 100 bench in an ultrasonic bath at 50°C.

After cleaning the S1813 photoresist was spin coated onto the negative z face of each sample at a speed of 5000 rpm for 60 seconds to produce a film approximately 1μm thick and then hard baked at 90°C for 35 minutes to remove all solvent and harden the resist. Investigations into PPLN fabrication during this research have found that 1μm of photoresist is the optimum thickness to hold off the charge during the electric poling process. Also it was found that higher quality and better-defined gratings are

obtained if the samples were patterned on the negative z face for poling. To ensure the samples were held perfectly flat and were not warped by the suction mount on the spin-coater, a specially designed mount was used in place of the typical o-ring mount.

Time (mins)	Cleaning Agent	Action
20	Ecoclear	Removes wax and other organic agents
20	Acetone	Removes Ecoclear and organic residue
20	IPA	Removes Acetone and organic residue
20	Microclean	A detergent, removes IPA and inorganic residue
10	Distilled water	Removes Microclean
10	Distilled water	Removes any remaining residue

Table 3-1 *Cleaning process*

To transfer the required gratings designs from a pre-defined photolithographic chrome on fused silica mask to the samples, a Karl Suss MA4 mask aligner was used to expose the photoresist for 7.5s with UV light of λ= 436nm. Due to the degradation of the photoresist and the UV lamp over time and the use of the mask aligner by other researchers it was necessary to process test structures on glass slides to confirm the exposure and developing parameters. The PPLN masks were designed using L-Edit software package and produced in-house in the Microelectronics department of Southampton University, thus allowing greater control over the quality of the mask and also allowing a greater freedom in design of gratings. Due to the small size of the samples, a specially designed sample holder was produced to ensure the samples were held perfectly parallel to the mask in the vacuum mount. The photoresist thickness and profile was measured using a Tencor Alphastep. Figure 3.1 shows a typical trace for a patterned PPLN grating. This method of assessment is only an approximate guide to the photoresist thickness and does not give a true photoresist profile due to the small size of the features in relation to the Alpha Step tip dimensions, hence the curved corners and sloping edges seen in Figure 3.1.

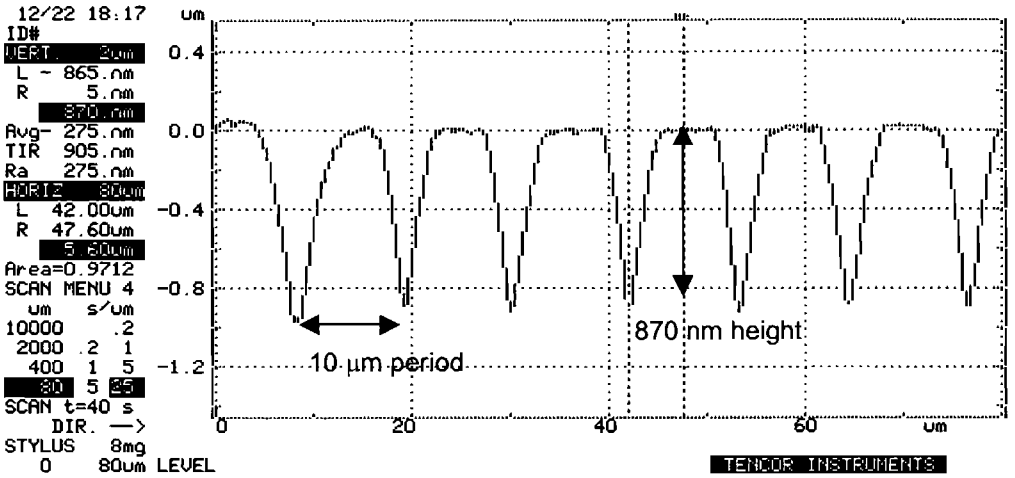

Figure 3.1 *Tencor Alphastep trace showing a typical PPLN grating photoresist profile*

The samples were then removed from the clean room for electric poling. Insulation tape was used to mask off at least 4mm round the edges of the negative z face of the 500µm thick samples. This prevents charge 'leaking' round the edges of the sample due to surface conduction, and causing electrical breakdown. For thinner samples a smaller insulating distance was found to be sufficient to prevent breakdown. Electrically conductive liquid gel was then applied to both sides of the sample over the unmasked area and the sample was then placed between two electrodes as shown in Figure 3.2.

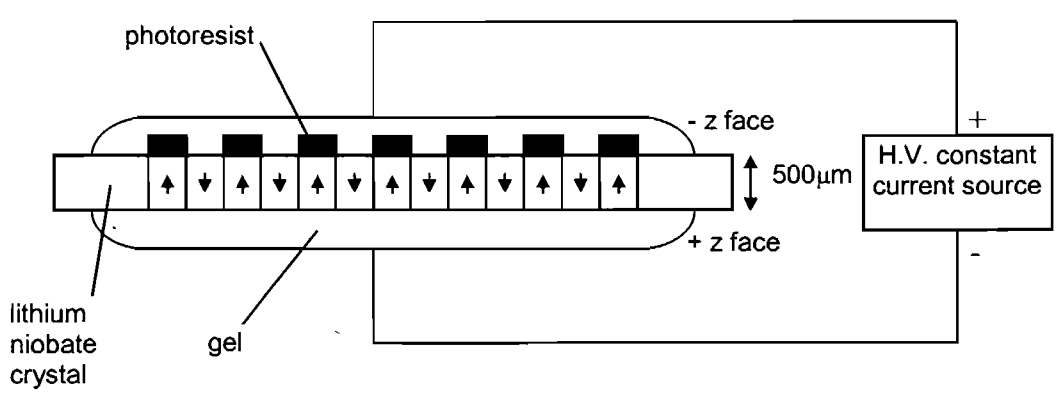

Figure 3.2 *PPLN electric field poling set up*

Lithium niobate possesses a spontaneous polarisation, P_s = 0.72 μCmm^{-2}, which is balanced by surface charges on the sample, Figure 3.3(a). The charge is given by $Q = P_s A$, where A is the area of the sample to be poled, and as $I = dQ / dt = 0$, there is no current flow between the surfaces and the polarisation is stable.

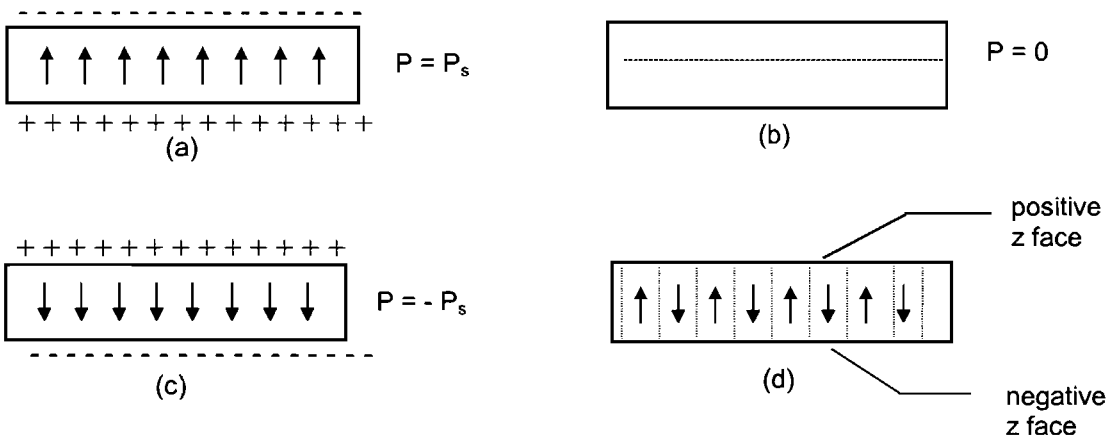

Figure 3.3 *Polarisation of lithium niobate sample during poling process*

To counteract this spontaneous polarisation, an opposite charge of $Q = P_s A$, must be applied, Figure 3.3(b) and to totally invert the spontaneous polarisation an opposite charge of $Q = 2 \times P_s A$ is required, Figure 3.3(c). To produce PPLN, the polarisation of half the sample needs to be inverted in periodic segments, as illustrated in Figure 3.3(d), for which the required charge is calculated from the equation ;

Equation 3-1 $$Q_{ppln} = 2\, P_s \times \tfrac{1}{2} A = P_s A$$

where the area, $A = L \times W \times N$, with L the length of the gratings in mm, W the width in mm and N the number of gratings being poled.

In order to invert the spontaneous polarisation of a lithium niobate crystal, an electric field greater than the coercive field, E_c = 22 $kVmm^{-1}$, must be applied [12]. To achieve this effect, most electrical poling circuits use a constant voltage supply which operates at a voltage close to the coercive field [17], allowing high voltage to be applied until the degree of domain inversion required is thought to have been obtained. Using this method a very small percentage change in the voltage will

greatly alter the poling rate and hence this method can be unstable, especially due to variations in crystal quality, as described later on in this Chapter.

The periodically poled devices used during the scope of this research are based on a current controlled system which involves varying the voltage to keep a constant generated current during poling. As the current is relatively small, 100 to 1000μA, universal control equipment will automatically adapt to give the correct voltage for poling from sample to sample. Using an auto-compensating technique is a more stable method than using a voltage controlled system and is less susceptible to electrical breakdown. The circuit used was based round a high voltage field effect transistor (FET) and a feedback loop, as illustrated in Figure 3.4. During a typical poling process the power supply was raised to give a field greater than the coercive field (22kV mm^{-1} for lithium niobate) and the current derived feedback initially clamped the voltage across the FET, setting point A to 1.2kV. The voltage was stopped from rising higher and destroying the FET by a very high voltage diode that started conducting at 1.2kV. The voltage across the sample was then increased to approximately 11kV, with the sample held at this set voltage level minus 1.2kV. The computer then controlled the poling process by allowing current to flow following a pre-programmed current profile for calculated and programmed values for max current and charge. A $\tanh^2$ current profile was found to give the best results. The feedback loop ensured that the current and therefore poling rate remained constant at the preset level. The system monitored the current across resistor, R, compared it to the desired current and fed back the difference to the FET. The FET's resistance was then altered accordingly, changing the voltage at A to a value between 0 and 1.2kV to keep the generated current constant at the required level. When the charge (integral of current with time) reached the pre-programmed level, Q_{set}, the voltage was dropped and the poling stopped.

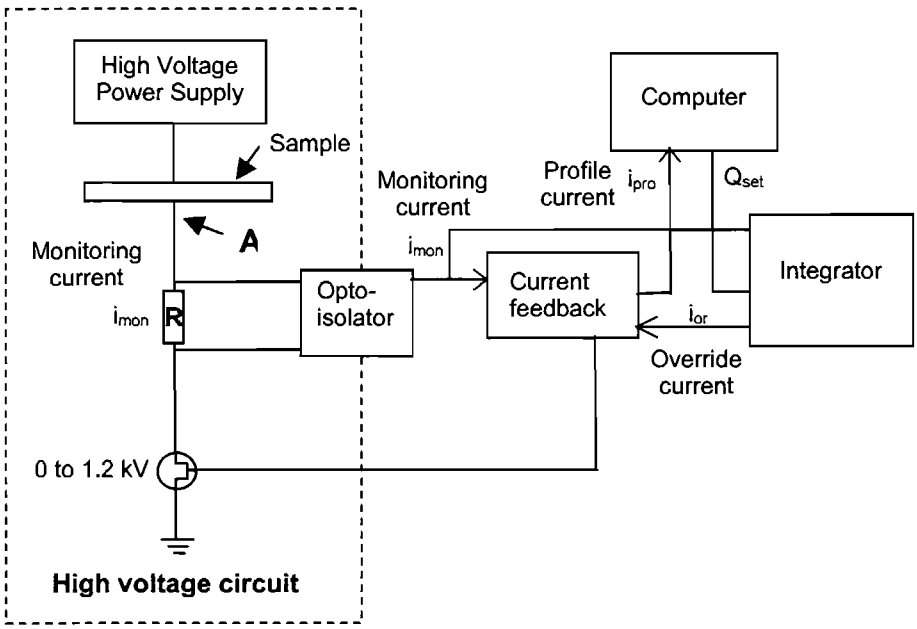

Figure 3.4 *Constant current power supply*

Typical current and voltage traces are shown in Figure 3.5, where Figure 3.5 a) shows a sample poled with a small charge and b) with a much larger charge. The $\tanh^2$ current profile can be seen and the maximum current and charge can be measured from this trace. The bottom trace in each case is the monitored voltage across resistor, R, showing the voltage drop across the FET from 1.2kV required to produce domain inversion. From this trace we can calculate the actual voltage at which domain inversion occurred for each sample according to ;

Equation 3-2 $$V_{inversion} = \text{Set Voltage} - 1.2\text{kV} + \text{Average Clamp Voltage}$$

In this particular case the voltage was $V = 11.8 - 1.2 + 0.3 = 10.9$ kV.

It is thought that the spikiness in the voltage trace in Figure 3.5b) is caused when growing domains reach defects in the crystal and when new domains are nucleated at random spacing during the poling process. It has been seen that domain nucleation requires a higher voltage than domain spreading and growth [25].

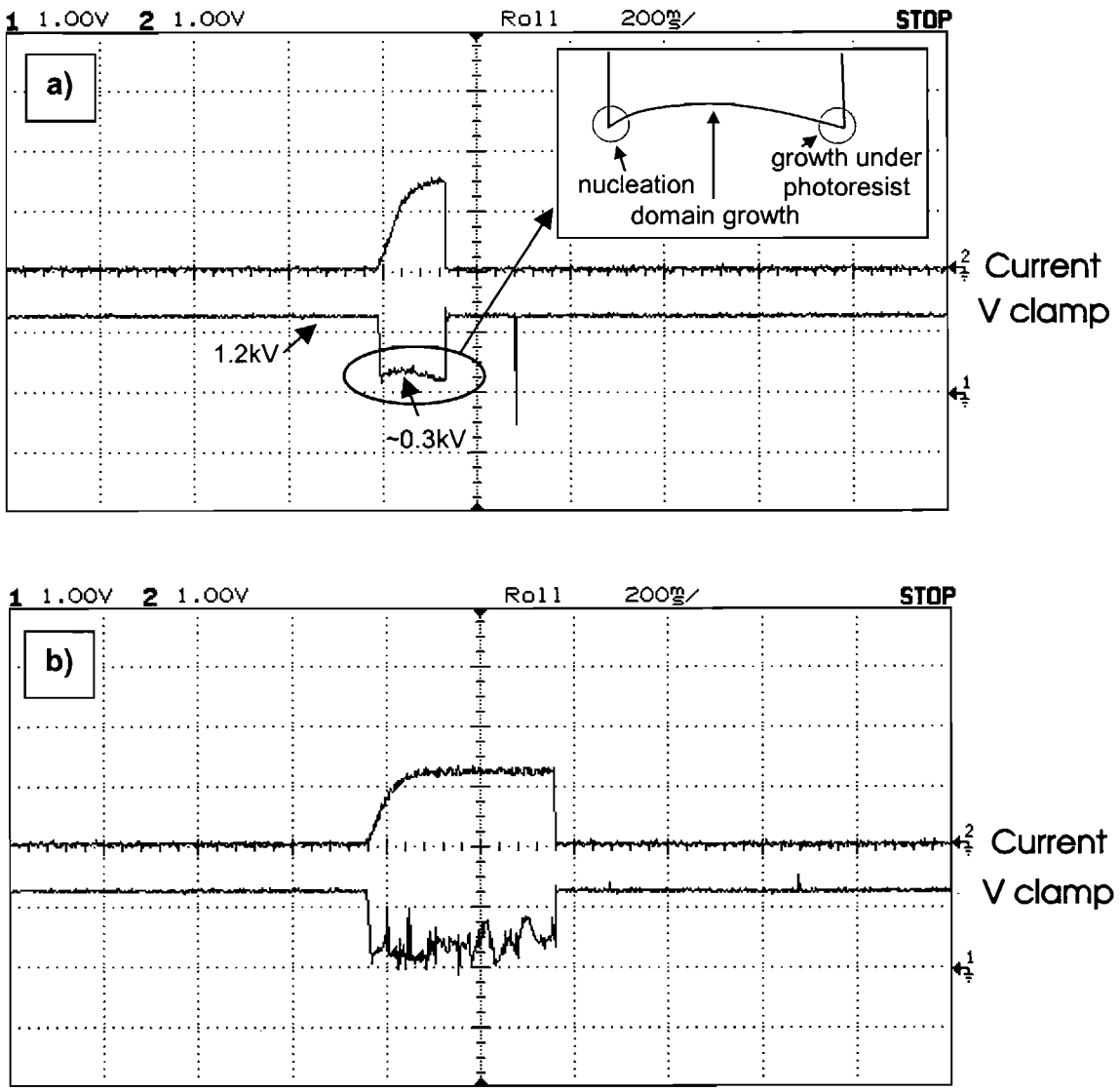

Figure 3.5 *Poling current and voltage traces*

3.1.2 Alternative methods of poling

The samples used during this research were all fabricated using the liquid gel electrode electric field poling technique described above, but several alternative methods of poling have been reported by other groups.

As described in Chapter 1, one of the original methods for producing periodic poled samples was domain inversion during crystal growth [26]. As the crystal is pulled from melt the electric field across it is periodically switched. This is an accurate but very slow method of production and only short lengths of PPLN can be produced. A

faster method is the laser-heated pedestal technique used by Jundt et al. to grow periodically poled magnesium oxide doped lithium niobate with growth speeds up to 2mm/minute [27].

Variations of the electric field poling process have been used, including a contact electrode method [20], high voltage pulses [28] and systems based on spontaneous Curie temperature poling using applied heat [29].

Poling may also be induced by chemical reactions or substitution of impurities. Proton exchange followed by heat treatments produces a reversed pattern on the positive z face of the lithium niobate sample [30]. Titanium diffused into lithium niobate also gives rise to domain alteration [31]. This technique has been applied to produce waveguide structures for processes such as SHG [32].

Pendergrass studied the possibility of using either the pyroelectric or piezoelectric effect to induce poling [33]. Stress applied to a lithium niobate crystal will produce a component of electric field along the crystalline z-axis, likewise the pyroelectric effect can be used to produce fields of up to 10^3 $kVmm^{-1}$.

Research has also been carried out into the direct writing of domains without the need for the use of a mask by using an electron beam [34,35,36,37]. The incident electrons generate a space charge beneath the surface and cause the emission of a secondary electron. The surface potential greatly increases to compensate for this process, generating a high field across the sample and hence causing domain reversal. However the main limitation of this technique is the slow writing speeds of about 30 to 50 $\mu m\ s^{-1}$.

Many of these techniques are limited by high coercive fields, slow writing speed, limited sample length, or finest achievable grating periods. The particular liquid gel electrode technique used for this work had an absolute grating period limit of approximately 4 or 5 micron due to the resolution of the photolithography process, which is acceptable for the devices required in this research. However there is a drive to produce finer period gratings, currently achievable grating periods of around 6μm

are useful for first order SHG of green light, but first order SHG of blue and UV light requires shorter grating periods. Finer periods have been achieved by using electron beam writing [38], but this is a time consuming process and still cannot obtain submicron gratings. Recently a new poling technique, known as backswitching, has emerged which can be used to obtain nanoscale domains in lithium niobate [39,25]. Grating periods as fine as 30nm have been achieved by Shur et al. [40]. Research has also started in the ORC to investigate this new backswitching process. The mechanism behind this method is the presence of an internal field in lithium niobate which results in an axial anisotropy of the coercive field and produces spontaneous backswitching upon abrupt removal of the external poling field [41].

A similar technique to backswitching is that of reverse poling of lithium niobate. The samples are bulk forward poled and then reverse poled with the required grating pattern. The main advantage of this method is the lower coercive fields involved, and thus the reduced risk of electrical breakdown. The built-in internal coercive field of unprocessed lithium niobate material is approximately 22kVmm^{-1} at room temperature, parallel to the direction of the spontaneous polarisation. When the polarisation of the crystal is reversed by applying an external electric field at room temperature (forward poling) the internal field becomes anti-parallel to the new polarisation direction. The internal field in this new domain reversed state tends to realign parallel to the new polarisation direction with time and temperature [42, 43]. This realignment is not a fast process and is incomplete after a month at ambient room temperature and only 95% complete after annealing above 200°C for 30s. During this realignment process the coercive field required to reverse pole the sample is much lower, but increasing with time or temperature, than that to forward pole the sample. The following section describes work carried out into reverse poling as part of this research.

3.1.2.1 Reverse poling method

This Section discusses the research carried out to investigate and compare an alternative poling method to that more regularly used in the group. The coercive field required to invert a domain in lithium niobate is 22 kVmm^{-1}, after the application of which a period of time is required for the domains to become fully stable. This time

can range from seconds to hours depending on the material and poling process used. However, if a sample was to be reverse poled within this stabilisation period, a much lower coercive field would be required than for the forward poling and the domains would invert much more readily and uniformly.

The first method used to achieve reverse poling is shown in Figure 3.6 and described below. The samples were bulk forward poled using room temperature electric field poling with uniform liquid gel electrodes as described in Section 3.1.1, then they were photolithographically patterned with the required grating pattern on the original +z face, this took place within approximately 12-24 hours after the forward poling process. The polarity of the connections to the sample was then reversed by switching the connecting wires and the sample was reverse poled with parameters calculated for the required gratings.

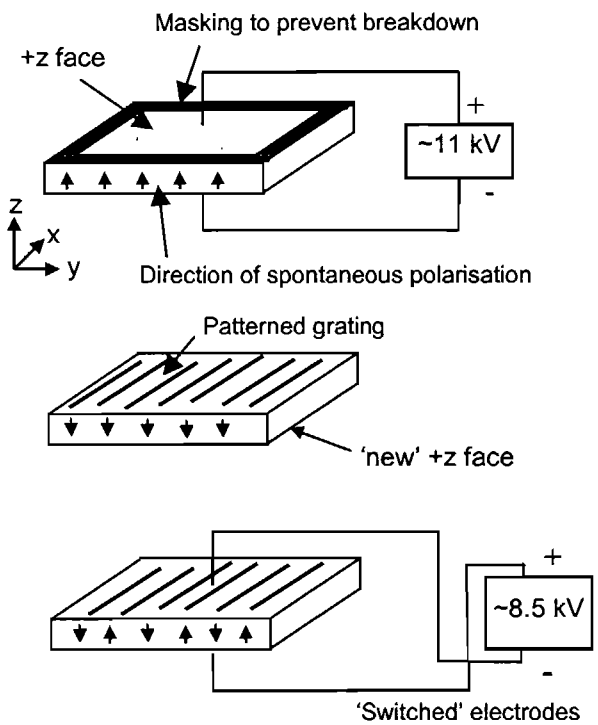

Figure 3.6 *Reverse poling process*

A second reverse poling method was also investigated, which involved patterning the samples with the required grating pattern first, then bulk poling them by calculating a charge which overpoled the gratings, producing a uniform block of inverted domain. The polarity of the electrodes was then immediately switched round and the PPLN

gratings were reverse poled a few seconds after the forward poling using the correctly calculated charge, as illustrated in Figure 3.6.

In both cases the samples were patterned with a set of 1mm wide, 20mm long gratings with periods ranging from 25.0μm to 6.5μm and poled with a constant current of around 500μA. Previous investigations carried out for this thesis showed that for 'regular' forward electric field poling with liquid gel electrodes, patterning the negative z face with photoresist gives better results. However for reverse poling the direction of the spontaneous polarisation is inverted, swapping the positive and negative z faces compared to virgin material. To investigate the effect of this, samples were patterned on both negative and positive z faces and reverse poled. The results are shown in Table 3-2.

Time between forward and reverse poling	Patterned side	Comments
24hrs	- z	Reverse poled at 8.4 kV
24hrs	+ z	Reverse poled at 8.7 kV
A few seconds	- z	Photoresist problems, no poling
A few seconds	- z	Photoresist problems but some reverse poling at ~6 kV
A few seconds	+ z	Photoresist problems, no poling

Table 3-2 *Results of reverse poling investigations*

The average coercive field for the reverse inversion was found to be ~8.5kV for samples left overnight and ~6.0kV for samples reverse poled immediately after forward inversion, indicating the time dependence of the reverse poling coercive field. Samples which were re-patterned over a timescale of approximately 24hrs gave some reasonable PPLN gratings, as shown in
Figure 3.7. The samples which were patterned on the negative z face (originally the positive z face) gave slightly better results than the samples patterned on the new positive face.

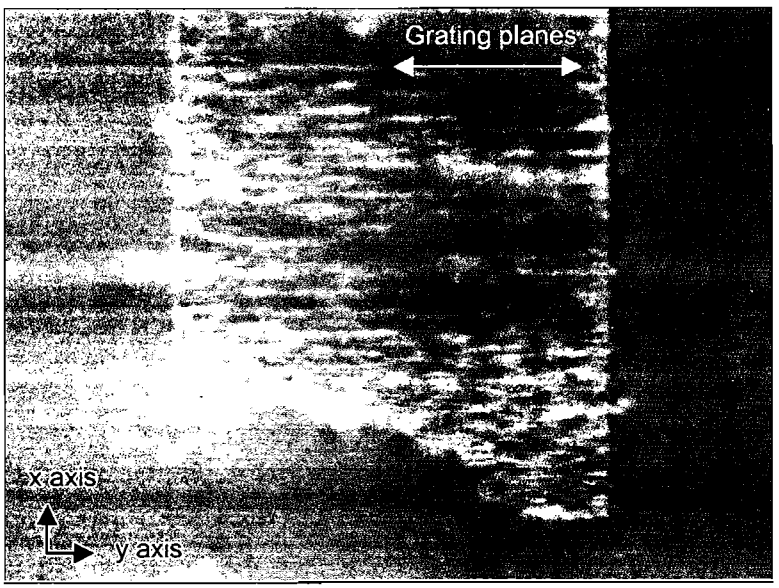

Figure 3.7 *Photograph of sample viewed through crossed polarisers, showing evidence of PPLN gratings of period 6.78μm*

Some interesting results were obtained for the immediate reverse poling method. During the reverse poling process all the samples showed problems with the photoresist coming away from the surface of the sample. The photoresist appeared to fall off the samples, following the triangular orientation of the crystal lattices. This can be seen from the photographs in Figure 3.8. Any domain reversal in these cases followed these triangular patterns rather than the gratings. The most likely explanation for this new phenomenon of photoresist fall off during reverse poling is that charge builds up under the photoresist during the forward bulk poling, an effect which could weaken the bonds between the sample surface and the photoresist causing it to lift up and fall off the surface. If the samples are then poled for a patterned grating, the poling will preferentially follow the triangular gaps in the photoresist rather than the grating pattern.

It was concluded that for the fabrication of devices investigated in the scope of this thesis that the regular forward poling method was preferential to the reverse poling technique. However reverse poling techniques are successfully used by other research groups, for example at Stanford University [27,32] a reverse poling technique using deposited metal electrodes has been developed which does not incur the same problems seen in this work with poor adhesion of photoresist.

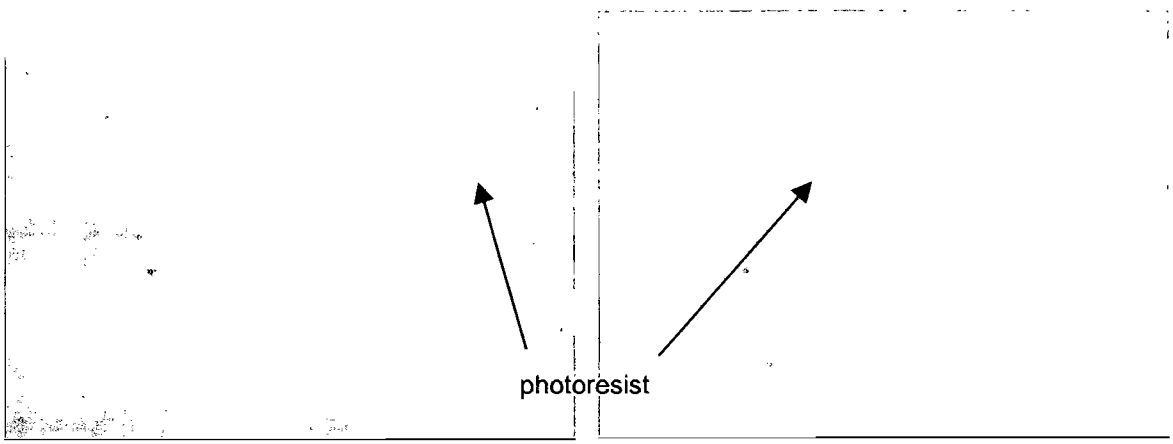

Figure 3.8 *Photographs of sample where resist has come away from the sample surface*

3.1.3 Assessment of PPLN gratings

To enable different poling methods, grating periods, surface treatments and types of crystals to be compared and advancements made in producing new and improved PPLN devices, a method of evaluating the quality of a nonlinear PPLN grating is required. A number of methods are used to do this which mainly rely on the pyroelectric and piezoelectric properties of lithium niobate, and methods such as chemical etching.

The first test after a sample has been poled is a visual inspection of the domain gratings under a microscope using crossed polarisers, as demonstrated in Figure 3.9. The domain boundaries can be clearly seen after poling due to residual stress and associated birefringence via the piezoelectric effect, an effect described in Chapter 2. This initial inspection gives a rough estimate of domain boundary straightness, under or overpoling and grating uniformity. As part of the efforts made by the author and others to improve poling quality we have developed a grading system for periodically poled gratings in lithium niobate. A grade is given to the grating, where an 'A' Grade indicates an excellent grating and an 'F' Grade indicates a very poor grating. This enables direct comparison of different fabrication methods, crystal suppliers, etc.

If the grating is not visible, for example the residual poling stresses are weak or have been annealed out, the domains can be revealed by heating then cooling the crystal, for example on a hotplate. The grating will become visible particularly in the cooling stage due to charge build up on the positive z face via to the pyroelectric effect, see Chapter 2. This method is only temporary, as when the sample reaches room temperature the charge build up begins to dissipate and the grating becomes less visible.

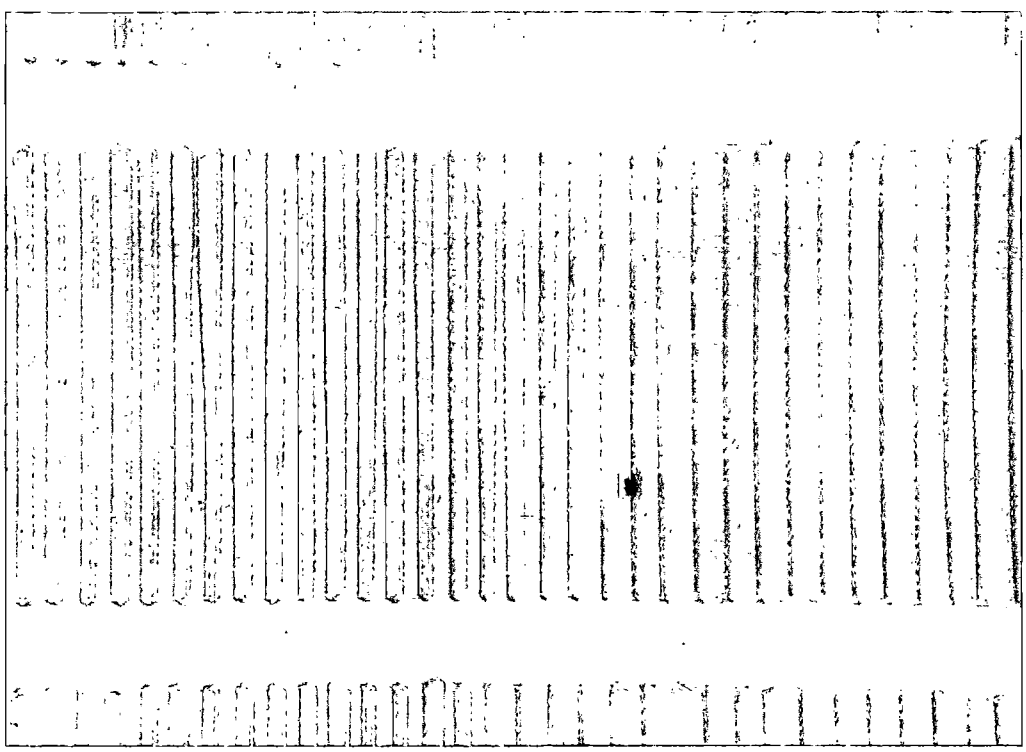

Figure 3.9 *An 'A' Grade PPLN grating of period 30μm viewed through crossed polarisers*

A third method which is used to permanently reveal the PPLN gratings, is by etching the samples in a $HF:HNO_3$ (1:2 ratio) mixture. This method has been widely used over the past four decades to reveal the domain structure in lithium niobate [44,45,46]. The $HF:HNO_3$ mixture attacks the negative z face at a rate that is appreciably higher than the positive face, removing approximately 700nm per hour at room temperature, and leaving the positive face relatively untouched. The etching rate increases exponentionally with temperature according to Arrhenius law ;

Equation 3-3 $$k = Ae^{-E_a/RT}$$

where the removal rate is described in microns per hour, $A = e^{(20.37)}$, $E_a / R = 6300$, and T is the absolute temperature of the etchant.

The dramatic effect of $HF:HNO_3$ etching on lithium niobate can clearly be seen in the scanning electron microscope (SEM) photograph in Figure 3.10, taken from the thesis of another member of the research group. This sample was etched for 48 hours in $HF:HNO_3$ and features exposed ridges of domain inverted material designed for use in waveguide applications [47].

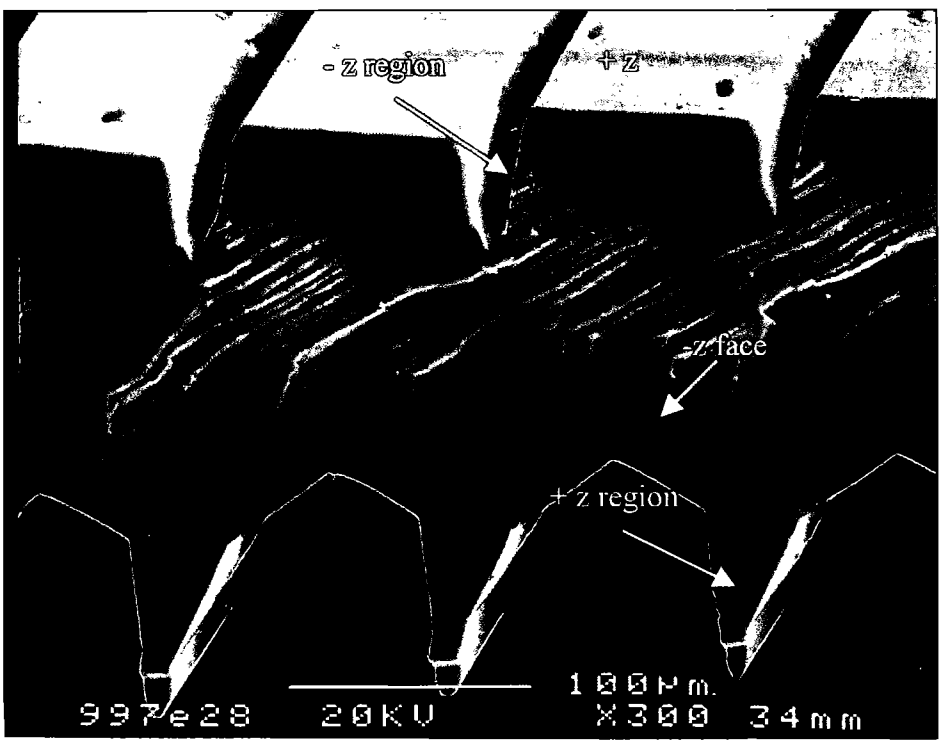

Figure 3.10 *Etched periodically poled lithium niobate [photograph provided by Ian Barry, ORC]*

Non-visual methods of grating inspection are also used and include; atomic force microscopy [48], electrostatic force microscopy [49,50] or X-ray diffraction which is used to investigate the crystal structure at the domain inverted boundaries [51,52]. The piezoelectric effect of lithium niobate can also be employed to determine the local domain orientation in poled lithium niobate material. This is performed by inducing stress in the crystal by squeezing it between electrodes. The sign of the voltage produced on release determines the orientation of the polarisation of the crystal at that point.

An optical assessment of the grating may also be done by testing the nonlinearity of the sample via second harmonic generation (SHG) (see Chapter 6 for more details on SHG). From SHG measurements the effective nonlinear coefficient d_{eff} can be estimated. A perfect sample would have a d_{eff} of 17pmV^{-1} at a wavelength of 1μm [53]. Any defects in the PPLN grating such as missing periods, random fluctuations or non 50:50 period duty cycle will reduce the measured value for d_{eff}. The grating quality can also be assessed from the phase matching curve which indicates how the second harmonic intensity varies with fundamental wavelength or temperature. For example the temperature bandwidth is found by measuring the SH power with temperature and is fitted by the function ;

Equation 3-4

$$F(T) \propto \frac{\sin^2(\Delta kL/2)}{(\Delta kL/2)^2}$$

where Δk is the phase mismatch and L is the length of the sample. Divergence from this function indicates poor quality gratings. A quantitative measure of this divergence is found by comparing the half widths ($F(T)$=0.5) for the measured and theoretical data.

3.2 Material and fabrication issues

The fabrication of high quality PPLN devices is not a simple matter, particularly for grating periods less than 10μm. Poor reproducibility, random defects, and large differences in poling behaviour between material from different suppliers, all make the fabrication of high quality PPLN a very hit and miss process. Continuous research into the development of new and improved fabrication and poling techniques provides a strong motivational factor behind the research performed within this project. In particular there are several material-related factors which have been discovered to inhibit the quality and reproducibility of grating production. This section looks at several of these issues and discusses the appropriate steps which were investigated to reduce or alleviate the problems.

3.2.1 Material discrepancies

During the work for this thesis several differences were discovered in poling quality between lithium niobate crystals from different suppliers. Identically specified material, namely z-cut optical grade lithium niobate wafers, from some suppliers produced consistently worse results than others using the same standard poling process as described in Section 3.1.1 (see Table 3-3). Material from Koto, Japan gave the best results both in terms of the smallest achievable feature size and the consistency of poling. However in 1997 the supply of material from both Koto and another Japanese supplier, Mitsui, stopped and it has never been possible to gain any further material from these suppliers.

Although a large range of suppliers have now been sourced each has good and bad aspects as shown in Table 3-3; Ideally Crystal Technology would be the supplier of choice due to the high availability and short delivery times, but material from this supplier was inconsistent between wafers and gave on average poorer results than the other suppliers. Wafers from INGCRYS in Russia were seen to have a yellow-ish tinge compared to the others, indicating high levels of iron impurities and therefore making them more prone to photorefractive damage. Also the delivery time for the Russian material was much longer than from the other suppliers. Devices fabricated in material from Yamaju in Japan gave good results but this was one of the more difficult suppliers to get hold of and varying delivery times.

Another of the differences seen between samples sourced from different suppliers was that during the poling process required different amounts of charge for the same grating pattern. A 'correction factor' was introduced to the charge calculation, the values for material from the different suppliers is shown in Table 3-3. The values presented were developed over time during several fabrication trials. The gratings were visually inspected and the applied charge altered according to the amount of over or under poling seen in the grating. Initially the reason for this was not fully understood but was thought to relate to growth techniques, material composition, method of wafer polishing and surface defects. Research into stoichiometric lithium niobate [54,55] has shown that the spontaneous polarisation randomly varies with different levels of stoichiometricity.

Supplier	Average quality of gratings produced	Availability and delivery times	Correction Factor
Crystal Technology, UK	Poor	2-3 days	1.0
Yamaju, Japan	Good	1-2 months	1.3
INGCRYS, Russia	Good	6-12 months	1.1
Castech, China	Good	6-8 weeks	1.1
Koto, Japan	Excellent	Unavailable	1.0
Mitsui, Japan	Good	Unavailable	1.2

Table 3-3 *Comparison of different suppliers of lithium niobate material*

It is very important to have consistency between suppliers, resulting in reliable processing and yield. The following sections detail the further investigations which were carried out to investigate some of the reasons behind the inconsistencies between material from different suppliers, and to find any methods or treatments which would standardise the quality of gratings produced between different sources of material, allowing a greater choice of suppliers.

3.2.1.1 Thickness variations

The coercive field in lithium niobate depends on the thickness of the sample, with a value of approximately $22kVmm^{-1}$. As such, any variations in wafer thickness may result in uneven poling, with thinner areas preferentially poling at lower voltages. A Sodium lamp interferometer was set up to look at wafer thickness and compare material from different suppliers. Figure 3.11 shows photographs taken in the interferometer of 3 inch diameter wafers with quoted thickness of 500μm from three different suppliers. The fringes seen could be due to either variations in the thickness of the wafer or the refractive index, or both. As the wafers are supplied as single domain crystals it is unlikely that the fringes are due to refractive index alone, although small refractive index variations may be present. Most wafers exhibit over 30 fringes across the wafer, if these were caused purely by refractive index then this would correspond to a change in refractive index of around 0.01, which is too large. It would be expected that any refractive index fluctuations across the crystal would be of the order 10^{-4} to 10^{-5}. Therefore it was assumed that the interferometric fringes seen were due to thickness variations and not refractive index variations.

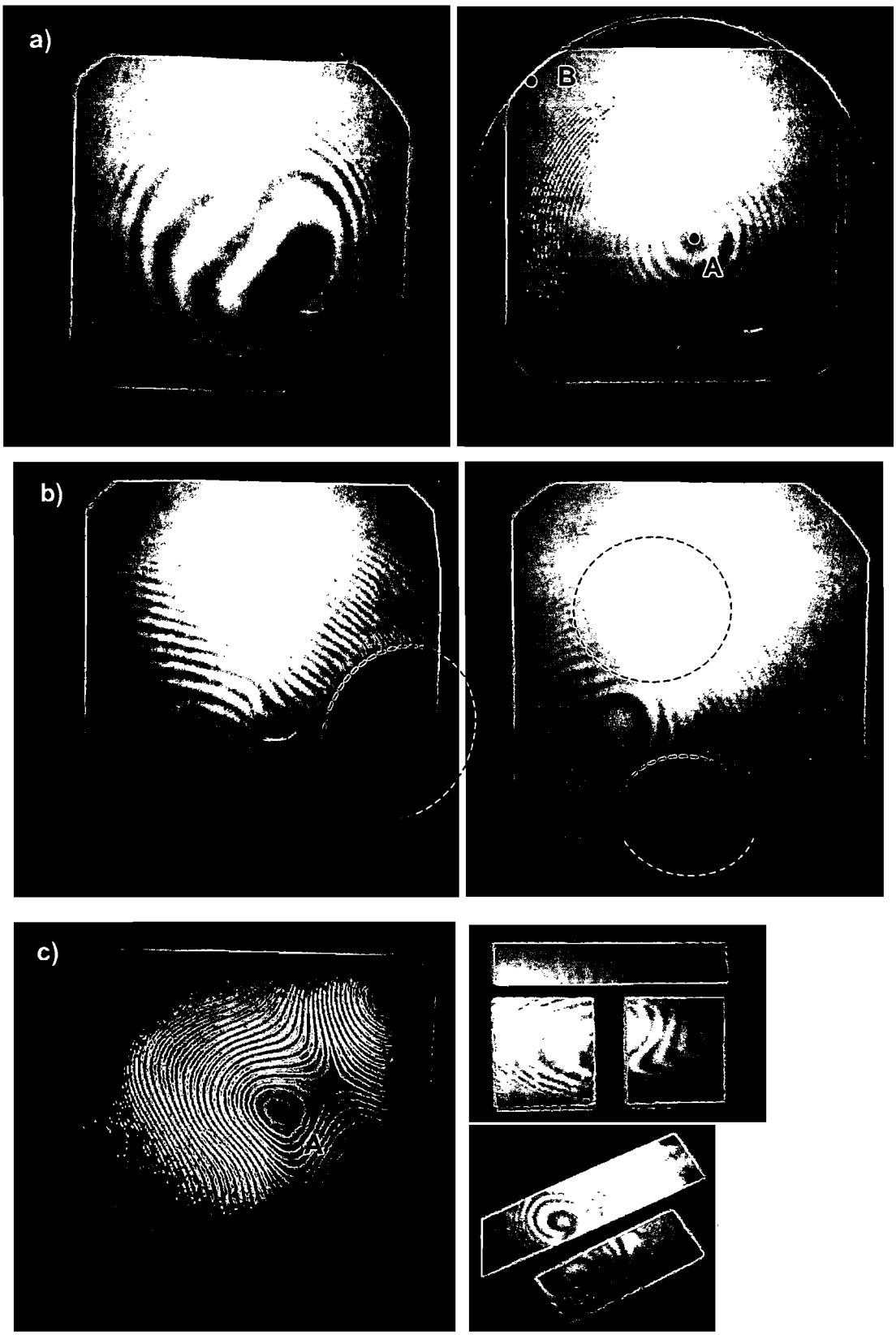

Figure 3.11 Photographs of lithium niobate wafers and samples in a Sodium lamp interferometer a) Wafers from Crystal Technology, UK, b) Wafers from INGCRYS, Russia, c) Wafer & samples from Yamaju, Japan [red dashed circles indicate areas of exceptionally tight fringes]

It can clearly be seen that there are variations in thickness across the area of the wafer, and in *c)* even across the area of a sample. It was interesting to note that each supplier had a characteristic interferometer pattern indicating that the variations in thickness are most likely due to the polishing techniques used by each supplier, possibly from particular polishing mounts. The wafers sourced from INGCRYS, Russia showed the most unusual patterns with circles of very closely spaced fringes, indicated by the red dashed circles in *b)*. In some cases over 60 fringes were seen across a distance of less than 2 centimetres. The actual thickness variation was calculated between points A and B as marked in *a)* for wafers from Crystal Technology, UK and *b)* for wafers from Yamaju, Japan. The thickness variation is given by; $\Delta t = N\lambda/2n$, where N is the number of fringes, λ is the wavelength of the sodium light, 589nm, and n is the refractive index of the wafer, ~2.24. For the wafer in *a)* there are 56 fringes over a distance of 4cm, corresponding to a thickness variation of 7.36μm. In *c)* there are 32 fringes over 3.5cm indicating a thickness variation of 4.20μm. These correspond to percentage variations of 1.5% and 0.84%, and changes in coercive field of approximately 160V and 92V respectively for 500μm thick samples, which is a large enough change to affect the poling process.

3.2.1.2 Refractive index variations

Conoscopic holography is an interferometric technique that relies on spatially incoherent light interference in birefringent crystals [56,57]. A conoscope was built as shown in Figure 3.12 and the technique was used to examine defect structures present in the untreated, as-supplied lithium niobate wafers caused by random fluctuations in refractive index, stresses or defects in the crystal.

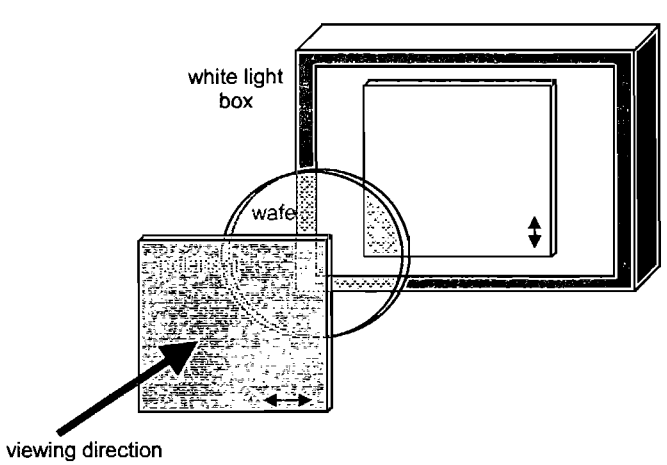

Figure 3.12 Conoscope set up

The classic 'Maltese Cross' pattern was observed – this is seen for all birefringent materials viewed through crossed polarisers due to the interference of the two transmission axes. Figure 3.13 shows this pattern for a 'perfect' wafer with no intrinsic deviations in the refractive index uniformity. The four photographs in Figure 3.14 each demonstrate variations in the pattern, indicating fluctuations and defects in the refractive index of the material. It should be noted that the photographs only give an approximate picture, it is much clearer to see the structure in real-life.

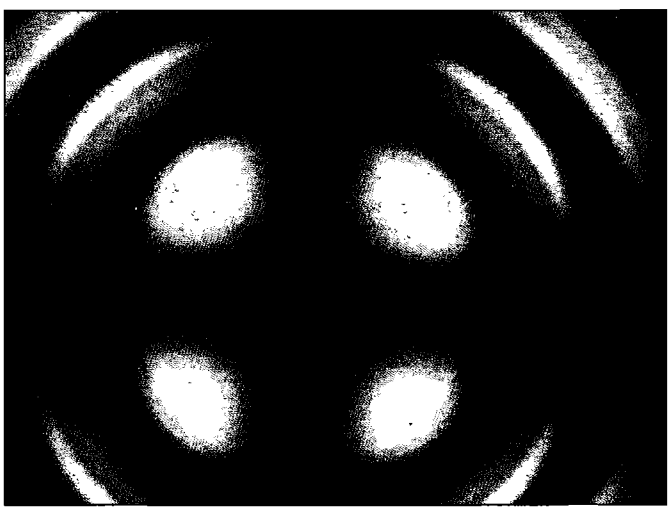

Figure 3.13 Photograph of interference pattern in 'perfect' wafer from Castech, China

The degree of crystal non-uniformity observed in the patterns for individual wafers was related to the overall poling quality achieved for material from each supplier. Also, work was started to map conoscopic patterns to specific poled samples to investigate any relation between areas of good or bad poling. Overall it was found that material with non-uniform crystal structure gave slightly better poling quality, however for specific samples no conclusions were able to be drawn as there are several other factors which have been found to have a greater influence on the poling quality. However this is still a useful technique to investigate the internal structure of wafers and samples.

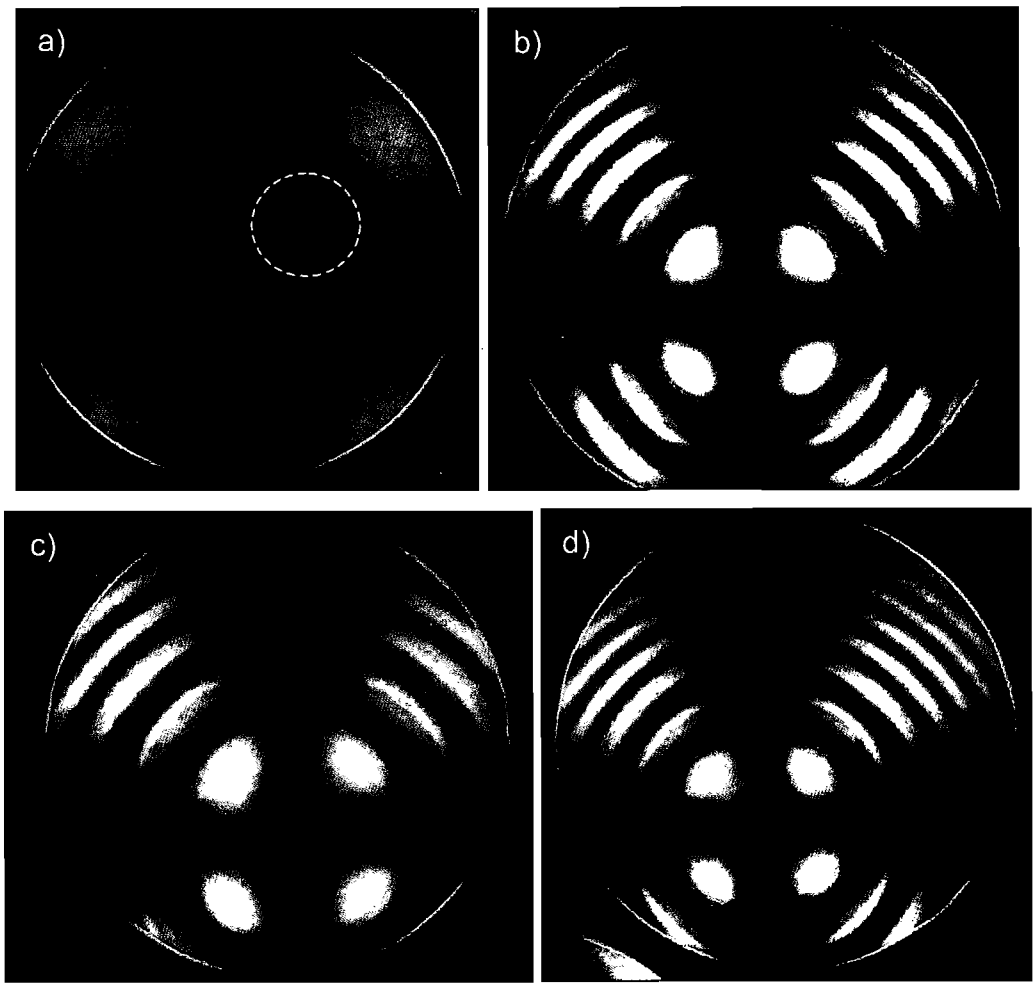

Figure 3.14 *Photographs demonstrating non-uniform refractive index profiles across wafers from a) INGCRYS, Russia b) and c) Yamaju, Japan d) Koto, Japan*

3.2.1.3 Domain wall deviation

Another material effect seen was deviation of domain wall boundaries from the hexagonal crystal lattice. This can clearly be seen from the photographs in Figure 3.15 which was taken using a sample with 21.8μm period PPLN gratings etched in HF:HNO_3 to reveal the gratings. Domain inversion of lithium niobate results in domain walls which closely follow the crystalline symmetry of the material [33,46,58]. Therefore it can be concluded that any deviations from this are due to underlying defects in the crystalline structure occurring during crystal growth, and are not due to the poling process. As such, nothing can be done at the fabrication stage to alleviate this problem, instead better quality material must be obtained.

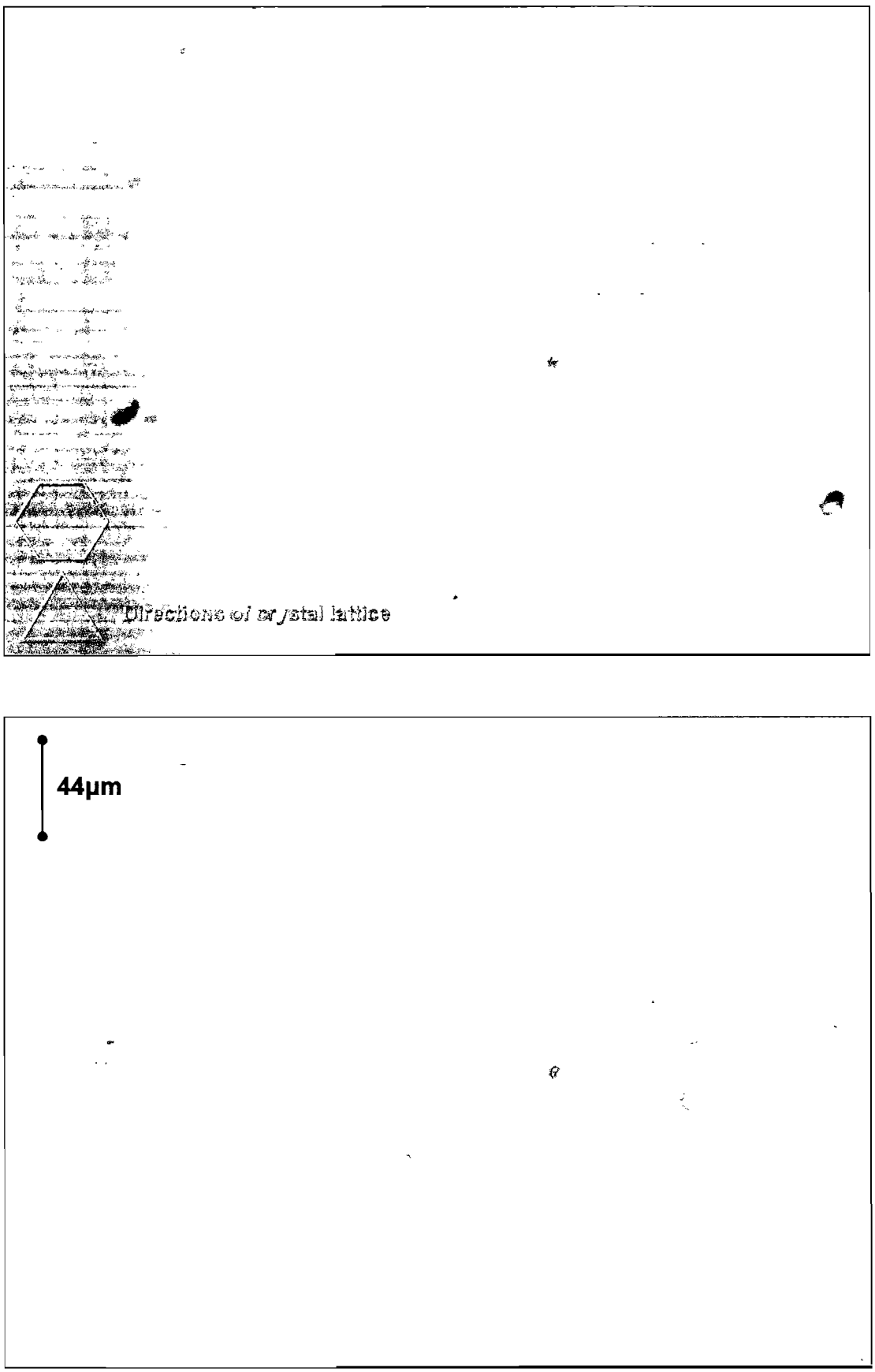

Figure 3.15 *Photographs of etched PPLN gratings showing non straight domain walls and deviations from crystal lattice*

3.2.1.4 Surface defects

There is ongoing investigation to try to understand the actual mechanisms behind domain inversion in lithium niobate [59,25]. Several groups worldwide are investigating the domain inversion process in more depth, in particular their work focuses on how, why and where the domain inversion process starts and how it develops to form large, poled patterns of material. While there are currently no definitive results, the most commonly accepted theory is that domain inversion starts at nucleation sites arising from surface defects or irregularities in the crystal surface. In order to investigate this phenomenon, two lithium niobate crystal samples from different suppliers were sent to Warwick University for X-ray analysis of the surface layers. The results showed that one sample clearly exhibited greater numbers of surface and sub-surface defects. When related to poling quality achieve in these wafers it was concluded that the better poling results where achieved in the sample which had more surface and sub-surface defects.

Although both samples were of the same optical finish, the difference in sub-surface defects could be explained by differences in the final polishing stage. There are two methods of polishing [60] - chemical polishing and mechanical polishing, where one 'advantage' of chemical polishing over mechanical polishing is that it reduces sub-surface damage to the crystal structure. In mechanical polishing, fine scratches are introduced into the material during the initial coarse polishing, and associated with these scratches are dislocations and deformations of the underlying material. As polishing proceeds with finer polishing agents, the surface quality improves until no surface defects are visible - even under a microscope. However, this appearance is very misleading since considerable damage can still exist in the form of covered scratches, microcracks, pits and dislocations concealed by the surface flow of the material being polished, a phenomenon referred to as the 'amorphous' or 'Beilby' layer [61]. This area of microcracks hidden by this layer represents lapping damage which has not yet been removed by polishing, and underneath this are the dislocations left over from the mechanical polishing process. It is underneath this zone that the undisturbed material with a crystallographic perfection representative of the interior of the sample can be found, Figure 3.16.

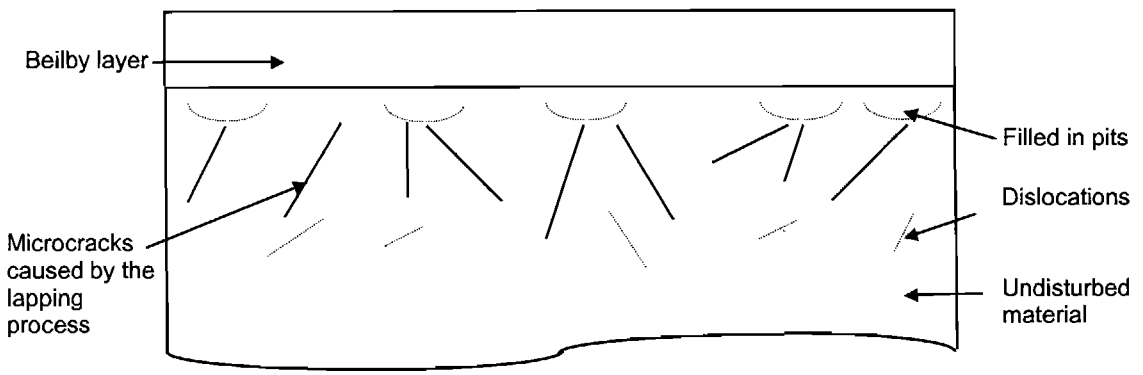

Figure 3.16 Cross-section of lithium niobate wafer showing surface damage due to mechanical polishing

In chemical polishing, material is removed from the surface of the sample by a dissolving process which does not disturb the sub-surface structure and there is no evidence of a 'Beilby' layer or the associated microcracks and dislocations occurring [62].

This is one explanation for the discrepancy between samples from different suppliers. The x-ray analysis suggests that a mechanical polish with microcracks and sub-surface damage leads to better quality poling. Therefore to improve the poling quality of samples from suppliers who use a chemical polish a mechanical re-polish is required. This is a long and expensive process and is unpractical for the quantity of lithium niobate wafers used in this research. Clearly another method of standardising the material from different suppliers was needed.

The remainder of this Section describes an in depth investigation carried out into quicker and cheaper methods of creating sub-surface defects in lithium niobate samples and the resultant effect on poling quality. The poled samples were visually assessed as described in Section 3.1.3, and graded accordingly, where an 'A' Grade indicates an excellent grating across the whole sample and an 'F' Grade indicates very poor poling. One hundred lithium niobate samples from Crystal Technology Ltd., a supplier which previously gave the poorest poling results, were tested and the results shown in Table 3-4. The fabrication process after the extra surface treatment was kept the same and the same grating periods were patterned onto each sample.

Surface Treatment	Average Grade	Comments
None	'E'	Traces of poling, but not periodically
+ z face hand polished with household cream cleaner	'E'	Patches of periodic poling around large scratches
+ and - z face hand polished with household cream cleaner	'F'	Overpoled along large scratches, areas of periodic poling along smaller scratches
+ z face hand polished with 3 μm polishing paper	'F'	Nucleations and traces of periodic poling along scratches, overpoled elsewhere
+ and - z face hand polished with 3 μm polishing paper	'F'	'Frosty' appearance, traces of poling along large scratches
+ z face polished using diamond paste using Dremel polisher	'E'	Periodic poling at scratches, some lengths of grating at longer periods
+ z face polished with 3 μm Calcium Aluminium Oxide using Dremel	'F'	Small patches of poling, but not periodic
+ z face polished with 0.3 μm Calcium Aluminium Oxide using Dremel polisher	'E'	Traces of periodic poling along scratches, nucleations following scratches rather than pattern
+ z face polished with Syton using Dremel polisher	'E'	Traces of periodic poling along scratches
+ z face polished with 0.1 μm diamond lapping paper	'F'	Traces of poling along scratches
+ z face polished with 0.1 μm diamond lapping paper followed by 6 mins HF:HNO_3 1:2 etch	'F'	Poling along large scratches, overpoled elsewhere
+ z face polished with 0.5 μm diamond lapping paper	'E'	Traces of periodic poling along scratches
+ z face polished with 0.5 μm diamond lapping paper followed by 6 mins HF:HNO_3 1:2 etch	'F'	Poling along scratches, not periodically
Heated in furnace for a 4 hours at 1000°C in an Argon atmosphere	'F'	Traces of periodic poling
15 mins in Pirhana [H_2O_2:H_2SO_4]	'D'	Patches of periodic poling
6 mins in pure HF	'B+'	Good uniformity where poled, some poling gaps
6 mins in pure HNO_3	'C'	Quite good, some gaps in poling
1 min in HF:HNO_3 1:2	'B'	Patches of good periodic poling
6 mins in HF:HNO_3 1:2	'B'	Good, some lengths of useable gratings at longer periods
30 mins in HF:HNO_3 1:2	'A-'	Very good in general, some patches of overpoling

Table 3-4 Results of surface preparation investigations

It can be seen from Table 3-4 that polishing the samples with any kind of abrasive material does not significantly improve the poling. It was found that in all cases that the widths of the scratches were much larger than the grating periods and dominated the poling. As a result the poled domains followed the scratches and not the patterned PPLN grating.

However it was found that any kind of acid etch treatment before the cleaning process greatly improved the quality of poling. In particular, samples etched in HF and $HF:HNO_3$ produced the best results.

Material from other suppliers was etched in $HF:HNO_3$ and this was found to enhance, or not adversely affect, the poling quality achievable. It was therefore decided to make a 10 min etch in $HF:HNO_3$ 1:2 a standard step in the preparation process of lithium niobate samples. In practice this has shown consistently improved poling results, with good gratings around 6μm period and smaller being obtained.

3.2.1.5 Conclusions to material discrepancies

It has been seen that the discrepancies arising between lithium niobate wafer material from different suppliers stem from defects in the crystal structure caused by crystal growth techniques, non-uniform wafer polishing (resulting in variations in the wafer thickness) and differing polishing techniques. As such factors cannot be directly influenced during the fabrication process, ways to adapt the available material to the requirements of this research need to be found, such as acid treatments.

3.2.2 Defects arising from the fabrication process

This Section describes several possible causes of defects found in the poled gratings and suggests solutions where appropriate.

3.2.2.1 Poling Dots

Several of the poling defects can be attributed to the fabrication process. The first problem which had to be eliminated was that of 'poling dots'. Due to the pyroelectric

effect, as described in Chapter 2, a rise or fall in temperature across a sample results in increased charge build up on the positive and negative z surfaces of the sample. For lithium niobate the pyroelectric coefficient is 4×10^{-5}C cm^{-2}K^{-1} [63].

It was observed that samples 'crack' and spark with any sudden change in temperature during the fabrication process, such as removal from a drying oven. On inspection the samples were subsequently covered in numerous domain inverted dots up to 6μm in diameter. Figure 3.17 shows a photograph taken through crossed polarisers of such a sample. The dots are visible due to the local stress induced at the domain boundaries. To investigate the shape and actual dimensions of these dots the sample was annealed and the etched for 1 hour at room temperature in HF:HNO_3, Figure 3.18. The triagonal and hexagonal shape, following the crystal structure, of the dots can be seen. The dots ranged in dimensions from sub-micron to several microns across. When these samples were patterned with a photoresist grating and poled, the poling was adversely influenced & dominated by the poling dots rather than following the patterned grating. It was also noticed that the poling dots did not occur in the 4mm border around the sample edges. This confirms the use of an insulating a border during poling, as surface charge can migrate and dissipate around the sample edges.

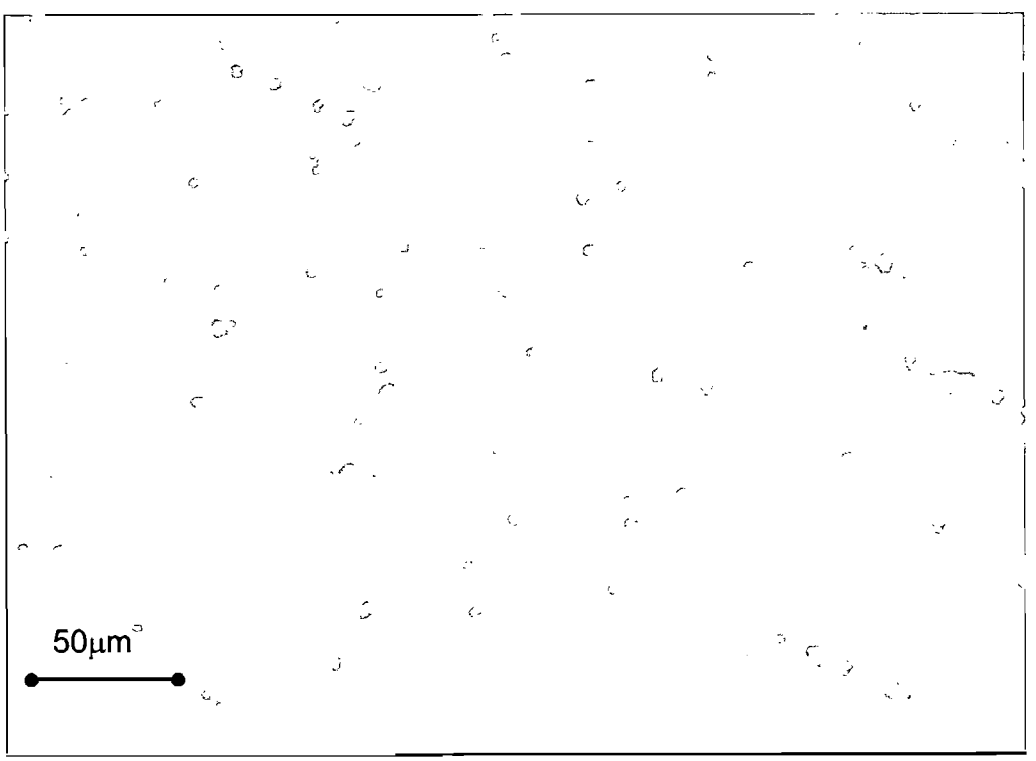

Figure 3.17 Photograph of poling dots taken through crossed polarisers

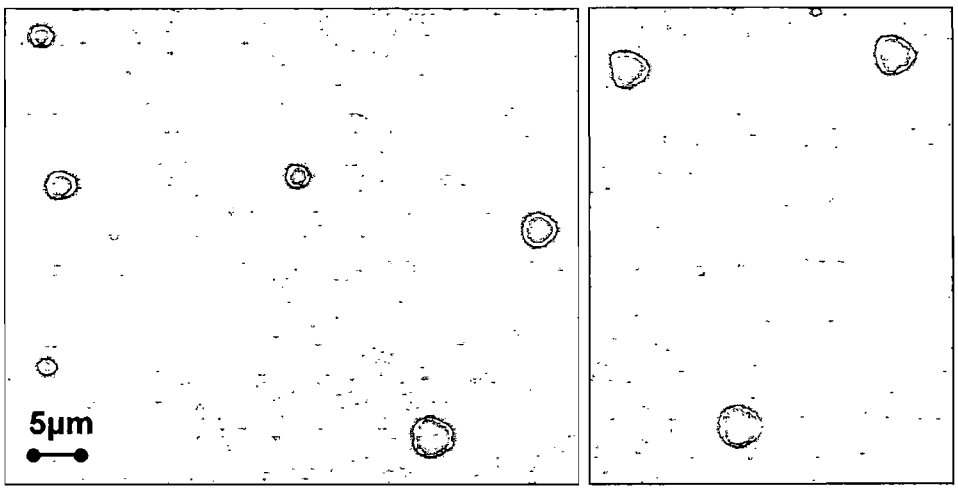

Figure 3.18 Photograph of etched poling dots

Chapter 6 discusses the fabrication of titanium diffused waveguide PPLN devices for frequency conversion. The fabrication of such devices is a two step process – the diffusion of the titanium waveguides and the poling of the PPLN grating. The optimum order of which has been investigated and is described in Chapter 6. In both cases the fabrication was found to be inhibited by poling dots. Figure 3.19 shows photographs of two samples taken through crossed polarisers after diffusion of titanium waveguides in a 1100°C furnace for 10 hours. Poling dots can clearly be seen across the whole surface. These occur particularly in the rapid cooling phase of the diffusion process and it was noticed that on cooling and removal of the samples from the furnace a 'cracking' sound related to discharge was heard. If these samples were to be patterned and poled with PPLN gratings they would not give good results as the poling dots would dominate the gratings.

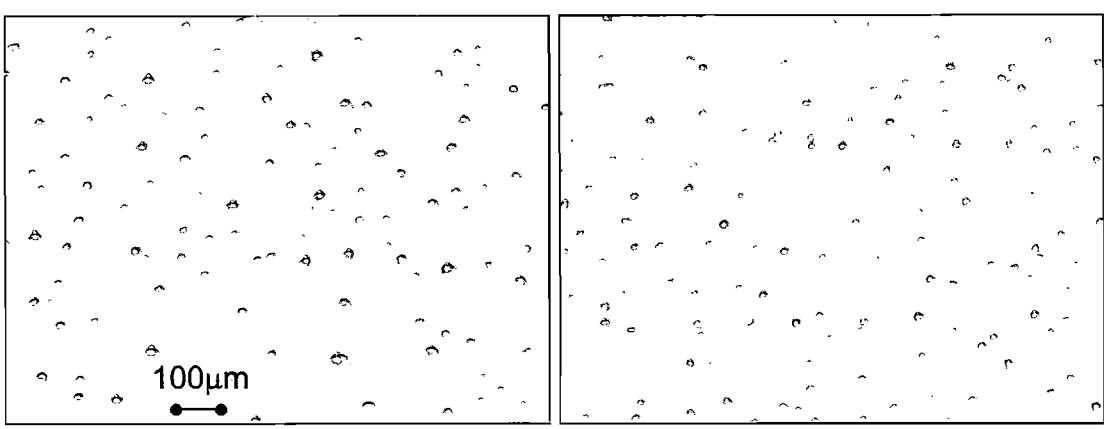

Figure 3.19 Photographs of lithium niobate samples after diffusion of titanium waveguides

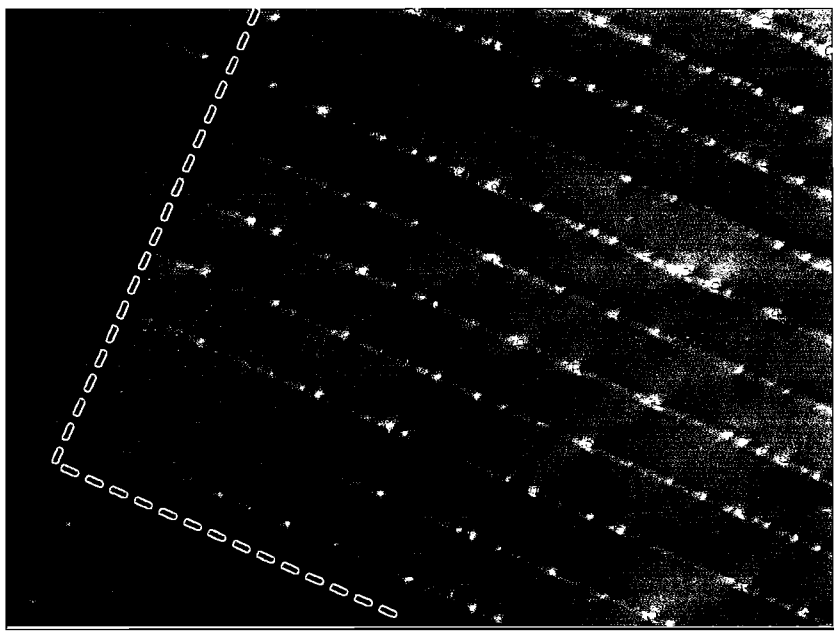

Figure 3.20 Photograph of a poled titanium waveguide devices

Figure 3.20 shows a 'clean' titanium waveguide sample which was then processed for poling. During a drying step in the fabrication process this sample was placed in a 120°C oven, on removal from this oven poling dots were incurred. The photograph shown was taken near a corner of the sample and the 4mm boundary from the edge of the sample is indicated by the dashed blue lines. It can be seen that no dots occur outside these lines. The solution to the poling dots problem is to avoid any heating and cooling of the samples during the fabrication process. If this is unavoidable, for example during the 50°C cleaning process, the 90°C photoresist bake or the 1000°C titanium diffusion, the samples should be raise or lowered in temperature gradually or mechanisms put in place to dissipate the surface charge. This is examined again in Chapter 6.

3.2.2.2 Stitching errors

The second major cause of poling defects encountered during the fabrication process was due to defects in the chrome on fused silica masks used in the UV mask aligner. The masks were made by the Microelectronics group at the University of Southampton by electron beam lithography of a thin layer of metal on to a quartz substrate. The mask is written in small subsections of ~100μm^2 and the beam is magnetically steered to the next subsection. After several subsections the mask is

mechanically translated to the next section. Stitching errors between subsections and sections occurred with observable defects in several of the masks produced. Figure 3.21 shows such defects running in both the horizontal and vertical directions.

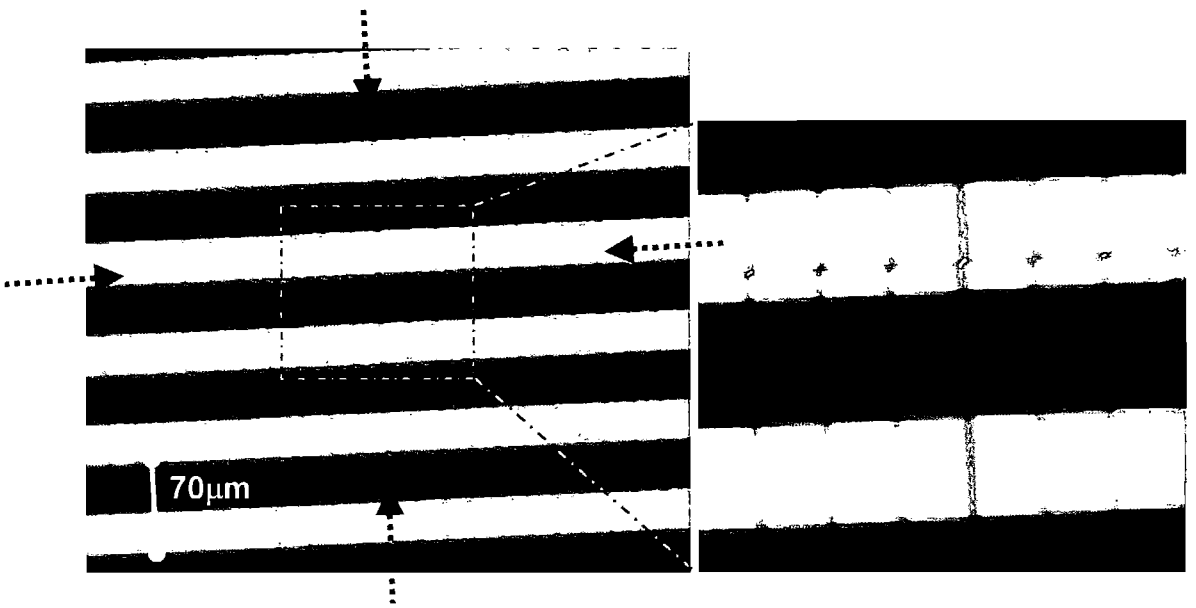

Figure 3.21 *Photographs of mask defects in both horizontal and vertical directions*

These defects are then projected onto the patterned gratings, Figure 3.22, which then adversely affects the poling quality and therefore the device performance. The blue lines indicate the direction of the stitching errors. Figure 3.23 shows inversed domains terminating at the defects in the patterned gratings.

To remove these stitching errors perfect masks are required. After manufacture the masks are individually scrutinised for any stitching errors or other defects.

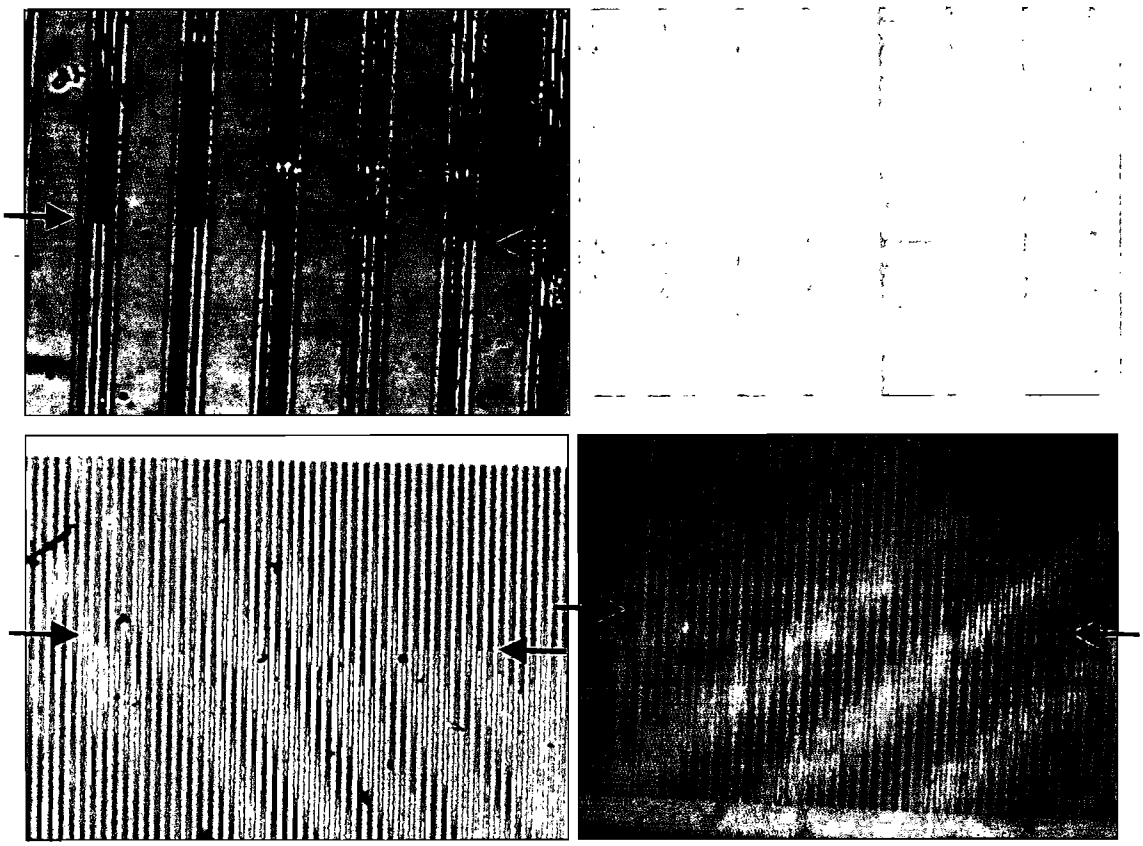

Figure 3.22 *Photographs of defects in the patterned photoresist gratings caused by mask defects*

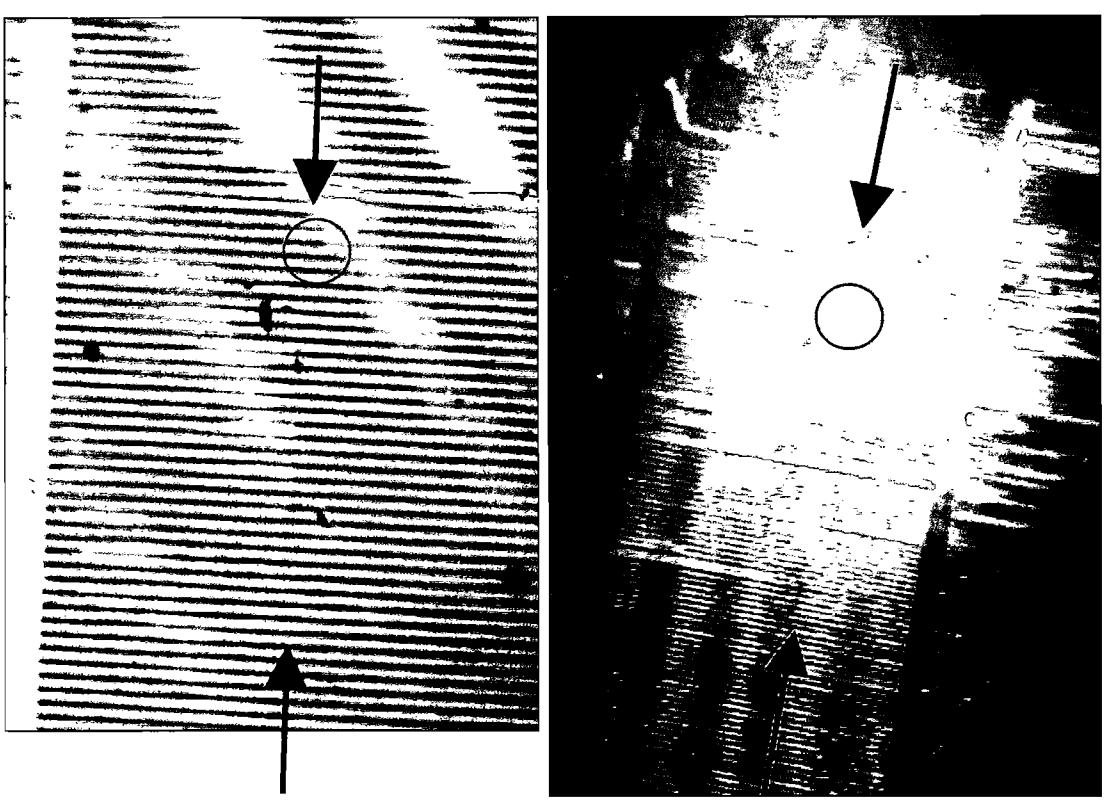

Figure 3.23 *Photographs showing influence of poling on defects in the patterned grating*

3.2.2.3 Photolithography issues

Other factors in the fabrication process which may contribute to poling defects include the variation found in photoresist thickness after spinning and oval interference rings caused by the varying forces upon the sample and photoresist during the acceleration and spinning process. The variation is of order 0.1μm across a typical sample and is thought to only have a significant effect for longer samples with very fine periods.

The photoresist thickness was also examined after UV exposure and development. Initial traces obtained using a Tencor Alphastep Profilometer were not found to give an accurate profile due to the geometry of the Alphastep tip. An atomic force microscope (AFM) scan was found to give better resolution. Figure 3.24 shows a typical spun and patterned photoresist profile for a multiple opening modulator grating and the mask it was imaged from. There are several points of interest. The thickness of the spun resist is approximately 1.75μm, however a strip of lower height can be seen to the left of the gratings, possibly due to a defect in the mask or overexposure. Secondly, the exposed regions in the resist do not all reach the surface of the sample, in particular the outer two stripes still show 0.4μm of photoresist on the sample surface. Also it is interesting to note that the exposed regions do not exhibit a square profile as expected, but a triangular one, this is partly due to the geometry of the AFM tip but may also be due to underexposure. The unexposed regions show thicknesses of only 1.3μm compared to the spun 1.75μm of photoresist. These properties will all have effects on the poling of this sample. However it was found that the photoresist remaining in the exposed regions was thin enough to provide nucleation points and still allowed the current to flow during poling, and that the thinner resist found in the unexposed regions was thick enough to hold off the voltage during poling. In all cases the resist was visually assessed after exposure and developing under a microscope to look for any major under or over exposure or developing. This is particularly important for finer period gratings where the resist profile plays a much larger role in the resultant grating quality.

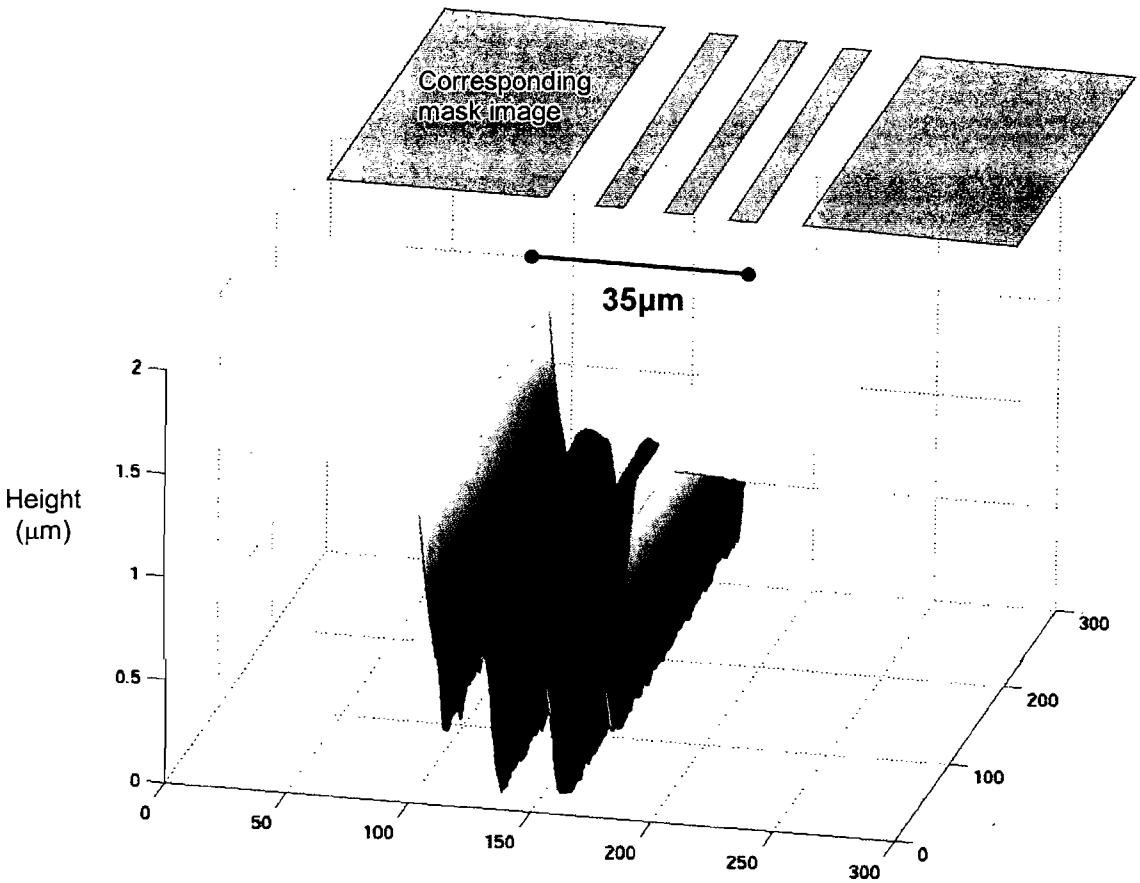

Figure 3.24 AFM scan of photoresist profile (not to scale)

3.2.2.4 Conclusions to fabrication issues

It has been shown that the control of the fabrication process is highly critical towards achieving high quality domain inverted gratings. Several causes of domain inverted grating defects caused by steps in the fabrication process have been highlighted. To eliminate or alleviate these problems several measures or additional fabrication steps have been introduced.

3.2.3 Conclusions to material and fabrication investigation

This Section has presented substantial research carried out to investigate, and better understand material aspects of domain inversion in lithium niobate. To be able to improve device quality and develop new devices it is essential to fully understand the

domain inversion process and all the influencing factors. From this investigation the following interesting conclusions were made :

- Identically specified lithium niobate material from different suppliers exhibits different qualities and properties
- Material from certain suppliers consistently gave better quality domain inversion gratings
- Material from different suppliers required different amounts of charge for an identical domain inverted grating
- Defects in domain inverted gratings were found to be caused by both material and fabrication aspects
- Material aspects included thickness variations across the wafers, fluctuations in crystal structure within the wafers, deviations in domain inverted boundaries and differences in surface and sub-surface defects
- Fabrication aspects included stitching errors in the masks, photolithography issues and dots of domain inversion across the samples caused by the pyroelectric effect
- Techniques have been developed to remove or alleviate the grating defects caused during fabrication
- Some of the material aspects can be standardised between material from different supplier by the addition of a further fabrication process such as surface treatments
- Other material aspects are out with our control and we turn to the crystal growers to help develop more suitable lithium niobate material for domain inversion

Recent crystal growth developments have realised a possible solution to the poor quality gratings achievable in currently available material [64]. In 2001, 3 inch stoichiometric lithium niobate and lithium tantalate crystals became commercially available from a Japanese company, Oxide Corporation (www.opt-oxide.com) [65]. Stoichiometric lithium niobate offers several superior qualities compared to congruent lithium niobate [66,54]. It has reduced defect density, larger nonlinear and electro-optic coefficients, improved transparency in the UV, increased resistance to optic damage and most important in the fabrication of PPLN, a 5 to 10 reduction in the coercive field required for poling compared to congruent lithium niobate [55].

3.3 Effect of periodic poling on lithium niobate properties

Having reviewed the fabrication process of periodically poled lithium niobate and discussed associated fabrication issues such as inconsistencies in material quality and surface defects, this Section goes on to look at some of the properties of lithium niobate and how they are affected by periodic domain inversion. Lithium niobate, because of its high nonlinear, piezoelectric, electro-optic, and pyroelectric coefficients and its photorefractive properties has become widely used for applications in a wide range of fields such as acousto-optic modulation, parametric frequency conversion, phase conjugation, and holographic data processing.

3.3.1 Periodic domain inversion and the photorefractive effect

Lithium niobate displays a very strong photovoltaic effect that, combined with the electro-optic effect, can produce significant changes in refractive index [67], see Chapter 2. This photorefractive effect, first observed nearly thirty years ago [68], is the basis of a number of applications such as holography [69,70] and optical limiting [71]. In other applications, particularly those at visible wavelengths, where preserving good beam quality is vital, it is an unwelcome effect, causing substantial beam distortion and photorefractive damage in single domain lithium niobate. Continuous annealing of the sample at elevated temperatures will reduce photorefractive damage [72], however periodic poling, or domain inversion, has been shown to almost completely eliminate the photorefractive damage in lithium niobate [73,74]. Experimental tests using green light from a cw argon ion laser [75,18] confirm that photorefractive damage is essentially absent in PPLN while being strongly present in single domain lithium niobate.

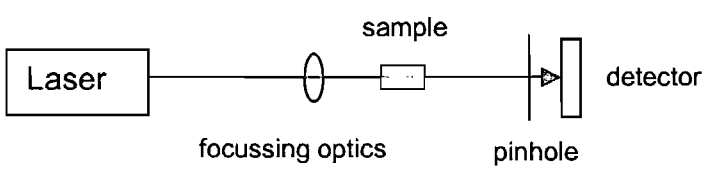

Figure 3.25 Experimental set up for photorefractive investigations

For the devices investigated as part of this research, in particular the visible operation of the Bragg grating modulator described in Chapter 5, the photorefractive effect causes reduced performance and unwanted effects. Therefore the effect of periodic poling on the photorefractive effect was investigated using the set up in Figure 3.25. It was shown that the photorefractive effect is greatest at blue-green wavelengths, however it is very well known that at an operating wavelength of 1064nm the effect of a focussed beam through a 2cm long bulk lithium niobate sample is insignificant (Figure 3.26). Using the same sample, the transmitted power of a focussed beam of beam waist 100μm was taken for areas of bulk and periodic poling with 12μm grating period. It can clearly be seen that the beam passing through the poled grating exhibits greatly reduced photorefractive damage.

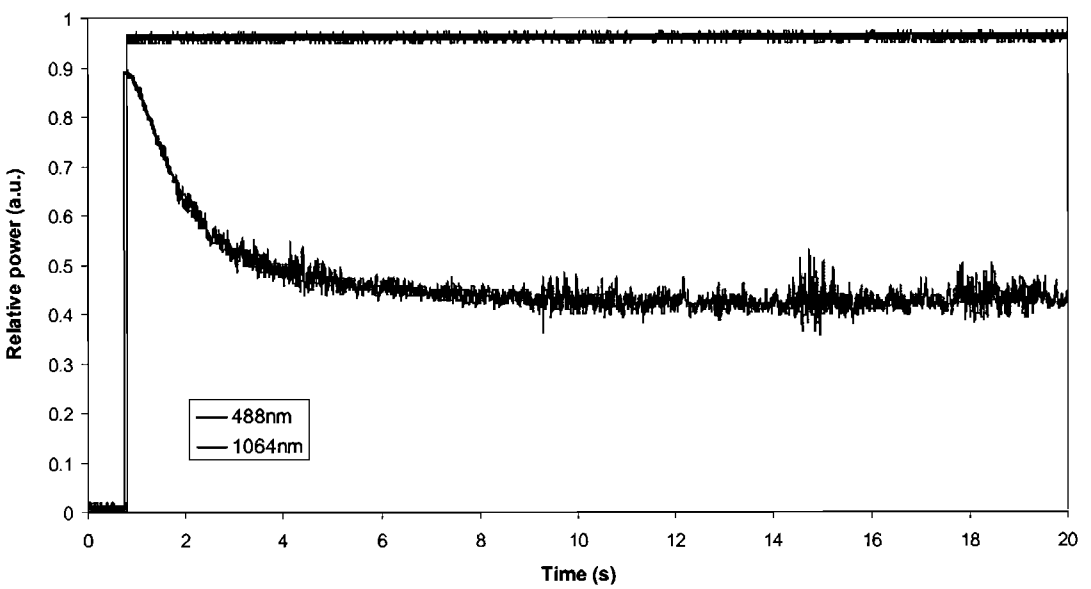

Figure 3.26 *Output power of a focussed beam through bulk lithium niobate with elapsed time for 120mW of 488nm and 70mW 1064nm light*

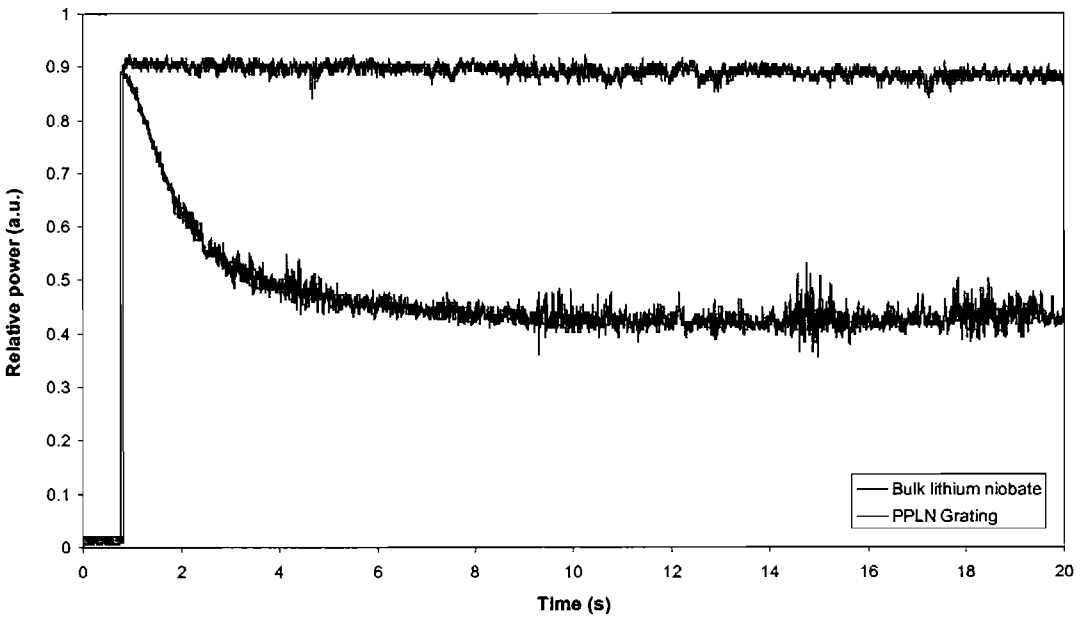

Figure 3.27 *Output power with elapsed time for 120mW 488nm light through bulk lithium niobate and a 12μm PPLN grating*

3.3.2 Periodic domain inversion and the electro-optic coefficient

Lithium niobate exhibits a linear electro-optic effect, as described in Chapter 2, where the resultant change in refractive index from application of an electric field E_k, is given by; $\Delta n = -\frac{n_o^3}{2} r_{ijk} E_j$ The form of the electro-optic tensor, r_{ijk}, depends on the crystal symmetry. If the sign of this tensor is reversed then the resultant change in refractive index will be reversed, for example producing an increase in refractive index instead of a decrease.

In the case of PPLN, the sign of the electro-optic tensor is reversed when a domain is inverted, therefore application of an electric field to a PPLN sample will result in a periodic increased and decrease in refractive index, the strength of which is determined by the strength of the electric field. The application of this as a Bragg diffraction device is described in Chapters 4 and 5.

3.3.3 Periodic domain inversion and the nonlinear coefficient

Lithium niobate is a commonly used nonlinear optical crystal, however its largest nonlinear coefficient, d_{33}, is not birefringently phase matched, so it was not initially considered for phasematching applications (Chapter 2). In 1962 Bloembergen [76] proposed a scheme for quasi-phasematching by means of one-dimensional spatial periodic modulation of nonlinear susceptibilities, with a period equal to $2l_c$, where l_c is the coherence length of the material. See Chapter 6 for a more in depth description. This type of phasematching may be applied to non-birefringent crystals as well as to birefringent crystals with nonlinear optical coefficients which cannot be phase matched. Although this suggestion and the subsequent demonstration [77] of quasi-phasematching took place over thirty years ago, it is only recently that fabrication techniques have been developed to allow quality devices to be produced. Periodic poling is now commonly carried out using a number of different techniques as described previously. Efficient frequency conversion devices based on PPLN now exist which can be used to generate new sources anywhere between 0.4μm and 7.2μm [21,78].

3.3.4 Periodic domain inversion and acid etching

As discussed in Section 3.1.3 lithium niobate is preferentially etched on the negative z face by a $HF:HNO_3$ mixture. This is not only useful to enhance the visibility of PPLN gratings but can be exploited for several microstructuring applications [46]. Any pattern can be poled using electric field poling and then preferentially etched to create three-dimensional structures such as fibre grooves or ridge waveguides, as described in Section 3.4.3.

3.4 Novel PPLN devices

The properties of periodically poled lithium niobate discussed above have been exploited in several novel applications as part of this project. Two specific applications, namely electro-optically controlled Bragg grating modulators in PPLN and titanium diffused PPLN for frequency conversion, are briefly mentioned here and

then expanded upon in Chapters 4, 5 and 6. The remainder of the Section describes devices fabricated using previously outlined fabrication methods.

3.4.1 Modulation and switching devices

This Section briefly introduces electro-optically controlled periodically poled Bragg grating modulators which form the basis of Chapters 4 and 5 and then describes the work carried out in this research group by Boyland et al. to develop a total internal reflection switching device in lithium niobate.

3.4.1.1 Bragg grating modulators

Chapters 4 and 5 discuss in detail the research carried out into the design, fabrication and testing of Bragg grating modulators. These devices are based on the principle of alternating sign of the electro-optic tensor with PPLN. An applied electric field can be used to create a refractive index grating. If the grating period, operating wavelength and incident angle satisfy the Bragg relation, then efficient diffraction into the first order can be achieved. The design of such a modulator device is shown in Figure 3.28 and consists of an area of periodically domain-inverted regions forming a grating of length d (mm) with grating period Λ (μm) and grating planes parallel to the y-axis of the crystal.

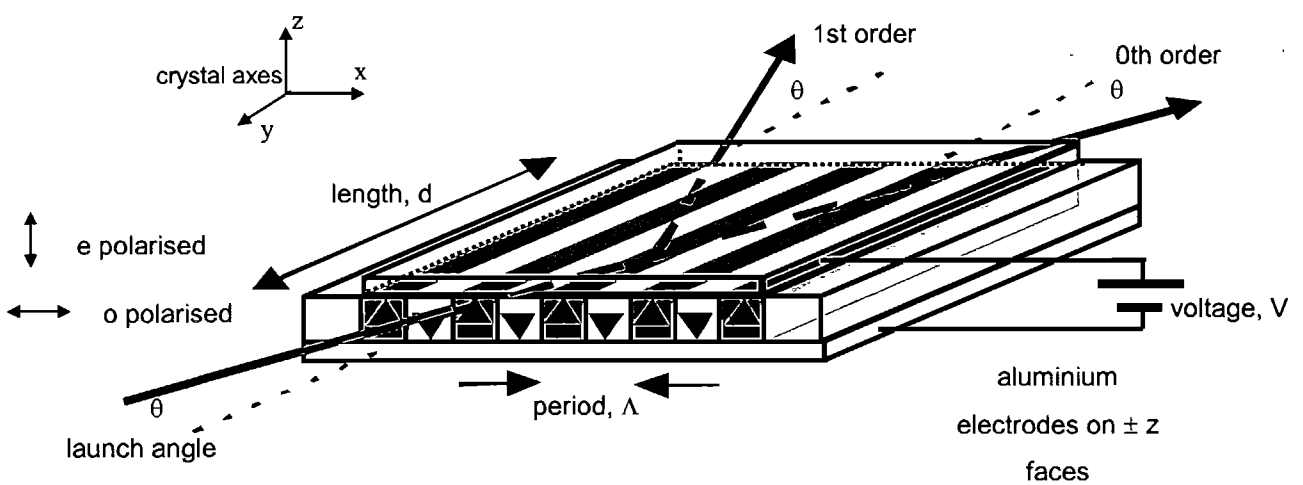

Figure 3.28 Schematic diagram of the periodically poled $LiNbO_3$ modulator device

3.4.1.2 *Total internal reflection switches*

A typical total internal reflection (TIR) device developed by Boyland et al. is shown in Figure 3.29 [79,80]. These devices consist of a domain inverted region and a non-inverted region and use the electro-optic effect to induce a refractive index difference across the domain boundary. When a beam is incident on this boundary at a suitable angle and the refractive index difference is great enough, total internal reflection can occur. Results were obtained for a 300μm thick device of dimensions 13.5mm × 15mm operating at wavelengths of 543nm and 1520nm and power 0.6mW. Contrast ratios of greater than 100:1 for an on/off voltage of approximately 450V and at an incident angle of 89° to the normal were achieved.

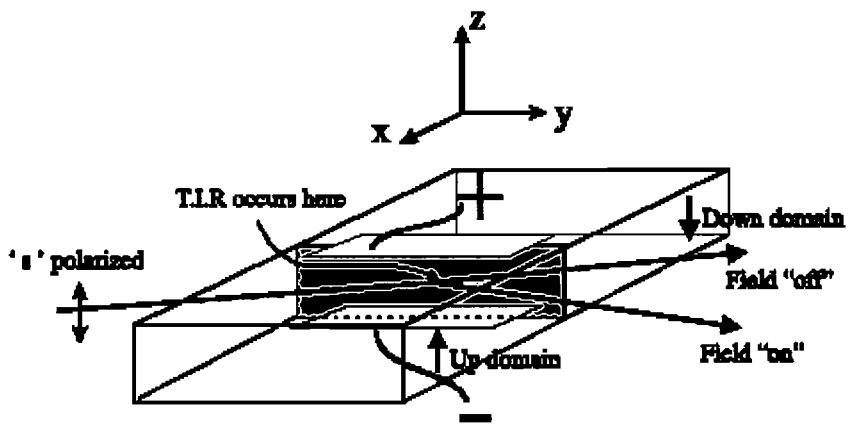

Figure 3.29 Diagram of a typical TIR switch [79,80]

These devices are limited by the high drive voltages required, ie. at an incident angle of 88.4° an on/off voltage of over 1kV is required. Problems were also encountered with the material quality, including domain wall deviations and dots of spontaneous domain inversion, similar to those outlined earlier in this Chapter. Future work is currently being carried out to investigate the dynamic operation of these devices.

3.4.2 Nonlinear frequency generation devices

PPLN for frequency conversion is being used more and more in everyday applications such as printing and scanning, entertainment systems, remote sensing and medical lasers. It is commercially available in a wide range of grating periods from companies such as Crystal Technology [81], Photox [82], Isowave [83], INO [84] and

Stratophase [85]. Due to this ease of availability research into applications of PPLN for frequency conversion has exploded. Just within the ORC there is research using PPLN to create synchronously pumped optical parametric oscillators (SPOPOs) [86,87], including fibre pumped parametric SPOPO devices [88,89,90,91] and generation of femtosecond pulses using pulse compression in a SPOPO [92], long wavelength operation of optical parametric oscillators (OPO's) [78,93], tuneable Ti:sapphire pumped OPO's [94], multi-line OPO's [95], observation of spatial solitons in PPLN [96, 97] and high power second harmonic blue generation [21].

However fabrication techniques and novel PPLN frequency conversion devices are also still being developed. Current publications have reported fabrication of shorter period PPLN, <5μm, for frequency doubling of infrared to generate blue and UV radiation [39], and combining PPLN with waveguides for more efficient devices [98,99,100]. As part of this research two PPLN areas for frequency conversion were investigated, as described below.

3.4.2.1 Titanium waveguides and PPLN

For many nonlinear optical applications in telecommunications it is highly desirable to have a waveguide geometry, firstly because of the compatibility with an optical fibres mode profile, but also because the high degree of optical confinement allows high peak power densities whilst overcoming diffraction. This is means that highly efficient nonlinear processes can be achieved with efficiencies approaching $500\%W^{-1}cm^{-2}$ [101].

To date the principle methods for producing waveguides in PPLN have been proton exchange, pioneered at Stanford [101] and by Michelli in Nice [102], titanium indiffusion which was first demonstrated at the ORC [103] and more recently developed by Sohler's group at Paderborn [104], and direct bonding first demonstrated at the ORC [99]. Chapter 6 presents the extensive research into titanium indiffused waveguides in PPLN carried out for this thesis.

3.4.2.2 *HexLN*

'Normal' PPLN achieves phasematching by modulating the nonlinearity periodically in one dimension. In 1998 Berger suggested the idea of a 2-dimensional nonlinear photonic crystal [105]. The reciprocal lattice is shown in Figure 3.30. The existence of lattice vectors in multiple directions allows for quasi-phasematching along different paths, as indicated for two cases in Figure 3.30, and for different harmonics simultaneously. Second harmonic conversion efficiencies greater than 60% have been achieved using 1531nm picosecond pulses, with simultaneous generation of the second, third and forth harmonic wavelengths [106,107].

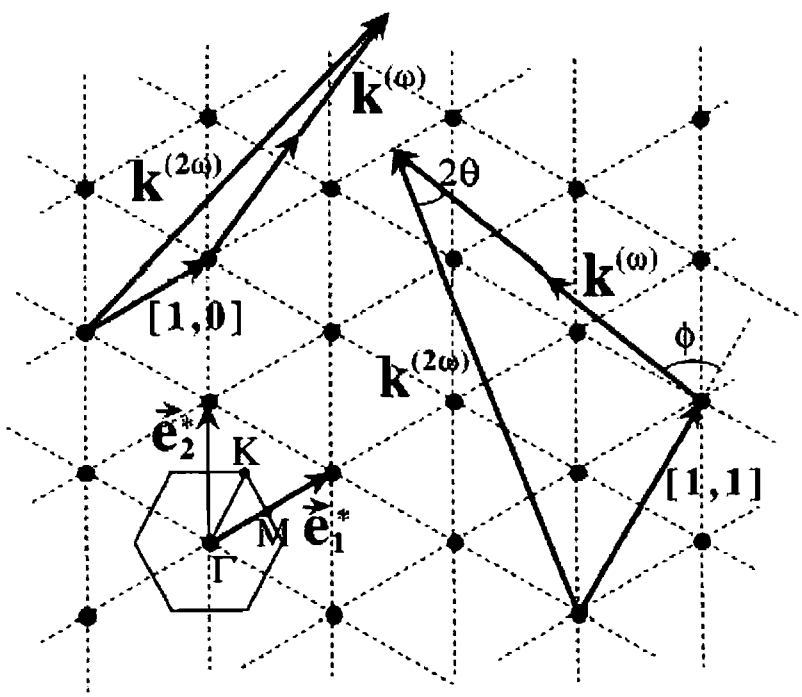

Figure 3.30 *Reciprocal lattice of HexLN structure showing two different QPM processes [106]*

The research reported in this section was carried as part of the study into two-dimensional nonlinear crystals by Broderick et al. in the ORC. Using the same fabrication method outlined earlier in this Chapter but with hexagonal inverted domains, HexLN samples were fabricated as shown in Figure 3.31. Using these devices second harmonic conversion efficiencies of greater than 60% were achieved.

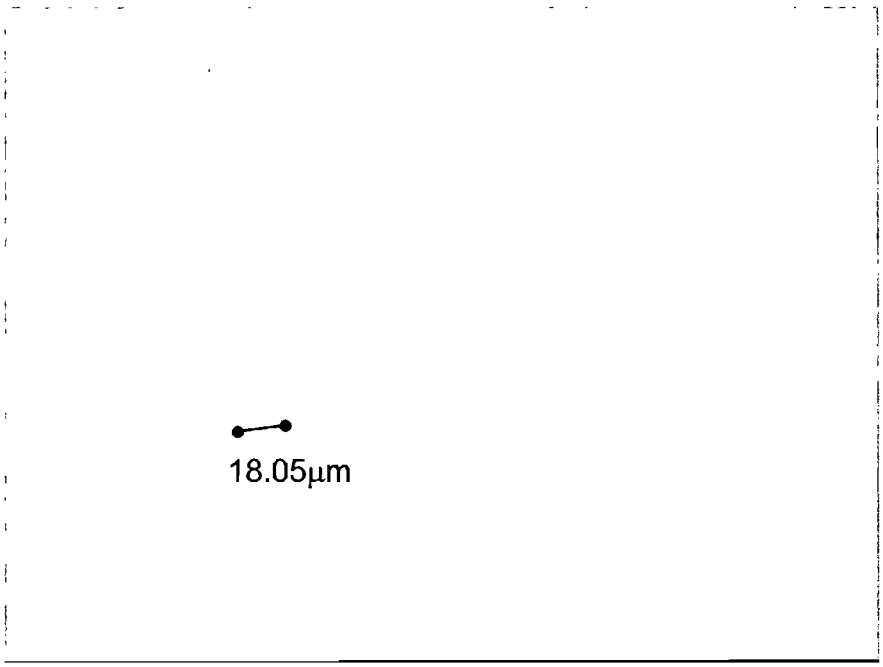

Figure 3.31 Photograph of 18.05 μm period HexLN etched for 10mins in $HF:HNO_3$ to reveal the domains

Although lithium niobate preferentially forms domains along the y-axis and at ±60°, the 2-dimensional lattice is not restricted to hexagonal domains, in fact any pattern whose unit cell is either a triangle or hexagon could be created. Current research is being carried out into more complicated 2-dimensional structures and also into the combination of HexLN and planar titanium diffused waveguides.

Initial fabrication trials have showed limited success due to incompatibility problems between the titanium indiffusion and electric field poling processes, this is discussed further in Chapter 6.

3.4.3 Microstructuring of lithium niobate using differential acid etching

The fact that lithium niobate etches in acid at a different rate on the negative and positive z face can be exploited to create three dimensional structures and devices [46]. Recent research in the ORC by Barry et al. has used this technique of patterning, electric field poling followed by acid etching to create ridge waveguides [47], optical fibre alignment grooves [108] and combined with direct bonding techniques, micro-cantilevers [109].

Figure 3.32 shows ridge structures in lithium niobate fabricated by poling a periodic grating followed by etching in $HF:HNO_3$ at 49°C for approximately 4 hours. These were then combined with ion beam implantation, titanium indiffusion and proton exchange to produce ridge waveguide structures. The lowest losses of 0.8 dB cm^{-1} were obtained using titanium indiffused ridge waveguide structures.

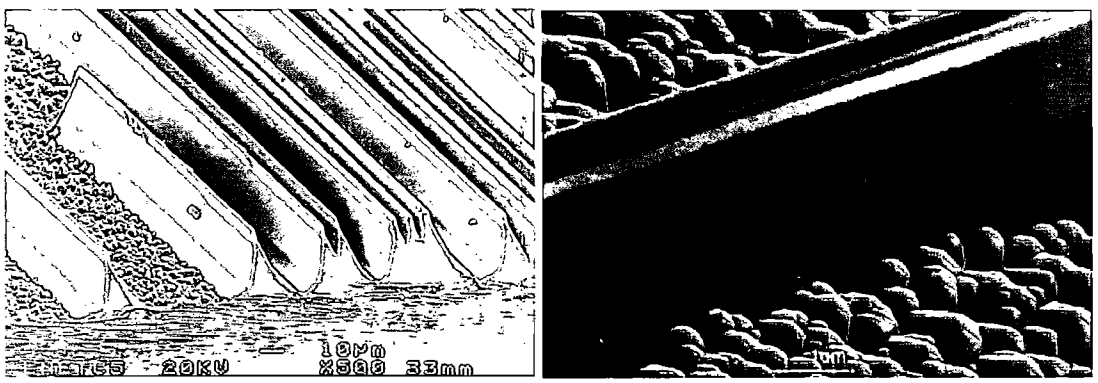

Figure 3.32 *SEM photograph of ridge structures in lithium niobate fabricated via etched domain inverted patterns [photographs provided by Ian Barry, ORC]*

Figure 3.33 shows a micro-cantilever, 20μm wide fabricated by Sones, Gawith, et al. at the ORC by direct bonding two pieces of lithium niobate, one poled with the cantilever pattern and then etched in $HF:HNO_3$ to reveal the structure.

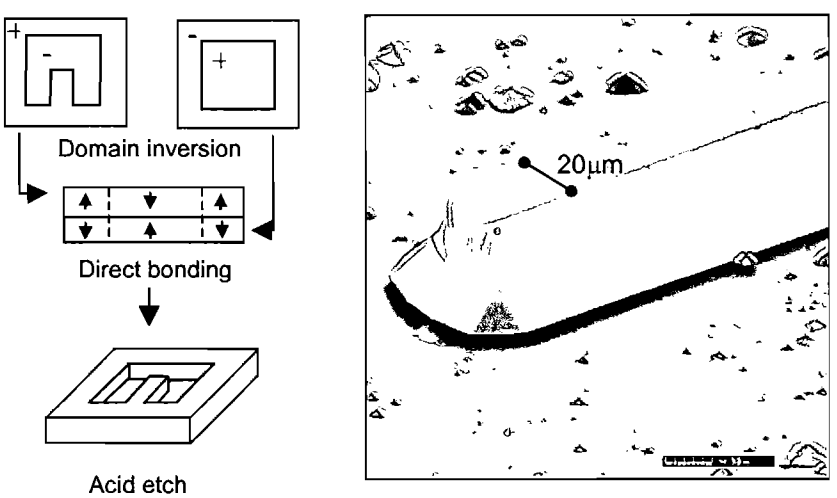

Figure 3.33 *SEM picture of a micro-cantilever [photograph provided by Collin Sones, ORC]*

3.4.3.1 Surface relief gratings

The use of light can modify the etch behaviour of lithium niobate. Barry et al. showed light induced frustrated etching in iron doped lithium niobate using Ar ion light at 488nm [110,111]. Also in the ORC, work by Mailis et al. reported preferential etching of lithium niobate which had been exposed to UV light.

This section describes work carried out as part of this thesis in collaboration with Mailis at the ORC to combine titanium waveguides with preferential acid etching resulting in interferometrically patterned surface relief gratings in lithium niobate, Figure 3.34, for wavelength filtering, wavelength division multiplexing and distributed feedback were produced [112,113,114]. Several techniques of surface patterning have been proposed but they are either very complicated [115] or of limited quality and not easily controllable since they are based solely on direct laser ablation [116]. The method used here involved combining the surface damage produced on the lithium niobate crystal by a pulse UV excimer laser followed by wet acid etching. The acid preferentially attacked the laser modified areas and the depth of the pattern was controllable via the etching time.

The fabrication method was as follows. The titanium channel waveguides were diffused as described in Chapter 6 - 90nm thick titanium strips, ranging from 3-18μm wide at 100μm spacing, were patterned and deposited on the positive z face and diffused at 1100°C for 9 hours in oxygen.

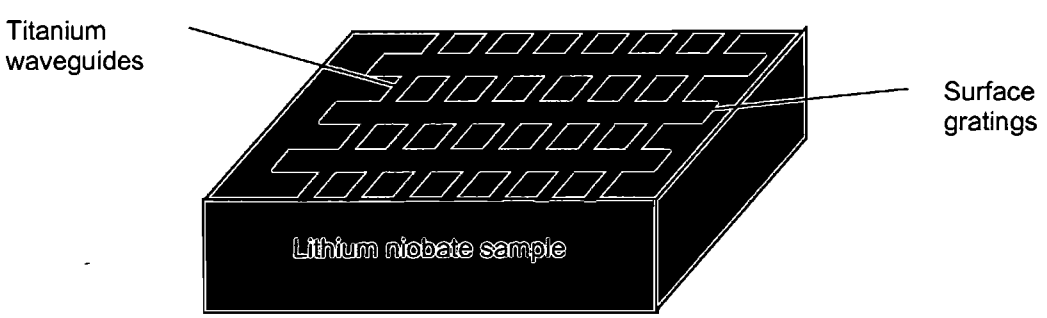

Figure 3.34 Surface relief gratings and titanium indiffused waveguides

Gratings were produced on the positive z face of z cut, 500μm thick lithium niobate samples using two main steps, namely patterning with an excimer laser and then etch in an $HF:HNO_3$ mixture. The positive z face was chosen due to the etch properties of lithium niobate. The surface was patterned interferometrically using an excimer laser (KrF) at 248nm and a phasemask, Figure 3.35. The excimer laser induces damage on the surface which increases the etch rate in that area due to the change in crystal structure.

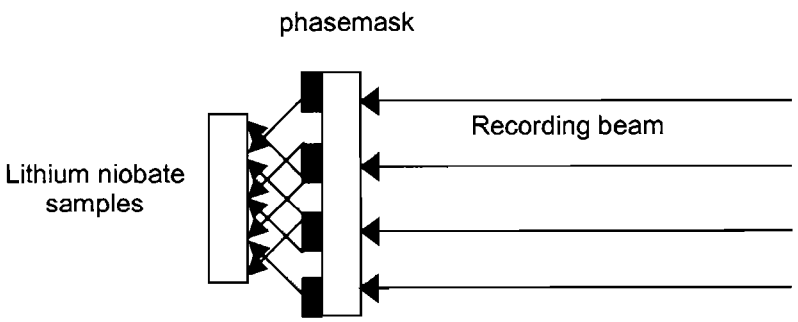

Figure 3.35 Interferometric patterning of sample

Once patterned, the samples were etched in a 1:2 mixture of $HF:HNO_3$. The length of etch was dependent on the depth of grating required, approximately 1 hour for a 100nm deep grating. Figure 3.36 shows the surface profile taken with an atomic force microscope of the gratings produced in a lithium niobate sample.

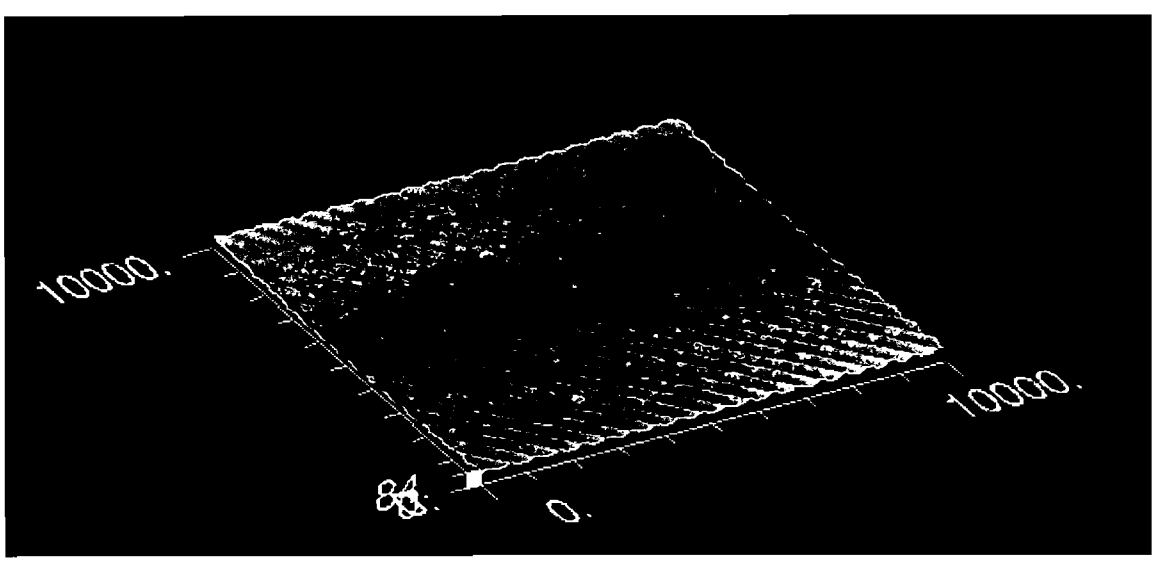

Figure 3.36 AFM profile of surface gratings

Initial samples were interferometrically patterned and then diffused with waveguides. However it was discovered that the long exposure to the high temperature in the furnace caused surface annealing which removed the gratings.

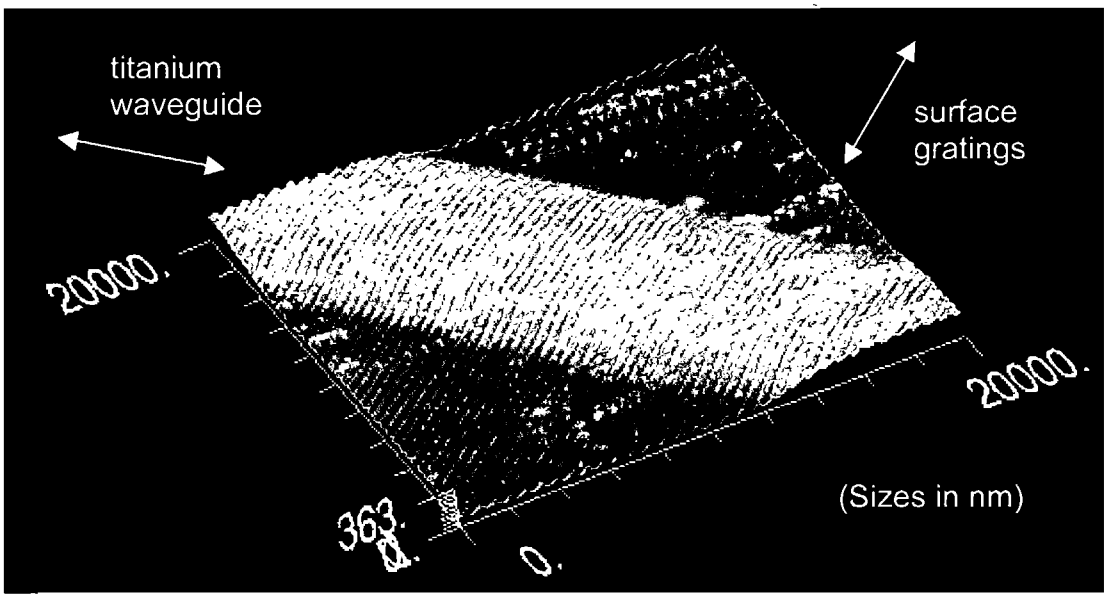

Figure 3.37 AFM profile showing gratings through a titanium indiffused waveguide

Successful devices were realised by diffusing the waveguides first and then patterning the gratings. Figure 3.37 shows the surface profile of a waveguide running through a grating. These devices were tested by Mailis et al. and Figure 3.38 shows the transmission spectra for the etched grating, the effect of the grating can clearly be seen around 1555nm.

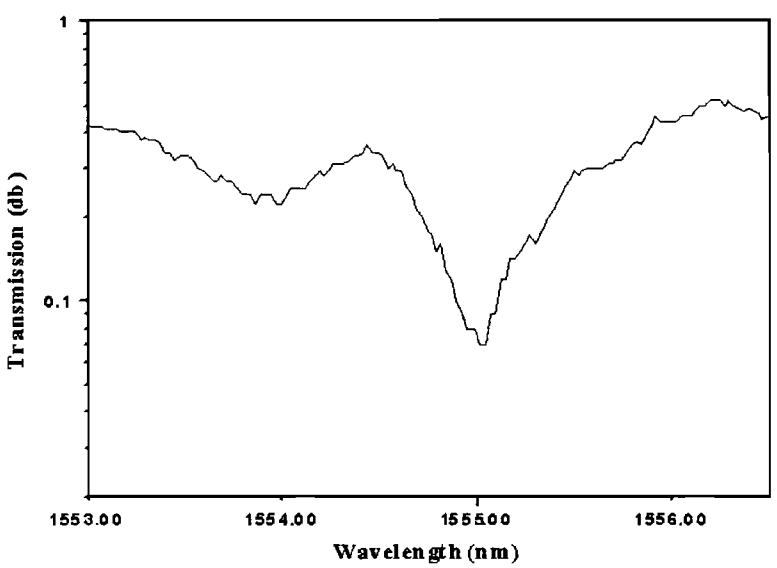

Figure 3.38 Transmission spectra for the etched grating

3.4.4 Novel PPLN devices summary

This Section has described work carried out solely by the author and work done in collaboration with other members of the research group. Table 3-5 summarises the contribution made to each of these devices by the author.

Device	Section	Contribution: Design	Fabrication	Testing
Bragg grating modulator	3.4.1.1	✓	✓	✓
Total internal reflection switch	3.4.1.2	✓	✓	
Titanium waveguides in PPLN	3.4.2.1	✓	✓	✓
HexLN	3.4.2.2		✓	
Titanium ridge waveguide	3.4.3	✓	✓	
Micro-cantilever	3.4.3		✓	
Surface relief grating	3.4.3.1		✓	

Table 3-5 Summary of research carried out into novel PPLN devices

3.5 Chapter summary

This Chapter has outlined the fabrication process of PPLN using a room temperature electric field poling technique using liquid gel electrodes and methods of grating quality assessment presented. Alternative methods of domain inversion in lithium niobate were discussed, in particular investigations into a reverse poling technique were presented. The significant difference in grating quality achievable in material from different suppliers was investigated. This was found to be caused by several factors, including different crystal growth techniques, polishing methods and material quality. Defects such as dots of domain inversion and mask stitching errors caused by procedures in the fabrication process have been investigated and linked to defects in subsequently poled devices. It was concluded that the primary cause of grating defects in poled devices is poor quality lithium niobate material. Therefore to

improve PPLN quality we rely on the crystal growers to develop more reliable, more consistent and better quality raw material.

The effect of periodic poling on several of the properties of lithium niobate, such as the electro-optic coefficient, nonlinear coefficient, differential acid etching and the photorefractive effect can be exploited to produce novel PPLN devices. Recent research carried out into the microstructuring of lithium niobate using differential acid etching to produce devices such as ridge waveguides, optical fibre alignment guides and micro-cantilevers has been reviewed. The combination of differential etching and titanium indiffused waveguides has been investigated and surface relief grating waveguides for use in wavelength filtering, wavelength division multiplexing and distributed feedback have been successfully fabricated. Initial results showing the modification of an erbium doped fibre amplifier spectrum were presented. Two-dimensional nonlinear photonic crystals, known as HexLN, which allow quasi-phasematching along several different paths and for several different harmonics simultaneously have been described and images of samples fabricated presented. Current work to combine these devices with planar titanium indiffused waveguides is ongoing.

An electro-optically controlled Bragg grating modulation and diffraction device was introduced and is further examined in Chapters 4 and 5. In Chapter 4 the first results for such a device operating in the infrared is presented. Initial results and previously published work show several discrepancies between the measured data and a theoretical model based on Kogelnick's coupled wave analysis [117]. Chapter 5 details extensive investigations into the mechanisms behind these discrepancies and proposed solutions of methods of reduction where appropriate.

The combination of PPLN with titanium indiffused channel waveguides for frequency generation was introduced and is investigated further in Chapter 6 with initial results presented for second harmonic generation of 417nm light using a 8.7μm period PPLN grating in a 12μm wide titanium indiffused waveguide.

It has been seen that there is already an extensive range of devices based on periodic domain inversion in lithium niobate. As material quality, fabrication techniques and understanding of the domain inversion process improve the number of device possibilities will increase even more rapidly.

3.6 References

[1] W P Robbins *'Ferroelectric-based microactuators' Int. Ferroelectrics* **11** p179 (1995)

[2] R W Whatmore, S B Stringfellow and N M Shorrocks *Proc. SPIE* **2020** p391 (1993)

[3] R E Jones Jr, P D Maniar, R Moazzami, P Zurcher, J Z Witowski, Y T Lii, P Chu and S J Gillespie *'Ferroelectric non-volatile memories for low-voltage, low-power applications' Thin Solid Films* **270** p584 (1995)

[4] V V Lemanov and Y V Llisavsky *'Piezoelectricity and acoustoelectronics' Ferroelectrics* **42** (1-4) p465-489 (1982)

[5] K Kintaka, M Fujimura, T Suhara and H Nishihara *'High-efficiency $LiNbO_3$ waveguide second-harmonic generation devices with ferroelectric-domain-inverted gratings fabricated by applying voltage' J. Lightwave Technol.* **14** p462 (1996)

[6] V Gopalan, M Kawas, T E Schlesinger, M C Gupta and D D Stancil *'Integrated quasi-phasematched second harmonic generator and electro-optic scanner on $LiTaO_3$ single crystals' IEEE Photonics Technol. Lett.* **8** p1704 (1996)

[7] S Odoulov, A Shumelyuk, O Shinkarenko, D Barilov, S Pavljuk and B Sturman *'Photorefractive wave mixing in periodically poled LiNbO3 : Y : Fe' Acta Physica Polonica* **101** (1) p159-174 (2002)

[8] M Yamada, M Saitoh and H Ooki *'Electric-field induced cylindrical lens, switching and deflection devices composed of the inverted domains in $LiNbO_3$ crystals' Appl. Phys. Lett.* **69** p3659 (1996)

[9] J Webjorn, F Laurell and G Arvidsson *'Blue light generated by frequency doubling of laser diode light in a lithium niobate channel waveguide' IEEE Photon. Tech. Lett.* **1** p316 (1989)

[10] M Fujimura, K Kintaka, T Suhara and H Nishihara *'Blue-light generation in $LiNbO_3$ waveguide SHG device with 1^{st} order domain inverted grating formed by EB scanning' Electron. Lette.* **28** (20) p1868-1869 (1992)

[11] M Yamada, N Nada, M Saitoh and K Watanabe *'First-order quasi-phase matched $LiNbO_3$ waveguide periodically poled by applying an external field for efficient blue second-harmonic generation' Appl. Phys. Lett.* **62** (5) p435 (1993)

[12] M Houe and P D Townsend *'An introduction to methods of periodic poling for second-harmonic generation' J. Phys. D: Appl. Phys.* **28** p1747-1763 (1995)

[13] M J Jongerius, R J Bolt and N A Sweep *'Blue second-harmonic generation in waveguides fabricated in undoped and scandium-doped $KTiOPO_4$' J. Appl. Phys.* **75** (7) p3316 (1994)

[14] G Rosenman, A Skliar, Y Findling, P Urenski, A Englander, P A Thomas and Z W Hu *'Periodically poled $KTiOAsO_4$ crystals for optical parametric oscillation' J. Phys. D: Appl. Phys.* **32** (14) pL49-L52 (1999)

[15] P G R Smith and R W Eason *'Influence of light on the coercive field of repoled strontium barium niobate (SBN); the role of secondary repoling' Appl. Phys. Lett.* **68** p1509-1511 (1996)

[16] V Krylov, J Gallus, U P Wild, A Kalintsev and A Rebane *'Femtosecond noncollinear and collinear parametric generation and amplification in BBO crystal'* Appl. Phys. B-Lasers **70** (2) p163-168 (2000)

[17] R Byer *'Quasi-phasematched nonlinear interactions and devices' J. Nonlinear Opt. Phys and Mat.* **6** (4) p549-592 (1997)

[18] J Webjorn, V Pruneri, P St J Russell, J R M Barr and D C Hanna *'Quasi-phasematched blue light generation in bulk lithium niobate, electrically poled via periodic liquid electrodes' Electronic Letters* **30** 11 p894 (1994)

[19] M Sato, P G R Smith and D C Hanna *'Contact electrode method for bulk periodically poled $LiNbO_3$' TuE1* p178 *LEOS* (1997)

[20] M Sato, P G R Smith and D C Hanna *'Contact electrode method for fabricating bulk periodically poled LiNbO3' Electron. Lett.* **34** (7) p660-661 (1998)

[21] G W Ross, M Pollnau, P G R Smith, W A Clarkson, P E Britton and D C Hanna *'Generation of high-power blue light in periodically-poled $LiNbO_3$ (PPLN)' Opt. Letts* **23** (3) p171-173 (1998)

[22] www.crystaltechnology.com

[23] www.yamajuceramics.co.jp/english

[24] www.castech-us.com

[25] V Y Shur, E L Rumyantsev et al. *'Regular ferroelectric domain array in lithium niobate crystals for nonlinear optic applications' Ferroelectrics* **236** p129-144 (2000)

[26] D Feng, N Ming, J Hong, Y Yang, J Zhu, Z Yang and Y Wang *Appl. Phys. Lett.* **37** (7) p607-609 (1980)

[27] D H Jundt, G A Magel, M M Fejer and R L Byer *'Periodically poled $LiNbO_3$ for high efficiency second-harmonic generation' Appl. Phys. Lett.* **59** (21) p2657-2659 (1991)

[28] M Yamada, N Nada, M Saitoh and K Watanabe *'1st order quasi-phasematched $LiNbO_3$ waveguide periodically poled by applying an external field for efficiency blue second harmonic generation' Appl. Phys. Lett.* **62** (5) p435-436 (1993)

[29] M Houe and P D Townsend *'Thermal polarization reversal of lithium niobate' Appl. Phys. Lett.* **66** p2667 (1995)

[30] K Yamamoto and K Mizuuchi *'Blue light generation by frequency doubling of a laser diode in a domain inverted $LiTaO_3$waveguide' IEEE Photon. Tech. Letts.* **4** (5) p435-437 (1992)

[31] S Miyazawa *'Ferroelectric domain inversion in Ti-diffused $LiNbO_3$ optical waveguide' J. Appl. Phys.* **50** (7) p4599-4603 (1979)

[32] E J Lim, M M Fejer, R L Byer and W J Kozlovsky *'Blue light generation by frequency doubling in periodically poled lithium niobate channel waveguide' Electron. Letts.* **25** (3) p174-175 (1989)

[33] L L Pendergrass *'Ferroelectric microdomain reversal at room temperature in lithium niobate' J. Appl. Phys.* **62** (1) p231-236 (1987)

[34] C Restoin, C Darraud-Taupiac, J L Decossas, J C Vareille and J Hauden *'Ferroelectric domain inverted gratings by electron beam on $LiNbO_3$' Mat. Sci. in Semiconductor Processing* **3** p405-407 (2000)

[35] H Ito, C Takaya and H Inabu *'Fabrication of periodic domain grating in $LiNbO_3$ by electron-beam writing for application of nonlinear optical processes' Electron. Letts.* **27** (14) p1221-1222 (1991)

[36] M Fujimura, K Kintaka, T Suhara and H Nishihara *'Blue light generation in $LiNbO_3$ waveguide SHG device with 1st order domain inverted grating formed by EB scanning' Electron. Letts* **28** (20) p1868-1867 (1992)

[37] P W Haycock and P D Townsend *'A method of poling $LiNbO_3$ and $LiTaO_3$ below T_c' Appl. Phys. Lett.* **48** (11) p698-700 (1986)

[38] A C G Nutt, V Gopalan and M C Gupta *'Domain inversion in $LiNbO_3$ using direct electron-beam writing' Appl. Phys. Lett.* **60** (23) p2828-2830 (1992)

[39] R G Batchko, V Y Shur, M M Feyer and R L Byer *'Backswitch poling in lithium niobate for high-fidelity domain patterning and efficient blue light generation' Appl. Phys. Lett.* **75** (12) p1673 (1999)

[40] V Y Shur, E L Rumyantsev et al. *'Nanoscale backswitch domain patterning in lithium niobate' Appl. Phys. Lett.* **76** (2) p143 (2000)

[41] L-H Peng, Y-C Fang and Y-C Lin *'Polarization switching of lithium niobate with giant internal field' Appl. Phys. Lett.* **74** (14) p2070 (1999)

[42] J H Ro and M Cha *'Subsecond relaxation of internal field after polarization reversal in congruent $LiNbO_3$ and $LiTaO_3$ crystals' Appl. Phys. Lett.* **77** (15) p2391 (2000)

[43] V Gopalan and T E Mitchell *'Wall velocities, switching times and the stabilization mechanism of 180° domains in congruent $LiTaO_3$ crystals' J. Appl. Phys.* **83** (2) p941 (1998)

[44] K Nassau, H J Levinstein and G M Loiacono *Appl. Phys. Lett.* **6** (11) p228 (1965)

[45] V Bermudez, F Caccavale, C Sada, F Segato and E Dieguez *'Etching effect on periodic domain structures of lithium niobate crystals' J. Crystal Growth* **191** p589-593 (1998)

[46] I E Barry, G W Ross, P G R Smith, R W Eason and G Cook *'Microstructuring of lithium niobate using differential etch-rate between inverted and non-inverted ferroelectric domains' Material Lett.* **37** p246-254 (1998)

[47] I E Barry, G W Ross, P G R Smith and R W Eason *'Ridge waveguides in lithium niobate fabricated by differential etching following spatially selective domain inversion' Appl Phys Lett* **74** p1487 (1999)

[48] J Wittborn, C Canalias, K V Rao, R Clemens, H Karlsson and F Laurell *'Nanosecond imaging of domains and domain walls in periodically poled ferroelectrics using atomic force microscopy' Appl. Phys. Lett.* **80** (9) p1622-1624 (2002)

[49] H Bluhm, A Wadas, R Wiesendanger, A Roshko, J A Aust and D Nam *'Imaging of domain-inverted gratings in $LiNbO_3$ by electrostatic force microscopy' Appl. Phys. Lett.* **71** (1) p146-148 (1997)

[50] S Tsunekawa, J Ichikawa, H Nagata and T Fukuda *'Observation of ferroelectric microdomains in $LiNbO_3$ crystals by electrostatic force microscopy' Appl. Surface Sci.* **137** p61-70 (1999)

[51] Z W Hu, P A Thomas, A Snigirev, I Snigrireva, A Souvorov, P G R Smith, G W Ross and S Teat *'Phase-mapping of periodically domain inverted $LiNbO_3$ with coherent X-rays' Nature* **392** p690-693 (1998)

[52] M Drakopoulos, Z W Hu, S Kuznetsov, A Snigrirev, I Snigireva and P A Thomas *'Quantative x-ray Bragg diffraction topology of periodically domain inverted $LiNbO_3$' J. Phys. D: Appl. Phys.* **32** pA160-165 (1999)

[53] V Pruneri *'Electric field periodically inverted $LiNbO_3$ for optical frequency conversion' PhD Thesis* University of Southampton (1996)

[54] Y-L Chen, J-J Xu, X-J Chen, Y-F Kong and G-Y Zhang *'Domain reversion process in near-stoichiometric $LiNbO_3$ crystals' Optics Comms.* **188** p359-364 (2001)

[55] V Gopalan, T E Mitchell, K Kitamura and Y Furukawa *'The role of nonstoichiometry in 180 degrees domain switching of $LiNbO_3$ crystals' Appl. Phys. Lett.* **72** p1981 (1998)

[56] Anon 'Measuring system uses conoscopic holography' Opt. Laser Technol. **31** (4) VI-VI (1999)

[57] L M Mugnier 'Conoscopic Hologaphy – Towards 3-dimentional reconstructions of opaque objects' Appl. Opt. **34** (8) p1363-1371 (1995)

[58] V Y Shur, E L Rumyantsev, E V Nikolaeva and E I Shishkin *'Formation and evolution of charged domain walls in congruent lithium niobate' Appl. Phys. Lett.* **77** (22) p3636 (2000)

[59] L Huang and N A F Jaeger *'Discussion of domain inversion in $LiNbO_3$' Appl. Phys. Lett.* **65** (14) p1763 (1994)

[60] Logitech *Chemical polishing & Electro-optic materials technology brochures*

[61] F P Bowden and T P Hughes *'Physical properties of surfaces. IV: Polishing, surface flow and the formation of the Beilby layer' Proc. R. Soc. Lond.* **A160** p575-587 (1936)

[62] Logitech Technology Brochures *'Complete Systems for the Sawing, Lapping & Polishing of Electro-Optic Materials'* and *'Chemical Polishing'*

[63] A Savage *J. Appl. Phys.* **37** p3071 (1990)

[64] S Furukawa, K Kitamura, S Takekawa, K Niwa and H Hatano *'Improved properties of stoichiometric $LiNbO_3$ for electro-optic applications' J. Intel. Mat. Syst. Str.* **10** (6) p470-475 (1999)

[65] Newsbreak *Laser Focus World* p11 (May 2001)

[66] K Kitamura, S Takekawa, M Nakamura and Y Furukawa *'Commercialisation of stoichiometric $LiNbO_3$ and $LiTaO_3$ for optical devices' CLEO/PR July 2001* WH2-1

[67] L Arizmendi and F Agullo-Lopez *'$LiNbO_3$: A paradigm for photorefractive materials' MRS Bulletin* p32-38 March 1994

[68] A Ashkin, G D Boyd, J M Dziedzic, R G Smith, A A Ballman, J J Levinstein and K Nassau *'Optically-induced refractive index inhomogeneities in $LiNbO_3$ and $LiTaO_3$' Appl. Phys. Lett.* **9** p72-74 (1966)

[69] J-W An, N Kim, K-W Lee *'Volume holographic wavelength demultiplexer based on rotation multiplexing in the 90° geometry' Opt. Comms.* **197** p247-254 (2001)

[70] E M de Miguel, T Limeres, M Carrascosa and L Arizmendi *'Study of developing thermal fixed holograms in lithium niobate' J. Opt. Soc. Am. B* **17** (7) p1140-1146 (2000)

[71] C B G Gawith, P Hua, P G R Smith and G Cook *'Nonreciprocal transmission in a direct-bonded photorefractive Fe:$LiNbO_3$ buried waveguide' Appl. Phys. Lett.* **78** (26) p4106-4108 (2001)

[72] K C Burr, C L Tang, M A Arboure and M M Fejer *'High-repetition rate femtosecond optical parametric oscillator based on periodically poled lithium niobate' Appl. Phys. Lett.* **70** (25) p3341 (1997)

[73] M Taya, M C Bashaw and M M Fejer *'Photorefractive effects in periodically poled ferroelectrics' Opt. Lett.* **221** p857 (1996)

[74] V Bermudez, J Capmany, J G Sole and E Dieguez *'Growth and second harmonic generation characterization of Er^{3+} doped bulk periodically poled $LiNbO_3$' Appl. Phys. Lett.* **73** (5) p593 (1998)

[75] G A Magel, M M Fejer and R L Byer *'Quasi-phase matched second harmonic generation of blue light in periodically poled $LiNbO_3$' Appl. Phys. Lett.* **56** (2) p108 (1990)

[76] J A Armstrong, N Bloembergen, J Ducuing and P S Pershan *'Interactions between light waves in a nonlinear dielectric' Phys. Rev.* **127** p1918 (1962)

[77] R C Miller *'Optical second harmonic generation in piezoelectric crystals' Appl Phys Lett* **5** p17 (1964)

[78] M A Watson, M V O'Connor, P S Lloyd, O Balachninaite, D P Shepherd, and D C Hanna *'Long-wavelength operation of synchronously pumped optical parametric oscillators based on periodically poled LiNbO3' CLEO 2002* Long Beach, California 19-24th May (2002) ***CWA11***

[79] A J Boyland, S Mailis, J M Hendricks, P G R Smith and R W Eason *'Electro-optically controlled beam switching via total internal reflection at a domain engineered interface in $LiNbO_3$' Opt. Comms.* **197** p193-200 (2001)

[80] R W Eason, A J Boyland, S Mailis, P G R Smith *'Electro-optically controlled beam deflection for grazing incidence geometry on a domain engineered interface in $LiNbO_3$' Opt. Comms.* **197** p201-207 (2001)

[81] www.crystaltechnology.com

[82] www.photox.co.uk

[83] www.isowave.com

[84] www.ino.qc.ca

[85] www.stratophase.com

[86] D C Hanna *'Synchronously-pumped optical parametric oscillators' QEP 15* Glasgow p97 3-6th September (2001) ***Invited***

[87] D C Hanna, M V O'Connor, M A Watson and D P Shepherd *'Synchronously pumped optical parametric oscillator with diffraction-grating tuning' J. Physics D: Appl. Phys.* **34** p2440-2454 (2001)

[88] T Sudmeyer, J Aus der Au, R Paschotta, U Keller, P G R Smith, G W Ross and D C Hanna *'Femtosecond fiber-feedback optical parametric oscillator' Opt. Lett.* **26** (5) p304-306 (2001)

[89] D J Richardson, A B Grudinin and D C Hanna *'Fiber laser pumped parametric devices based on periodically poled lithium niobate' OSA Annual Meeting/ILS-XIV* Baltimore USA 4-9th Oct (1998) FL1 ***Invited***

[90] P E Britton, H L Offerhaus, D J Richardson, P G R Smith, G W Ross and D C Hanna *'A parametric oscillator directly pumped by a 1.55μm erbium fibre laser' Opt. Lett.* **24** (14) p975-977 (1999)

[91] P G R Smith, P E Britton, D Taverner, N G Broderick, D J Richardson, G W Ross, C B E Gawith, J A Abernethy, H L Offerhaus and D C Hanna *'Review of erbium fibre laser based nonlinear optics in periodically poled lithium niobate (PPLN)' International Workshop on Periodically Microstructured Nonlinear Optical Materials* Madrid 10-13th Jun (2001)

[92] L Lefort, K Puech, S D Butterworth, Y P Svirko and D C Hanna *'Generation of femtosecond pulses from order-of-magnitude pulse compression in a synchronously pumped optical parametric oscillator based on periodically poled lithium niobate' Opt. Lett.* **24** (1) p28-30 (1999)

[93] L Lefort, K Puech, G W Ross, Y P Svirko and D C Hanna *'Optical parametric oscillation out to 6.3μm in periodically poled lithium niobate under strong idler absorption' App. Phys. Lett.* **73** (12) p1610-1612 (1998)

[94] C J Lee, G W Baxter, J C Diettrich, I T McKinnie, D M Warrington, P G R Smith, G W Ross and D C Hanna *'Periodicaly poled lithium niobate optical parametric oscillator pump-tuned by a single-axial-mode ti:sapphire laser' Opt. Eng.* **41** (4) p848-851 (2002)

[95] T M J Kendall, W A Clarkson, P J Hardman, G W Ross and D C Hanna *'Multiline optical parametric oscillators based on periodically-poled lithium niobate' CLEO 2000* San Francisco 7-12th May (2000) **CMC7**

[96] B Bourliaguet, V Couderc, A Barthelemy, G W Ross, P G R Smith, D C Hanna and C de Angelis *'Observation of quadratic spatial solitons in periodically poled lithium niobate' Opt. Lett.* **24** (20) p1410-1412 (1999)

[97] A Barthelemy, B Bourliaguet, V Couderc, C De Angelis, F Gringoli, G W Ross, P G R Smith and D C Hanna *'Collisions between two dimensional quadratic spatial solitons in PPLN'* **3936** p250-258 *SPIE* 2000

[98] K P Parameswaran, R K Route, J R Kurz, R V Roussev, M M Fejer and M Fujimura *'Highly efficient second-harmonic generation in buried waveguides formed by annealed and reversed proton exchange in periodically poled lithium niobate' Opt. Letts.* **27** (3) p179-181 (2002)

[99] C B E Gawith, D P Shepherd, J A Abernethy, D C Hanna, G W Ross and P G R Smith *'Second-harmonic generation in a direct-bonded periodically poled LiNbO3 buried waveguide' Opt. Letts.* **24** (7) p481-483 (1999)

[100] S Tanzilli, W Tittel, H De Riedmatten, H Zbinden, P Baldi, M De Micheli, D B Ostrowsky and N Gisin *'PPLN waveguide for quantum communication' Eur. Phys. J. D* **18** (2) p155-160 (2002)

[101] M H Chou, K R Parameswaran, M M Fejer and I Brener *'Multiple channel wavelength conversion by use of engineered quasi-phase matching structures in $LiNbO_3$ waveguides' Optics Letters* **24** p1157 (1999) and *CLEO'99 CTuW7*

[102] P Baldi, M P De Micheli, K El Hadi, S Nouh, A C Cino, P Aschieri and D B Ostrowsky *'Proton exchange waveguides in $LiNbO_3$ and $LiTaO_3$ for integrated lasers and nonlinear frequency converters' Opt. Eng.* **37** (4) p1193 (1998)

[103] J Amin, V Pruneri, J Webjorn, P St J Russell, D C Hanna and J S Wilkinson *'Blue light generation in a periodically poled Ti:$LiNbO_3$ channel waveguide' Opt. Comms.* **135** (1-3) p41-44 (1996)

[104] D Hofmann, G Schreiber, C Haase, H Herrmann, W Grundkotter, R Ricken, W Sohler *'Quasi-phasematched difference frequency generation in periodically poled Ti:$LiNbO_3$ channel waveguides' Opt. Letts.* **24** (13) p896-898 (1999) and *ECIO'99 Turin*

[105] V Berger *'Nonlinear photonic crystals' Phy. Rev. Lett.* **81** p4136-4139 (1998)

[106] N G R Broderick, G W Ross, H L Offerhaus, D J Richardson and D C Hanna *'Hexagonally poled lithium niobate: a two-dimensional nonlinear photonic crystal' Phys. Rev. Lett.* **84** p4345-4348 (2000)

[107] N G Broderick, T M Monro, G W Ross, D J Richardson, D C Hanna and P G R Smith *'Comparison of 2nd harmonic generation in 1 and 2D nonlinear periodic crystals' CLEO/Europe 2000* Nice 10-15th Sep (2000) **CFA1**

[108] R W Eason, I E Barry, G W Ross and P G R Smith *'Fabrication of alignment grooves in $LiNbO_3$ substrates for simplified optical fibre pigtailing' Electron. Letts.* **35** (4) p328-329 (1999)

[109] C Sones, S Mailis, V Apostolopoulos, I E Barry, C B E Gawith, P G R Smith and R W Eason *'Fabrication of piezoelectric micro-cantilevers in domain engineered $LiNbO_3$ single crystals' J. Micromech. Microeng.* **12** (1) p53-57 (2002)

[110] I E Barry, R W Eason and G Cook *'Light induced frustration of etching in Fe-doped $LiNbO_3$' Appl. Surf. Sci.* **143** (1-4) p328-331 (1999)

[111] A J Boyland, S Mailis, I E Barry, R W Eason and M Kaczmarek *'Latency effects and periodic structures in light induced frustrated etching of Fe-doped $LiNbO_3$' Appl. Phys. Lett.* **77** (18) p2792-2794 (2000)

[112] S Mailis, G W Ross, L Reekie, J A Abernethy and R W Eason *'Fabrication of surface relief gratings on lithium niobate by combined UV laser and wet etching' Electronics Letters* **36** (21) p1801-1803 (2000)

[113] S Mailis, G W Ross, L Reekie, J A Abernethy and R W Eason *'New technique for fabrication of surface relief Ti-indiffused $LiNbO_3$ waveguides' CLEO 2000* San Francisco 7-12 May 2000 CWK46

[114] S Mailis, G W Ross, L Reekie, J A Abernethy, I E Barry, R W Eason, I Nee, M Muller and K Buse *'Optically assisted chemical surface microstructuring of $LiNbO_3$' CLEO/Europe 2000* Nice 10-15 Sep 2000 CTuO7

[115] J Sochtig, H Schutz, R Widmer, R Corsini, D Hiller, C Carmannini, G Consonni, S Bosso and L Gobbi *'Monolithically integrated DBR waveguide laser and intensity modulator in erbium doped $LiNbO_3$' Electron. Lett.* **32** p89 (1996)

[116] K Chen, J Ihlemann, P Simon, I Baumann and W Sohler *'Generation of submicron surface gratings on $LiNbO_3$ by ultrashort UV laser pulses' Applied Physics A* **65** p517 (1997)

[117] H Kogelnik *'Coupled wave theory for thick hologram gratings' The Bell System Technical Journal* **48** 9 p2909-2947 (1969)

Chapter 4

Electro-optic Bragg grating modulators in periodically poled lithium niobate

This Chapter presents work carried out to develop an electro-optic Bragg grating modulator in periodically poled lithium niobate. It starts by reviewing existing electro- and acousto-optic modulators and describes previous work carried out by other authors on Bragg grating modulators [1,2]. A theoretical model of the diffraction efficiency based on Kogelnik's coupled wave theory [3] is presented. The design and fabrication of such devices is discussed and finally results showing the first infrared demonstration of a Bragg modulator based on periodically poled lithium niobate at 1.064μm are presented [4,5,6].

4.1 Introduction to laser modulation devices

Acousto-optic [7,8] and electro-optic devices [9] have ever-expanding applications in laser technology. These include telecommunications, information storage, optical processing, laser printing, Q-switches, beam deflectors & modulators, high frequency scanning, and mode-lockers. This Section briefly reviews the basic operation of acousto- and electro-optic devices and summarises current commercially available devices.

4.1.1 Acousto-optic devices

Acousto-optic Bragg modulators [7,8] are used in laser systems for electronic control of the frequency, intensity and direction of the laser beam. Acousto-optic interaction occurs in all optical mediums when an acoustic wave and a laser beam are present in the medium. Acousto-optic devices require materials with good acoustic and optical properties and high optical transmission, such as lithium niobate, tellurium dioxide, lead molybdate, fused silica or quartz and gallium phosphide.

When an acoustic wave is launched into the optical medium, the elasto-optic properties of the medium respond to the acoustic wave and generate a refractive index wave that behaves like a sinusoidal grating. An incident laser beam passing through this grating will diffract into several orders, just like in a regular diffraction grating. In the case of Bragg diffraction, the device design and operating conditions are set so that the Bragg condition is met and therefore the first order beam has the highest efficiency. The angular position of the diffracted beam is linearly proportional to the acoustic frequency, so that the higher the frequency, the larger the diffracted angle, given by;

Equation 4-1

$$\Delta\phi \approx \lambda \frac{\Delta f}{V_a}$$

where, λ, is the free space wavelength, f is the acoustic frequency, V_a is the acoustic velocity and ϕ is the angle between the incident laser beam and the diffracted laser beam. A diagram of a typical acousto-optic modulator taken from a New Focus application note is shown in Figure 4.1.

Acousto-optic modulators and deflectors have a number of important desirable features as they are simple in design and operation, compact, and offer an advantage for systems where size and weight are important. The electrical power required to excite the acoustic wave is relatively small and can be less than one Watt in some cases. High extinction ratios are obtained easily because no light emerges in the direction of the diffracted beam when the device is off. At visible wavelengths, a large fraction (up to 85% for some commercial models) of the incident light may be

diffracted into the transmitted beam. Rise/fall times of up to 5ns can be achieved within certain constraints. In the case of acousto-optic deflectors, larger numbers of resolvable spots are possible compared to electro-optic devices (commercial models offer up to 1000 resolvable spots) with access times typically in the range of 5-50 microseconds. A two-dimensional deflection may be obtained by using two deflectors in series, with their directions of deflection at right angles.

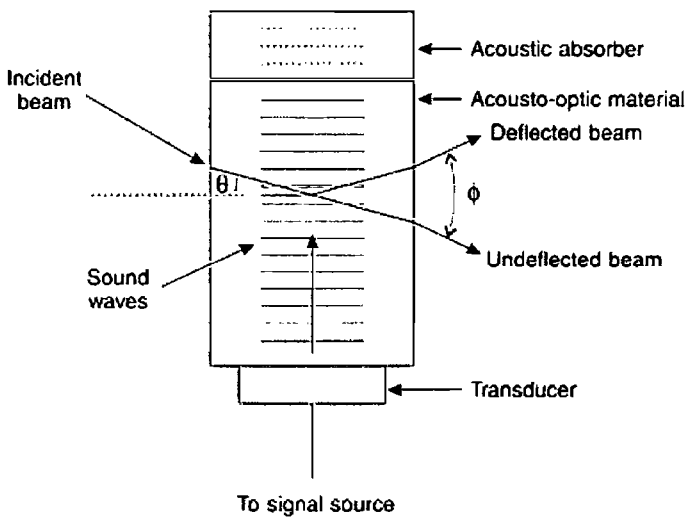

Figure 4.1 *Typical acousto-optic modulator [10]*

However, the design and performance of acousto-optic beam modulators have several limitations. The transducer and acousto-optic medium must be carefully designed to provide maximum light intensity in a single diffracted beam, and the transit time of the acoustic beam across the diameter of the light imposes a limitation on the rise time of the switching and therefore limits the modulation bandwidth. The acoustic wave travels with a finite velocity and the light beam cannot be switched fully on or fully off until the acoustic wave has traveled all the way across the light beam. To increase bandwidth therefore, the light must be tightly focused to a small diameter at the position of the interaction, minimizing the transit time. Frequently the diameter to which the beam may be focused is the ultimate limitation for the bandwidth. Also, if the laser beam is of high power, it cannot be focused in the acousto-optic medium without damage. As tight focusing allows fast switching times, high power beams result in slow switching times and low bandwidths due to the larger diameters necessary. Finally, for operation in the infra-red region, diffraction efficiencies of acousto-optic modulators are greatly reduced. For applications where higher

switching speeds, no frequency shift, and only a moderate extinction ratio are required, electro-optic deflectors are preferable [9].

Manufacturer	Model number	Wavelength (nm)	Rise / Fall Time	Diffraction efficiency	Interaction Material
Brimrose	LND-2500-1000	633 & 830	1μs	10-15 %	Lithium Niobate
Brimrose	LND-2500-1500	633 & 830	1μs	5 %	Lithium Niobate
Brimrose	GPD-250-100	633	0.7μs	70 %	Gallium Phosphide
Gooch & Housego plc	M080-1B/E-GH2	450 - 650	180ns mm^{-1}	85 %	Lead Molybdate
Gooch & Housego plc	M350-2B	488	5ns (30μm beam)	80 %	Tellurium Dioxide
Gooch & Housego plc	M250-2E-O2	633	10ns (65μm beam)	85 %	Tellurium Dioxide
Harris Corp.	H-501	351 - 364	25ns	90 $\%W^{-1}$	Fused Quartz
Harris Corp.	H-800	830	75ns	50 $\%W^{-1}$	Gallium Phosphide
AA Opto-Electronic	AA.DT.230/ B120/A0.5-VIS	450 - 670	4.2μs	50 %	Tellurium Dioxide
AA Opto-Electronic	AA.DTS.X	633	2.6μs	70 %	Tellurium Dioxide
EO Products Corp.	MT-80-VIS	450 – 700	160ns mm^{-1}	85 %	Tellurium Dioxide
Crystal Technology	3980-120	442 - 633	25ns	-	Tellurium Dioxide
Crystal Technology	3200-121	515 – 633	10ns	-	Tellurium Dioxide
Isomet Corp.	1250C	633	12ns (50μm beam)	55 %	Lead Molybdate

Table 4-1 Performance Characteristics of currently available bulk Bragg grating acousto-optic modulators

Table 4-1 shows the performance characteristics for several current commercial acousto-optic modulators and deflectors. There are several different types of interaction materials used for acousto-optic modulators and it can be seen that the lithium niobate acousto-optic modulators exhibit poorer performance with only 15% maximum diffraction efficiency and 1μs risetimes.

4.1.2 Electro-optic devices

The electro-optic effect is a change in the index of refraction as a function of voltage, as described in Chapter 2. This effect is intrinsically fast in all materials, thus allowing electro-optic modulators to operate in the nanosecond timescale, compared

to the seconds to milliseconds timescale of other modulators such as liquid crystal modulators [11,12], and the microsecond timescale of acousto-optic modulators.

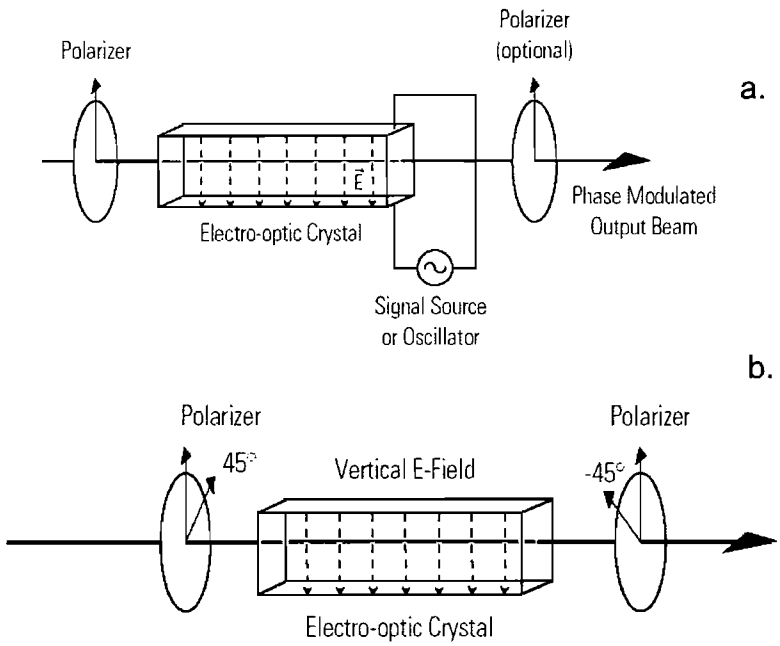

Figure 4.2 *Bulk lithium niobate electro-optic modulators a) phase modulator, b) amplitude modulator [10]*

Electro-optic devices can be used to modulate the amplitude, intensity, phase or direction of the input beam. Such bulk optical grating modulators using electro-optic modulation in single domain lithium niobate were demonstrated more than 25 years ago [13,14]. Figure 4.2 shows schematics of typical bulk lithium niobate transverse electro-optic phase and amplitude modulators [10]. However, increasing diffraction efficiency in such devices requires controlled beam shaping techniques.

4.1.3 Summary

It has been shown that acousto- and electro-optic devices both have limitations and restrictions in terms of speed, integration, drive voltages, power and useable wavelengths. This is highlighted quite well by Wilson & Hawkes [15];

> *"Acousto-optic modulators can generally be used for similar applications to electro-optic modulators, though they are not so fast. On the other hand,*

> *because the electro-optic effect usually requires voltages in the kV range, the drive circuitry for modulators based on this effect is much more expensive than for acousto-optic modulators which operate with a few volts."*
>
> *Wilson & Hawkes p116*

From this description it is clear that a device which is as fast as bulk electro-optic devices with acousto-optic drive voltages is desired. To this end, a new class of modulators has been developed which overcomes these limitations of conventional types of modulators, such as low efficiency, slow risetimes and high drive voltages. These modulators are based on electro-optically controlled Bragg diffraction in periodically poled lithium niobate [16] and are an extension of early work on grating based electro-optic devices such as those by Hammer [14] and Barros & Wilson [13]. The use of periodic poled structures in lithium niobate provides the potential for fast switching, high efficiency and simple construction leading to more compact, integrated and faster devices which can be used in the infrared and at higher powers.

In this Chapter the background to these new Bragg modulators is described, including previous work in this field, a theoretical model of diffraction efficiency, the design and fabrication of such devices, and finally the results which demonstrate the first infrared operation of electro-optically controlled Bragg modulation based on a periodically poled lithium niobate grating at 1064nm.

4.2 Electro-optic Bragg modulators in PPLN

The design of the modulator devices presented in this thesis is shown in Figure 4.3. They consist of an area of periodically domain-inverted regions forming a grating of length d (mm) with grating period Λ (μm) and grating planes parallel to the y-axis of the crystal.

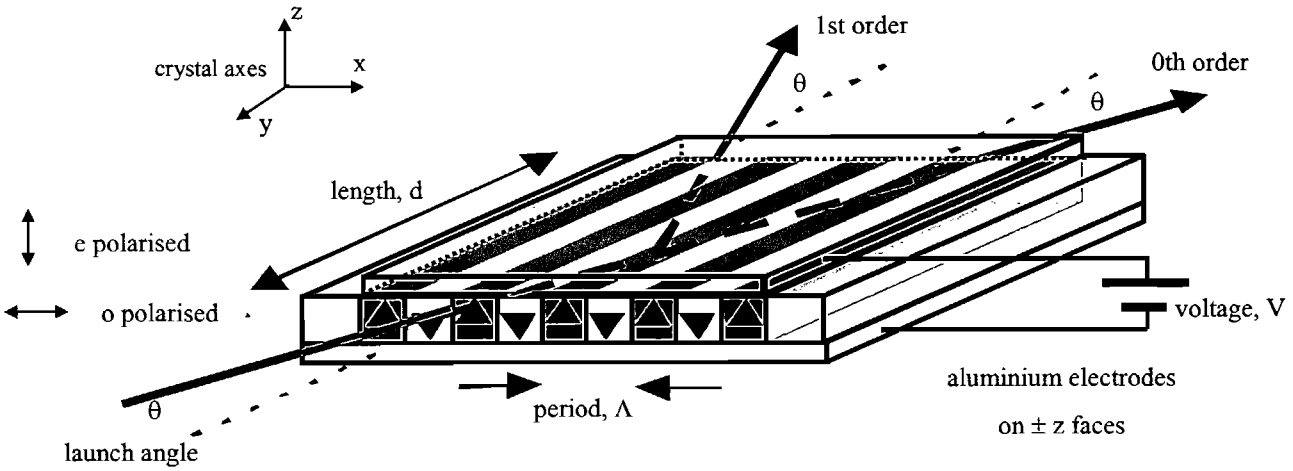

Figure 4.3 *Schematic diagram of the periodically poled $LiNbO_3$ modulator device*

To create a refractive index grating a uniform electric field, E, is applied between the z faces. This induces a refractive index change, periodic in sign, with an amplitude given by the equation [17] :

Equation 4-2

$$\Delta n = -\frac{n_o^3}{2} r_{ij} E_j$$

The largest electro-optic coefficient in lithium niobate is given for extraordinary (e) or z polarised light as shown in

Figure 4.3, with a value of $r_{33} = 32.2 \times 10^{-12}$ mV^{-1}. [18]

The Bragg relation is given by [17];

Equation 4-3

$$\sin\theta_{int} = \frac{\lambda_0}{2n\Lambda}$$

where Λ is the period of the grating, λ_0 is the wavelength of light in free space, n is the refractive index of the material and θ_{int} is the internal angle between the incident light and the grating planes. This is shown in graphical form in Figure 4.4.

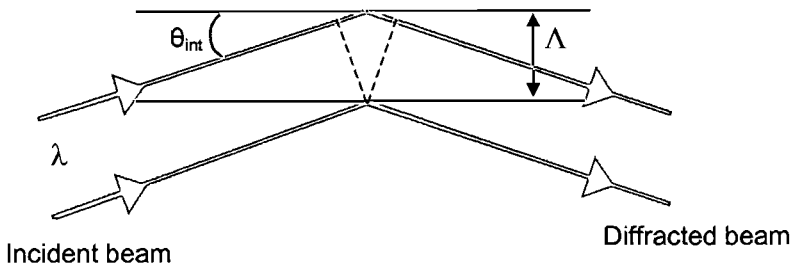

Figure 4.4: Schematic diagram of Bragg condition

From the Bragg relation, it can be seen that for a given grating period a large range of wavelengths can satisfy the Bragg relation by altering the launch angle, with the only constraints being set by the device geometry and fabrication limitations. This means that for any given wavelength it is possible to design the device to give high diffraction efficiency whilst taking into consideration fabrication constraints, as described in Chapter 3.

4.2.1 Previous work

Figure 4.5 shows results obtained by Yamada, Saitoh and Ooki in 1996 [1]. This was the first demonstration of a periodically inverted domain electro-optically induced Bragg grating switch in lithium niobate. The device was fabricated in 200μm thick lithium niobate of length 4mm and grating period 8μm, and was tested using light of wavelength 633nm. The power ratio of the light in the diffracted order with applied voltage is shown in Figure 4.5. A cylindrical lens and deflection device fabricated in a similar way to the Bragg grating switch are also discussed.

In their paper, Yamada et al. fitted their data to the function $\sin^2(aV)+V_0$, where a and V_0 are constants. It is probable that this is a typographical error and they intended $\sin^2(a[V-V_0])$ which would then be of a similar form to the theoretical model we derive in Section 4.3 , but with an added voltage offset, V_0. It would be expected that with no applied voltage there would be no power in the diffracted order, however we can see from Figure 4.5 that this is not the case and a voltage offset of approximately +30V can be seen. Yamada et al. hypothesise that this offset is due to a residual stress-induced refractive index grating remaining in the crystal after poling. This agrees with our own findings which are discussed in much greater detail in Chapter 5.

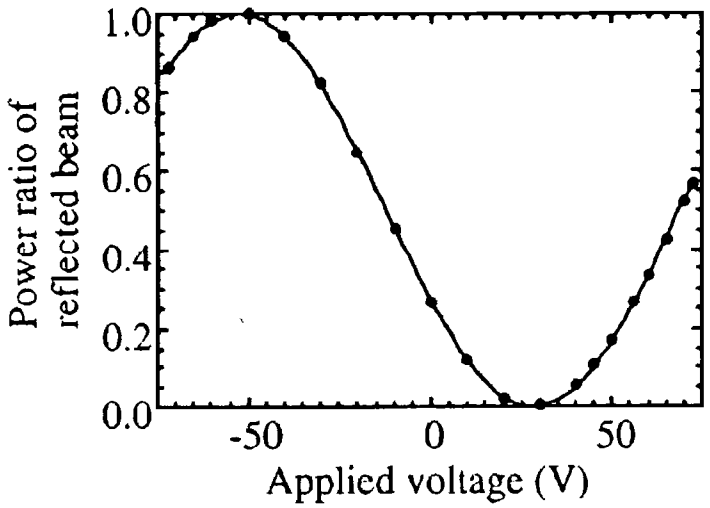

Figure 4.5 *Power ratio of diffracted light plotted against applied voltage (Yamada et al. Appl. Phys. Lett.) [1]*

Although impressive, the results beg some important questions. In particular only the first order diffraction is discussed, there is no discussion of the non-diffracted or zeroth order, making it impossible to judge the on/off ratio or efficiency of the device. It can also be seen that the data presented is over a narrow voltage range, there is no indication about performance at higher voltages. The y-axis in Figure 4.5 shows the 'power ratio' of the diffracted order, which is not adequately defined. It seems likely that this power ratio is scaled to the maximum and minimum diffracted power.

Overall, the results by Yamada provide the first demonstration of an optical switching device using an electro-optically induced Bragg grating in periodically poled lithium niobate. The data shows a good fit to a sinusoidal curve and the on/off voltage of approximately 75V corresponds to that predicted by theory (see Section 4.3). However it can be seen that further work is needed to answer some of the questions arising from this work. One of the aims of this thesis is to clarify some of these issues and to investigate them in much greater detail.

The next Bragg grating switch in periodically poled lithium niobate was developed by Gnewuch et al. in 1998 [2]. They demonstrated both static operation of such a device and its nanosecond response. The device used was 300μm thick, with an area of

periodically domain-inverted regions forming a grating of length 20mm and period 40μm, and was tested at a wavelength of 633nm. Results were also obtained for the response of the device to 100ns, 20ns and 5ns pulses.

Figure 4.6 shows the static efficiency of the diffracted (first order) and non-diffracted (zeroth order) light with applied voltage (U_{th}) and fitted sinusoidal curves. The curves seen are similar to those found by Yamada et al. and also exhibit the voltage offset as seen by Yamada. The data presented by Gnewuch shows both the diffracted and non-diffracted orders and is given in terms of efficiency rather than 'power ratio' as presented by Yamada. This allows us to understand a lot more about the operation of the device, although Gnewuch presents no discussion of the theory behind the device or the fitted sinusoids. It should be noted that the fitted sinusoids are offset in efficiency, as can be seen from Figure 4.6. Gnewuch explained this reduction in the efficiency contrast as occurring due to a non-uniform grating or varying mark to space ratio. Gnewuch et al. also present results which demonstrate the suppression of thickness acoustic modes by using a periodically poled device compared to a bulk electro-optic modulator. The operation of electro-optic devices can be limited by the excitation of acoustic modes in the device via the piezoelectric effect [19]. Their conclusion was that periodic poling brings substantial benefits by its suppression of acoustic modes.

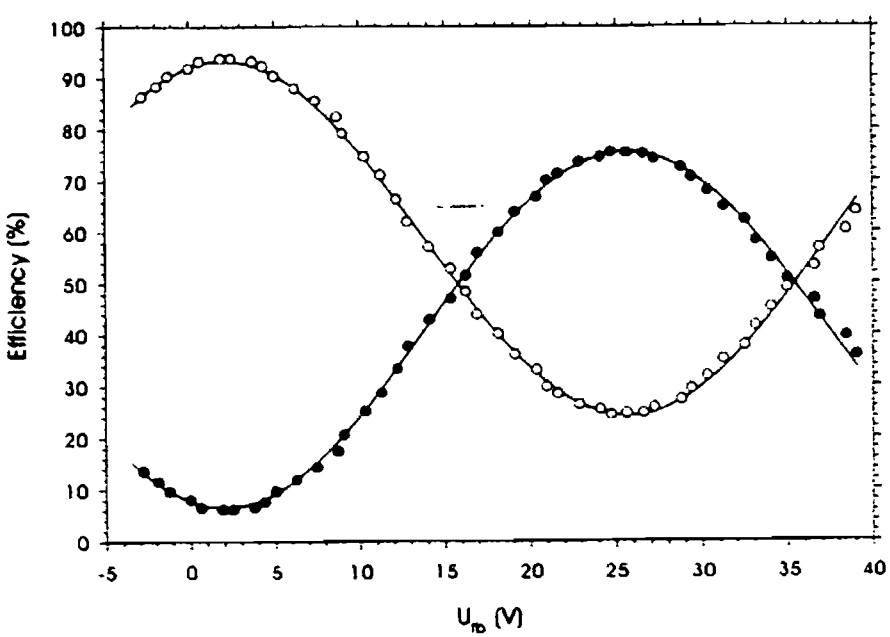

Figure 4.6 *Efficiency of zeroth order (o) and first order (•) diffraction with applied voltage (U_{th}) (Gnewuch et al. IEEE Photonics Tech Lett) [2]*

Yamada and Gnewuch present interesting and notable results on electro-optic induced Bragg grating switches. Both give limited analysis of the theory behind the device and limited discussion of the choices leading to the design of the device. In 2000, Yamada [20] published results containing a more in depth theoretical analysis and comparison of theory to experimental data. They used the Klein and Cook method [21] to solve the wave equation obtaining a sinc function for the diffracted power with incident angle, which they found was in good agreement with the results they obtained. They also derived an equation [20 Eqn 8] for diffracted power incident at the Bragg angle, in terms of device length, L, wavelength, λ, and change in refractive index, Δn. This is of similar form to the theoretical approach presented in Section 4.3

.

Equation 4-4

$$I = \sin^2\left(\frac{\Delta n L \pi}{\lambda}\right)$$

In his 2000 paper Yamada presents results for the device discussed in the 1996 paper, and then goes on to develop the idea of a poled Bragg grating device further. An optical switch with one input port and six output ports was fabricated and tested at 633nm and a wide band optical modulator for violet-blue light which achieved 75% diffraction into the first order. The frequency response of this device was also tested and results are shown for 1GHz operation [20 Fig.17]. A diffraction efficiency of 70% was achieved under these conditions. Fabrication and testing specifications for these, and the previous devices can be found in Table 4-2.

The work presented by Yamada in his second paper gives much more detail about the devices than the previous paper, however it can be noticed that the data for the Bragg diffraction device was only taken over a limited voltage range [20 Fig.4] and shows only the diffracted order with no information about the non-diffracted order. The data presented appears to be the same data as presented in their first paper, however this time the y-axis is labelled 'Diffracted optical power' rather than 'Power ratio of reflected beam', and again this gives us no real insight into the actual data taken. Like

the previous paper and the work by Gnewuch, this paper highlights areas that need further investigation, which the rest of this Chapter and Chapter 5 go on to explore.

	Yamada [1,20] (1996), (2000)	Gnewuch [9] (1998)	Yamada [20] (2000)	Yamada [20] (2000)
Grating period (μm)	8	40	6.3	20
Device length (mm)	4	20	6 × 3.1	9
Operating wavelength (nm)	633	633	633	407
Sample thickness (μm)	200	300	200	200
On / Off Voltage (V)	75	75	80	15
Diffracted Efficiency (%)	75	76	-	75
Non-diffracted Efficiency (%)	-	6	-	-
Diffracted On / Off Ratio	-	-	-	100:1
Non-diffracted On / Off Ratio	-	-	-	5:1

Table 4-2 Comparison of Previous Devices

The papers from Yamada and Gnewuch present interesting new results, demonstrating diffraction efficiencies of up to 75% and show good relations with simple theoretical models. However some areas of work remain undeveloped. No theoretical analysis was given in Gnewuch's paper and only a very simple theoretical analysis is given in Yamada's final paper where the refractive index profile of the induced grating is assumed to be sinusoidal. In reality a poled grating has a square profile and the affect of this assumption is not discussed. Results are only taken over a relatively narrow voltage range and the performance at higher voltages is not studied. A voltage offset is seen in both works, which is attributed to a residual grating after poling, but this is not investigated further. Theory predicts that 100% diffraction efficiencies should be possible, but a maximum of only 75% was achieved and no further exploration undertaken. The devices were only tested at visible wavelengths of 633nm and 407nm, in particular there is no research into the device performance at infrared

wavelengths. Yamada presents results at 407nm and uses an elevated operating temperature of 120°C to overcome optical damage due to the photorefractive effect, but the affect of periodic poling on the photorefractive effect is not investigated further.

The work presented in this thesis takes these previous studies and extends them further. A full theoretical analysis behind the basic mechanisms of the device is presented in Chapter 4.3 . A full investigation into the influencing factors and design considerations is presented in Chapter 4.3.9 and in Chapter 4.5.1 the first demonstration of devices working outside the visible region at a wavelength of 1064nm are presented. Chapter 5 looks at some of the anomalies arising from this, and previous work, and researches them further, looking at the effect of grating period, device length, operating wavelength and photorefractive effects. Several possible theories are put forward explaining some of the discrepancies found.

4.3 Theoretical Model

Several different theoretical models have been developed for diffraction by volume gratings, but the best know is that of Kogelnick [3]. In 1969 Kogelnik published a coupled wave analysis for Bragg diffraction of light by thick holographic gratings using theory similar to that used for analysis of acoustic gratings [22,23], electro-optic gratings [24] and dynamic X-ray diffraction [25]. This theory is widely used and has the great value of giving analytical results for high diffraction efficiencies.

A detailed mathematical analysis of off-Bragg incident light is outside the scope of this thesis. Therefore the validity of the theory outlined in this Chapter is limited to "thick" gratings, where the phase synchronism between the two coupled waves has enough time to develop a strong and dominating effect. One definition of a "thick" grating comes from acoustic diffraction gratings where the following parameter, Q (sometimes known as the Klein-Cook parameter), is defined as an measure of grating thickness [21]:

Equation 4-5

$$Q = \frac{2\pi\lambda d}{n\Lambda^2}$$

where λ is the wavelength of light, d is the grating length, n is the refractive index of the material and Λ is the grating period.

When $Q < 1$ the grating is said to be "thin" and corresponds to Raman-Nath diffraction with several diffracted orders [21]. A grating is regarded as "thick" and operates in the Bragg regime with only one diffracted order when the condition $Q \gg 1$ holds [26]. The limits of Raman-Nath and Bragg diffraction have been studied by several authors [27], but in particular Willard [28] gives the condition for the lower limit of Bragg diffraction as $Q=4\pi$, above which the coupled wave theory begins to give good results [29,27]. For many practical gratings Q is sometimes much larger than 10. For example, the Q parameter for the Bragg grating modulator developed in Chapter 4 with grating period 70μm and length 3cm, operating at 1064nm, works out to be approximately 18, which falls comfortably into the Bragg regime.

The remainder of this Chapter includes a more in-depth theoretical analysis than presented in previous work. This will give a clearer picture of the operation of electro-optically induced Bragg grating devices and their behaviour. Bandwidths and tolerances of the device are investigated, enabling an optimised device to be designed. In particular, a theoretical analysis will help to obtain an understanding of the amount of light that can be diffracted into the first order of the device as a function of applied voltage (ie. refractive index variation), and also as a function of incident angle. The significance of higher Fourier components can then be considered and also the influence of grating quality, grating boundaries and the effect of a non-sinusoidal refractive index grating. It is also useful to investigate how much light can be diffracted into higher orders and methods of reducing this.

4.3.1 Assumptions for coupled wave analysis

In the following theoretical approach it is assumed that the spatial modulation of the refractive index grating and the absorption is sinusoidal. More complicated gratings, such as square or triangular gratings, can be analysed as multiples of the coupled

wave theory. In the case of the gratings used in this thesis, only the fundamental grating period satisfies the Bragg condition, and therefore is the most important. However other grating terms arising from a non-sinusoidal grating profile will affect the diffraction efficiency, as discussed in Chapter 5. It is also assumed that there is a small absorption loss and a slow energy interchange (in the case of two different wavelengths) between the two coupled waves, know as the slow varying approximation.

The coupled wave theory assumes monochromatic light incident on the grating at or near the Bragg angle. Only the incident wave and the first order diffracted wave are considered, as these obey the Bragg condition, while other orders are neglected in this model. The same average refractive index is assumed for the region inside and outside the grating and the incident light is assumed to be polarised perpendicular to the plane of incidence. The case of light polarised parallel to the plane of incidence is discussed in Chapter 4.3.6.

4.3.2 Derivation of the coupled wave equations

This Section presents a tailored Kogelnick theory, specific to the grating devices investigated in this thesis.

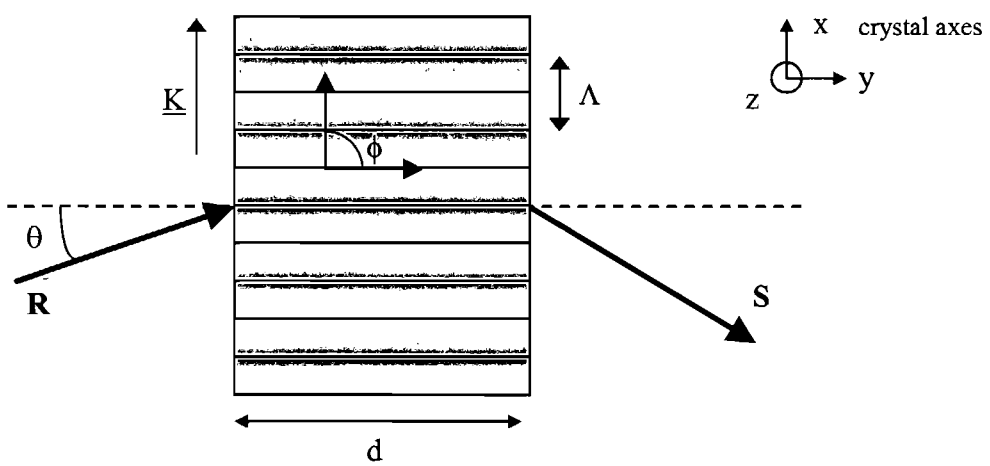

Figure 4.7 Model of a Bragg grating

Consider the model of a periodically poled Bragg grating shown in Figure 4.7 with the crystal axes as indicated. ***R*** is the light incident at an internal angle θ to the grating planes and polarised perpendicular to the plane of incidence (this corresponds to e–polarised light for the specific Bragg grating shown) and ***S*** is the outgoing wave. The grating period is shown by Λ, $\underline{K}$ is the grating vector of length $K = 2\pi / \Lambda$ and ϕ is the angle between the direction of $\underline{K}$ and the crystal y-axis. The length of the grating is given by d.

The Scalar Wave Equation is given by [3, 30 Eqn 16.4]:

Equation 4-6
$$\nabla^2 E(x,y) + k^2 E(x,y) = 0$$

where the propagation constant is given by :

Equation 4-7
$$k^2 = \frac{\omega^2}{c^2}\varepsilon(x,y) - i\omega\mu\sigma = \frac{\omega^2}{c^2}n^2(x,y) - i\omega\mu\sigma$$

where c is the velocity of light in free space, ω is angular frequency and μ is the permeability of the medium which is assumed to be equal to that of free space. ε(x,y) is the relative dielectric constant and σ(x,y) is the conductivity of the medium.

The average propagation constant is given by;

Equation 4-8 $\beta = \frac{2n\pi}{\lambda}$ where n is the average refractive index.

The average absorption constant is;

Equation 4-9 $\alpha = \frac{c\mu\sigma_0}{2(\varepsilon_0)^{\frac{1}{2}}}$ and the coupling constant is defined as;

Equation 4-10 $\kappa = \frac{n\pi}{\lambda} - \frac{i\alpha_1}{2}$ where α_1 is the amplitude of the spatial modulation of the absorption constant.

The coupling constant describes the coupling between the reference wave ***R*** and the signal wave ***S*** and is the central parameter in the coupled wave theory. When $\kappa = 0$ there is no coupling between ***R*** and ***S*** and therefore no diffraction.

By substituting in the above, the propagation constant, k, can be written as :

Equation 4-11
$$k^2 = \beta^2 - 2i\alpha\beta + 2\kappa\beta\left(e^{iK.x} + e^{-iK.x}\right)$$

The spatial modulation described by α_1 forms a grating which couples the two waves, ***R*** and ***S***, and leads to an exchange of energy between them. These waves can be described by complex amplitudes ***R(y)*** and ***S(y)*** which vary along y as a result of this energy exchange or because of an energy loss due to absorption. The total electric field in the grating is the superposition of the two waves :

Equation 4-12
$$E = R(y)e^{-i\xi.x} + S(y)e^{-i\delta.x}$$

The propagation vectors ξ and δ contain the information about the propagation constants and the directions of propagation of ***R*** and ***S***. ξ is assumed to be equal to the propagation vector of the free reference wave in the absence of coupling. δ is forced by the grating and related to ξ and the grating vector by $\delta = \xi - K$, which has the appearance of a conservation of momentum equation.

The components of ξ and δ are given by :

Equation 4-13
$$\xi = \begin{pmatrix} \xi_x \\ \xi_y \\ 0 \end{pmatrix} = \beta \begin{pmatrix} \sin\theta \\ \cos\theta \\ 0 \end{pmatrix} \quad \text{and} \quad \delta = \begin{pmatrix} \delta_x \\ \delta_y \\ 0 \end{pmatrix} = \beta \begin{pmatrix} \sin\theta - \frac{K}{\beta}\sin\phi \\ \cos\theta - \frac{K}{\beta}\cos\phi \\ 0 \end{pmatrix}$$

The dephasing measure is defined as :

Equation 4-14
$$\vartheta \equiv \frac{\left(\beta^2 - \delta^2\right)}{2\beta} = K\cos(\phi - \theta) - \frac{K^2}{4n\pi}\lambda$$

Using the above definitions the coupled wave equations can now be derived. The equation for the propagation constant, Equation 4-11, is combined with the wave equation, Equation 4-6, and the expressions for the total electric field, Equation 4-12, and corresponding propagation vectors, Equation 4-13, are inserted. By comparing equal exponentials, the following expressions can be obtained :

Equation 4-15

$$R''-2iR'\xi_y-2i\alpha\beta R+2\kappa\beta S=0$$
$$S''-2iS'\delta_y-2i\alpha\beta S+\left(\beta^2-\delta^2\right)S+2\kappa\beta R=0$$

where the primes indicate differentiation with respect to y. These equations neglect all other higher order diffraction orders. In addition it is assumed that the energy interchange between $\boldsymbol{R}$ and $\boldsymbol{S}$ is slow compared to the rapid oscillations at optical frequency ω, and that energy is absorbed slowly, allowing $\boldsymbol{R''}$ and $\boldsymbol{S''}$ to be neglected. This is known as the slowly varying envelope (SVE) approximation [30].

By introducing the dephasing measure, Equation 4-14, the equations can be rewritten as :

Equation 4-16

$$c_R R'+\alpha R=-i\kappa S$$
$$c_S S'+\left(\alpha+i\vartheta\right)S=-i\kappa R$$

These are the coupled wave equations, which form the basis of this theoretical analysis.

The constants c_R and c_S stand for :

Equation 4-17

$$c_R=\frac{\xi_y}{\beta}=\cos\theta$$
$$c_S=\frac{\delta_y}{\beta}=\cos\theta-\frac{K}{\beta}\cos\phi$$

These coupled wave equations describe the diffraction process occurring in the grating. The wave changes in amplitude along y because of coupling to the other wave ($\kappa\boldsymbol{R}$, $\kappa\boldsymbol{S}$) or absorption ($\alpha\boldsymbol{R}$, $\alpha\boldsymbol{S}$). For deviations from the Bragg condition $\boldsymbol{S}$ is forced out of synchronisation with $\boldsymbol{R}$ and the coupling interaction decreases ($\vartheta\boldsymbol{S}$).

4.3.3 Solutions of the coupled wave equations

General solutions of the coupled wave equations are given by :

Equation 4-18

$$R(y) = r_1 e^{\gamma_1 y} + r_2 e^{\gamma_2 y}$$
$$S(y) = s_1 e^{\gamma_1 y} + s_2 e^{\gamma_2 y}$$

where $r_{1,2}$ and $s_{1,2}$ are constants which depend on the boundary conditions.

The constants $\gamma_{1,2}$ are determined by inserting the above solutions into the coupled wave equations to obtain :

Equation 4-19

$$(c_R\gamma_i + \alpha)r_i = -i\kappa s_i$$
$$(c_S\gamma_i + \alpha + i\vartheta)s_i = -i\kappa r_i \qquad i = 1,2$$

giving the solution :

Equation 4-20

$$\gamma_i = -\frac{1}{2}\left(\frac{\alpha}{c_R} + \frac{\alpha}{c_S} + i\frac{\vartheta}{c_S}\right) \pm \frac{1}{2}\left[\left(\frac{\alpha}{c_R} - \frac{\alpha}{c_S} - i\frac{\vartheta}{c_S}\right)^2 - 4\frac{\kappa^2}{c_R c_S}\right]^{\frac{1}{2}}$$

The constants r_i and s_i are found by introducing boundary conditions as follows; Consider a transmission grating where the boundary conditions are *R(0)* = 1 and *S(0)* = 0. By inserting these into the general solutions it follows that $r_1 + r_2 = 1$ and $s_1 + s_2 = 0$.

Combining these relations with Equation 4-19 gives $s_1 = -s_2 = -\frac{i\kappa}{c_S}(\gamma_1 - \gamma_2)$ and therefore:

Equation 4-21

$$S(d) = i\frac{\kappa}{c_S(\gamma_1 - \gamma_2)}\left(e^{\gamma_2 d} - e^{\gamma_1 d}\right)$$

This is a general expression which is valid for all types of thick transmission gratings, including cases of off-Bragg incidence, lossy gratings and slanted fringe planes.

4.3.4 Diffraction efficiency of a grating

The diffraction efficiency of a grating is given by;

Equation 4-22

$$\eta = \frac{|c_S|}{c_R} SS^*$$

where ***S*** is the complex amplitude of the output signal for a reference wave ***R*** incident with unit amplitude. η is the fraction of the incident light power which is diffracted into the signal wave. In the case of transmission holograms ***S*** is equal to ***S(d)***.

4.3.5 Diffraction efficiency of an unslanted, lossless dielectric transmission grating

By using the general formulas derived in Chapters 4.3.2, 4.3.3 and 4.3.4, an expression for the diffraction efficiency for the specific devices investigated in this thesis can be found. The Bragg grating devices used in this work can be compared to an unslanted, lossless, dielectric transmission hologram grating.

In the case of no slant, ie. the grating planes are parallel to the y axis, $\phi = \frac{\pi}{2}$. For a lossless grating $\alpha = \alpha_1 = 0$ and the coupling constant, Equation 4-10, becomes $\kappa = \frac{n_1 \pi}{\lambda}$. For a transmission grating the signal appears at $y = d$. These conditions greatly simplify the equation for diffraction efficiency.

The Bragg condition is given by ;

Equation 4-23 $$\sin\theta_{int} = \frac{\lambda}{2n\Lambda}$$ where Λ is the period of the grating.

If this condition is also satisfied then $c_R = c_S = \cos\theta_0$, and the equation for the first order diffraction efficiency becomes the well known relation :

Equation 4-24 $$\eta = \sin^2\left(\frac{\pi \Delta n d}{\lambda \cos\theta_{int}}\right)$$

where η is the diffraction efficiency, λ is the wavelength in free space, θ_{int} is the internal angle between the incident light and y-axis of the crystal, d is the length of the grating and Δn is the change in refractive index due to the applied field. This concludes the main derivation based on the treatment by Kogelnick. Equation 4-24 describes the diffraction efficiency in the first order for the particular device configuration used in this thesis.

4.3.6 O-polarised incident light

The above derivation assumed that the incident light was extraordinary polarised. For the case of incident light polarised parallel to the plane of incidence (corresponding to ordinary or o-polarised light, as in the case of the Bragg gratings investigated in this thesis), the effective coupling constant κ is reduced by :

Equation 4-25

$$\kappa_{o-pol} = -\kappa_{e-pol}\cos(2\theta - \pi)$$

For small incident angles, as in the case of the work presented in this thesis, $\kappa_{o\text{-}pol} \approx \kappa_{e\text{-}pol}$, and the diffraction efficiency equation is assumed to be the same for both polarisations of incident light.

4.3.7 Deviations in incident angle and wavelength

Having now developed results for first order diffraction efficiency assuming perfect conditions where the Bragg condition is met exactly, we are now in a position to consider deviations in incident angle and operating wavelength. For a fixed wavelength the Bragg condition can be violated by angular deviations Δθ from the Bragg angle θ_0, for example due to beam focussing. For a fixed angle of incidence a similar violation can take place for changes Δλ from the correct wavelength λ_0, as in the case of a dye laser with a typical wavelength bandwidth of Δλ=15nm. The adjusted angle of incidence and wavelength can be written as :

Equation 4-26

$$\theta = \theta_0 + \Delta\theta$$
$$\lambda = \lambda_0 + \Delta\lambda$$

where Δθ and Δλ are small.

The equation for diffraction efficiency is not as simple as in Equation 4-24 when off-Bragg angles and wavelength deviations are considered, but is still calculable. Taking deviations into consideration, the signal amplitude can be written as :

Equation 4-27

$$S = -i\left(\frac{c_R}{c_S}\right)^{\frac{1}{2}} e^{-i\rho}\frac{\sin\left(\nu^2+\rho^2\right)^{\frac{1}{2}}}{\left(\nu^2+\rho^2\right)^{\frac{1}{2}}}$$

where $\nu = \frac{n_1 d\pi}{\lambda(c_R c_S)^{\frac{1}{2}}}$ and $\rho = \frac{d\vartheta}{2c_S}$.

The dephasing parameter, ϑ, Equation 4-14, can be rewritten using a Taylor series expansion, correct to the first order in the derivations $\Delta\theta$ and $\Delta\lambda$, giving :

Equation 4-28
$$\vartheta = \Delta\theta \cdot K\sin(\phi - \theta) - \Delta\lambda \cdot \frac{K^2}{4n\pi}$$

The parameter ρ then becomes :

Equation 4-29
$$\rho = \Delta\theta \cdot \frac{Kd\sin(\phi - \theta_0)}{2c_S} - \Delta\lambda \cdot \frac{K^2 d}{8nc_S\pi}$$

The diffraction efficiency is given by :

Equation 4-30
$$\eta = \left(\frac{\sin(\nu^2 + \rho^2)^{\frac{1}{2}}}{(\nu^2 + \rho^2)^{\frac{1}{2}}} \right)^2$$

where the angular and wavelength deviations are represented through the parameter ρ. It can be seen from these equations that the diffraction efficiency has a sinc dependence on wavelength deviation and angular deviation.

4.3.8 Analysis of Kogelnik theory

From the Kogelnik diffraction efficiency equation (Equation 4-24), it can be seen that the first order diffraction efficiency of a Bragg grating modulator is dependent on the length of the grating, d, the change in refractive index, Δn, and therefore (through the electro-optic equation), the applied voltage, V, the wavelength of light, λ, the angle of the incident light, θ_{int}, and through the Bragg Equation, the grating period, Λ.

These dependencies can been seen more clearly in graphical form. The diffraction efficiency for both the first and zeroth order is shown in Figure 4.8. The sinusoidal dependence can clearly be seen, along with the predicted 100% achievable diffraction efficiencies of both the zeroth and first orders.

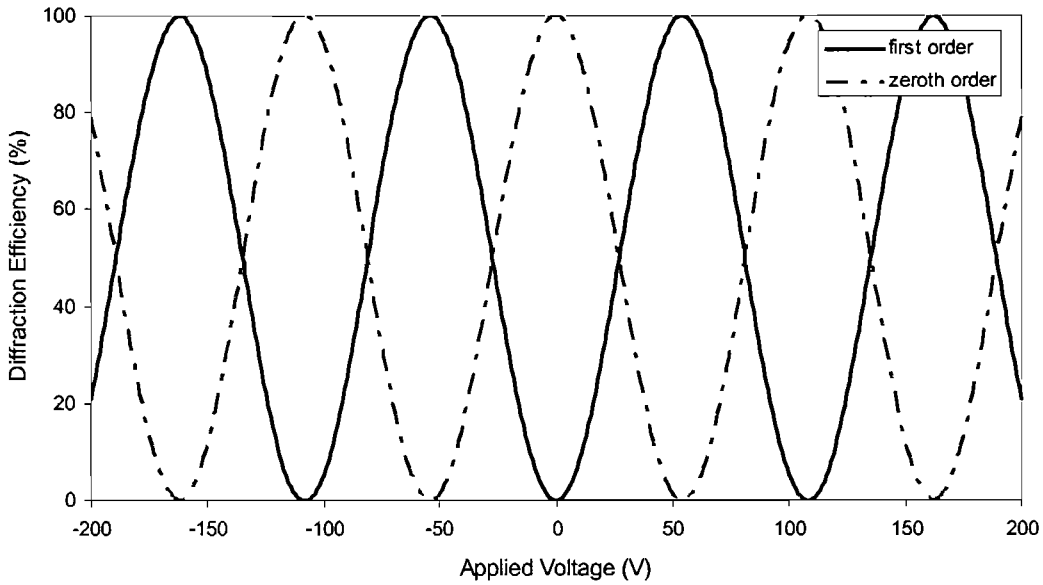

Figure 4.8 *Theoretical Diffraction Efficiency for zeroth and first order (for e-polarised light at λ = 633nm, for grating Λ = 70mm, length d = 2cm and thickness 500μm)*

The effect of the polarisation of the incident wave can be seen in Figure 4.9, which shows the theoretical first order diffraction efficiency for light incident of e- and o-polarisation. It can be seen that a device operating with o-polarised requires a much higher drive voltage to achieve maximum diffraction, over three times the voltage. This is an important factor when designing devices and choosing operating conditions.

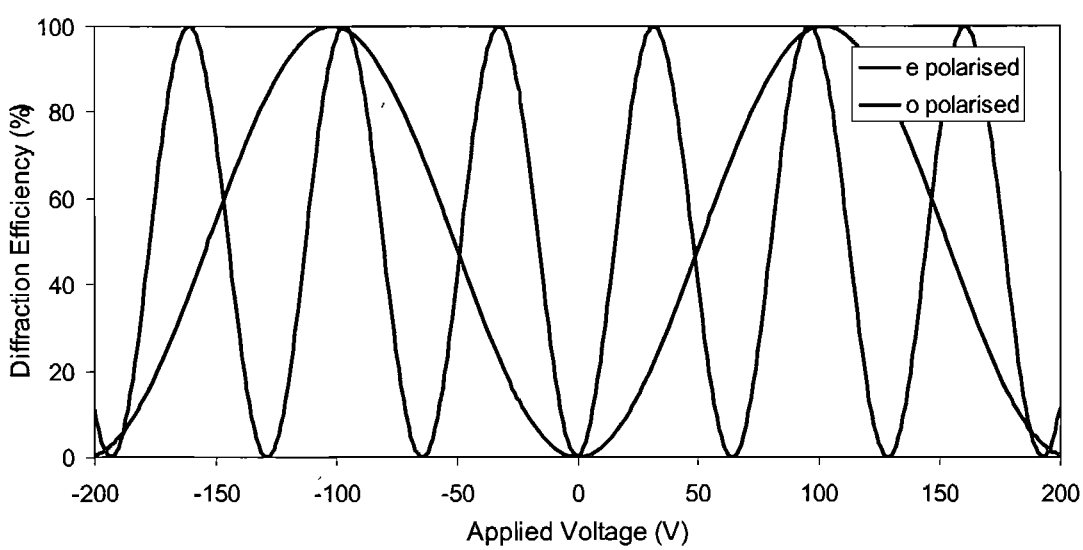

Figure 4.9 *Diffraction efficiency of the first order for e- and o-polarised incident light at λ = 633nm, for grating Λ = 70mm, length d = 3cm and thickness 500μm*

The drive voltage required for maximum diffraction efficiency for a Bragg grating modulator also depends on the grating length, grating period and operating wavelength (Equation 4-24). The effect on the drive voltage due to change in these parameters is summarised in Table 4-3.

The grating period, operating wavelength and incident angle are linked through the Bragg condition, Equation 4-23. As such, when the grating period is altered for a fixed wavelength the incident angle must change to keep the Bragg condition satisfied. As the diffraction efficiency depends on the cosine of the incident angle and not the grating period, and as these angles are very small, (less than half a degree), the effect of varying grating period on voltage is negligible.

Increase Wavelength, λ	⇒	Increase in Voltage
Increase Grating Period, Λ	⇒	Negligible increase in Voltage
Increase Grating Length, *d*	⇒	Decrease in Voltage

Table 4-3 *Effect of wavelength, grating length and grating period on drive Voltage required for maximum efficiency.*

From the analysis of the theoretical model of Bragg grating devices it can be seen that there is a high degree of flexibility available in the operating parameters of each device by controlling the device specifications. This makes these devices highly versatile and suitable for use in many applications under a variety of different conditions.

4.3.9 Comparison to bulk electro-optic lithium niobate modulators

The drive voltage for a bulk longitudinal electro-optic lithium niobate modulator for maximum switching, or half-wave voltage, is given by [30]:

Equation 4-31

$$V = \frac{\lambda}{2n^3 r_{ij}}$$

where λ is the free space wavelength, n is the refractive index, and r_{ij} is the electro-optic coefficient. Figure 4.10 shows this voltage for both e- and o-polarised light over a large wavelength range for the same device and operating specifications as used for the devices in this thesis. At the visible and infrared wavelengths used in this work the equivalent voltage required to drive a bulk electro-optic device would be in the kV range, with very little room for tuning. It can be seen from Chapter 4.3.8, that the voltages required for maximum diffraction efficiency for Bragg grating devices are much lower, a few volts is typical for the devices studied in this work, with a high degree of flexibility through design choice.

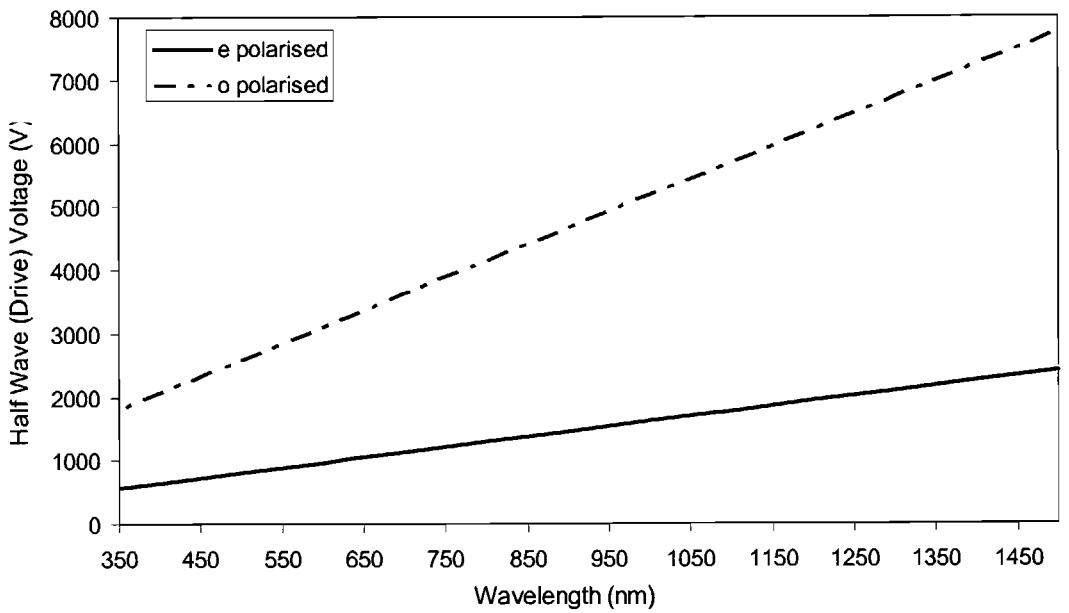

Figure 4.10 *Theoretical drive voltage required for maximum switching in a bulk electro-optic modulator with wavelength for e-polarised and o-polarised light (thickness 500μ).*

4.4 Design and fabrication of Bragg modulators

4.4.1 Design considerations

The basic design of a Bragg grating modulator was previously described in Section 4.2 . However, when choosing the device specifications and operating conditions there are several design parameters which must be considered. The first is to ensure

that the device is indeed operating in the Bragg regime. As discussed in Chapter 4.3 , the lower limit of the Bragg regime is defined by :

Equation 4-32

$$Q = \frac{2\pi\lambda d}{n\Lambda^2} \geq 4\pi$$

and once the device specifications have been chosen the Q factor should be calculated using this equation to ensure that the device is in the Bragg regime.

For most applications a low drive voltage is desired. As was discussed in Chapter 4.3.8 this can be achieved by using e-polarised light, by decreasing the wavelength, and by increasing the device length, *d*. If the wavelength is set by the application and e-polarised light is used, then the final controllable parameter is the device length, which can be increased up to the fabrication limitations.

4.4.2 Fabrication procedure

Bragg modulators are fabricated in lithium niobate using standard photolithography and electric field poling techniques, as described in Chapter 3. Alignment marks were etched onto the samples using hydrofluoric acid, after which the grating designs were patterned photolithographically and periodic domains achieved using liquid gel electrodes and a constant current source [31]. The aluminium electrodes used to control the variation in refractive index via an applied electric field were then defined photolithographically and vacuum deposited.

4.4.3 Fabrication issues due to design

The design of Bragg modulators is very different to standard periodically poled devices in lithium niobate as the gratings are very long in the y-axis (typically centimetres), and very narrow in the x-axis (typically microns), compared to classical PPLN grating periods which are millimetres long and a few microns wide. Figure 4.11 shows the difference in orientation between PPLN and the Bragg grating modulators under normal operation.

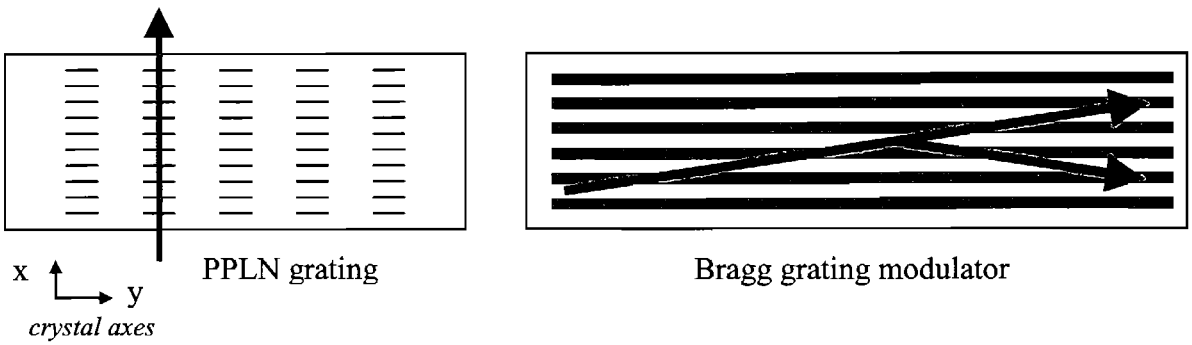

Figure 4.11 *Grating orientation of PPLN grating vs. Bragg grating modulator (red arrow indicates the direction of the incident light)*

After the application of an electric field to photolithographically defined gratings, it is thought that poling in lithium niobate starts at nucleation points in the crystal which are found at defects on the crystal surface, particularly at the edges & corners of photoresist where the electric field is stronger [32,Chapter 3]. During the scope of this project it was found that better quality poling was achieved using multiple smaller openings within a domain, allowing increased photoresist edges. However, the design of Bragg grating modulators leads to very large openings with few edges and therefore fewer nucleation sites. As such, poorer quality domain inversion was initially achieved for Bragg gratings compared to PPLN gratings, Figure 4.12 a).

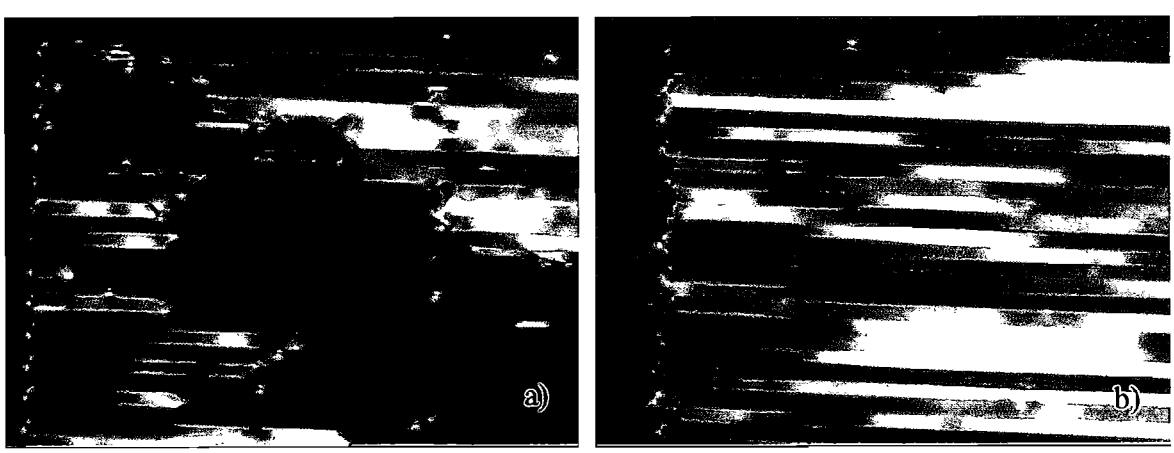

Figure 4.12 *Photographs taken using crossed polarisers showing a) poor quality domain inversion in a Bragg grating. b) good quality domain inversion using multiple opening design.*

To overcome this problem a new mask was designed with multiple openings in each grating domain as shown in Figure 4.13. By using the same charge required to invert the whole grating domain, the smaller multiple opening domains spread in the y

direction to form the full domain. This produced much better quality gratings, as shown in Figure 4.12 b).

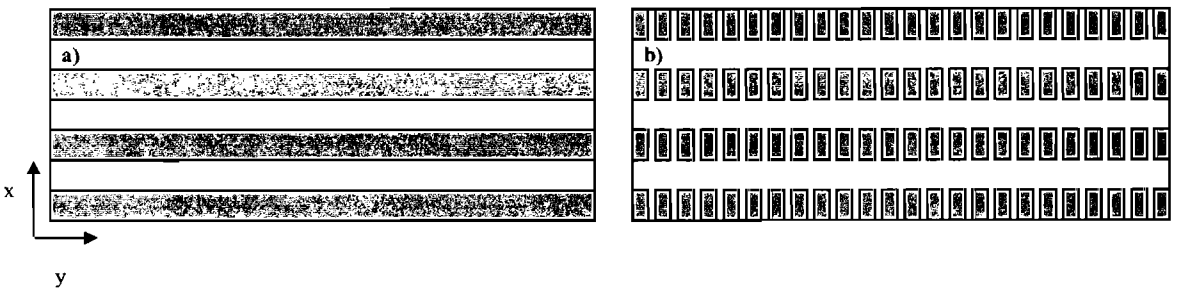

Figure 4.13 Schematic showing a) Single opening modulator design. b) Multiple opening modulator design (not to scale)

Furthermore, a PPLN grating consists of many narrow openings, whereas the modulator grating consists of a few very long gratings parallel to the y axis. It is known that intrinsic defects in the lithium niobate crystal cause 'meandering' of the domain walls [33], an effect much more apparent with the long grating edges present in the modulator grating than the much shorter openings in the PPLN gratings. The non-straight domain walls can be seen from the photograph in Figure 4.14. This problem does not become apparent until inverted domains are introduced in to the crystal. As this effect is due to the crystal growth process and there is no treatment or process which can be done at the poling stage to improve it. A study of the material from different suppliers is reported in Chapter 3, however no supply of lithium niobate has yet been found to produce noticeably straighter domain walls.

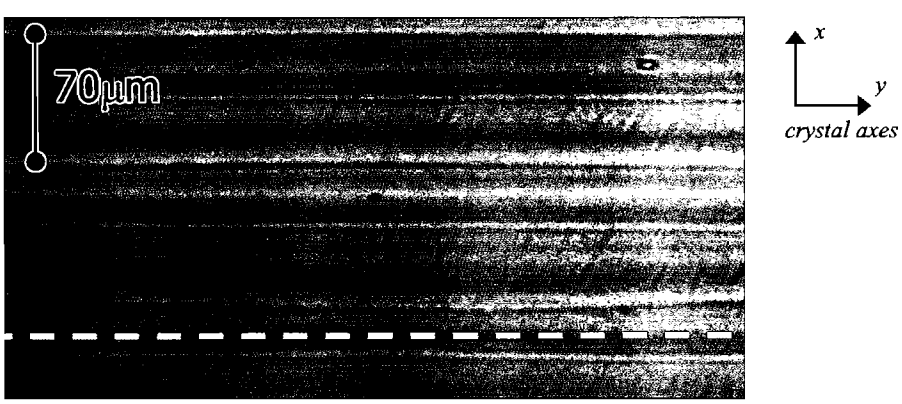

Figure 4.14: Photograph taken using cross polarisers showing domain wandering along y axis

The third fabrication issue which affects the performance of the device is the presence of non 50:50 mark to space ratio domains (ie. the ratio of the up and down domains of the grating is not equal), and variations in grating period. Changes in the mark to space ratio may induce a phase mismatch which would lead to reduced diffraction efficiency. It was seen in Section 4.3.8 that changes in the grating period have negligible effect on the drive voltage, however from the Kogelnik diffraction efficiency equation, Equation 4-24, it can be seen that the first order diffraction efficiency of a Bragg grating modulator is indirectly dependent on the grating period, Λ, from the wavelength of light, λ, and the angle of the incident light, θ_{int}. As the Bragg condition must be met at all times, a change in grating period, for example due to imperfect gratings caused by crystal defects, must be compensated for by changes in the wavelength or incident angle. In most cases the wavelength is fixed, therefore the incident angle will change. To re-achieve maximum diffraction efficiency again the incident angle could be changed accordingly. However, if no alteration is made to the set up, the diffraction efficiency in the first order will be reduced as described in Section 4.3.7, for the case of off-Bragg angular deviations.

4.5 Set up and testing of modulator devices

The arrangement used for testing the modulator devices is shown in Figure 4.15. The laser is passed through a polarising beam splitter and half wave plate to allow control of the polarisation of the beam. The light is then focussed using a 300mm lens into the sample, which is mounted on a 5-axis micropositioner, a photograph of which is shown in Figure 4.16. This allows movement in the x, y and z axis and also tilt about the centre of the sample in the x-y plane and the y-z plane. The required incident angle for Bragg matching is set using the micropositioner. The signal generator provides the required voltage waveform, which is then amplified and applied to the top and bottom electrodes on the sample. The range of voltages available for this experiment is ±200V, determined by the maximum working range of the voltage amplifier [NewFocus model 3211]. Calibrated detectors are positioned at the zeroth and first orders and pinholes used to eliminate any background signal. The signal from the detectors is fed to an oscilloscope for comparison and recording.

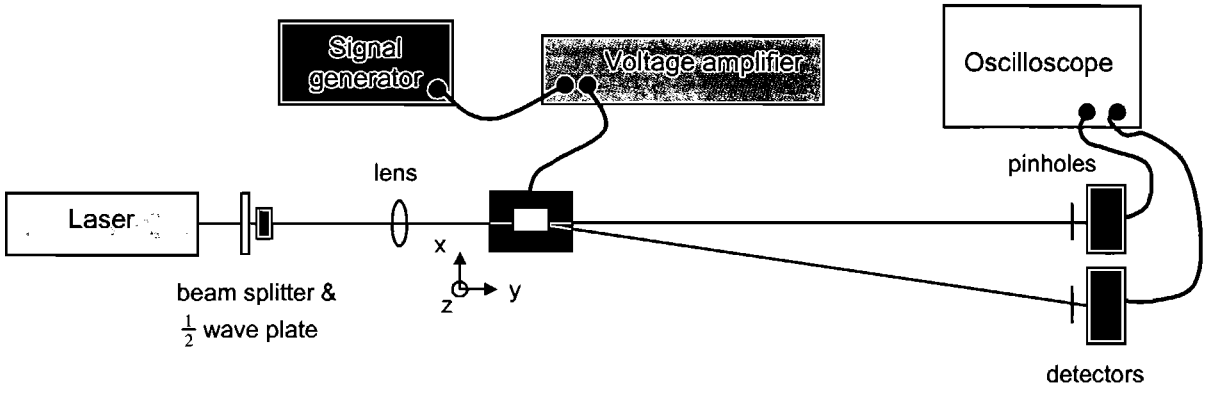

Figure 4.15: Experimental set up

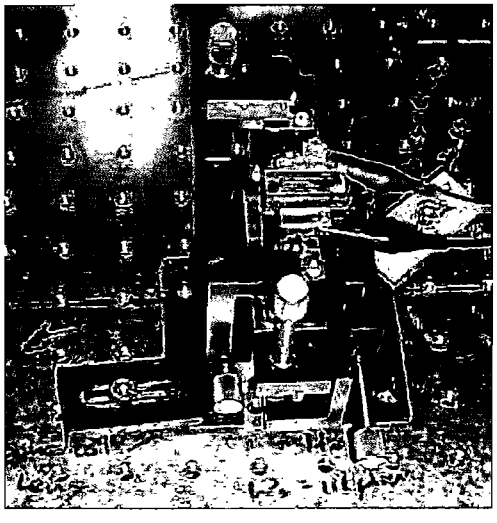

Figure 4.16 Photograph of sample mounted on micropositioner

4.5.1 Set up considerations

For optimum device performance the wavefronts of the incident wave should be parallel. As a general rule of thumb for focussing Gaussian beams, the distance over which the wavefronts can be assumed to be parallel is defined by the confocal parameter or Rayleigh range. The distance from the beam waist to the edge of the Rayleigh range is defined as :

Equation 4-33

$$z_o = \frac{n\pi\omega_0^2}{\lambda_0}$$

where n is the refractive index of the material, λ_0 is the free space wavelength, and ω_0 is the radius of the beam at the waist. The focal length of the lens should be carefully

chosen to ensure that full length of the grating lies within the Rayleigh range, ensuring parallel wavefronts along the whole length of the grating.

4.6 Bragg grating modulator operating at 1064nm

This section describes part of the main practical investigation carried out within the scope of this thesis. Results are presented for the first infrared demonstration of an electro-optically controlled Bragg modulator based on a periodically poled grating in lithium niobate, operating at 1064nm [4,5,6].

4.6.1 Device specifications

Bragg modulators were fabricated using the method described in Section 4.4.2. The first set of devices were of length 3cm with grating periods of 30, 40, 50, 70 and 90 μm. The second were of grating period 70 μm with lengths 2, 3, 4 and 5 cm. Using the set up described in Section 4.5 the diffraction efficiencies in the zeroth and first orders was measured for each device with both e- and o-polarised light of wavelength 1064nm. The angle for maximum diffraction into the first order was also measured for each device.

4.6.2 Results

The first demonstration of a Bragg grating modulator operating at 1064nm is shown in Figure 4.17 and Figure 4.18. The device shown was of grating period 70μm and length 3cm, and 53mW of light at a wavelength of 1064nm was used. This corresponded to an internal Bragg angle of 0.19 degrees, and an external angle, via Snell's Law, of 0.44 degrees. The actual external angle for maximum diffraction efficiency was measured to be 0.5 degrees ±0.25 degrees, which is in good agreement.

On / off voltages of 55V for e-polarised light and 225V for o-polarised light were measured. Diffraction efficiencies in the first order of 44% for e-polarised light and 30% for o-polarised light can be seen from the graphs. Maximum on/off ratios in the

first order of 15:1 for e polarised and 9:1 for o polarised light and in the zeroth order of 1:7 for e polarised and 1:5 for o polarised light were achieved, Table 4-4.

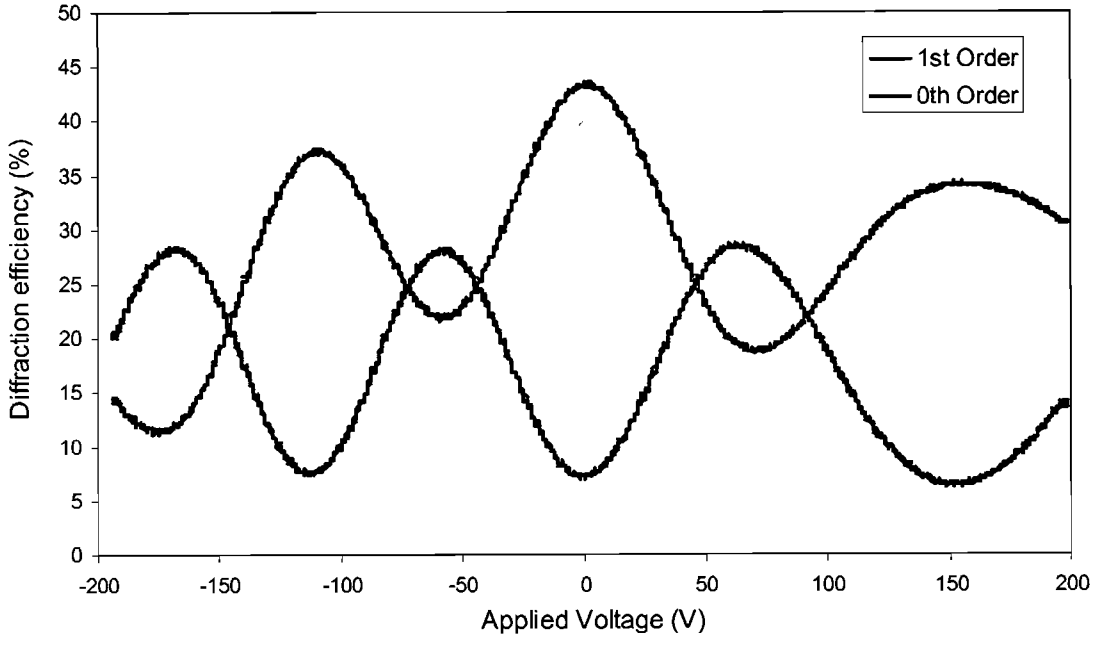

Figure 4.17 *Diffraction efficiency with applied voltage for zeroth and first orders for e-polarised light (device thickness = 500μm)*

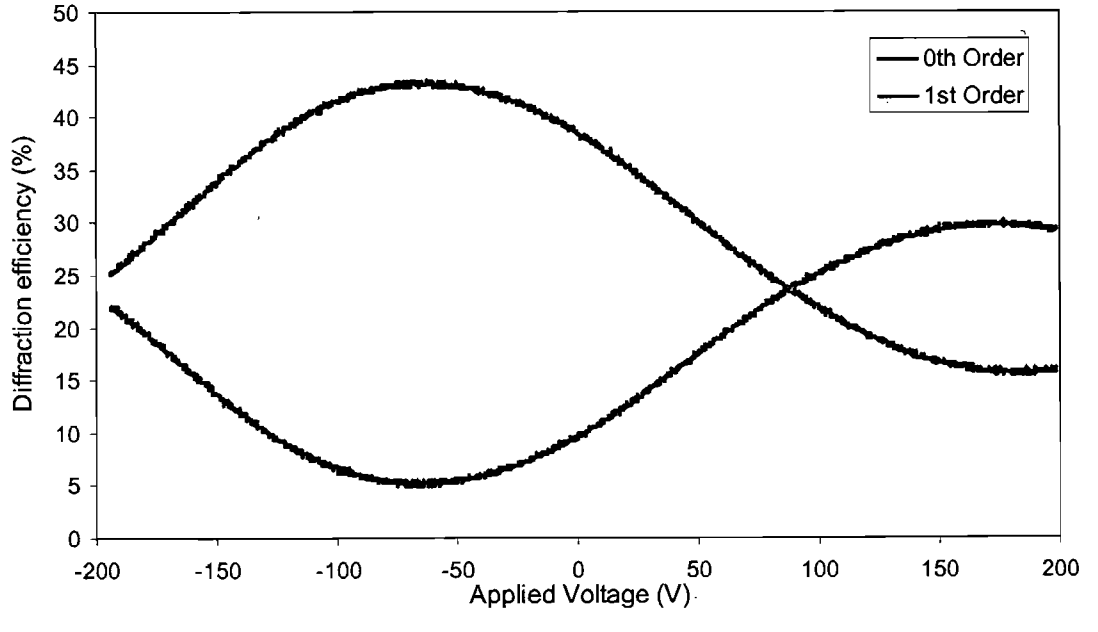

Figure 4.18 *Diffraction efficiency with applied voltage for zeroth and first orders for o-polarised light (device thickness = 500μm)*

Polarisation	Diffraction order	On / off ratio
e-polarised	0^{th}	1 : 7
e-polarised	1^{st}	15 : 1
o-polarised	0^{th}	1 : 5
o-polarised	1^{st}	9 : 1

Table 4-4 Maximum on / off ratios for 1064nm diffraction

The corresponding theoretical diffraction efficiencies for the first order for e- and o-polarised light are shown in Figure 4.19.

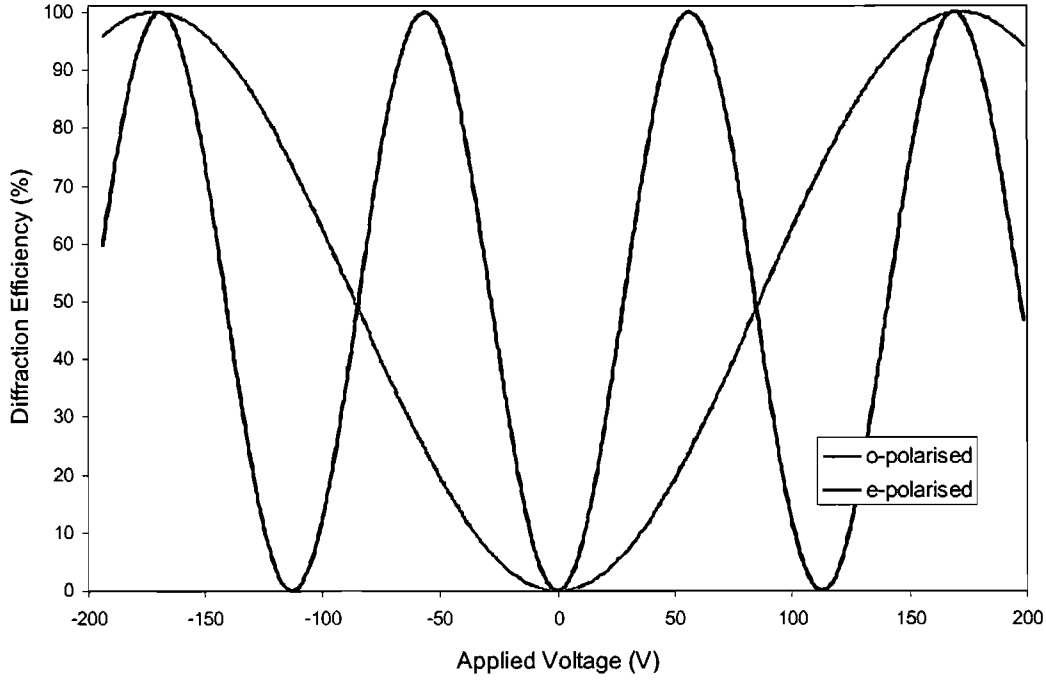

Figure 4.19 Theoretical diffraction efficiency for first order diffraction for e- and o-polarised light showing the much lower drive voltage required for operation with e-polarised light (device thickness = 500μm)

Figure 4.20 shows the measured incident external angles for maximum efficiency in the first order, shown as dots, against the theoretical Bragg angle, indicated by the solid line, for each of the five 3cm long devices. Due to the small angles involved the error in the measured angles is very high, ±0.25 degrees. The voltage required to switch the device from minimum diffraction in the first order to maximum diffraction, called the on / off voltage, is shown in Figure 4.21. This voltage was measured for 4 samples with grating period 70μm, and grating lengths of 2, 3, 4 and 5 cm, for both e- and o-polarised light. The solid lines represent the theoretically calculated on / off voltage.

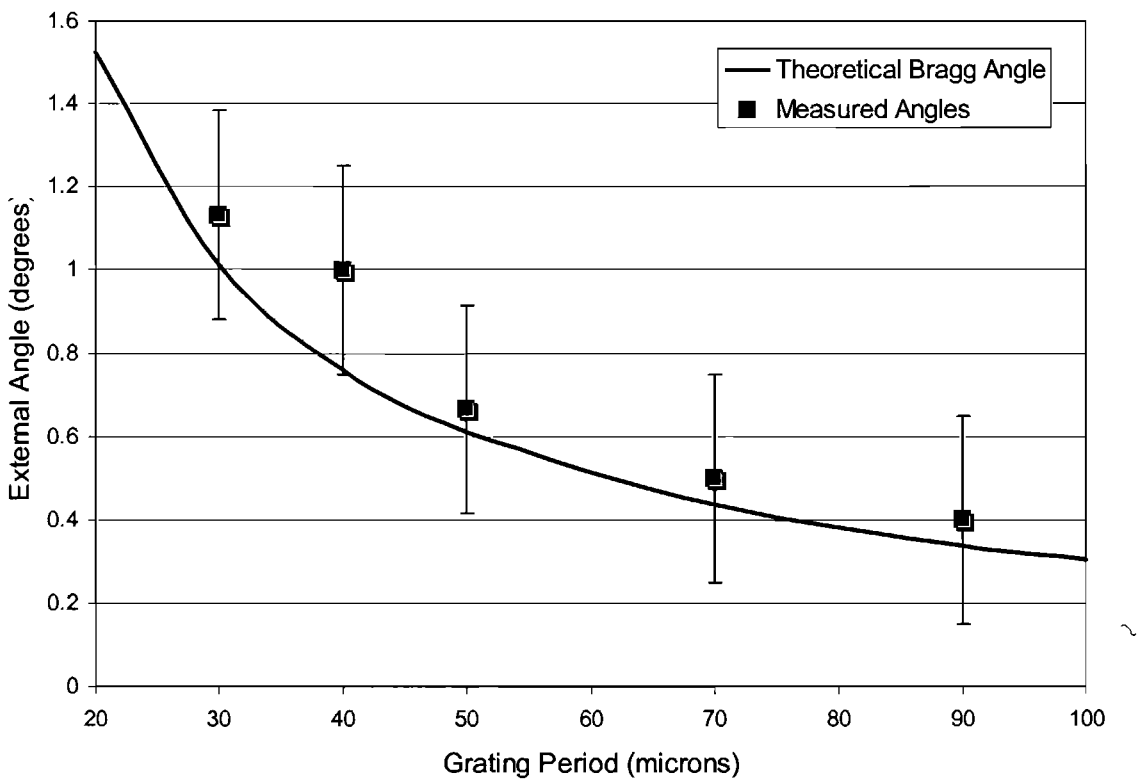

Figure 4.20 Theoretical and measured Bragg angles for Bragg gratings operating at 1064nm. (Error of ±0.25 degrees in measured angles)

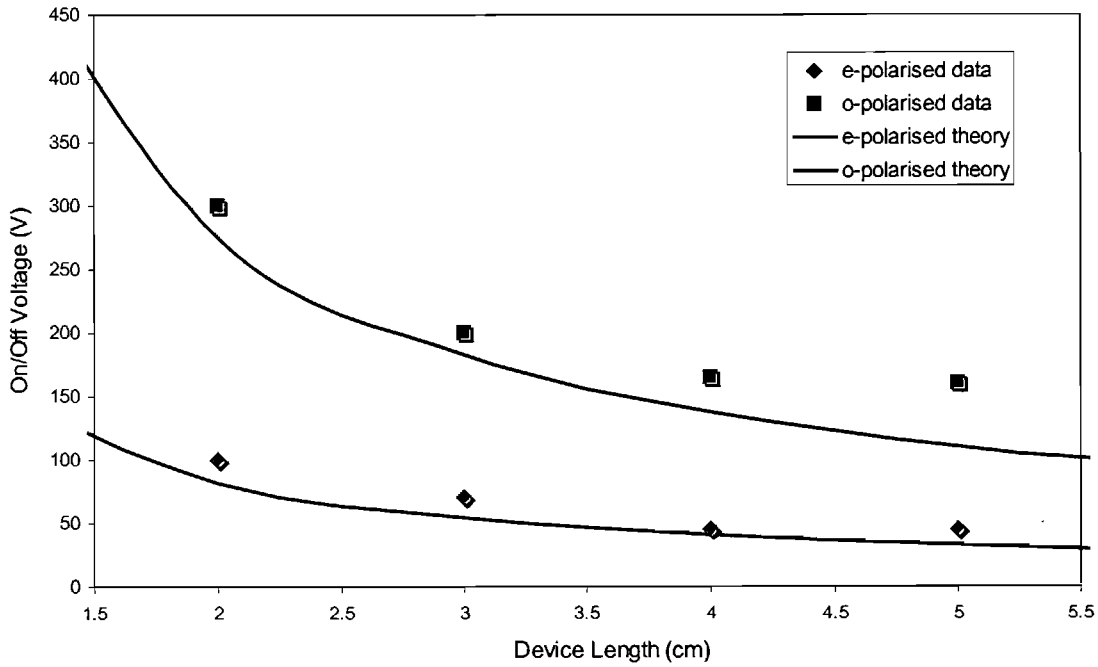

Figure 4.21 *On / Off Voltage with device length for e- and o-polarised light of λ=1064nm & grating period, Λ=70μm.*

4.6.3 Discussion

In Figure 4.17 and Figure 4.18 the sinusoidal dependence seen by Yamada [1,20] and Gnewuch [2] can clearly be seen. On / off voltages of 55V for e-polarised light and 225V for o-polarised light were measured, compared to theoretical values of 54.6V and 183.5V, as shown in Figure 4.19, calculated using r coefficients of $r_{33} = 30.8 \times 10^{-12} mV^{-1}$ (accessed by e-polarised) and $r_{13} = 8.6 \times 10^{-12} mV^{-1}$ (accessed by o-polarised) [17]. This shows good correlation for e-polarised light, but poor for o-polarised light. However, a large range in the electro-optic coefficient, r, is reported for lithium niobate, for example Weis & Gaylord [18] report values from 28 to $34 \times 10^{-12} mV^{-1}$ for r_{33} and from 6.5 to 10×10^{-12} mV^{-1} for r_{13}. Therefore by appropriate selection of the electro-optic coefficient we can achieve good match for both e- and o-polarised light.

Figure 4.20 shows that within the error margins the measured angles for maximum diffraction efficiency for devices of grating periods 30, 40, 50, 70 and 90μm are in good agreement with the theoretical Bragg angles. The measured on / off voltages shown in Figure 4.21 are also in good agreement with the predicted voltages shown

by the solid lines. The measured voltages for the 5cm device are slightly higher than expected; this is believed to be due to a decrease in effective grating length as discussed in Section 4.4.1, as a result of the operating conditions and device specifications.

An offset in applied voltage, similar to that seen by Gnewuch, of –55V in this particular experiment can be seen in both the e- and o-polarised diffraction efficiencies. It is believed that the origin of this offset is due to a residual stress induced refractive index grating after poling and is a phenomenon reported by other groups but not yet fully understood [20]. Annealing has been found to help, but does not fully alleviate this problem, Chapter 5.

Diffraction efficiencies of 44% for e-polarised light and 30% for o-polarised light were achieved with these devices, representing a result lower than the 70% and 75% diffraction efficiencies seen by Yamada and Gnewuch at the lower wavelength of 633nm. The diffraction efficiencies achieved when operating in the infra-red were found to be consistently lower than for visible operation. Also, higher field maxima (corresponding to higher orders in the argument of Equation 4-24 of π, 3π, 5π...) have been found to exhibit increasingly lower diffraction efficiencies. The diffraction efficiency is thought to be reduced by parasitic higher order spots due to non-sinusoidal grating components present in the periodically poled grating and voltage induced scattering at increased drive voltages. It can also be seen from the efficiency graphs that the diffraction minima are non-zero. This is likely to be due to non uniform grating periods and the non-sinusoidal characteristic of poled grating profiles causing diffraction due to higher order grating components. These anomalies are investigated in greater depth in Chapter 5.

4.7 Chapter conclusions

This Chapter has reviewed current acousto-optic and bulk electro-optic modulators. An electro-optically induced Bragg grating modulator in periodically poled lithium niobate was introduced, previous work in this area reviewed, and a full theoretical

analysis based on the Kogelnik coupled wave theory for thick holograms presented. This theoretical analysis allowed several issues to be taken into consideration during the design phase of this project. The fabrication of the devices was described, and fabrication issues due to design highlighted. Analysing and characterisation of the devices was also described. The last section presented results for the first infrared operation of a Bragg grating modulator at 1064nm with first order diffraction efficiencies of 44% and 30 % achieved for e- and o- polarised light. An offset of -55V was seen in the efficiency graphs which was believed to be due to a residual internal electric field cause by the poling process. The diffraction efficiency curves exhibited similar sinusoidal characteristics to the theoretical curves and good correlation was seen between theoretical and measured Bragg angles for several devices with different grating periods. The measured on/off voltage for differing lengths of device was also seen to match well with theoretical values. However several anomalies between the theoretical and measured data were highlighted and it was concluded that further work is needed to fully understand the operation of these devices. The results taken at 1064nm backed up discrepancies seen before by other authors, in particular the offset in drive voltage, lower peak diffraction efficiencies than predicted by theory, and non-zero minima in diffraction efficiency. Work towards understanding and explaining these inconsistencies is presented in Chapter 5.

4.8 References

[1] M Yamada, M Saitoh and H Ooki *'Electric-field induced cylindrical lens, switching and deflection devices composed of the inverted domains in $LiNbO_3$ crystals'* *Appl Phys Lett* **69** p3659-3661 (1996)

[2] H Gnewuch, C N Pannell, G W Ross, P G R Smith and H Geiger *'Nonosecond response of Bragg deflectors in periodically poled $LiNbO_3$'* *IEEE Photonics Tech Lett* **10** p1730-1732 (1998)

[3] H Kogelnik *'Coupled wave theory for thick hologram gratings'* *The Bell System Technical Journal* **48** no.9 p2909-2947 (1969)

[4] J A Abernethy, C B E Gawith, R W Eason and P G R Smith *'Demonstration and optical characteristics of electro-optic Bragg modulators in periodically poled lithium niobate in the near infrared'* *Appl. Phys. Lett.* **81** (14) (2002)

[5] J A Abernethy, R W Eason and P G R Smith *'Bulk optical Bragg deflectors at 1.064μm based on an electro-optically induced grating in periodically poled lithium niobate' CLEO/Pacific Rim* Chiba **ME2-3** p102-103 15-19th Jul (2001)

[6] J A Abernethy, R W Eason and P G R Smith *'Investigation into bulk optical Bragg deflectors based on an electro-optically induced grating in periodically poled lithium niobate' International Workshop on Periodically Microstructured Nonlinear Optical Materials* Madrid 10-13th Jun (2001)

[7] D Maydan *'Acousto-optic pulse modulators' IEEE J Quantum Elec* **QE6** p15 (1970)

[8] E I Gordon *'A review of acousto-optical deflection and modulation devices' Proc. IEEE* p1391-1401 (1966)

[9] H Gnewuch, CN Pannell, PGR Smith *'Electro-optic devices' British patent, Application number 9 807 738.1*

[10] New Focus *'Practical Uses and applications of electro-optic modulators' Application Note 2*

[11] B Lofving *'Measurement of the spatial phase modulation of a ferroelectric liquid-crystal modulator' Appl. Opt.* **35** (17) p3097-3103 (1996)

[12] C I Wilkinson, J Woodhead, J E F Frost, J S Roberts, R Wilson R and M F Lewis *'Enhancement of a liquid-crystal modulator using an external-cavity VCSEL' IEE Photonic. Tech. Lett.* **11** (8) p940-942 (1999)

[13] M A R P de Barros, M G F Wilson *'Nanosecond baseband optical diffraction modulator' Elec. Lett.* **7** p267 (1971)

[14] J M Hammer *'Digital electro-optic grating deflector and modulator' Appl. Phys. Lett* **18** p147-149 (1971)

[15] J Wilson and J F B Hawkes *'Optoelectronics: An Introduction' Prentice Hall* (1983)

[16] M J Brinkman, A Romanovsky, X Shao, K Watanabe *'Electro-optic switches in poled lithium niobate' CLEO '96* CWD3

[17] A Yariv *'Quantum Electronics' John Wiley & sons* (1989)

[18] R S Weis and T K Gaylord *'Lithium niobate: summary of physical properties and crystal structure' Appl Phys* **A37** p191 (1985)

[19] P Basseras, R J D Miller and S M Gracewski *'Theoretical-analysis of acoustic transients in lithium niobate electro-optic modulators' J. Appl Phys.* **68** p7774-7781 (1991)

[20] M Yamada *'Electrically induced Bragg-diffraction grating composed of periodically inverted domains in lithium niobate crystals and its application devices' Rev. Sci. Inst.* **71** no.11 p4010-4016 (2000)

[21] W R Klein and B D Cook *'Unified approach to ultrasonic light diffraction' IEEE Trans. Sonics Ultrason.* **SU-14** p123 (1967)

[22] P Phariseau *'On the diffraction of light by progressive supersonic waves' Proc. Ind. Acad. Sci* **44A** p165-170 (1956)

[23] C F Quate, C D Wilkinson and D K Winslow *'Interaction of light and microwave sound' Proc IEEE* **53** no.10 p1604-1623 (1956)

[24] E I Gordon and M G Cohen *'Electro-optic diffraction grating for light beam modulation and diffraction' IEEE J. Quantum Elec.* **QE-1** no.5 p191-198 (1965)

[25] B Batterman and H Cole *'Dynamical diffraction of X-rays by perfect crystals' Rev. Modern Physics* **36** no.3 p681-717 (1964)

[26] W R Klein, C B Tipnis and E A Hiedemann *'Experimental study of Fraunhofer light diffraction by ultrasonic beams of moderately high frequency at oblique incidence' J. Acoustic Society of America* **38** no.2 p229-233 (1965)

[27] W R Klein *'Light diffraction by ultrasonic beams of high frequency near Bragg angle' Proc 5th Congress Int. D'Acoustique, Liege, Belgium* **D24** (1965)

[28] G W Willard *'Criteria for normal and abnormal ultrasonic light diffraction effects' J. Acoust. Soc. Am.* **21** p101-108 (1949)

[29] W R Klein *'Theoretical efficiency of Bragg devices' Proc. IEEE* **54** no.5 p803-804 (1966)

[30] C C Davis *'Lasers and electro-optics' Cambridge University Press* (1996)

[31] J Webjorn, V Pruneri, P St J Russell, J R M Barr and D C Hanna *'Quasi-phasematched blue light generation in bulk lithium niobate, electrically poled via periodic liquid electrodes' Electronic Letters* **30** 11 p894 (1994)

[32] V Y Shur, E L Rumyantsev, E V Nikolaeva and E I Shishkin *'Formation and evolution of charged domain walls in congruent lithium niobate' Appl. Phys. Lett.* **77** (22) p3636 (2000)

[33] Z W Hu, P A Thomas, A Snigirev, I Snigrireva, A Souvorov, P G R Smith, G W Ross and S Teat *'Phase-mapping of periodically domain inverted $LiNbO_3$ with coherent X-rays' Nature* **392** p690-693 (1998)

Chapter 5

Further investigation into electro-optic Bragg grating modulators in PPLN

In Chapter 4 an electro-optically induced Bragg grating modulator in periodically poled lithium niobate was introduced. A theoretical analysis based on Kogelnick's coupled wave analysis of Bragg diffraction [1] was developed and results for a Bragg grating device operating in the infrared at 1064nm were presented. From these results, and from previous work by Yamada [2,3] and Gnewuch [4] several discrepancies and anomalies were found between the experimental results and the theoretical predictions.

This Chapter looks at several of these findings, investigating them in greater detail to understand the mechanisms behind them, with the aim of preventing or reducing the effects to improve performance. Results at visible wavelengths of 633nm and 488nm are presented and compared alongside the results in Chapter 4.6 to the theoretical analysis in Chapter 4.3. A discussion and experimental data showing the effect of the photorefractive effect on the lithium niobate devices are presented. The effect on device performance of residual gratings after poling, multiple reflections from the end faces and a new field induced light scattering effect at higher drive voltages due to poling is researched.

5.1 Visible operation of Bragg grating modulators

To further investigate some of the differences and inconsistencies seen between experimental data and theoretical analysis for infrared operation, and as seen in previous work by Gnewuch [4] and Yamada [2,3], the Bragg grating devices were tested at the visible wavelengths of 633nm and 488nm. The five devices of length 3cm with grating periods 30, 40, 50, 70 and 90μm, as described in Chapter 4.6, were used. The set up was as used for infrared operation (Chapter 4.5) with the 1064nm Nd:YAG laser replaced by a 633nm HeNe or a 488nm Ar ion laser.

Diffraction efficiencies for applied voltages ranging from -200V to +200V were measured for each of the devices at both 633nm and 488nm. From these results different aspects of the device performance can be analysed.

5.1.1 On / off drive voltage with wavelength

Figure 5.1 shows a comparison of theoretical and measured on / off voltage with wavelength for both e- and o-polarised light. If low drive voltage is an important issue in device design for a particular application, it can be seen that shorter operating wavelengths involve lower on / off voltages than longer wavelengths.

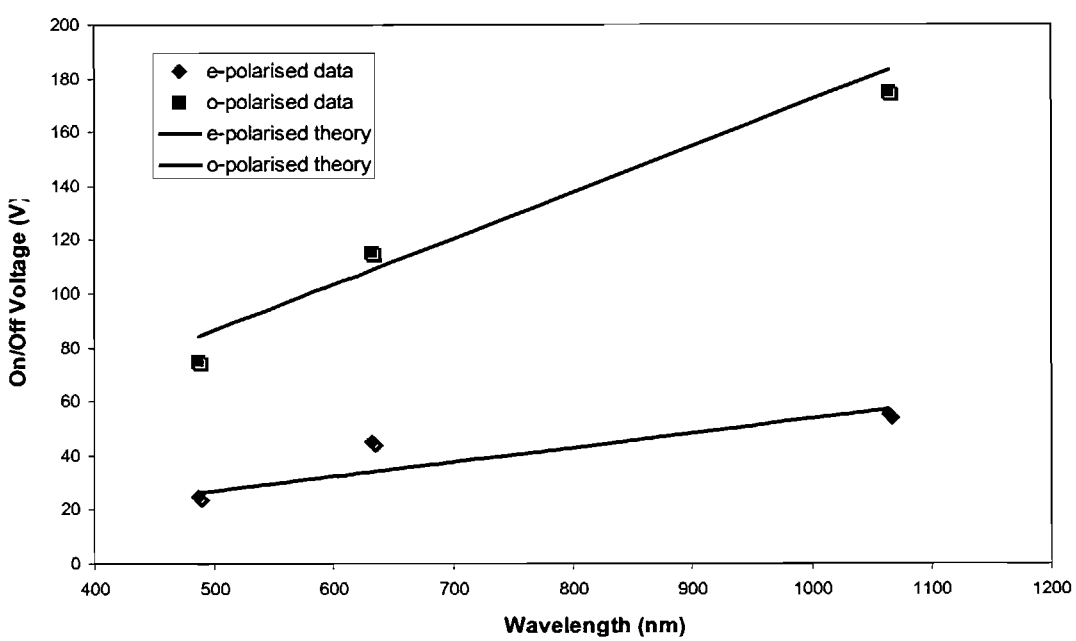

Figure 5.1 *Graph of theoretical (solid line) and measured (dots) on/off drive voltage with incident wavelength (thickness 500μm)*

5.1.2 Effect of wavelength and grating period on Bragg angle

The five devices were each tested at wavelengths of 1064nm, 633nm and 488nm and the external angle measured for peak diffraction into the first order. These values are plotted against the theoretical Bragg angle in Figure 5.2. The error due to inaccuracies in measurement was high, ±0.25 degrees, due to the experimental set up and the small angles involved. Considering this error, the measured angles show a good correlation with the theoretical Bragg angle.

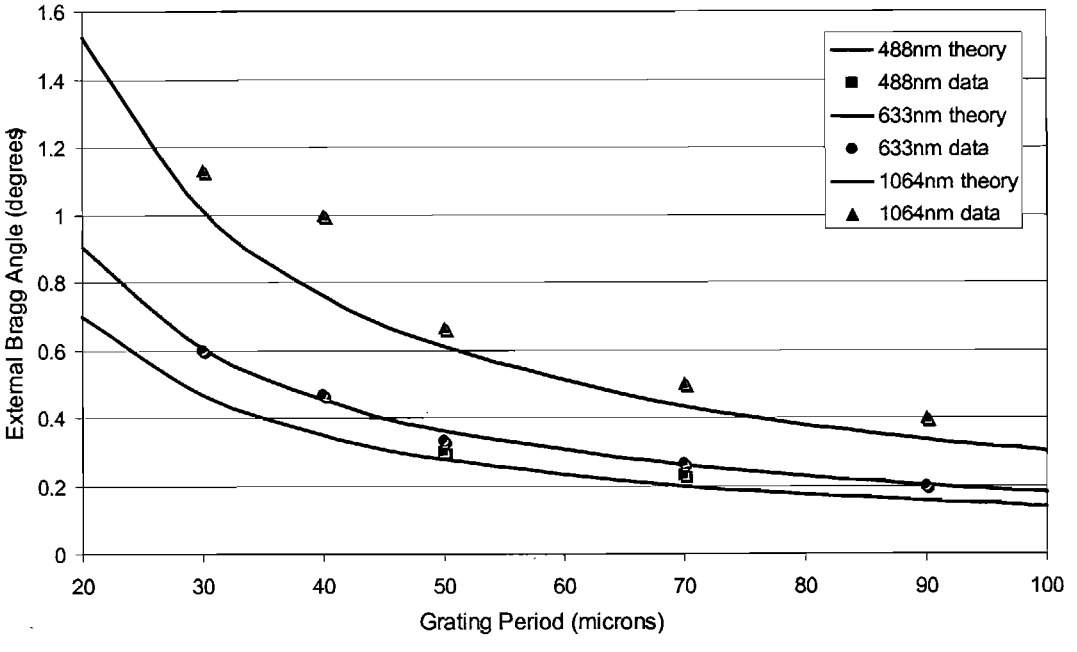

Figure 5.2 *Graph of theoretical and measured Bragg angles with grating period for different operating wavelengths (reading error ±0.25 degrees)*

5.1.3 Operation at 633nm

Figure 5.3 and Figure 5.4 below show the diffraction efficiency in the zeroth and first orders taken for both e- and o-polarised light at 633nm for a device of grating period 40μm and length 3cm. Figure 5.5 shows the theoretical first order diffraction efficiency for e- and o-polarised light for an identical device and conditions. It can be seen that experimental curves exhibit similar sinusoidal patterns of corresponding period. The performance characteristics for operation at 633nm are summarised in Table 5-1, which is in keeping with Table 4-2 for previously published results.

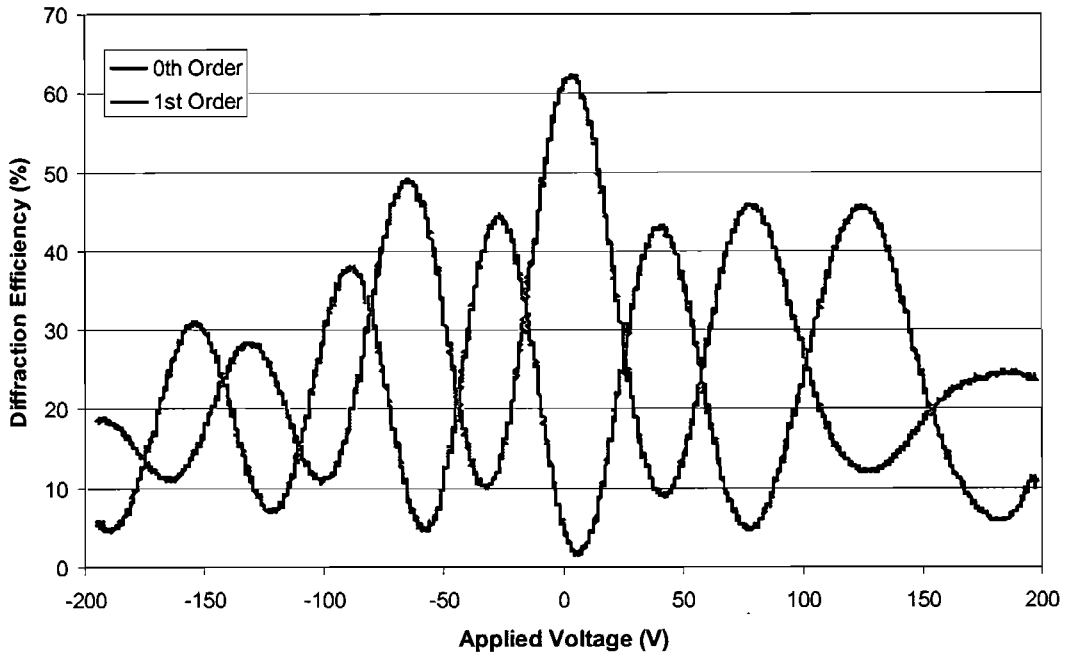

Figure 5.3 *Experimental diffraction efficiency of a Bragg grating modulator, period 40μm, length 3cm, thickness 500μm, in the first and zeroth order for 633nm e-polarised light*

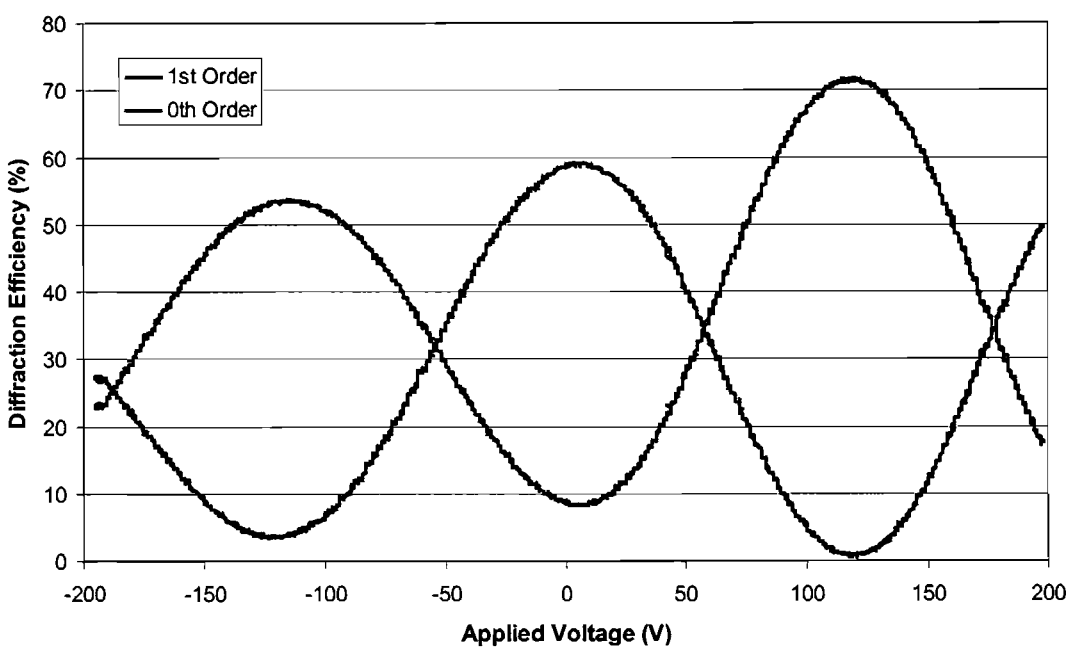

Figure 5.4 *Experimental diffraction efficiency of a Bragg grating modulator, period 40μm, length 3cm,thickness 500μm, in the first and zeroth order for 633nm o-polarised light*

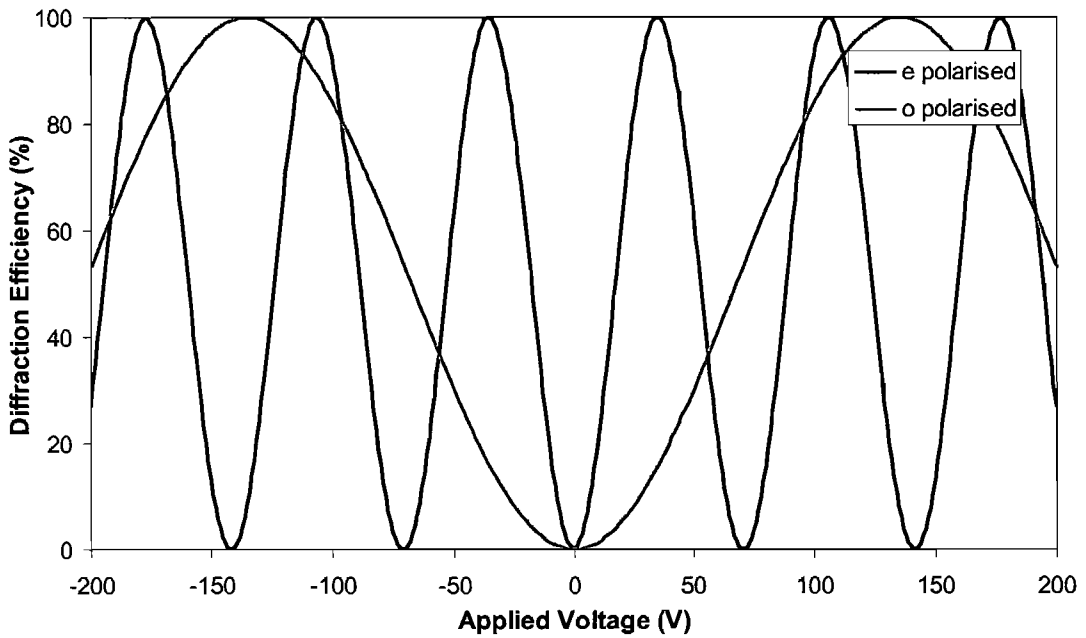

Figure 5.5 *Theoretical first order diffraction efficiency for 633nm e- and o-polarised light, period 40μm, length 3cm and thickness 500μm*

Polarisation	e-	o-
On / off voltage (V) [t = 500μm]	36	120
Theoretical on / off voltage (V)	35	135
Diffracted efficiency	46 %	72 %
Non-diffracted efficiency	63 %	69 %
Diffracted on / off ratio	22 : 1	10 : 1
Non-diffracted on / off ratio	7 : 1	40 : 1

Table 5-1 *Summary of performance characteristics at 633nm*

5.1.4 Operation at 488nm

Initial results at room temperature at 488nm were unsuccessful due to the high level of photorefractive damage seen in lithium niobate at shorter wavelengths. The counteractive effect of periodic poling in lithium niobate on photorefractive damage has been greatly studied [5,6], and is described in Chapter 3. The poled grating in the

Bragg modulator devices provided some improvement, but due to the relatively few grating planes accessed in the Bragg gratings, there was only a marginal improvement through the grating compared to bulk. Continuous annealing of the sample helped to offset the photorefractive damage.

To find out the optimum operating temperature a Bragg grating modulator device of grating period 40μm and length 3cm was set up as before for peak diffraction into the first order. The power in the first order was measured with time at room temperature and for three elevated temperatures of 100, 150 and 200°C. The results are shown in Figure 5.6. It can be seen that as the temperature is increased the rate of photorefractive damage is reduced, until at approximately 200°C the damage and annealing rates reach equilibrium.

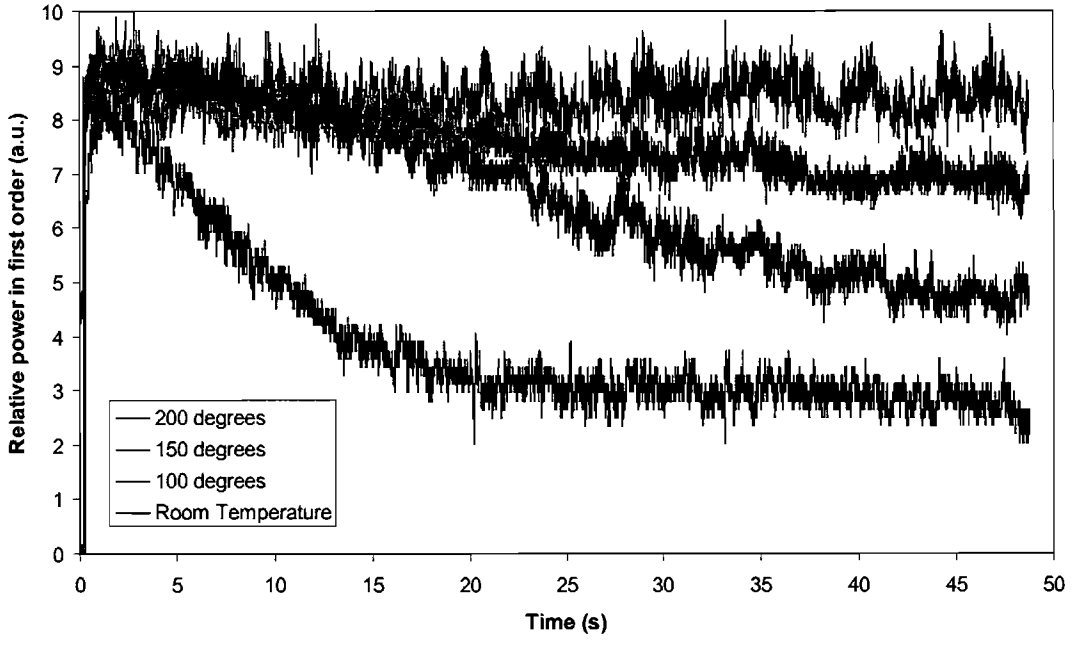

Figure 5.6 *Graph of relative power in the first order with time at room temperature and at elevated temperatures of 200°C, 150°C and 100°C for 10mW of 488nm light*

The efficiency measurements were then re-taken at the elevated temperature of 200°C and are shown for o-polarised light in Figure 5.7.

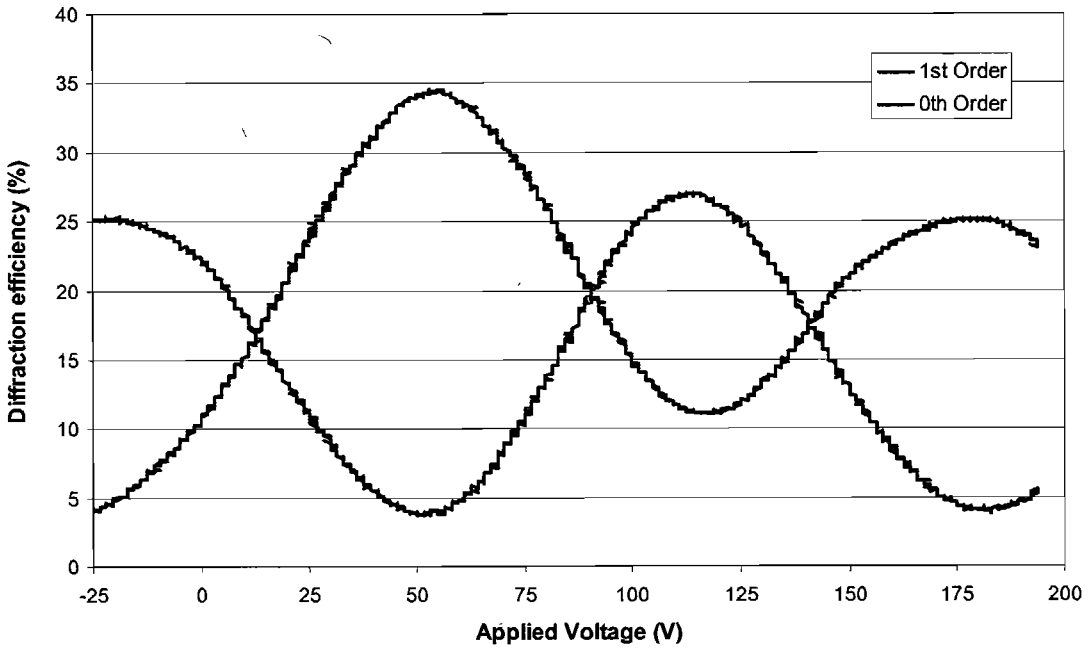

Figure 5.7 Graph of experimental diffraction efficiency with applied voltage for a device of grating period 50μm, length 3cm, thickness 500μm and with 488nm o-polarised light at 200 °C

It can be seen that although the characteristic sinusoidal diffraction efficiency with voltage is seen, there is a drop in diffraction efficiency, particularly at higher applied voltages, and an offset in effective zero field point of 52V.

5.2 Investigation into discrepancies

Previously published results have looked at performance of the Bragg grating modulators over a relatively narrow voltage range and have only considered the first peak in diffraction efficiency. This has hidden several of the anomalies and phenomena seen in the further investigation carried out in this work. This is highlighted more clearly if the range of applied voltages is restricted for the results shown in this work to show only the first peak in first order diffraction, see Figure 5.8 for 633nm results and Figure 5.9 for 488nm results. If only these results are considered, then a good match with the theoretical model would be concluded. This is effectively the approach taken by Yamada [2,3] and Gnewuch [4] in their presentation of their results.

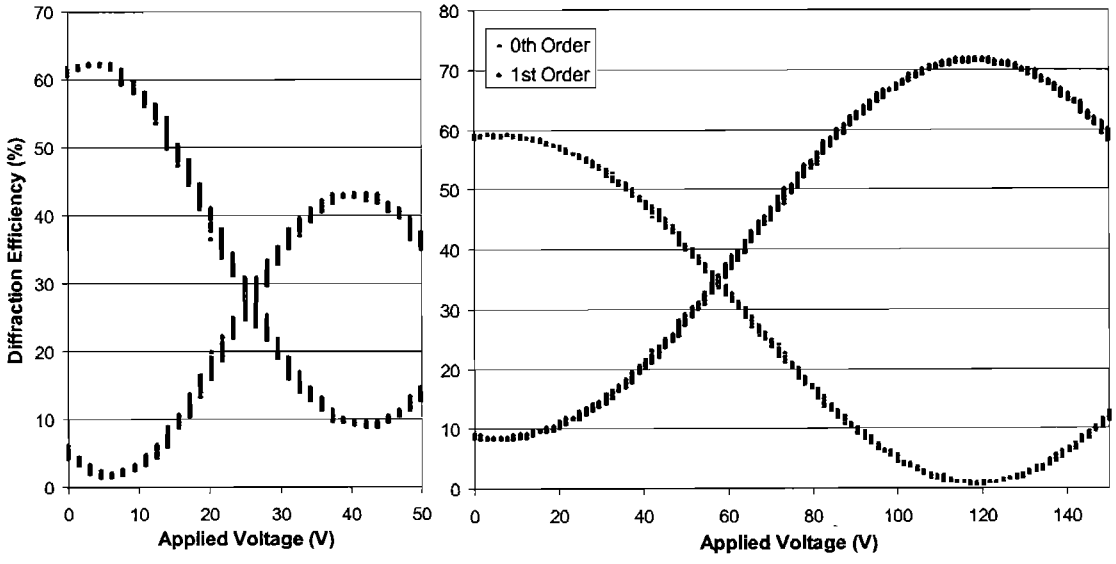

Figure 5.8 *Graphs of experimental diffraction efficiency with applied voltage for a) e-polarised and b) o-polarised 633nm light (thickness 500μm)*

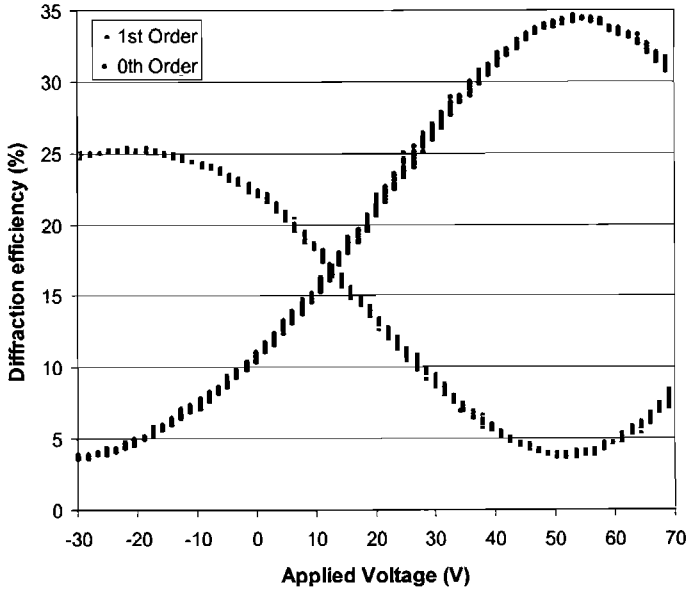

Figure 5.9 *Graph of experimental diffraction efficiency with applied voltage for o-polarised 488nm light (thickness 500μm)*

However, the results presented in this thesis look at a much wider picture, over larger voltage ranges showing several higher orders of diffraction efficiency peaks. Overall the results have shown good correlation with the theoretical analysis based on Kogelnik's coupled wave analysis for Bragg diffraction of light by thick hologram

gratings. Good matches were seen in Bragg angle with grating period and wavelength and in on / off voltage with operating wavelength and with device length for both e- and o-polarised light. However several new phenomena have been uncovered or seen more clearly during the further investigations.

Anomalies seen previously, such as an offset in the effective zero field point and non 100% diffraction efficiencies in the initial zeroth and first order peaks have been reconfirmed in our results at 1064nm, 633nm and 488nm. New discrepancies between the experimental data and the theoretical model not previously seen have also been found, including an increase in on / off voltage at higher applied voltages, reduced diffraction efficiencies during infrared operation and an increasing reduction in diffraction efficiency at peaks at increasing applied voltage. Other unexpected phenomena were seen during device testing such as diffraction into higher order spots and in-plane scatter into the general background, particularly at higher applied voltages.

The previous Section reviewed the operation of the electro-optically controlled Bragg grating modulator at 633nm and 488nm and discussed the need for high temperature operation at shorter wavelengths to overcome photorefractive damage. This Section moves on to look at the discrepancies arising between the experimental data and the theoretical predictions with the aim of understanding the mechanisms causing them and, if possible, proposing solutions or methods of reduction.

5.2.1 Offset in effective zero field point

With no applied voltage unexpected diffraction into the first order was seen. This was made even clearer when a diffraction efficiency with applied voltage measurement is taken over a range of voltages. This was most apparent in Figure 5.7 for o-polarised 488nm light where the effective zero field point was found at approximately 52V. This effect was also been seen by other authors; Yamada [2Fig4, 3Fig4] reported an offset of 30V in the 633nm modulator results and Gnewuch [4Fig2] reported an offset of 2.5V.

This effect is believed to be due to a residual grating remaining in the crystal after poling caused by stress induced refractive index changes via the piezoelectric effect. In Figure 5.7 this effect can be seen to cancel out at 52V. These stress induced gratings are seen in PPLN for other applications such as frequency conversion, Chapter 3, but due to the nature of the devices and its operation in those cases, this effect does not cause such a problem.

PPLN is frequently annealed after poling to re-align the internal field and remove any stress induced changes. The effect of annealing of the devices on the residual grating left after poling was measured by taking an intensity line scan with output angle for a device before and after annealing. The device in this case was of grating period 70μm, length 3cm and the measurements were taken using 633nm e-polarised light with no applied field. Several scans were taken for each case, at and just around the Bragg angle to highlight the extent of the stress induced grating present in the crystal. From Figure 5.10, taken before annealing, it can be seen that a large percentage of the power is being diffracted and scattered into higher orders and into the general background. Figure 5.11, taken after annealing at 250°C for 20 hours, shows that the residual grating has decreased significantly, less power is being diffracted into other orders and into the general background and the power in the zeroth order is increased.

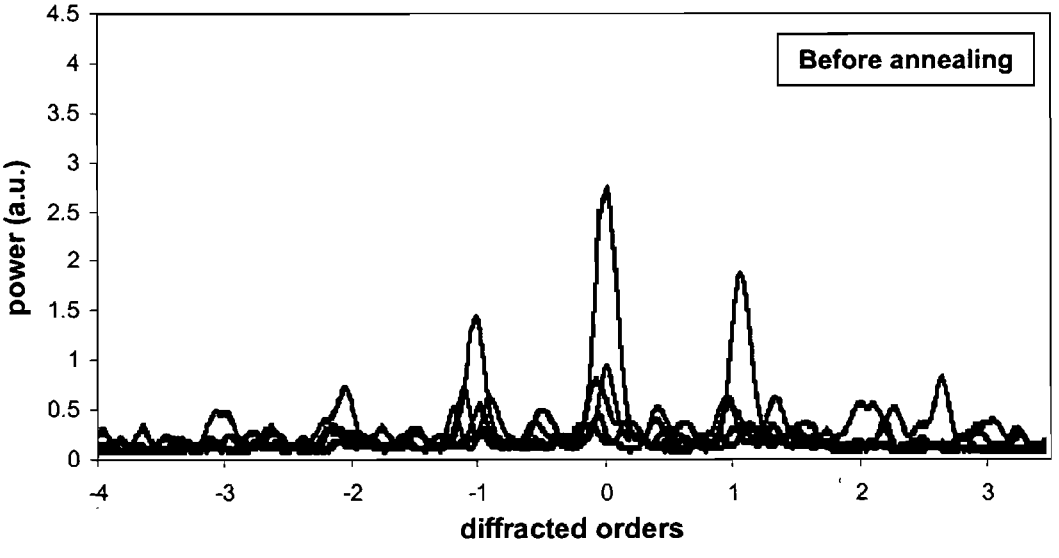

Figure 5.10 Line scan of output power with angle before annealing

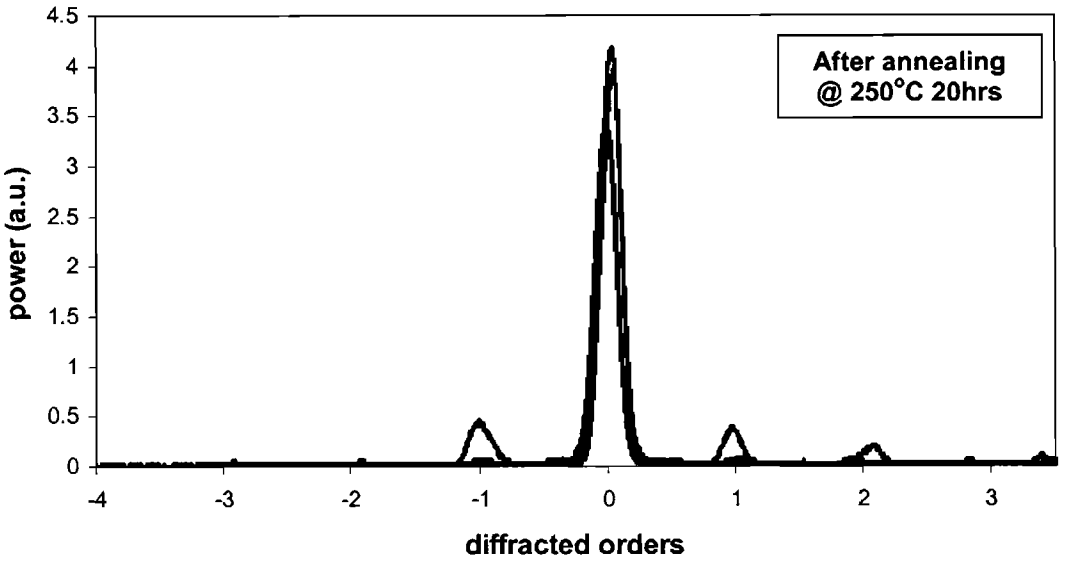

Figure 5.11 *Line scan of output power with angle after annealing at 250°C for 20 hours*

Annealing was found to help, but not alleviate the residual grating present in the crystal after poling. However the offset in effective zero field point was found to be reduced, thus confirming that this effect is, at least partly, caused by a residual internal refractive index grating.

5.2.2 Increased on / off voltage at higher applied voltages

A new effect seen in the results in this thesis was the increase in on / off voltage at higher applied voltages. It can be seen most clearly in Figure 5.3 and in Figure 4.17. In Figure 5.3 the peak in first order diffraction efficiency at 125V has an on/off voltage of 50V compared to 35V for the peak at 40V. This is thought to be due to the increased change in refractive index at higher voltages enhancing defects in the grating which alter the output angle of the diffracted beam causing it to misalign with the detector. Another similar explanation may be due to refraction at the interfaces again causing misalignment with the detector and therefore altering the on / off voltages. Further investigation is necessary.

5.2.3 Reduced diffraction efficiency

Maximum diffraction efficiencies of around 75% were achieved compared to the 100% theoretical predictions. This Section looks at several possibilities behind this to try to better understand them and work towards solutions or methods of reduction.

5.2.3.1 Grating quality

The first factor affecting the diffraction efficiency is associated with imperfections in the crystal structure and the quality of the poled gratings. Imperfect gratings and non 50:50 mark to space ratios caused by factors such as deviations in the domain walls due to variations in the crystal lattice, over or under poling due to variations in the wafer thickness over the grating area, poling dots due to the fabrication process, areas without poling due to reduced nucleation sites, etc. These are all fabrication and crystal growth issues which have been looked at in great detail in Chapter 3. Most are out with our control by this stage in the device fabrication and we rely on advancements in crystal growth resulting in better quality and more suitable lithium niobate material and improved poling quality to improve the devices. Stoichiometric lithium niobate has been shown to produce better quality poled gratings [7] and it would be interesting to see its effect on the quality of Bragg grating modulators.

Annealing helps remove the stress induced refractive index changes caused by the poling dots, and therefore reduce the scatter from these with no applied field. However as the dots are actually inverted domains, when a field is applied they will experience an opposite change in refractive index than the surrounding material and will act as a random scatterer in the device. This effect will be more pronounced the higher the voltage as the refractive index difference increases.

5.2.3.2 Wavelength and angular sensitivity

Another factor influencing the diffraction efficiency is associated with the wavelength and angular sensitivity of the device. Since the operation of the Bragg grating modulators is based upon Bragg reflection and since the Bragg condition is dependent on the wavelength, grating period and incident angle, any deviation from the unperturbed values will reduce efficiency. Deviations occur in practice due to the divergence of the incident beam, poling defects varying the grating period, the

wavelength bandwidth of the particular laser used, etc. A simple argument may be used to predict the reduction in efficiency.

It is assumed that there is a failure of p (%) (where p <<1) in satisfying the Bragg condition. This means that subsequent reflections, instead of being in phase, will differ from each other by a phase angle $2\pi p$. The total amplitude of the diffracted wave may be obtained by summing the reflections from N layers, yielding [8] ;

Equation 5-1

$$S = A\left|\sum_{l=1}^{N} e^{il2\pi p}\right| = A\left|\frac{\sin(Np\pi)}{\sin(p\pi)}\right|$$

where A is the reflection from each layer. For no dephasing, ie. perfect conditions with p = 0, it follows that $S=NA$. As the dephasing increases, the value of S decreases, reaching zero at $Np=1$. In the case of Bragg gratings the number of grating planes, N, is give by ; $N = \frac{d\tan\theta}{\Lambda}$ where d is the length of the grating, θ the internal incident angle and Λ the grating period. It then follows that the diffraction efficiency will fall to zero when ; $p = \frac{1}{N} = \frac{\Lambda}{d\tan\theta}$. Therefore for a typical Bragg grating modulator used in this work of length 3cm and grating period 70μm operating at 633nm, the fractional bandwidth comes out to be 1.16% which is very narrow. In practice the beam divergence and poling defects result in deviations greater than this fractional bandwidth and thus reduce the diffraction efficiency. To reduce this effect beam expanding and focussing techniques should be optimised to minimise the beam divergence in the grating. To improve the accuracy in grating period improved material quality is required to produce better quality gratings as discussed in Chapter 3.

5.2.3.3 Parasitic higher diffraction orders

The Kogelnick based theoretical model predicts diffraction only into the first Bragg diffraction order, however higher order spots are seen experimentally. Figure 5.12 shows a graphical representation of the Bragg condition in terms of the grating and wave K vectors.

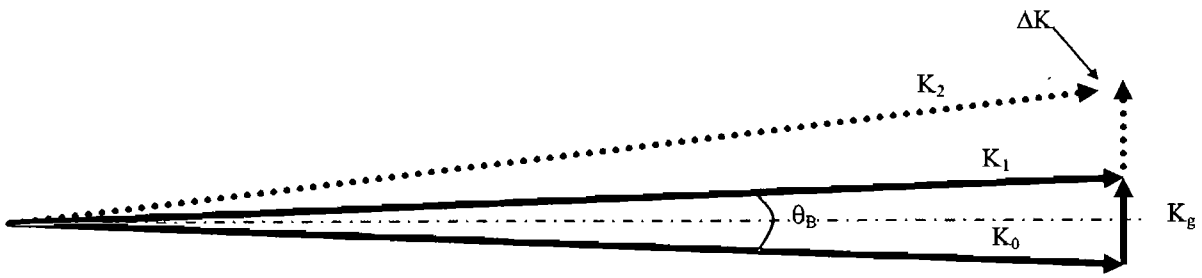

Figure 5.12 Schematic of Bragg condition in terms of K vectors (not to scale)

At the Bragg angle, θ_B, there is a perfect match between the K vectors of the incident wave, K_0, the diffracted wave, K_1, and the grating, K_g. The second Bragg diffraction order is represented by K_2, which does not form a perfect match with the second multiple of the grating. However, if the difference, ΔK, is very small then there may be some inefficient diffraction into the second order, which would reduce the diffraction efficiency in the first order. To minimise this effect ΔK should be maximised, ie. increase K_g as much as possible. This corresponds to gratings of smaller grating period, Λ, according to $K_g = \frac{2\pi}{\Lambda}$.

5.2.3.4 Field induced scattering

Another phenomenon found was that higher field maxima, corresponding to higher orders in the argument of Equation 4-24 [π, 3π, 5π...], exhibit lower diffraction efficiencies, as can clearly be seen in Figure 5.3. It was also found that generally the diffraction efficiencies achieved when operating in the infrared were consistently lower than for visible operation. New field induced light scattering effects were seen at increased drive voltages. These scattering effects were seen to increase for infrared operation, which requires higher on/off voltages than those for visible operation.

During operation at 633nm it was clearly seen that at higher voltages the general background scatter was increased. This can be seen in Figure 5.13 which shows two photographs of the output spots at *a)* a low voltage first order diffraction peak of 30V and *b)* a high voltage peak of 170V. The increase of background scatter can clearly be seen.

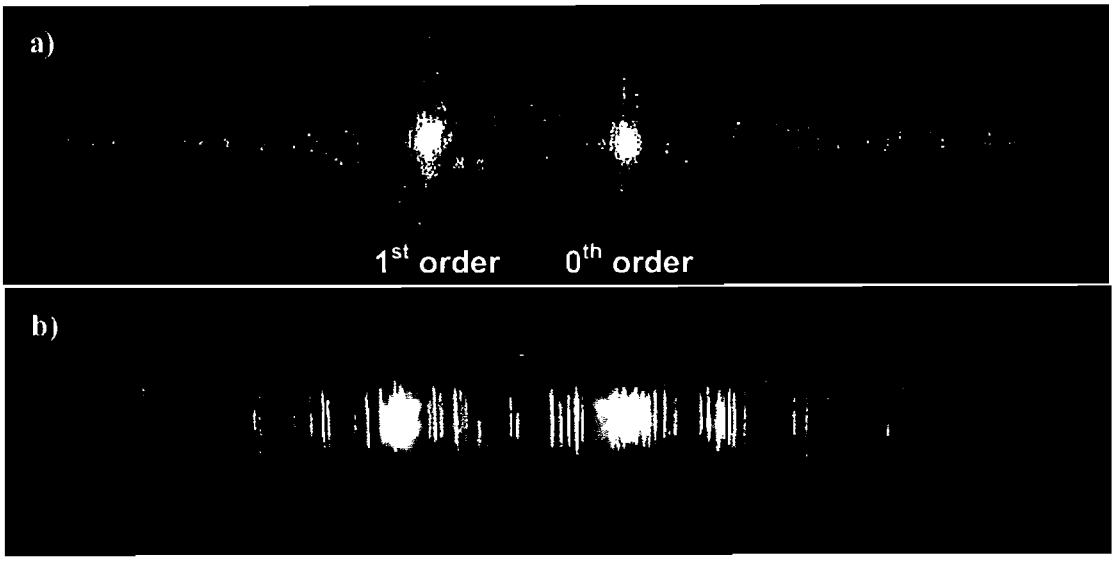

Figure 5.13 Photographs of output spots at a) low voltage peak and b) high voltage peak

To investigate the power redistribution phenomenon at increased drive voltages into higher order Bragg spots and to measure general scatter and beam degradation, angularly resolved beam measurements were made. A line scan with angle was taken across the output power at each of the peaks in first order diffraction for e-polarised light, corresponding to applied voltages of +45V, -90V and -220V. Figure 5.14 shows these line scans at 1064nm plus scans taken for the same device operating at 633nm. It can be seen that at higher voltages the diffraction efficiency is clearly reduced and there is increased power into other orders and into the general background. The output beam quality is clearly degraded. The scattering and beam degradation in the poled regions is dramatically stronger than in reference areas under the same applied field. Thus we can confidently associate this scatter with the poling process used to fabricate the gratings. Removing the problem of field induced scattering requires better quality lithium niobate material resulting in better quality poling. Again we turn to crystal growers for developments in growth and fabrication techniques. However we can take steps to reduce this problem by choosing the device operating parameters which result in lower on / off drive voltages, ie. operation at shorter wavelengths, using e-polarised light, and using longer devices.

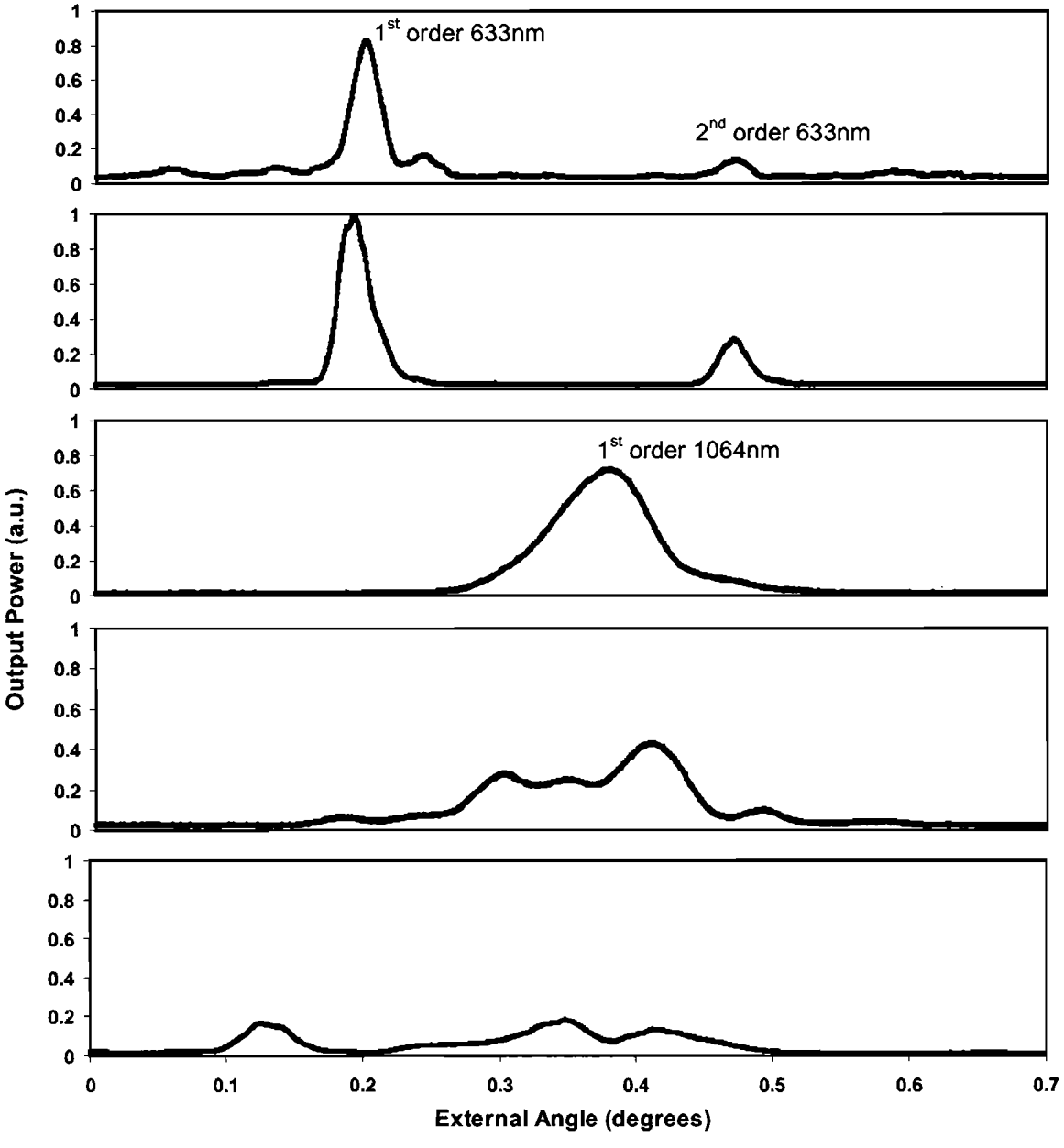

Figure 5.14 *Line scans of output at peaks of maximum diffraction into the first order for e-polarised light, showing;*

a) visible light (633nm) at low field peak of -40V/mm,

b) visible light (633nm) at high field peak of -160V/mm,

c) infra-red light (1064nm) at low field peak of +90V/mm,

d) infra-red light (1064nm) at medium field peak of -180V/mm

and e) infra-red light (1064nm) at high field peak of -460V/mm

5.2.3.5 *Grating profile assumption*

Another possible reason for the discrepancies between the experimental data and the theoretical analysis is the assumption in the theoretical analysis that the profile of the diffraction grating is a sine wave. In the case of a poled grating, the profile is not sinusoidal, it instead follows a square wave. A square wave can be represented by a series of sinusoids gratings of period; Λ, $\Lambda/3$, $\Lambda/5$, $\Lambda/7$,... which also decrease in intensity by $\frac{1}{3}, \frac{1}{5}, \frac{1}{7}$,... If we only consider the first component of this series, for n =1, then we obtain a sinusoidal grating profile as in the case of Kogelnik's theory. This is a semi-reasonable assumption as this component is the greatest in intensity and is the only grating component with the period required for Bragg matching. However to get a true theoretical model of the diffraction in the device, we cannot ignore the influence of the other grating components. Although not Bragg matched, they will still provide some diffraction and scatter in the device and therefore reduce the diffraction efficiency of the device. Therefore a full coupled wave theoretical solution is required for square gratings, but this is not a simple approach as multiple angles and beams from each of the grating planes must be taken into consideration. The following Section provides initial work carried out towards obtaining a theoretical model for square gratings.

5.3 Alternative theoretical analyses

Prior to the advent of volume holography [9], elementary theories of wave propagation in periodic media had been developed separately to describe the diffraction of light by ultrasonic gratings [10,11,12], the diffraction of X-rays by crystals [13,14] and electron diffraction [15]. From the studies into volume holography, two main theoretical models were developed. The analysis of ultrasonic gratings gave rise to the coupled wave theory, the best known being that of Kogelnik [1] whose 1969 paper received widespread acclaim. In their book, 'Volume Holography and Volume Gratings', Solymar and Cooke [8] develop a coupled wave theory for higher order modes. The coupled wave theory is probably the more frequently used of the two models due to its simplicity and versatility. Alongside this

an alternative approach was developed based on the dynamic theory used to explain X-ray and electron diffraction, known as the diffraction equation theory [16,17,18].

These theoretical approaches provide good approximations for diffraction from a grating, however as seen in Section 5.2 discrepancies appear between experimental and theoretical results. One major cause of this is the assumption that the grating profile follows a sinusoid. A second cause is that the diffraction theory based on scattering cannot deal with coupled waves, and thus is not applicable to high reflectivities. This is not too much of a problem provided that it is understood that this theory gives valid answers for predicting the angles of non-Bragg matched scattering spots but does not allow accurate calculation of the strength of these scattering spots. Indeed the theory will generally tend to under predict the strength of these non-Bragg matched scattering spots. The rest of this Section describes work done to develop a numerical theoretical model for a square wave grating profile.

5.3.1 Background theory

Consider the point scatterer shown in Figure 5.15, at position $\underline{r} = x\underline{i} + y\underline{j}$ and of scattering amplitude *A(θ)*, dependent on the Fresnel Equations. The amplitude of the scattered wave at an angle ϕ from an incident wave θ is given by [19];

Equation 5-2

$$S(\theta,\phi) = A(\theta)e^{i\underline{r}\cdot(\underline{k}-\underline{k}')}$$

where $\underline{k}$ is the k vector of the incident wave and $\underline{k}'$ is the k vector of the diffracted wave, with ;

Equation 5-3

$$\begin{aligned}\underline{k} - \underline{k}' &= |k|(\underline{n} - \underline{n}') \\ &= \frac{2\pi}{\lambda}(\underline{n} - \underline{n}') = \frac{2n\pi}{\lambda}\left[(\sin\theta\underline{i} + \cos\theta\underline{j}) - (-\sin\phi\underline{i} + \cos\phi\underline{j})\right] \\ &= \frac{2n\pi}{\lambda}\left[(\sin\theta + \sin\phi)\underline{i} + (\cos\theta - \cos\phi)\underline{j}\right]\end{aligned}$$

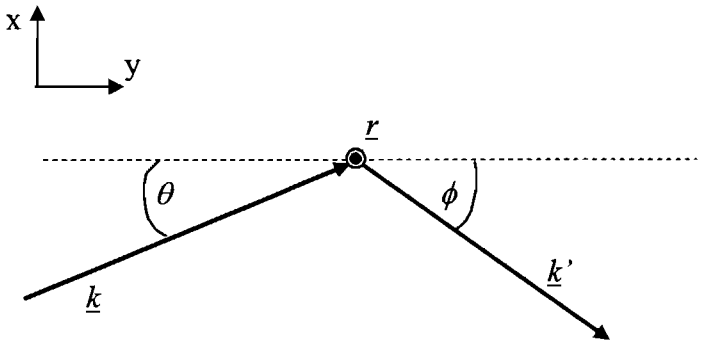

Figure 5.15 Schematic of a point scatterer

Therefore the scattering intensity of the point source at an output angle ϕ is given by ;

Equation 5-4

$$S(\theta,\phi) = A(\theta) e^{i\frac{2n\pi}{\lambda}[x(\sin\theta+\sin\phi)+y(\cos\theta-\cos\phi)]}$$

Now consider the total amount of scatter at a given output angle ϕ for a line of scatterers along the y axis, for example one grating plane, and integrating the above equation along y for a grating plane d in length gives ;

$$S(\theta,\phi) = A(\theta) \int_{y=0}^{d} e^{i\frac{2n\pi}{\lambda}[x(\sin\theta+\sin\phi)+y(\cos\theta-\cos\phi)]} dy$$

Equation 5-5

$$= A(\theta) e^{i\frac{2n\pi x}{\lambda}(\sin\theta+\sin\phi)} \cdot \left[\frac{\lambda}{i2n\pi(\cos\theta-\cos\phi)} \left(e^{\frac{i2n\pi d}{\lambda}(\cos\theta-\cos\phi)} - 1 \right) \right]$$

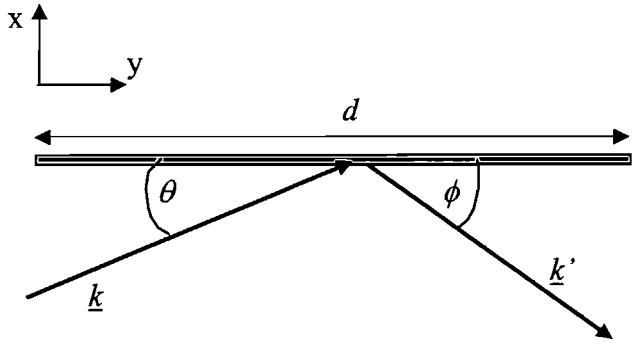

Figure 5.16 Schematic of a line of scatterers

Consider a number of these line scatterers, for example in a grating, then by summing Equation 5-5 for each of the grating planes at $m\Lambda$, where Λ is the grating period and m is an integer 0,1,2..., for $m\Lambda < w$, the grating width. As this must be done numerically, a MATLAB program was created to calculate the result, Appendix I.

Now we look at evaluating the scattering amplitude $A(\theta)$. The scattering mechanism in the case of the Bragg grating modulators is an interface in refractive index. The strength of the diffraction is given by the Fresnel equations which describe the behaviour of light at an interface of refractive index [19];

Equation 5-6

$$r_{\perp} = -\frac{\sin(\theta_i - \theta_t)}{\sin(\theta_i + \theta_t)} \qquad t_{\perp} = +\frac{2\sin\theta_t \cos\theta_i}{\sin(\theta_i + \theta_t)}$$

$$r_{\text{II}} = +\frac{\tan(\theta_i - \theta_t)}{\tan(\theta_i + \theta_t)} \qquad t_{\text{II}} = +\frac{2\sin\theta_t \cos\theta_i}{\sin(\theta_i + \theta_t)\cos(\theta_i - \theta_t)}$$

where $r_{\perp}$ is the reflectance for E perpendicular to the plane of incidence, and r_{II} is the reflectance for E parallel to the plane of incidence (the angles are measured from the normal to the interface). From Figure 5.17 it can be seen that $r_{\perp}$ corresponds to e-polarised light and r_{II} corresponds to o-polarised light.

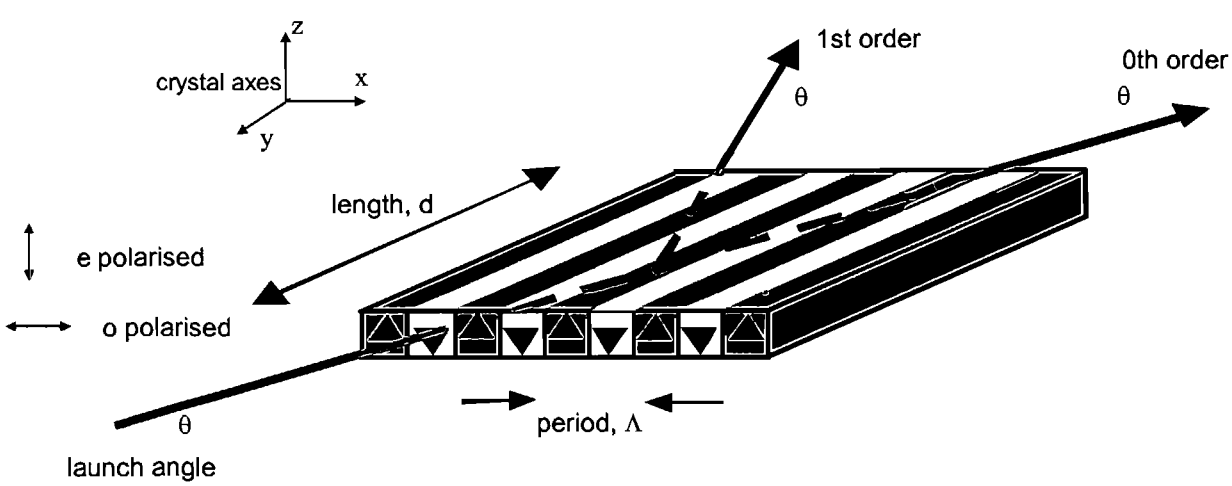

Figure 5.17 Schematic of Bragg grating modulator

It is at this point that the theoretical analysis begins to encounter restrictions. As the Fresnel equations hold only for $\theta_r=\theta_i$, the theoretical analysis is therefore limited to incident angles equal to the Bragg angle. Investigation of off-Bragg incidence is out with the scope of this thesis.

Another point to note is the presence of diffraction components from both the high to low *and* low to high refractive index interfaces. One occurs at spacing $m\Lambda$ and the other at $\left(m+\frac{1}{2}\right)\Lambda$. Both these are taken into consideration in the MATLAB program. The program also encompasses the differing incident angle, θ, in the high and low refractive index regions due to refraction at the interfaces.

5.3.2 Simulations

The MATLAB program was designed to output two graphs, for e- and o-polarised incident light, showing intensity with output angle for a given set of device and operating parameters which are written to a text file. A typical set of outputs is given in Figure 5.18 with the device and operating specifications indicated in the 'Specifications data file'.

5.3.3 Analysis

From the results it can be clearly seen that maximum diffraction occurs at the Bragg angle, however it can also be seen that light is diffracted into other output angles. This is made even clearer on a log scale,

Figure ***5.19***, as this is more akin to the response of the human eye. Furthermore, as explained earlier the theory tends to under estimate the strength of scattering away from the Bragg angle as the main Bragg peak shows saturation of reflection at high coupling whereas higher orders are unlikely to couple back into the main peak, so that the measured higher orders will tend to be stronger than predicted by the theory. This prediction of diffracted light at angles other than the Bragg angle ties up with observations made during experimental measurements. Other interesting features which were also seen in the practical work include the periodic structure of the output light intensity and the asymmetric nature of the output around the Bragg angle.

As expected, the theory also confirms that changing the grating period or incident wavelength results in a change in the Bragg angle required for maximum diffraction. When the device length was varied, the periodic structure in the output intensity was seen to be affected. This effect was not studied in practice, but would be an interesting investigation to perform in the future.

```
Specifications data file
........................

Width Grating, W              1.000000    mm
Length Grating, d             3.000000    cm
Wavelength in air             1064.000000 nm
Applied voltage, V            200.000000  V
Grating Period                70.000000   microns
Ordinary refractive index     2.240000
Extraordinary refractive index 2.160000

Phi start                     0.000000    degrees
Phi end                       0.500000    degrees
Phi Step                      0.001000    degrees
Internal incident angle       0.201597    degrees

The calculated internal Bragg Angle for these variables is 0.201597 degrees
```

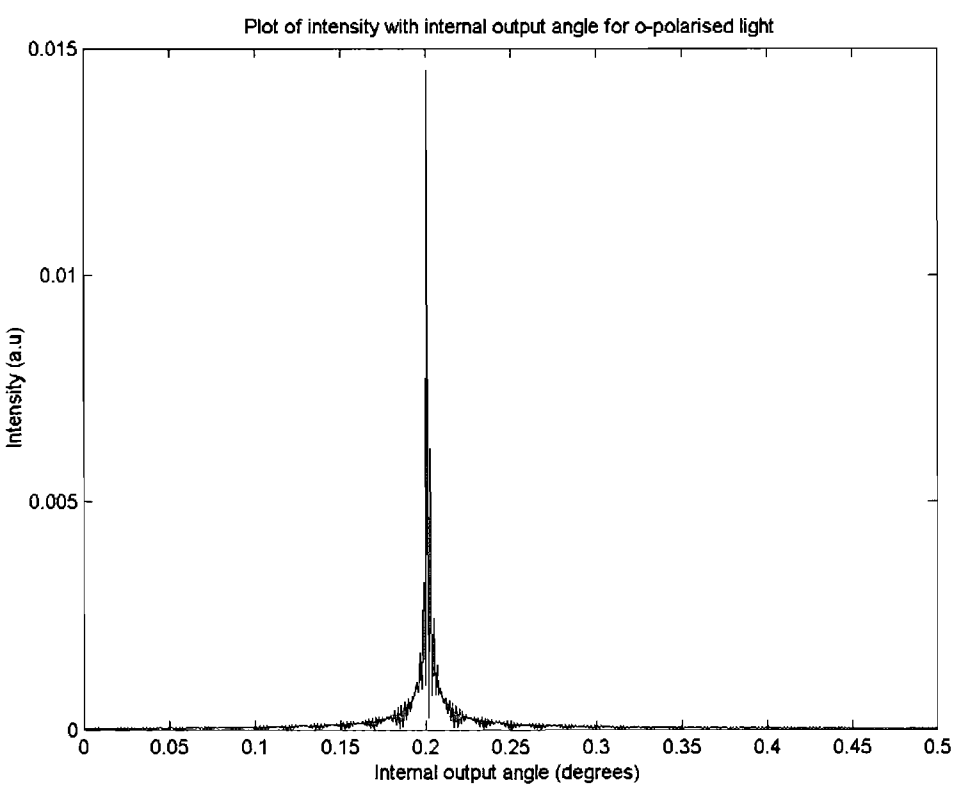

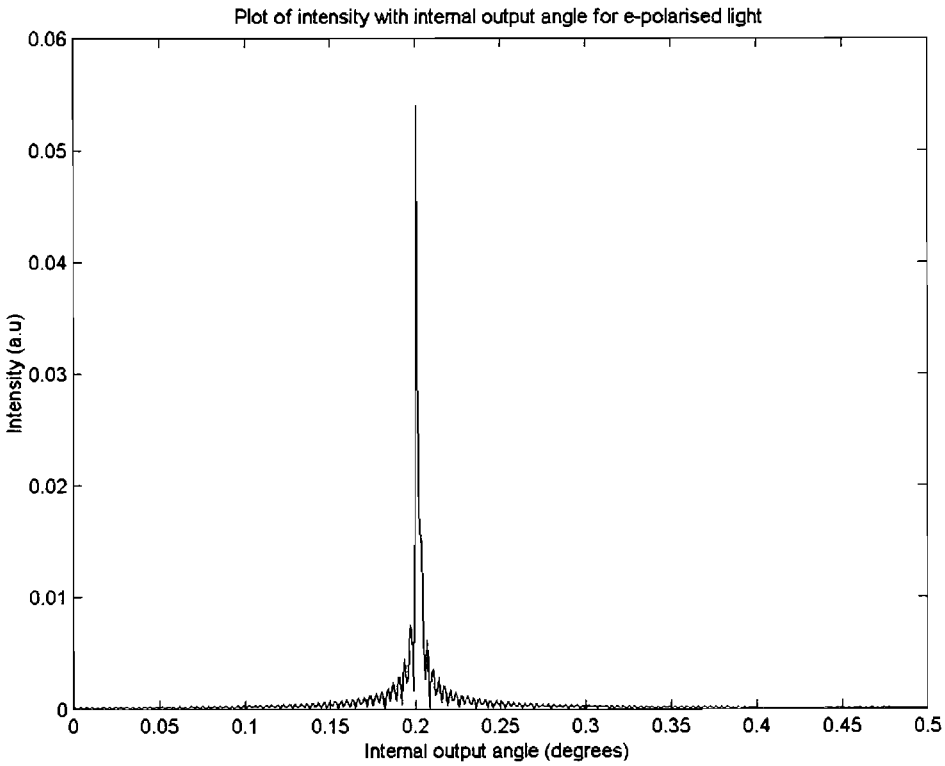

Figure 5.18 Typical set of outputs from MATLAB program

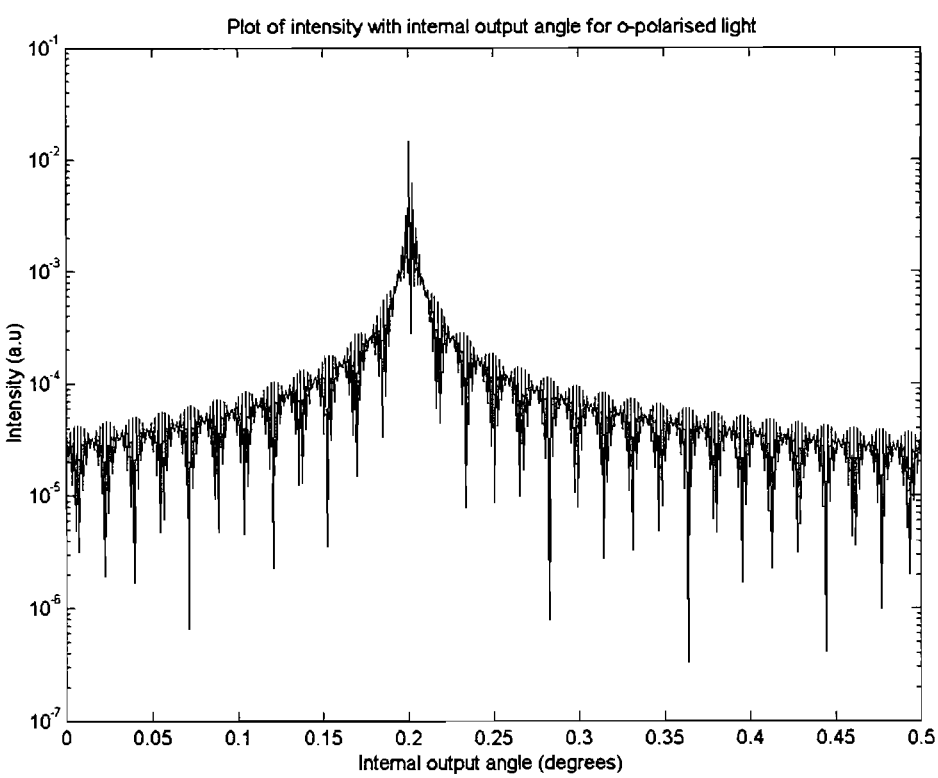

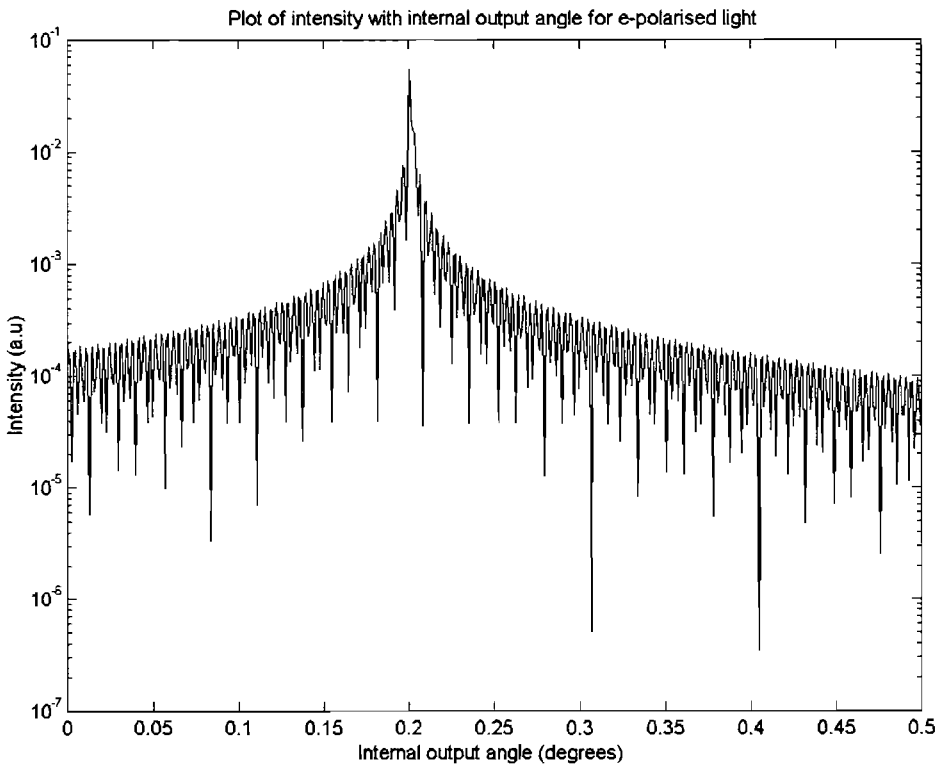

Figure 5.19 Intensity with output angle on a log scale for previous variables

5.3.4 Conclusions

This basic theoretical model is the first step to obtaining a more accurate representation of the complex processes taking place in the Bragg grating modulator devices. It shows diffraction into angles other than the Bragg angle, and can be used to model intensity with output angle for any set of device and operating parameters. However it does not allow investigation of imperfections in the gratings, variations in grating period across the device, non-straight domain walls, angular bandwidth of the incident beam or off-Bragg incidence, which are all critical to achieving a full understanding of these devices. Modelling these variations is not a simple process and is out with the scope of this thesis. Future work will involve investigating the possibility of developing the MATLAB program and theory to take these into account.

5.4 Chapter conclusions

This Chapter has further investigated the operation of Bragg grating modulators to better understand the discrepancies found between experimental and theoretical results. Results for operation in the visible region were presented, including a discussion of the photorefractive damage seen during 488nm operation. Anomalies seen by other groups were also seen in the results presented in this thesis, along with new phenomena. These phenomena were studied in greater detail and methods of preventing or alleviating their effects were presented, including device annealing and restricting operating conditions. Although Bragg grating modulator devices based on periodically poled lithium niobate have a high degree of flexibility in design choices and operating parameters, as any set of wavelength, grating period and incident angle which satisfy the Bragg condition may be used, it has been shown that for optimum device performance there are some operating restrictions. These favour visible operation, e-polarised light and longer device lengths resulting in lower on / off voltages and shorter grating periods which help to decrease the photorefractive effect and increase ΔK.

It has also been shown that it is the material quality that is the overriding restriction in device performance. Several of the factors causing degradation in the device performance are related to poling defects resulting from poor quality material. To alleviate these problems better quality lithium niobate material must be used, resulting in improved poling quality. Using stochiometric material also offers the potential for better devices [7].

A new theoretical approach was explored based on diffraction from planes rather than the coupled wave analysis used by Kogelnick. This model starts to explain some of the anomalies seen during experimental measurements, however it does not fully describe the inevitable random errors in real devices or the complexity of dealing with fully coupled equations to describe the square-step index profile of a real devices.

5.5 References

[1] H Kogelnik *'Coupled wave theory for thick hologram gratings'* *The Bell System Technical Journal* **48** no.9 p2909-2947 (1969)

[2] M Yamada, M Saitoh and H Ooki *'Electric-field induced cylindrical lens, switching and deflection devices composed of the inverted domains in $LiNbO_3$ crystals'* *Appl Phys Lett* **69** p3659-3661 (1996)

[3] M Yamada *'Electrically induced Bragg-diffraction grating composed of periodically inverted domains in lithium niobate crystals and its application devices'* *Rev. Sci. Inst.* **71** no.11 p4010-4016 (2000)

[4] H Gnewuch, C N Pannell, G W Ross, P G R Smith and H Geiger *'Nonosecond response of Bragg deflectors in periodically poled $LiNbO_3$'* *IEEE Photonics Tech Lett* **10** p1730-1732 (1998)

[5] M Taya, M C Bashaw and M M Fejer *'Photorefractive effects in periodically poled ferroelectrics'* *Opt. Lett.* **221** p857 (1996)

[6] V Bermudez, J Capmany, J G Sole and E Dieguez *'Growth and second harmonic generation characterization of Er^{3+} doped bulk periodically poled $LiNbO_3$'* *Appl. Phys. Lett.* **73** (5) p593 (1998)

[7] K Kitamura, S Takekawa, M Nakamura and Y Furukawa *'Commercialisation of stoichiometric $LiNbO_3$ and $LiTaO_3$ for optical devices'* *CLEO/PR July 2001* WH2-1

[8] L Solymar and D J Cooke *'Volume Holography and Volume Gratings'* Academic Press Inc (London) Ltd. (1981)

[9] Y N Denisyuk *'Photographic reconstruction of the optical properties of an object in its own scattered radiation field'* *Sov. Phys. Dokl.* **7** p543-545 (1962)

[10] L Brillouin *'Diffusion de la lumiere et des rayons X par un corps transparent homogene influence de l'agitation thermique'* *Ann. De Physique* **17** p88-122 (1922)

[11] P Deybe and F W Sears *'On the scattering of light by supersonic waves'* *Proc. Nat. Acad. Sci.* **18** p409-414 (1932)

[12] C V Raman and N S N Nath *'The diffraction of light by high frequency sound waves'* *Proc. Ind. Acad. Sci* **A2** *[Part 1]* p406-412, *[Part 2]* p413-20 (1935), *[Part 3]* **A3** p75-84, *[Part 4]* p119-125 and *[Part 5]* p459-465 (1936)

[13] J M Bijvoet, W G Burgers and G Hagg (Editors) *'Early papers on the diffraction of X-rays by crystals'* Utrecht (1962)

[14] P P Ewald *'Fifty years of X-ray diffraction'* Utrecht (1962)

[15] C J Davisson and L H Germer *'Diffraction of elevtrons by a crystal of nickel'* *Phys. Rev* **30** p705-740 (1927)

[16] P P Ewald *'Zur Begrundung der Kristalloptik' Ann. Phys. (Leipzig) [Part 1]* **49** p1-38, *[Part 2]* p117-143 (1916), *[Part 3]* **54** p519-597 (1917) and *[Part 4]* **56** p129-156 (1921)

[17] B W Batterman and H Cole *'Dynamical diffraction of X-rays by perfect crystals' Mod. Phys.* **36** p681-717 (1964)

[18] E J Saccocio *'Application of the dynamical theory of X-ray diffraction to holography' J. Appl. Phys.* **38** p3994-3998 (1967)

[19] E Hecht *'Optics' Addison-Wesley Publishing Company* Second Edition (1987)

Chapter 6

Titanium indiffused waveguides in periodically poled lithium niobate

Optoelectronic devices are used extensively for signal generation, transmission and processing in telecommunications and many other applications. An optical waveguide on a planar substrate is a basic component for many integrated optical devices such as switches, modulators and filters and can be manufactured by many different processes using a large variety of materials as substrates and dopants.

This Chapter describes the work carried out to integrate titanium indiffused waveguides and PPLN for use in harmonic frequency conversion. Different types of nonlinear waveguides are reviewed in Section 6.1 with titanium indiffusion shown to exhibit several potential advantages over other methods such as proton exchange and direct bonding. The mechanics of titanium diffusion in lithium niobate is discussed in Section 6.2, and a simple theoretical diffusion model developed in Section 6.3. Titanium waveguide fabrication and characterisation are described in Sections 6.4 and 6.5 and include investigations into fabrication issues such as spontaneous poling and lithium outdiffusion.

The research carried out to investigate the integration of titanium indiffused waveguides and periodically poled lithium niobate is described in Section 6.6. Although fundamental steps in the fabrication procedures suggest that these two techniques are incompatible, experimental work is presented which endeavours to overcome these problems by adapting or altering the fabrication processes.

The final Section in this Chapter presents results achieved in a successful Ti:PPLN device for third order second harmonic generation of 416nm light in a 12μm wide titanium waveguide running through an 8.7μm period PPLN grating.

6.1 Nonlinear optical waveguides

Optical waveguides are ideal for nonlinear interactions because they provide strong beam confinement over long propagation distances. Waveguides are characterised by regions of high refractive index bounded by regions of lower index and can be categorised as planar, channel and fibre guides. The first guided wave nonlinear experiments were on second harmonic generation in planar GaAs structures [1].

These early experiments took advantage of existing planar thin film and microlithography techniques. Progress in this area of nonlinear guided wave optics has concentrated on harmonic generation and parametric amplification, which utilise the large χ^2 obtained in noncentrosymmetric waveguides [2]. However, during the past few years there has been a great deal of interest in all optical signal processing, which has stimulated work on third order processes in integrated optics [3]. This evolution is in sharp contrast to the case of fibre nonlinear optics in which the materials used for optical fibres do not lead to noncentrosymmetric fibre cores and hence there is no second harmonic activity. However, for fibres the propagation losses are so low that the small third order nonlinearities in glasses could be compensated for by the long interaction length, and many third order processes were reported [4,5]. The initial experiments concentrated on phenomena such as stimulated Raman and Brillouin scattering and on self phase modulation.

The recent development of specialised fabrication techniques for producing single crystal core fibres [6] and the fortuitous discovery of SHG in some glass fibres [7] have extended nonlinear fibre research into efficient χ^2 processes. In the ORC, frequency conversion has been achieved in silica and germanosilicate optical fibres [8,9].

By combining channel waveguides and PPLN [10] we exploit the advantages of both PPLN and waveguide technologies to create nonlinear devices with higher efficiencies and lower pump thresholds than bulk PPLN. Waveguides have been recently used in combination with PPLN for frequency conversion at long wavelengths [11,12,13], for WDM channels [14] and in cascaded fibre nonlinearity [15].

For many applications in nonlinear optics for telecommunications it is highly desirable to have a waveguide geometry, firstly because of their compatibility with an optical fibre mode profile, but also because the high degree of optical confinement allows high peak power densities whilst overcoming diffraction. This is means that highly efficient nonlinear processes can be achieved with efficiencies approaching $500\%W^{-1}cm^{-2}$ [16].

To date the principle methods for producing waveguides in PPLN have been proton exchange, pioneered at Stanford [16] and by de Michelli in Nice [17], titanium indiffusion which was first demonstrated at the ORC [10] and more recently developed by Sohler's group at Paderborn [11], and direct bonding first demonstrated at the ORC [18]. Although attractive because the waveguide core is unmodified, direct bonding does not readily lead to channel waveguides and so the first two techniques are to be preferred.

In proton exchange the guides are formed by an exchange process in either phosphoric or benzoic acid at a temperature of up to 250°C. The guides are low loss, but unless carefully annealed lose a great deal of nonlinearity. Only one component of the refractive index increases in proton exchange, (Δn_e ~0.12, Δn_o ~-0.04), and so for the particular waveguide geometry used in this research, only e-polarised light would be guided, unless a complex double exchange process was used. This would prevent access to the large d_{33} coefficient in QPM. There is little evidence of photorefractive damage beyond that habitually found in bulk PPLN, although the long term stability of the devices is not known, particularly as the elevated temperatures at which PPLN is often used (100 to 200°C) are uncomfortably close to the proton exchange temperatures.

In titanium indiffusion the guides are formed by depositing a thin layer of titanium metal on the surface of the lithium niobate, which is then diffused at a temperature of around 1050°C for several hours to create a modified index region. The guides can be very low loss, and an increase in both ordinary and extraordinary refractive index (Δn_o ~0.01, Δn_e ~0.02), allowing guidance of both TM and TE modes. Photorefractive damage is generally higher in diffused waveguides, but titanium indiffusion does not degrade the nonlinearity in the way proton exchange does. The titanium indiffusion technique is routinely used in making telecommunication waveguides, can meet Bellcore standards and is compatible with high temperature (100 to 200°C) usage.

Each of these waveguide fabrication techniques has merits and disadvantages, however the titanium indiffusion approach seems the most attractive to study for this work as it has the greatest potential for telecommunication compatible devices. Successful fabrication of titanium waveguides in PPLN requires good control of a number of complex processes. It is essential that each step has a high yield to give a reasonable overall chance of success. There are two main steps in the fabrication of Ti:PPLN waveguides; the diffusion of titanium in the lithium niobate substrate to create waveguides, and the poling of the sample for a given QPM period to create a PPLN structure. Both these processes are established research areas of their own, and are described fully in Chapter 3 and Section 6.2 , including full fabrication details. What is less obvious about the process is the order in which these two steps should be carried out, ie. the poling before or after the diffusion. These two processing methods and their conditions are in many ways not ideally compatible because of the high temperatures and the movement of ions associated with titanium diffusion.

6.2 Diffusion of titanium into lithium niobate

Titanium indiffusion is the most common and most well known method of creating waveguides in lithium niobate, however several physical points of the process are still not fully understood [19]. This Section reviews work done in this area to try to understand the precise mechanisms involved in the diffusion process of titanium into lithium niobate.

Firstly, it is unclear whether the diffusion path of titanium ions in the crystal is through Li and / or Nb sites. Some papers [20,21] suggest that Ti diffuses in through Nb sites, Hauer et al. [22] report Ti diffusion into Li sites for concentrations of 1.4 mol%, and recently Kollewe and Kling [23] proposed that Ti diffuses through Li sites if the titanium concentration is below 5.9 wt% and via Nb crystal sites if the concentration is in excess of this.

Secondly, several papers [24,25] have reported anisotropic diffusion of titanium into lithium niobate with lateral titanium spreads of up to 2.5 times the diffusion depth. However the experimental results of Holmes and Smyth [26] do not indicate any anisotropy for diffusion of titanium in lithium niobate, and explain the enhanced lateral diffusion beneath the crystal surface by lithium depletion or outdiffusion caused by the diffusion conditions. Further disagreement is presented by practical studies that show diffusion into hexagonal crystal lattices, such as the oxygen lattice of lithium niobate, is isotropic [27].

The third unknown part of the process is the behaviour at the interface between the deposited titanium and the lithium niobate substrate. During the initial stages of diffusion the titanium is readily oxidised to TiO_2. It is thought that this is followed by a phase reaction in which a surface compound is formed from the TiO_2 and various components in the lithium niobate [25]. Because of the high diffusivity of titanium in this surface compound, the surface layer is rapidly homogenised and thus initially acts as a continuous source of titanium. At some time, t_{dep}, this layer will have completely transformed from a separate compound to the structure of the surface phase, i.e. the deposited titanium is depleted. After t_{dep}, the diffusion process involves spreading of the titanium deeper into the lithium niobate substrate.

SIMS analysis [25] to detect $^{7}Li^{+}$ and $^{48}Ti^{+}$ in a diffused sample is shown in Figure 6.1. We can see that both profiles show peaks just below the surface, and also that Li^{+} increases with depth as Ti^{+} decreases with depth.

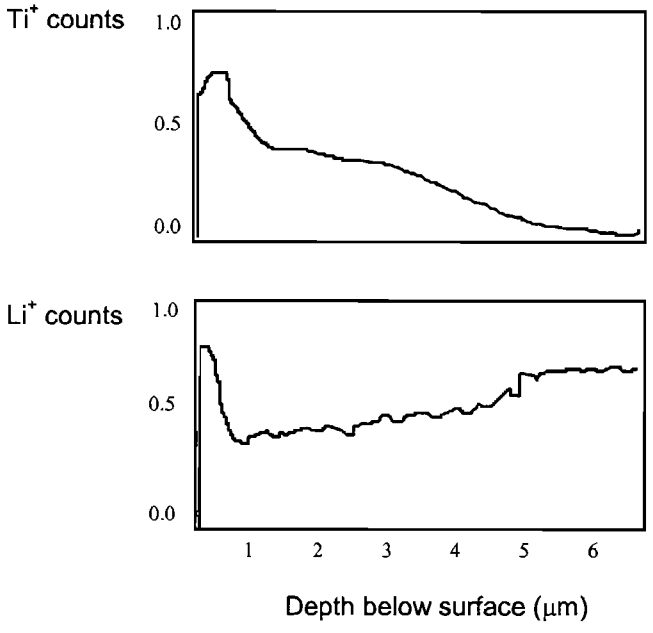

Figure 6.1 SIMS analysis of a titanium diffused lithium niobate sample, from [25]

This data would support the idea of a Li-Ti-O compound forming at the surface region. The exact composition of this compound depends on the ratio of TiO_2 and Li_2O present, and constitutes about 10% in the lithium niobate host. We can also see from Figure 6.1 that lithium outdiffusion occurs simultaneously with titanium indiffusion. Li_2O is lost from the lithium niobate to form Li-Ti-O compounds on the crystal surface, which acts as a source for titanium indiffusion and a barrier for lithium outdiffusion, leaving a lithium vacancy pool in the crystal near the surface. The Ti ions from the surface use these lithium vacancies to diffuse into the $LiNbO_3$. This may explain the apparent lateral diffusion, due to the high concentration of lithium vacancies present in the near-surface region. Lithium outdiffusion is a well known process, and some early waveguides in lithium niobate were made using this process [28]. However in many cases it is an unwanted effect and it may be prevented to a small extent by diffusing in a Li_2O rich atmosphere, or an oxygen atmosphere bubbled through H_2O. Another possible explanation of lateral diffusion is that crystal defects and ion vacancies at the crystal surface enhance titanium diffusion.

6.3 Channel waveguide diffusion model

This Section outlines a simple theoretical model of titanium diffusion into lithium niobate to create channel waveguides. This model allows sets of initial diffusion variables to be checked for validity and gives basic properties of the resultant diffused waveguide, such as waveguide depth. The second part of this Section briefly outlines a possible extension modelling process which would enable the resultant waveguide mode profile to be calculated from an initial set of diffusion variables.

6.3.1 Initial diffusion variables

To fabricate a titanium waveguide in lithium niobate, a strip of titanium, thickness *d*, width *2w* and length *l*, is deposited onto the z-cut lithium niobate substrate, as shown in Figure 6.2. This is then placed in an oven at temperature *T* °C, for time *t* hours, and allowed to diffuse.

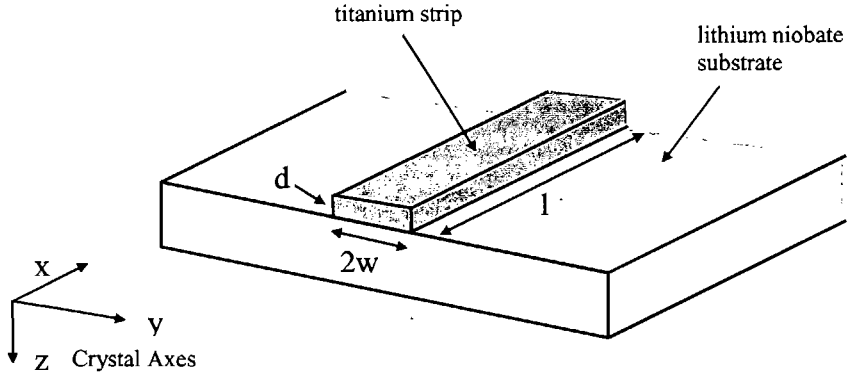

Figure 6.2 Deposited titanium strip

The thickness *d* determines the amount of titanium deposited, Ti_o, where Ti_o is related to the atomic density of solid titanium, 5.6×10^{28} atoms m^{-3}. The aim of the model is to determine the effect of these initial variables on the final titanium concentration profile.

The diffusion temperature and time are related to the diffusion coefficient, *D* (μm^2/hour), in the *x, y* and *z* directions by the equations ;

Equation 6-1

$$b_{x,y,z} = 2\sqrt{D_{x,y,z}t} \quad \text{and} \quad D_{x,y,z} = D_o^{x,y,z} e^{\left(-\frac{T_o}{T}\right)} = D_o^{x,y,z} e^{\left(-\frac{\varepsilon_a}{kT}\right)}$$

where b is the $1/e$ diffusion depth in μm, $D_o^{x,y,z}$ is the diffusion coefficients in the x, y and z directions at temperature T_o, where T_o is related to the activation energy, ε_a, as shown. By using previous experimental results [25,26,29], approximations can be made for $D_o^{x,y,z}$ (μm^2/hour) and ε_a (eV), and therefore values calculated for T_o (°K), $D_{x,y,z}$ (μm^2/hour) and b (μm) for particular values of time, t, and temperature, T.

6.3.2 Activation energy

The activation energy is composition dependent, as shown in Figure 6.3, with values ranging from 1.6 eV to 2.3 eV [25]. The lithium niobate wafers used in this research are congruent in composition, ie. they are 48.4% LiO by molar ratio [30]. From Figure 6.3, the corresponding value of activation energy for this composition is approximately 2.0eV, which is the value assumed for all further work.

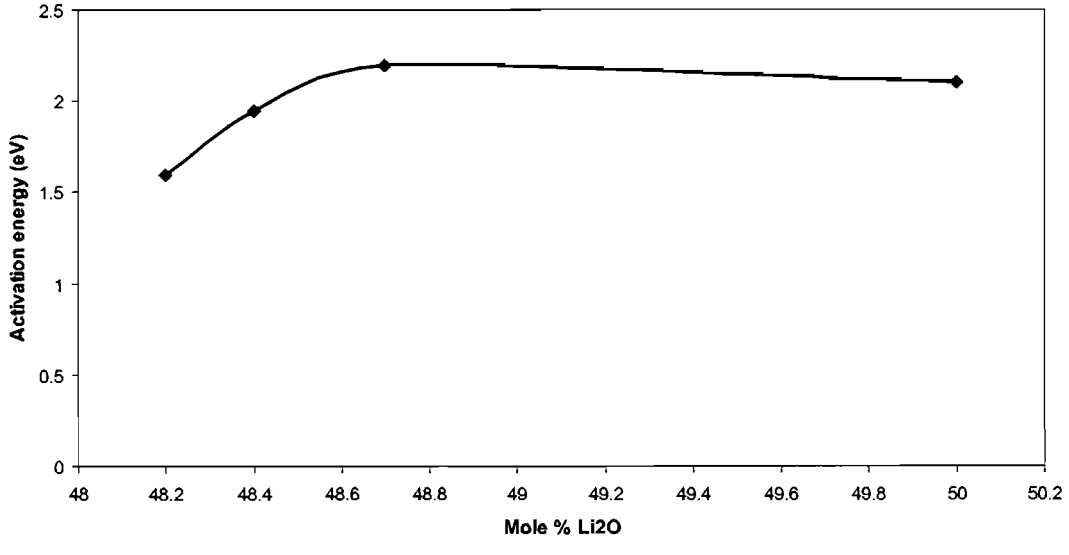

Figure 6.3 Activation energy as a function of composition [25]

6.3.3 Diffusion coefficient

Using the values for activation energy we can calculate T_o as shown in the table below, where k is Boltzman's constant, 1.38×10^{-23} J K^{-1}. Using Equation 6-1 we can then find a formula for the diffusion coefficient in terms of temperature, where the

initial diffusion coefficient in the z direction is 5.0×10^9 (μm^2 / hour) [29]. Figure 6.4 shows the diffusion coefficient against temperature for the maximum and minimum values of activation energy and for 2.0 eV.

Constant	Symbol	Congruent activation energy	Maximum value	Minimum value
Activation energy	ε_a	2.0 eV $= 3.204 \times 10^{-19}$ J	2.3 eV $= 3.6846 \times 10^{-19}$ J	1.6 eV $= 2.5632 \times 10^{-19}$ J
Initial temperature	$T_o = \varepsilon_a / k$	2.32×10^4 K	2.67×10^4 K	1.857×10^4 K
Diffusion coefficient	D_z ($\mu m^2 s^{-1}$)	$5.0 \times 10^9 e^{\left(-\frac{2.32 \times 10^4}{T}\right)}$	$5.0 \times 10^9 e^{\left(-\frac{2.67 \times 10^4}{T}\right)}$	$5.9 \times 10^9 e^{\left(-\frac{1.857 \times 10^4}{T}\right)}$

Table 6-1 Values of diffusion coefficient

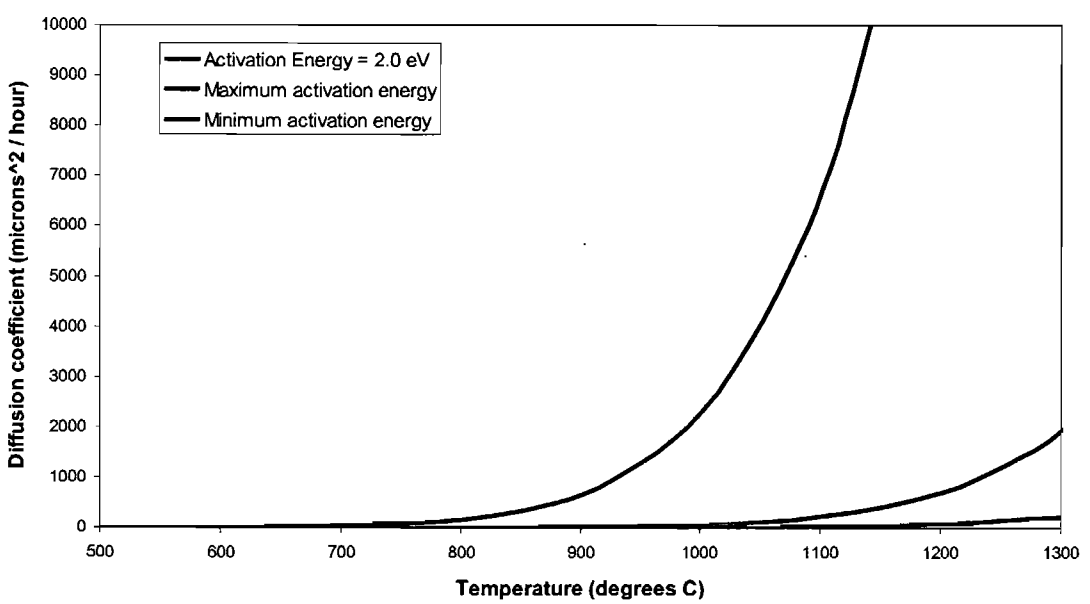

Figure 6.4 Diffusion coefficient with temperature

From Figure 6.4, we can see that the activation energy has a large effect on the resultant diffusion coefficient. As before, the material used in this work is assumed to have a material composition of 48.4% LiO, corresponding to an activation energy of 2.0 eV.

6.3.4 Diffusion depth

The diffusion depth for a non-depleted source can be plotted for varying temperature and time, Figure 6.5, using the values calculated with an activation energy of 2.0 eV. The diffusion time and temperature can therefore be determined by using this and the previous graph.

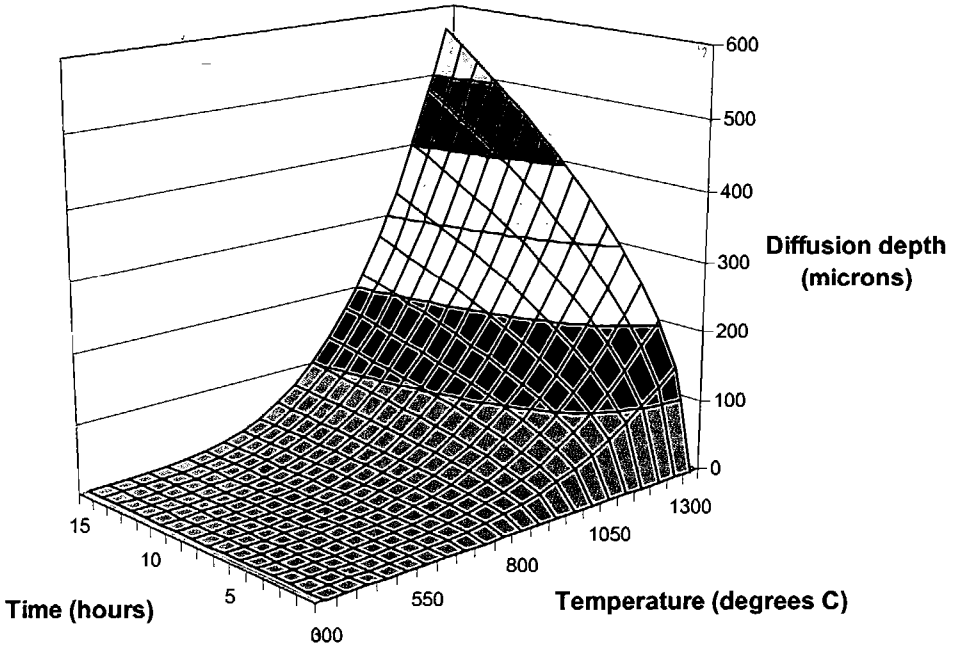

Figure 6.5 Diffusion depth with time and temperature for a non-depleted source

The above graph shows the theoretical diffusion depth for a non-depleted source with time and temperature, it does not take into consideration the case of a depleted source, as is more comparable to the experimental situation. For a depleted source it would be expected that the diffusion depth would be smaller than that predicted in Figure 6.5. Therefore to investigate the case of a depleted source an alternative theoretical model is needed, this is discussed in the following Section.

6.3.5 Possible modelling extension

Several authors present theoretical treatments of titanium diffused waveguides in lithium niobate, including Korotky et al. [31] who look at Ti:$LiNbO_3$ single mode strip waveguides, Bava et al. [32] who focus on Ti:$LiNbO_3$ channel waveguides in

integrated parametric oscillators and Koai et al. [33] who model Ti:$LiNbO_3$ channel waveguides used in directional couplers. In particular, the more general modelling of titanium in lithium niobate by da Silva et al. [34] and the completely general case of arbitrary optical diffused waveguides by Hocker and Burns [35] are of particular interest. The theoretical analysis in these papers provides optical mode profiles for a given set of diffusion variables and operating conditions. The basic process to achieve this is outlined below.

By solving the standard three-dimensional diffusion equation [36] using Fourier analysis, the concentration profile of the indiffused titanium dopant with time can be predicted for any particular set of initial diffusion variables. Appendix I outlines this calculation for the specific case of a depleted strip waveguide, as is the case for the devices fabricated within the scope of this research.

Using the concentration profile obtained the resulting refractive index profile of the Ti:$LiNbO_3$ waveguides can be calculated using the following equation :

Equation 6-2 $n_i(\lambda,T,y,z,t)=n_i(\lambda,T)+dn_i(\lambda,y,z,t)$ where λ is the wavelength and the subscript i is either 'o', referring to the ordinary crystal axis or 'e', referring to the extraordinary crystal axis. The first part of the equation is the wavelength dependent background index of lithium niobate as described by the Sellmeier equations (Chapter 2). The second term represents the refractive index change caused by the Ti^{4+} ions.

The index change due to the presence of titanium is different for the ordinary and extraordinary axis. For the extraordinary index, a linear dependence on titanium concentration $C(y,z,t)$ is assumed whereas the ordinary index shows a nonlinear refractive index change [37]. The second term of Equation 6-2 is given by :

Equation 6-3 $dn_i(\lambda,y,z,t)=d_i(\lambda)h_i(y,z,t)$ where $d_i(\lambda)$ accounts for the wavelength dependence of the refractive index change, approximated by means of a simple oscillator model in the infrared region [37]. After a comparison of the results given in literature, the following expressions were adopted by Strake et al. [38]:

Equation 6-4
$$d_e(\lambda)=\frac{0.839(\lambda)^2}{(\lambda)^2-0.0645} \qquad d_o(\lambda)=\frac{0.67(\lambda)^2}{(\lambda)^2-0.13}$$

The second part of Equation 6-3 is the titanium concentration dependant part, given by;

Equation 6-5 $h_o(y,z,t)=[E\times C(y,z,t)]^{\gamma}$ $h_e(y,z,t)=F\times C(y,z,t)$ where E, F and γ are material constants with the values [38], $E = 1.2\times10^{-23}$ cm^3, $F = 1.56\times10^{-22}$ cm^3 and $\gamma = 0.55$ at $\lambda \approx 633$nm.

Therefore for a Ti:$LiNbO_3$ waveguide with a known titanium concentration profile, $C(y,z,t)$, the refractive index profile could be calculated using the above equations for operation at a particular wavelength of light. The e- and o-polarised mode profiles can be found from the respective e- and o-polarised refractive index profiles for any set of initial variable, however this is outside the scope of this thesis. For this work the theoretical model serves to confirm the initial conditions that provide a basic starting recipe for titanium diffusion.

6.4 Waveguide fabrication

As comprehensively described in Chapter 3, extensive knowledge and expertise in poling lithium niobate exists in the ORC, however since the work of Amin [10], there has been no work on titanium diffusion in lithium niobate in this department. This Section describes the extensive investigation into the fabrication process for titanium diffused waveguides in lithium niobate to re-establish an optimum fabrication process for the devices described in the remainder of the Chapter.

The main variables in the fabrication of titanium diffused waveguides were the crystal face chosen for diffusion, thickness of titanium deposited, diffusion time and temperature. This Section describes the work done to optimise each one for low-loss, single mode waveguides in the infrared and blue regions of the electromagnetic spectrum.

The mask used to define the waveguides had a series of 10 waveguides of widths ranging from 3μm to 18μm at 100μm spacing. Initial parameters for titanium thickness, diffusion temperature and time were taken from previous work carried out in z cut lithium niobate [25,10], namely, 100nm of titanium deposited and diffused at 1050°C for 9 hours. A series of z cut, 500 μm thick, lithium niobate samples were diffused with titanium waveguides for different fabrication conditions. The resulting waveguides were then visually inspected under a microscope and comments noted.

Two types of waveguides were fabricated during trials, channel and planar waveguides. Both require slightly different fabrication processes as described below. All fabrication took place in class 1000 clean rooms at class 100 benches. Before any waveguide fabrication steps are carried out, the samples were thoroughly cleaned as described in Chapter 3.

6.4.1 Channel waveguides

The channel waveguides were patterned onto the sample surface using a lift-off photolithography technique. The samples were spun at 6000rpm for 1 minute with S1813 photoresist to produce a layer of photoresist of 1μm thick. The samples were then soft baked in an oven at 90°C for 35 minutes. A chrome on fused silica mask was used to image the channel waveguides onto the photoresist using a Karl Suss MA4 mask aligner with UV light, λ = 436nm for 7.5s. During developing, the samples were soaked in chlorobenzene for 5 minutes and then in developer for 5 minutes – much longer than normal photoresist developing. This extra step hardens the surface of the photoresist, producing an angled opening in the photoresist, aiding the removal of the excess titanium and photoresist after deposition, Figure 6.6. The titanium was then deposited under a vacuum of 4×10^{-6} Torrs. It was found that approximately 90nm of titanium was sufficient to produce single mode waveguides.

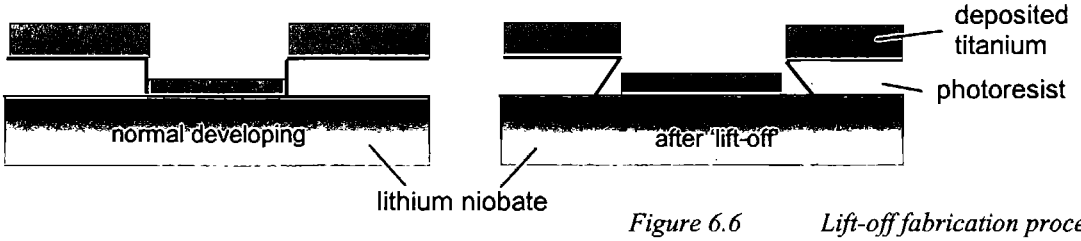

Figure 6.6 Lift-off fabrication process

The samples were then soaked in acetone in an ultrasonic bath for a few minutes to remove the photoresist and excess titanium, thus revealing the deposited titanium strips. The height profile of the titanium strips was then measured using a Tencor Alphastep, typical traces are shown in Figure 6.7.

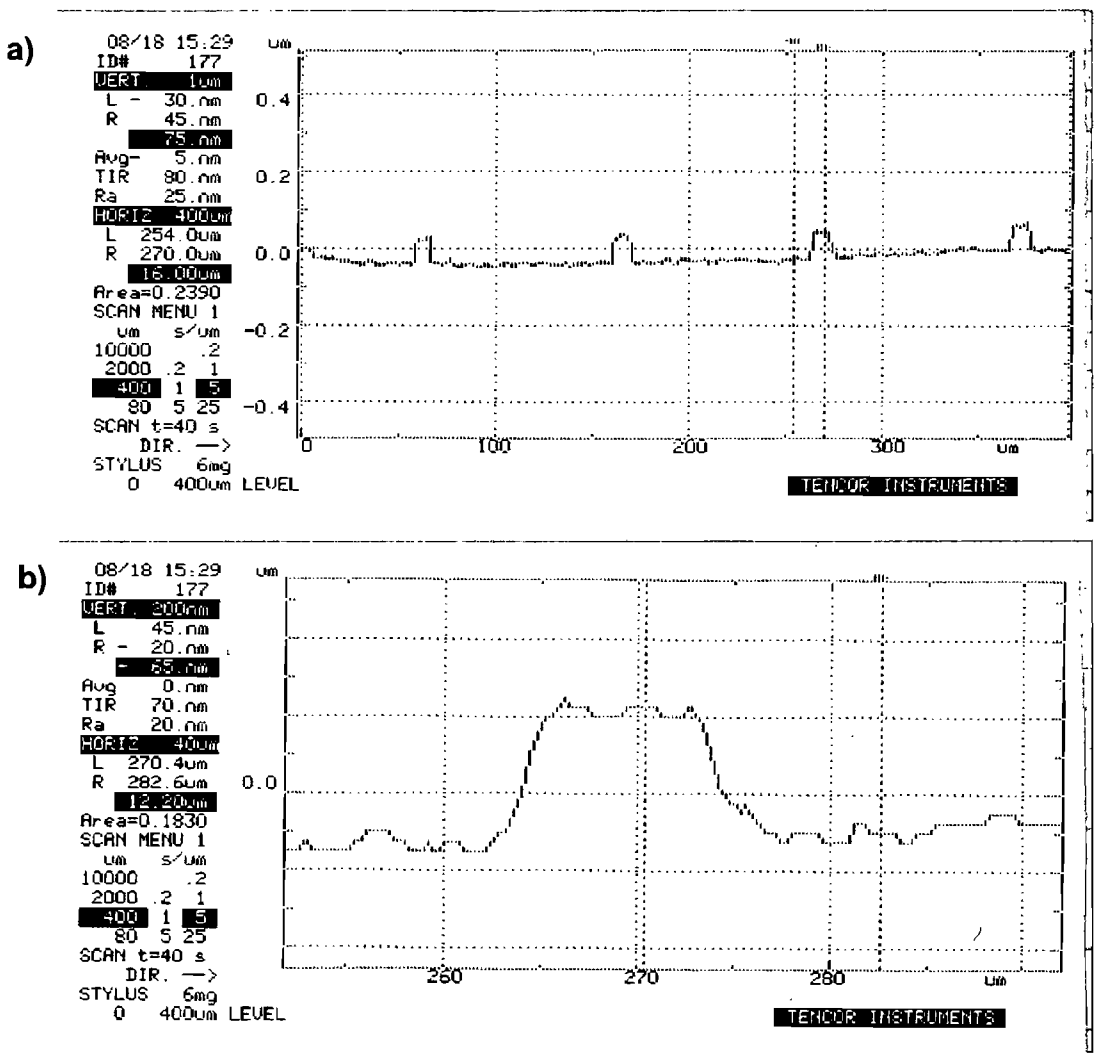

Figure 6.7 Alphastep profiles of a) four consecutive deposited titanium strips b) one titanium strip

6.4.2 Planar waveguides

No photolithography or lift-off was required for planar waveguides, after a standard cleaning as described in Chapter 3, titanium was deposited under a vacuum of 4×10^{-6} Torrs. Much less titanium was required compared to channel waveguides, and it was found that 25nm resulted in planar waveguides of reasonable mode profile when tested using a 1mW HeNe laser operating at a wavelength of 633nm.

6.4.3 Furnace diffusion

The titanium deposited samples were then diffused in a 70mm diameter single-zone Carbolite silica tube furnace. The furnace had a 10cm hot zone, ± 2°C at 1100°C. The diffusion parameters for the samples were taken from previous work, i.e. 1050°C for 9 hours [26,27,10].

The diffusion temperature quoted in all results presented in this thesis is the programmed temperature on the furnace. A temperature profile for 1200°C is shown in Figure 6.8. This was measured using a platinum rhodium thermocouple, with distances taken from the end of the hot zone, and the temperature was left to stabilise between each reading. Similar profiles were obtained for programmed temperatures of 1100°C and 1000°C, with the actual maximum temperature reaching approximately 80°C below the programmed temperature.

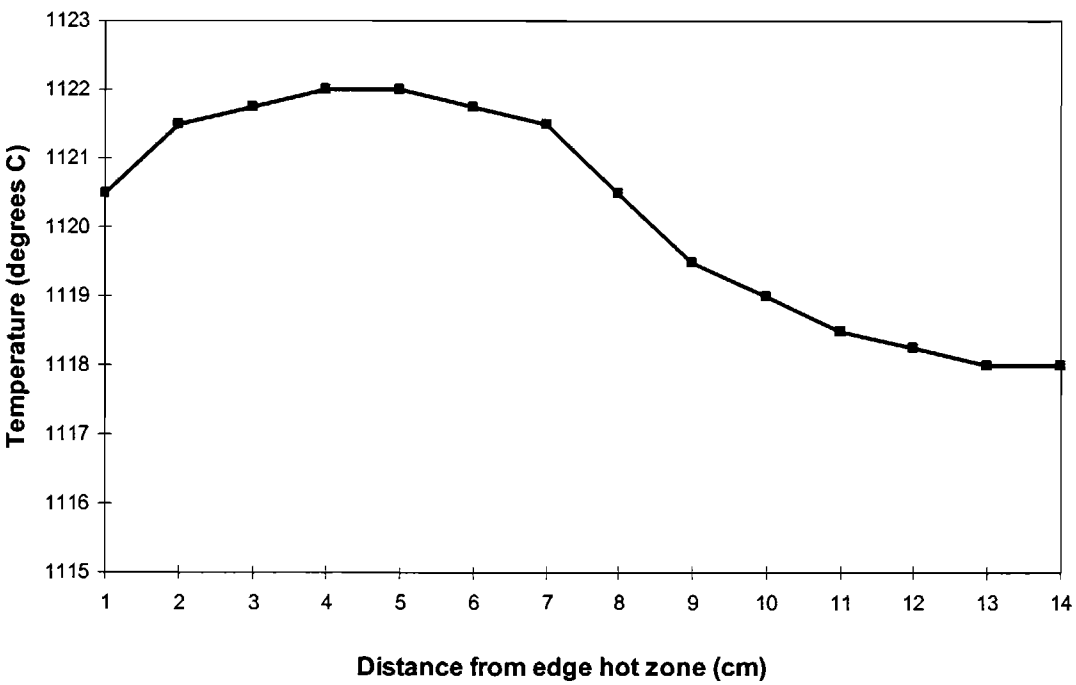

Figure 6.8 Profile of furnace at 1200 °C

As was shown in Chapter 3, changes in temperature can cause damage to lithium niobate crystals due to the pyroelectric effect. In practice it was found the maximum rate of change of temperature which did not adversely damage the crystals was ±50°C per minute. During diffusion the furnace was taken up from room temperature to the

required diffusion temperature at a rate less than this limit, and similarly for cooling. A typical diffusion run is outlined in Table 6-2 :

Atmosphere	Oxygen flowing at 200 ml min^{-1}
Start Temperature	20°C
Dwell	60 mins - [to allow any moisture to leave furnace, and for furnace atmosphere to stabilise]
Ramp	50 °C min^{-1}
To	1200 °C
Dwell	540 mins
Ramp	75 °C min^{-1}
To	20 °C

Table 6-2 Typical diffusion run

As the furnace cooled naturally slower than the programmed rate, the programmed ramp down rate was not as critical as the ramp up rate. It was also found that the pyroelectric effect caused more significant repoling during the cooling phase, therefore the naturally slower ramp down rate is beneficial.

6.4.4 Investigation into diffusion parameters

To investigate diffusion parameters such as diffusion side, time and temperature several channel waveguide samples were fabricated as described before, four samples with the waveguides on the positive z face and five samples on the negative z face. These were then visually inspected under a microscope and optically tested with a 1mW HeNe laser at 633nm. The visual inspection looked for the following properties; continuity of the waveguides along the full length of the sample, absence of defects and absence of deposits on the surface of the waveguides. During optical testing the assessment criteria included; absence of scattering along the waveguides, achievement of a reasonable launch and a well defined output in the near field image. To aid comparison between devices fabricated with different diffusion parameters a grade was given based on the above criteria for each sample for both visual inspection and optical testing, with A grade indicating a sample meeting all the criteria and an F

grade indicating that none of the criteria were met. The results are shown in Table 6-3.

Diffusion side	Visual inspection	Optical testing at 633nm
+ z	C	C -
+ z	C -	C -
+ z	E	F
+ z	B +	C -
- z	D	C
- z	B	B
- z	B	B
- z	B -	B
- z	C	C

Table 6-3 Investigation into diffusion side

From the table it can be seen that overall the waveguides diffused into the negative z crystal face gave better visual and optical results. It is known that during diffusion lithium outdiffusion occur on the positive z face which may affect the efficiency of the devices. As described in Chapter 3, it is the negative z face that is the preferred crystal face patterned for poling. It can be concluded that the negative z face is the favourable side for titanium waveguide diffusion. All further devices used in this work were fabricated with negative z waveguides.

Previous results [26,27,10] suggest the optimum fabrication parameters for single mode waveguides at visible wavelengths are diffusion for 9 hours at 1050°C for 90nm of deposited titanium. To confirm this several samples were fabricated as before for channel waveguides with 90nm of deposited titanium, and were diffused at different times and temperatures. To measure the level of titanium diffusion a Tencor Alphastep profile was taken of each sample for the narrowest, 3μm wide, waveguide and the widest, 18μm wide, waveguide. Table 6-4 shows the measured waveguide heights after diffusion for each set of diffusion conditions.

Ridge Heights	1000°C	1100°C	1200°C
6hrs	widest : 190nm narrowest : 225nm	widest : 100nm narrowest : 125nm	widest : 125nm narrowest : 75nm
9hrs	widest : 70nm narrowest : 75nm	widest : 45nm narrowest : 55nm	widest : 40nm narrowest : 45nm
12hrs	widest : 65nm narrowest : 75nm	widest : 40nm narrowest : 40nm	widest : n/a narrowest : n/a

Table 6-4 *Diffusion trials showing resultant waveguide ridge heights after diffusion with diffusion time and temperature*

From Table 6-4 it can be seen that the thickness of titanium and titanium compound on the surface of the samples varies with time for a given temperature, decreasing with longer diffusion times or increased diffusion temperatures. It appears to swell in the first few hours, the largest increase seen was an increase of 250% compared to the deposited thickness. This is most likely due to oxidisation of the titanium with simultaneous lithium outdiffusion, creating a Ti-Li-O compound on the surface of the samples. It can be seen that after 6 hours the thickness steadily decreases as the titanium diffuses in from this surface compound into the sample.

To further investigate the diffusion process three samples were diffused for 35 hours at 1100°C with the surface profile measured periodically during the diffusion run using the Alphastep. It can be seen in Figure 6.9 that the height of the titanium 'bump' levels out after 20 hours to around 50nm. It was found that even on further diffusion the height of the waveguides did not significantly reduce below this level. It is though that this is due to the physical swelling in the crystal caused by the indiffused titanium atoms.

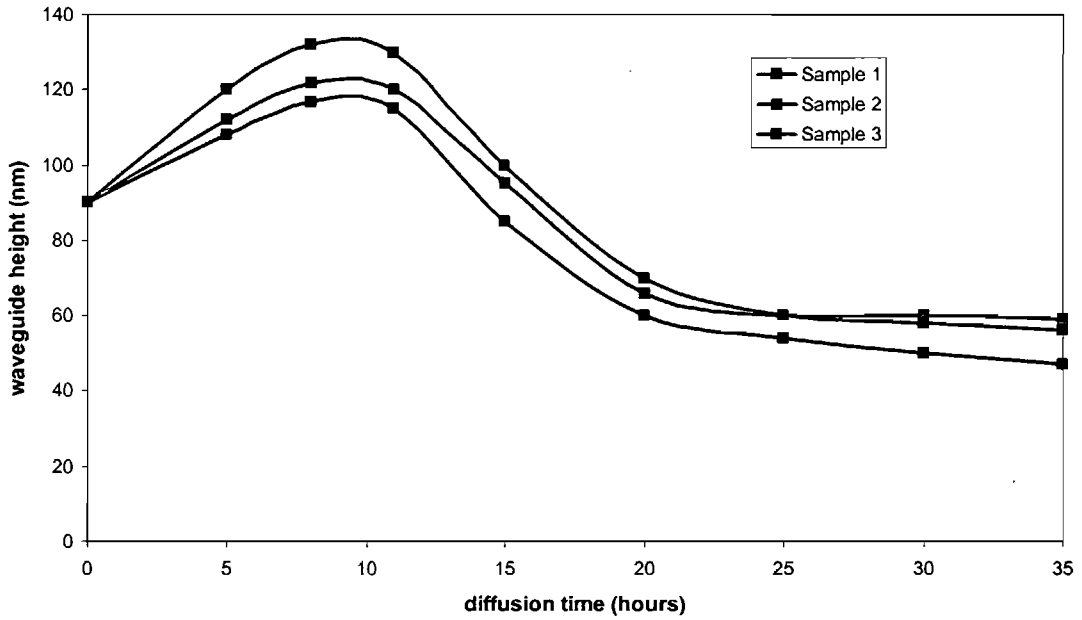

Figure 6.9 Titanium diffusion with diffusion time

Therefore it was concluded that to ensure complete diffusion of the titanium source, diffusion times of a minimum of 10 hours should be used.

6.4.5 Fabrication issues

During the initial fabrication of titanium waveguides it was noted that if the lithium niobate crystals were heated or cooled quickly they produced blue flashes and 'cracking' could be heard. On examination of the samples under crossed polarisers dots of domain inversion, up to 10 microns across, could be seen randomly distributed across the middle of the samples, Figure 6.10. This effect was experienced at temperatures as low as 100°C as well as during 1200°C furnace runs.

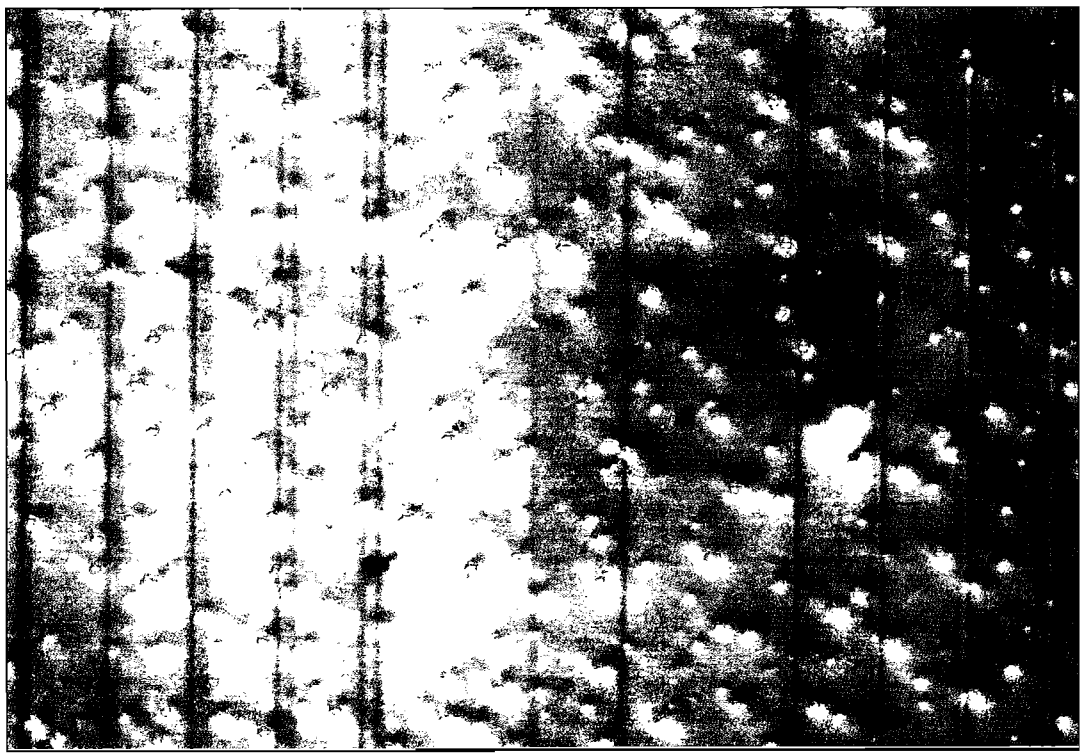

Figure 6.10 Photograph of poling dots in a Ti waveguide sample

For titanium diffused waveguides for other applications, this may not be such a problem; however as discussed in Chapter 3, for periodic poling it was found that these dots strongly influenced the poling and dominate the patterned gratings.

The spontaneous poling is believed to be due to a build up of charge on the faces as a result of the pyroelectric effect, Chapter 2. A border of about 4mm can be seen around the sample where no dots occur and this confirms experience of charge being able to flow round the edges of the samples during poling due to surface conductivity. Chapter 3 presented further investigations into spontaneous poling and an adapted fabrication process was developed to reduce the occurrence of these poling dots.

An investigation to find a method of dissipating the charge build up on the crystal faces during diffusion runs was carried out, and the results are shown in the Table below. The samples were photographed before and after to compare for evidence of poling dots. All samples were fabricated as described in Section 6.4 with 90nm thick titanium channels, and diffusion conditions as detailed below.

Special Conditions	*Time (hrs)*	*Temp (°C)*	*Atmosphere ($cm^3 min^{-1}$)*	*Comments*
Slow ramp rate	9	1100	200 O_2	No poling dots on first run, but some subsequent runs resulted in poling dots
Submerged in Tungsten powder	9	1050	200 O_2	Worked very well on first run, but subsequent runs the powder oxidised, turning yellow and doubling in volume. The lithium niobate was reduced to nothing
Tungsten powder	9	1100	200 $O_2 + N_2$	Similar results to oxygen only
Tungsten powder	9	1100	200 Ar	Still total oxidisation and poling dots appearing
Tin oxide powder	9	1050	200 Ar	No poling dots, but samples had changed colour slightly and EDAX measurements showed a slight increase in tin at the surface layers of the samples, possibly tin diffused into samples
Carbon powder	9	1100	200 Ar	Poling dots visible, sample changed colour
Wrapped in platinum foil	9	1100	200 O_2	No poling dots, good samples, but only enough foil to do one sample at once and very expensive to buy enough foil or powder to use efficiently
Submerged in Silicon powder	9	1050	200 N_2	No poling dots on first run, but dots appeared on subsequent runs. The silicon powder also oxidised turning blue. The sample appears to have changed colour
Sandwiched between Silicon wafers	9	1100	200 N_2	First run worked very well, no poling dots, even though the Si wafers oxidised, but during subsequent run the wafers bonded to the lithium niobate and shattered the sample
Lithium niobate powder	9	1100	200 O_2	Worked well, no poling dots, but very very difficult to clean powder from surface of sample afterwards, Figure 6.11
Lithium niobate powder	12	1200	200 O_2	Powder sintered and formed a ceramic type compound, diffused into and shattered quartz crucible and damaged furnace tube
Wet O_2 atmosphere	9	1100	Room temp wet 200 O_2	Poling dots seen

Table 6-5 Diffusion conditions and results for investigation into spontaneous poling

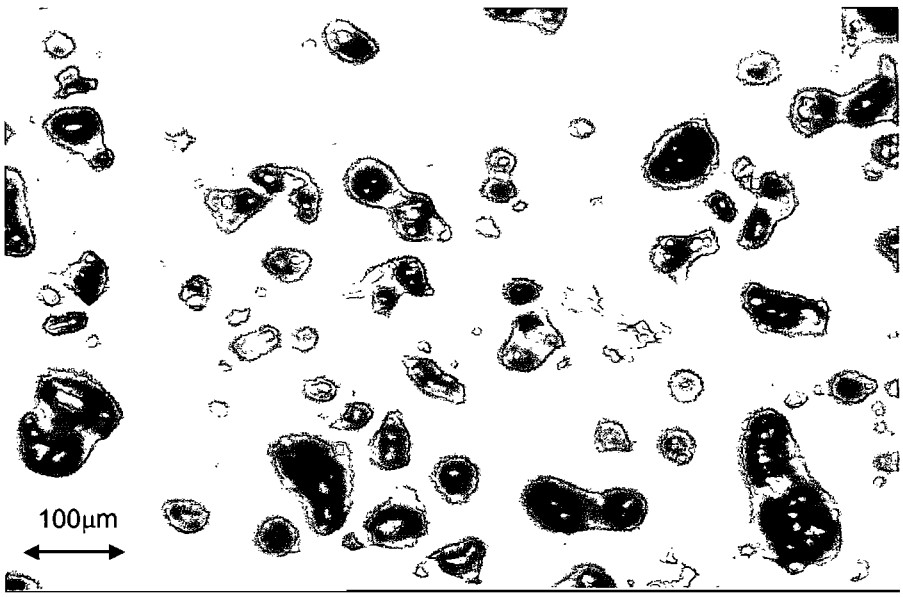

Figure 6.11 Photograph of lithium niobate powder fused onto surface of wafer

From Table 6-5 there is no obvious solution to dissipating the charge build up on the faces during diffusion. There are very few conductive materials that will survive the diffusion temperature and time, that will not react with the lithium niobate samples and are within a reasonable budget. However the most promising methods to alleviate the poling dots were using platinum foil, lithium niobate powder or silicon powder, albeit with the problems of cost, adhesion to the sample surface and oxidisation. Figure 6.11 shows a photograph of the surface of a sample which was submerged in lithium niobate power during the diffusion run. There is no evidence of poling dots on this sample, however the power has fused onto the sample surface and could not be removed afterwards.

A particular problem with these studies was the finding that second and subsequent runs often yielded different results. Possible explanations could be differing quality and property of raw material from different suppliers as discussed in Chapter 3, residual contamination in the furnace tube from previous runs by other researchers, the condition of the silica tube supply lines, slight changes in the fabrication process due to human variation and error resulting in very slight differences in temperatures and times of processes, and other variations in the fabrication process due to human error such as chemical ratios, thickness of photoresist or titanium, time between

processes, etc. Steps were taken to minimise all these issues as much as possible within our control, however considerable inconsistency between fabricated devices was still seen.

6.5 Waveguide characterisation

This Section describes the characterisation of the titanium waveguides fabricated as described before. Mode profiles for a typical set of waveguides are shown and an infrared transmission spectra is given.

6.5.1 Mode profiles

After diffusion the samples were end polished to allow efficient coupling into the waveguides. The mode profiles for a typical set of waveguides are shown in Figure 6.12. This particular set of waveguides were fabricated with 100nm of titanium deposited on the negative z face and diffused at 1050°C for 15 hours. It should be noted that this is an abnormally long diffusion time and resulted in several multi-mode waveguides in the horizontal direction, a more typical diffusion time of 10 hours would result in more single mode waveguides in the narrower channels. These images were taken using a HeNe laser at 633nm, fibre coupled into the waveguides and imaged using a ×10 microscope objective onto a CCD camera.

It can be seen that the waveguides are all single moded in the z direction and multiply moded in the x direction depending on the width of the patterned waveguide. In this case the 3μm wide waveguide shows two modes in the x direction at 633nm, but other samples exhibited single mode waveguides for several of the widths depending on the diffusion time and temperature. The differing quality between waveguides in the same sample can be seen, with the 3μm, 5μm, 6μm and 7μm showing the best quality.

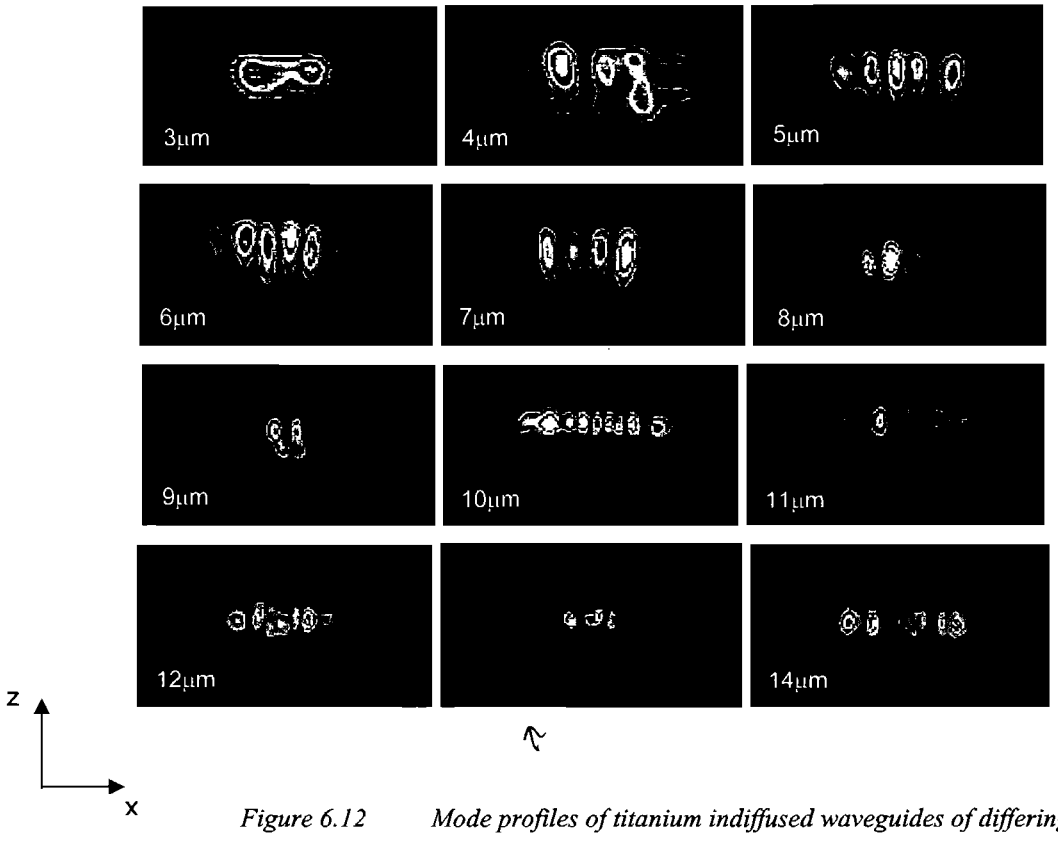

Figure 6.12 *Mode profiles of titanium indiffused waveguides of differing widths*

6.5.2 Transmission spectra

Figure 6.13 shows the near infrared transmission spectra for unpolarised light and both e- and o-polarised light through bulk lithium niobate and through a 2cm long waveguide of deposited width 6μm. The water absorption at 1400nm can clearly be seen. The sinusoidal fringes seen are thought to be due to residual birefringence in the samples, however this was never looked into as the aim of the measurement was purely to investigate waveguide loss in the infrared.

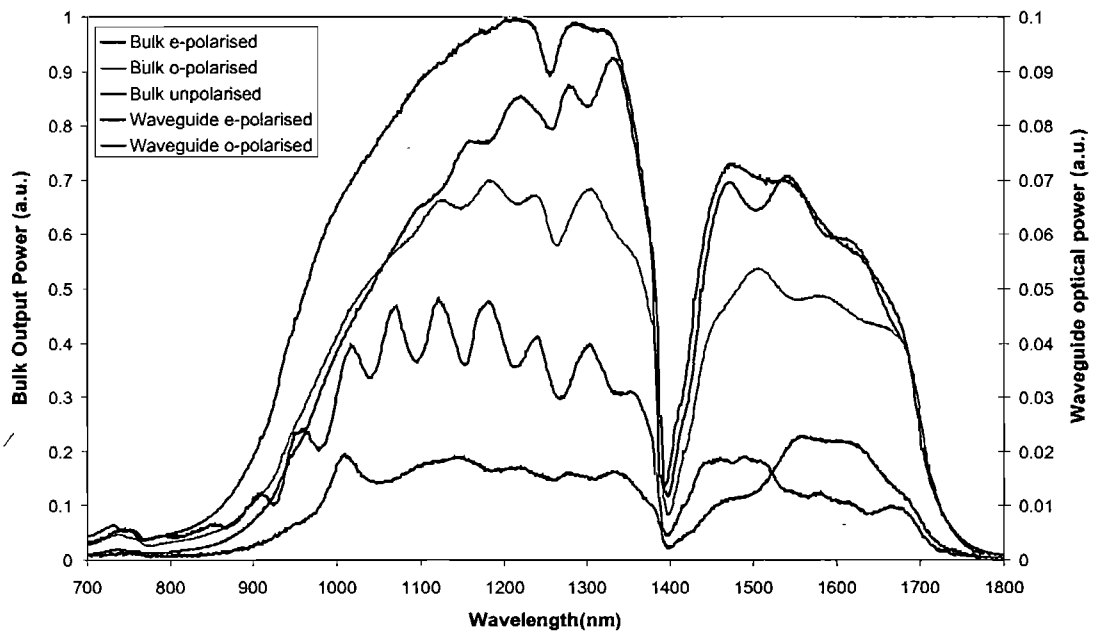

Figure 6.13 Graph showing near infrared transmission spectra for bulk and waveguide propagation

6.6 Titanium waveguides and periodically poled lithium niobate

This Section describes extensive studies into the fabrication of Ti:PPLN waveguides. By combining channel waveguides and PPLN [10], the advantages of both PPLN and waveguide technologies are exploited to create nonlinear devices with higher efficiencies and lower pump thresholds than bulk PPLN.

Waveguides are used in PPLN for frequency conversion at long wavelengths [12,13], for WDM channels [14] and in optical fibre systems [39]. In contrast, this work aims to design, fabricate and test a second harmonic generation (SHG) device for low power conversion from near infrared to visible radiation.

6.6.1 Issues involved in combining the two fabrication processes

Successful fabrication of titanium waveguides in PPLN requires good control of a number of complex processes. It is essential that each step has a high yield to give a reasonable overall chance of success. There are clearly two main steps to producing

Ti:PPLN waveguides; the diffusion of titanium in the lithium niobate substrate to create waveguides, and the poling of the sample for a given QPM period to create a PPLN structure. Both these processes are established research areas of their own, and are described fully in Chapter 3 and Section 6.2 respectively, including full fabrication details. What is less obvious about the process is the order in which these two steps should be carried out, ie. the poling before or after the diffusion. These two processing methods and their conditions are in many ways not ideally compatible because of the high temperatures and the movement of ions associated with titanium diffusion. Also, a large number of fabrication combinations exist, for example, the diffusion can be carried out on the positive or negative z face, the patterning for the PPLN poling can similarly be done on either face. To further complicate the procedure, a number of variants of both poling and diffusion exist and may be tried to alleviate the harmful alterations to the crystal made by the previous step.

These factors which affect the compatibility of titanium diffusion and periodic poling are discussed in the following Section along with any changes or adaptations to the fabrication process which would aid their integration.

6.6.1.1 Surface defects

Surface defects in lithium niobate crystals are thought to enhance the poling by providing nucleation sites [40,41,Chapter 3]. However defects in the crystal surface cause problems during diffusion, resulting in anisotropic diffusion, with higher diffusion coefficients laterally along the crystal surface than in the z direction into the sample, subsequently affecting the mode profiles of the waveguides. Therefore a compromise must be made with enough defects to encourage nucleation of domain inversion, but few enough not to drastically alter the profile of the titanium diffused waveguide.

6.6.1.2 Spontaneous poling

As seen in Chapter 3 and Section 6.4.5, when lithium niobate samples are heated or cooled rapidly spontaneous poling can occur at defects in the crystal, resulting in 'dots' of inverted domains of up to 10μm across. Spontaneous poling was seen to

occur during both the initial cleaning and photolithography stage in the fabrication process, and the subsequent diffusion stage. During the initial stage the poling dots followed intrinsic defects in the supplied wafers which were randomly scattered across the surface. These are then accentuated during the diffusion stage, Figure 6.10. However if the spontaneous poling occurred purely during the diffusion stage the poling dots followed the 'defects' caused by the indiffusion titanium atoms, Figure 6.14.

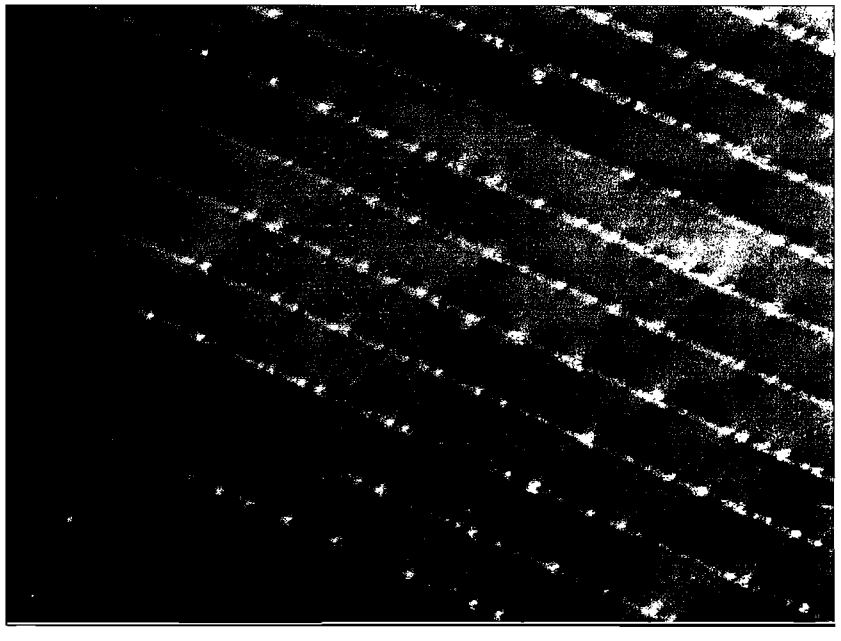

Figure 6.14 Photograph of poling dots following the titanium indiffused waveguides

The existence of dots of inverted domains will obviously affect any PPLN grating which is subsequently poled in the sample, with the gratings following the inverted dots, rather than the patterned period. In some cases the dots were seen to be several microns in size which would therefore dominate a fine period grating.

Alternatively if the PPLN grating is poled before diffusion, any spontaneous poling during the diffusion stage would seriously damage the gratings. A method of preventing the spontaneous poling must be found and efforts in this were described in Section 6.4.5. The most effective method found was to avoid any temperature change during the initial fabrication stages and during the diffusion stage to diffuse the

samples in platinum powder, allowing the charge to dissipate round the sample, rather than through it.

6.6.1.3 Thermal shock limit

High temperatures or high rates of change of temperature have a large effect on lithium niobate. In practice it was found that the 500μm thick lithium niobate samples used in this research survived a maximum temperature increase or decrease of approximately 50°C per minute without cracking or damaging the crystal. Therefore during the diffusion process the samples must be raised to and lowered from the diffusion temperature at a rate lower than this to avoid thermal shock.

6.6.1.4 Curie temperature

The Curie temperature of lithium niobate is 1210°C, Chapter 2. Above this temperature, lithium niobate ceases to be ferroelectric and becomes paraelectric and non-polar, therefore any PPLN gratings in the sample will be lost. On lowering of the temperature below the Curie temperature lithium niobate samples randomly take on domains of spontaneous polarisation, resulting in a marbled like appearance due to multiple domain formation, Figure 6.15. This effect of 'multidomain-isation' was first seen by Selyuk in 1971 [42]. Therefore the diffusion temperature must be well below the Curie temperature to preserve the polarisation.

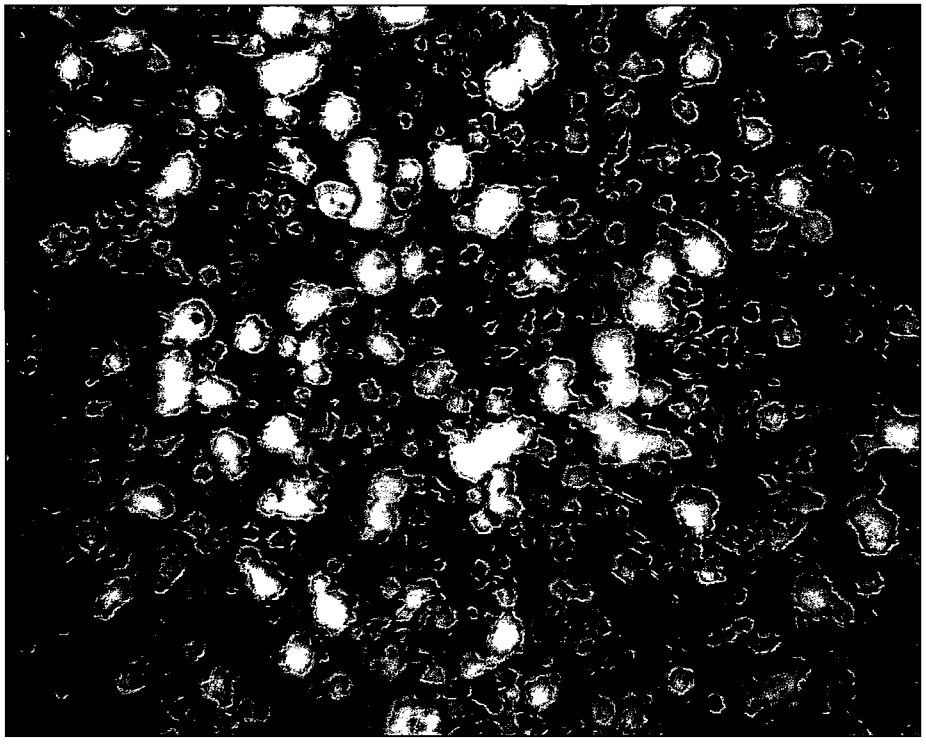

Figure 6.15 *Photograph of an HF etched sample showing multiple domain formation after being raised above the Curie temperature (dark areas indicate inverted domains)*

6.6.1.5 Lithium outdiffusion

When z cut lithium niobate wafers are subjected to high temperatures, of over 1000°C [43], lithium ions outdiffuse on the positive z face. Although this effect has been used in the past to fabricate waveguides in lithium niobate [44], it causes problems in this research with both the waveguide quality and the poling process as described below. Several methods have been reported to suppress or eliminate the lithium outdiffusion [45,46]. Although one clear preferred method has not been found, the most successful techniques were reported to be using a wet diffusion atmosphere or placing the sample in a closed platinum crucible.

During this research when waveguides were diffused on the positive z face, the lithium outdiffusion was found to affect the quality, resulting in lossy waveguides and less well determined mode profiles due to the altered crystal structure (measured as described in Section 6.4.4). The obvious solution is therefore to diffuse the waveguides into the negative z face. However if the positive z face is the preferred side for the waveguides as at Paderborn [11,13], a solution would be to diffuse much

deeper waveguides and then polish off a layer approximately 20μm thick from the positive z face.

Problems were also encountered during poling of all samples, irrespective of which side the waveguides were diffused into, due to the build up of lithium ions at the surface from lithium out diffusion acting as a barrier to nucleation and poling. The only solution to this is to polish off a layer from the positive z face before poling.

Another effect of lithium outdiffusion, when combined with titanium indiffusion is the formation of a surface compound of Ti-Li-O along the channel waveguides, Section 6.2. This layer was found to cause problems during poling, altering the surface conductivity and acting as a barrier to nucleation. The depth affected by this is less than 1μm, and the diffused waveguides are only a few μm's deep, therefore removal techniques such as mechanical polishing would not be suitable.

6.6.1.6 Domain inversion due to titanium indiffusion

When titanium diffuses into lithium niobate it can invert the polarisation in the diffused region depending on the diffusion side. This has been used to fabricate domain inverted gratings in lithium niobate [47]. When titanium diffuses into the positive z face of a lithium niobate crystal, a domain inversion layer is formed with the spontaneous polarisation opposite to that of the substrate [48]. This effect is not observed when diffusion is carried out on the negative z face. Obviously a domain inverted layer would have an adverse effect on poling quality, therefore the negative z face would be more favourable for diffusion of titanium waveguides.

6.6.1.7 Crystal impurities

The effect on the poling process of the presence of the titanium 'impurities' diffused into the crystal to form the waveguides has not been fully investigated. Experimental investigations in Section 6.6.2.2 suggest that the presence of titanium atoms in the crystal aids nucleation and poling, with titanium diffused regions preferentially poling over undiffused regions.

6.6.1.8 *Compatibility conclusions*

This Section has highlighted several modifications to aid the compatibility of titanium diffusion and periodic poling in lithium niobate which can be summarised as follows.

- The temperature change during fabrication should be less than 50°C per minute to avoid thermal shock.
- During diffusion the samples should be submerged in platinum powder to dissipate charge and avoid spontaneous poling.
- The diffusion temperature should be comfortably below the Curie temperature to preserve polarisation.
- The waveguides should be diffused into the negative z face to avoid problems cause by lithium outdiffusion and domain inversion due to titanium indiffusion.
- After diffusion the lithium outdiffused layer should be polished off the positive z face to aid poling.

6.6.2 Fabrication order

In this Section initial investigations into the compatibility and the optimum fabrication procedure for Ti:PPLN waveguides are presented. A series of samples were fabricated, half by diffusing the titanium waveguides first and then poling, and half poling first and then diffusing. Previous work by Amin [10] used the technique of poling after the waveguides had been diffused, however the alternative method of poling the gratings first and then diffusing the waveguides would be preferential as it would potentially allow greater control over the more critical poling stage. Therefore it was decided to investigate both fabrication methods to contrast and compare.

6.6.2.1 *Method one: PPLN gratings poled first*

The first sequence looked at in fabricating Ti:PPLN waveguides involved poling the samples with PPLN gratings first and then diffusing the titanium waveguides.

Four 500μm thick, lithium niobate samples, 20mm by 35mm, were patterned and poled with PPLN gratings of grating period 6-12μm following the method described in Chapter 3. Channel waveguides of widths 8-13μm, with 100μm separation, were

photolithographically patterned, two samples on the positive z face and two on the negative z face, following the process described in Section 6.4. 90nm of titanium was deposited onto the samples under a vacuum of 4×10^{-6} Torr and then the photoresist was removed by soaking the samples in acetone in an ultrasonic bath for a few minutes, thus revealing the deposited titanium strips. Finally the samples were diffused in a single zone Carbolite silica tube furnace following the steps outlined in Section 6.4.3. The diffusion parameters, taken from previous work [29,10,49,50], were 9 hrs at 1050°C in an oxygen atmosphere.

After diffusion of the waveguides, the residual stresses typically seen in PPLN gratings after poling were no longer visible under a crossed polariser microscope. It is most likely that the stresses in the crystal at the domain boundaries were annealed out due to the high temperatures experienced during diffusion. To investigate this further, two of the samples, one with waveguides on the positive z face and the other with waveguides on the negative z face, were etched in $HF:HNO_3$ 1:2 for approximately 10 minutes to reveal the domain boundaries. In both cases the PPLN structure was seen to have been detrimentally altered by the diffusion process. There was evidence of domain inversion, but not defined gratings. Incidentally, it was also observed that the titanium channels etched slower than the undiffused regions.

This effect of high temperatures on PPLN gratings is not recorded or discussed by any research group in any literature that we could find, possibly because PPLN gratings are not normally subjected to high temperature treatments. Other research groups investigating titanium waveguides in PPLN, such as Paderborn [11,12,13], favour poling the PPLN gratings after the waveguides have been diffused and therefore do not report such findings. Therefore to better understand the effect of the diffusion process on the PPLN gratings further investigations were carried out. PPLN samples were placed in a furnace without any deposited titanium. The furnace runs were carried out as described before, with the maximum temperature and dwell times shown below. The degradation seen in the PPLN gratings under a visual inspection through a crossed-polariser microscope was recorded as an approximate percentage, where 0 % indicates no degradation and 100 % indicates complete destruction of the gratings.

Temperature (°C)	Dwell Time (hours)	PPLN degradation
1000	0	10 %
1000	9	50 %
1000	24	75 %
800	9	15 %
800	24	60 %

Table 6-6 Affect on PPLN of diffusion process

From this table it can be seen that it is a combination of both time and temperature which damages the PPLN structure with the least damaged samples were obtained for low temperatures and shorter times. However as given in Section 6.3.1, the resultant depth of the diffused waveguide is proportional to both time and temperature. Therefore for the waveguide depth and profile to remain constant the diffusion time and temperature cannot both be decreased. To shorten the time would require an increase in temperature which is not possible as the diffusion already takes place very near the Curie temperature. The other option is to lower the temperature and increase the diffusion time, however prolonged temperatures increase lithium outdiffusion which detrimentally affects the quality of the waveguides on the positive z face.

6.6.2.2 Method two : titanium waveguides diffused first

Titanium waveguides were diffused in four samples as described in Section 6.4, with 90nm of titanium deposited, two samples on the negative z face and two on the positive z face. PPLN gratings were then patterned and poled as described before for QPM periods of 6-12μm.

On examination the gratings did not pole uniformly, instead exhibiting areas of strong underpoling and overpoling, influenced by the titanium waveguides, Figure 6.16. The two samples diffused on the negative z face exhibited higher quality gratings along the waveguides, and hence were optically tested, Section 6.6.3.

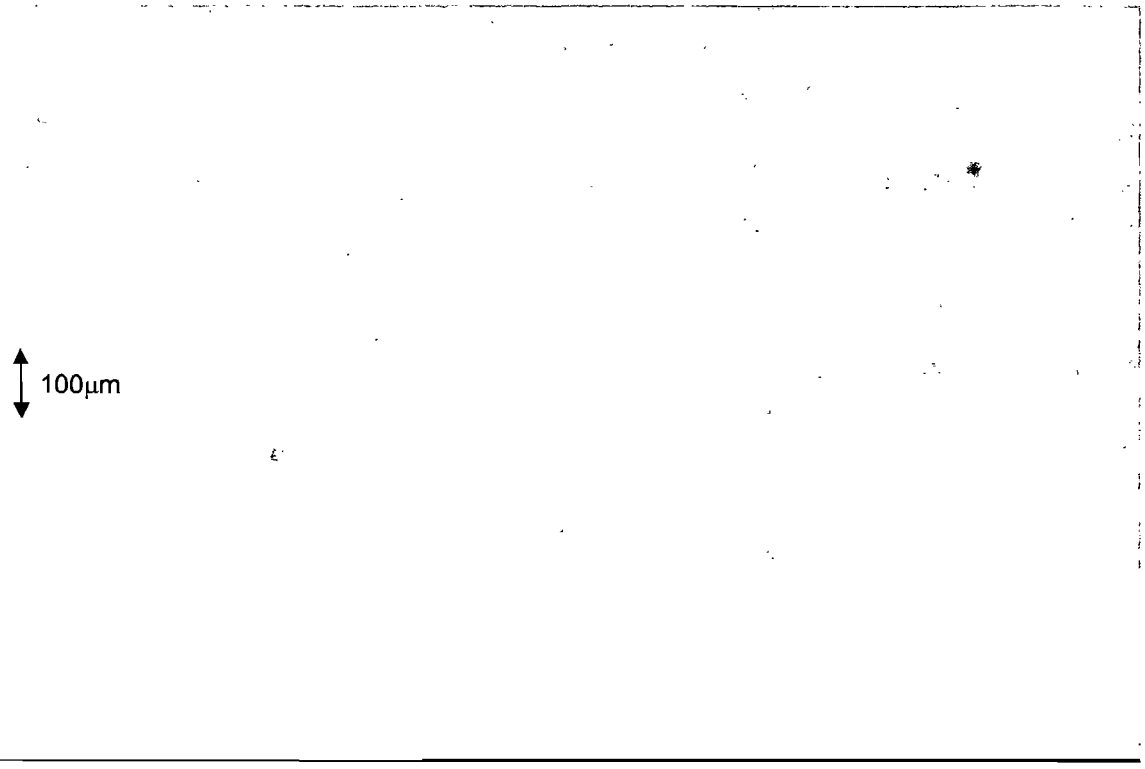

Figure 6.16 Patches of poling in a titanium waveguide sample

From these results it can be seen that the nucleation of the inverted domains is affected by the presence of titanium ions in the crystal lattice. To investigate this further, two lithium niobate samples from the supplier Yamaju were deposited with 90nm of titanium as shown in Figure 6.17 and diffused as before.

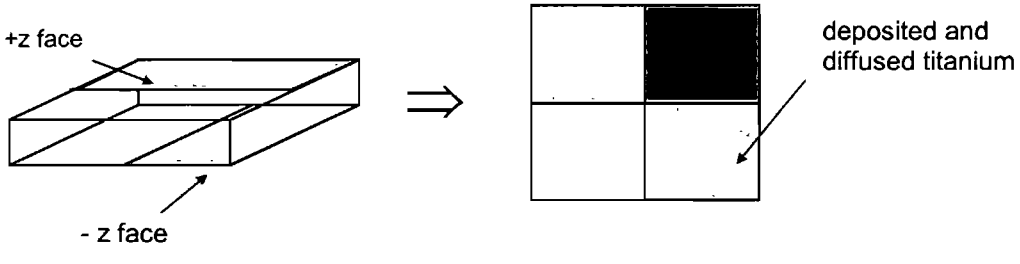

Figure 6.17 Deposited titanium

The samples were then bulk poled with insulation tape marking off an area 4mm from the sample edges to prevent breakdown during poling. On examination it was found that the region diffused on both sides with titanium poled first, followed by the region diffused only on the negative z side, then the region diffused only on the positive z side and finally the region without titanium.

Also, by comparing the quality of the poling on areas diffused on one side only, it could be seen that the areas with titanium diffusion on the negative z face poled more uniformly with straighter domain boundaries than those with titanium diffusion on the positive z face. One explanation for this is that the presence of the diffused titanium ions on the positive z face of the crystal is preventing nucleation of the inverted domains which is thought to start on the positive z face [41].

For samples from this supplier the presence of titanium 'impurities' was seen to enhance nucleation and poling, with areas diffused with titanium poling preferentially to those without. To investigate this further several samples were diffused with titanium channel waveguides and then patterned with QPM gratings. The samples were then poled with different amounts of charge. The results are shown below.

% of calculated charge	Results
100	Areas of over and under poling – no gratings
75	Overpoled along and near waveguides – no gratings
50	Patchy poling in the bulk – no gratings
25	Poling in the waveguides and in the bulk – patches of grating
10	Evidence of poling in the waveguides – some possible gratings

Table 6-7 Investigation of poling charge

A charge of about 10 % the calculated value gave the most defined gratings of domain inversion in the waveguides, with very little poling in the bulk. This would tie in with the percentage area of the sample which is diffused with titanium. Another unexpected effect was that although the gratings were visible directly after poling, after approximately 24 hours they were not visible under a crossed polariser microscope. The presence of the titanium in the crystal lattice may affect the residual stresses that are normally seen, speeding up the crystal relaxation process which normally takes several days or months.

Another significant observation was the huge difference in grating quality and poling nucleation areas between material from different suppliers. In some cases the poling

was seen to be prohibited in the titanium diffused areas, opposite to that observed above for material from Yamaju, this effect was most strong in samples from the Russian company, INGCRYS. This therefore makes it very difficult to develop and improve the fabrication process but instead leads to several optimal fabrication techniques for different material. It is clear from these observations and the investigations in Chapter 3 that the crystal structure and growth techniques for different suppliers need to be more fully understood and investigated before any development can be made in the fabrication of these devices.

6.6.3 Fabrication conclusions

This Section has looked at the issues involved in combining titanium indiffused waveguides and periodic poling in lithium niobate and the preferred fabrication order. It has been seen that both methods of fabrication exhibit problems, however in this research better results were achieved by diffusing the waveguides first and then poling.

If the PPLN gratings are to be poled first, then the diffusion temperature must be greatly reduced (and hence the diffusion time greatly increased) to prevent annealing and damage to the poled grating. Also the waveguides should be diffused in the negative z face avoiding the lithium outdiffusion on the positive z face.

If the titanium waveguides are to be diffused first, then the lithium outdiffused layer on the positive z face should be polished off before poling and the poling charge reduced to avoid overpoling of the waveguide regions.

6.7 Second harmonic generation in a Ti:PPLN waveguide

This Section presents second harmonic generation results obtained in a Ti:PPLN waveguide. The Ti:PPLN device was fabricated with QPM periods of 8.6–9.8μm, calculated using a Maple worksheet using the Sellmeier equations as described in Chapter 2 and the QPM equation, to give third order SHG from infrared radiation of wavelengths 830–860nm to blue radiation of wavelengths 415–430nm at a

temperature of 150°C. A tuneable Ti:Sapphire laser provided the required pump wavelength.

6.7.1 Optical set up

The optical set up used for testing the Ti:PPLN waveguides is shown in Figure 6.18. The Ti:sapphire laser was pumped using an argon ion laser and tuned to the required wavelength using birefringent filters. An infrared filter ensured that any unconverted argon ion light was blocked. The pair of infrared mirrors allowed the beam to be adjusted to the correct height for the sample.

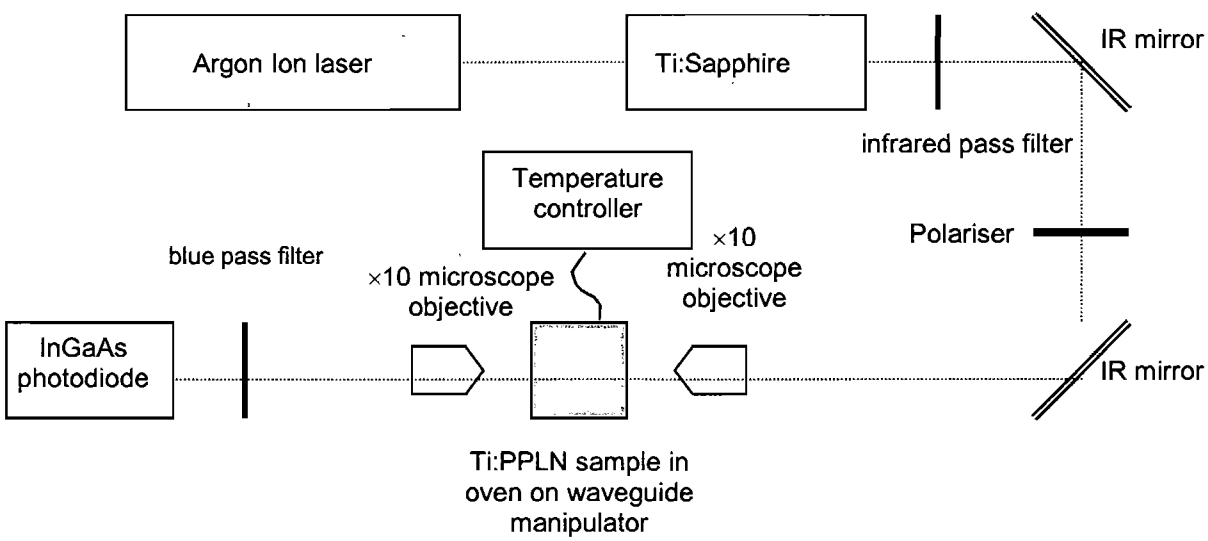

Figure 6.18 Optical set up

For *z*-cut lithium niobate with PPLN gratings along the *x* axis and waveguides along the *y* axis, e-polarised light as shown in Figure 6.19, is used to access the large d_{33} coefficient. A polariser designed for 833nm was used along with a Glan Taylor prism to give e-polarised light. A ×10 microscope lens was used to focus the beam on the end face of the sample using a back reflection technique. The sample was held at 150°C in an oven as discussed in Section 6.7.1.1, and was manipulated using a 4-axis waveguide micro-controller, thus allowing the optimum launch into the channel waveguides to be achieved. The beam was focussed onto an InGaAs photodiode detector using a ×10 microscope objective, and a blue pass filter ensured that all unconverted infrared radiation was blocked.

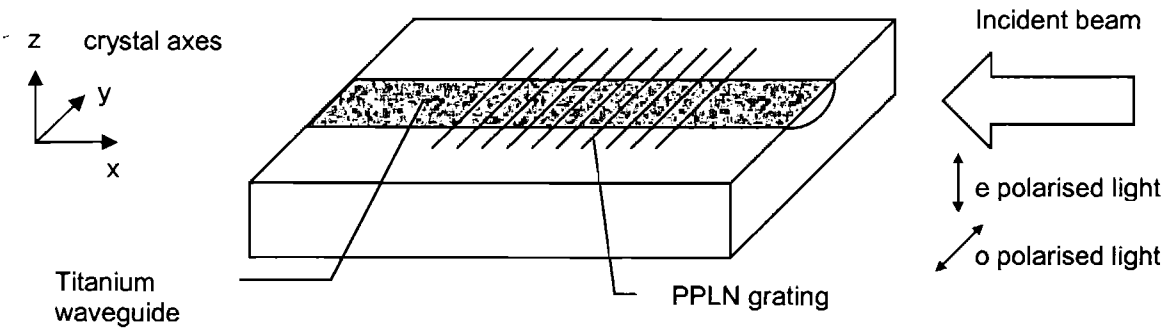

Figure 6.19 Polarisation of incident radiation

6.7.1.1 Oven design

The requirements for a PPLN oven are that it should minimise thermal gradients across the PPLN sample and therefore should be made of a highly insulating material. Secondly the temperature of the sample must be able to be controlled to very high accuracy and must be very stable, therefore the monitoring thermocouple should be very close to the sample to allow good feedback. And finally the oven must take varying sizes of sample and for the testing of waveguides the microscope objectives must be able to come as close as a few mm's to the sample.

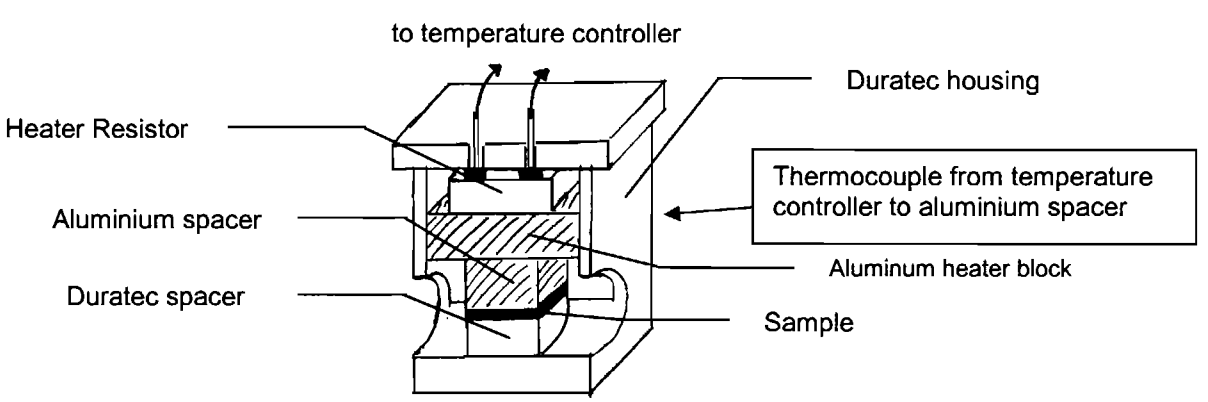

Figure 6.20 Cross-section of PPLN oven design

Taking into consideration these requirements the oven in Figure 6.20 was made. It was fabricated from Duratec, with aluminium mounting blocks. The heater resistor

chosen was a 5W thick film power heater resistor, operational up to 200°C. Samples were mounted on the correct size of aluminium block using silver paint and then placed on the matching sized Duratec mount. The thermocouple was fixed into the aluminium block using heat sink compound. The temperature controller was then programmed to the required temperature and the oven left to stabilise.

In practice the oven has proved to be very stable, reaching temperature and stabilising very quickly and could be used with any length of sample up to 20mm long.

6.7.2 Experimental results

Second harmonic generation was observed in a 12μm wide, 6.5mm long waveguide, running through an 8.7μm period PPLN grating with a pump wavelength of 833nm. An efficiency curve was plotted of the resultant output power at 416nm, corrected for Fresnel reflection, against the input power at 833nm, Figure 6.21. It can be seen that this curve shows the characteristic quadratic shape of SHG in bulk PPLN. Figure 6.22 shows pump power launched in the waveguide against the square root of the SHG power and exhibits the expected straight line behaviour.

The theoretical conversion efficiency in a waveguide is rather complicated to calculate as it depends on factors such as losses and modal overlap which are difficult to measure accurately. In view of the fabrication difficulties described earlier in the Chapter in producing waveguides it was decided to use a simpler approach to analyse the results of the single successful waveguide. This simpler approach is to compare the experimental results to those predicted for bulk conversion with optical focusing - this allows for a fair comparison of the benefits and disadvantages of choosing a waveguide format [51,52].

The effective nonlinear susceptibility, d_{eff}, can be calculated using the following equation which describes the second harmonic generation efficiency in bulk PPLN [53,54].

Equation 6-6

$$\frac{P_{out}}{P_{in}} = \left(\frac{2\omega^2 d_{eff}^{\ 2}}{\pi n_{\omega}^{\ 2} n_{2\omega} \varepsilon_o c^3} \right) P_{in} L k_{\omega} h(B,\xi) \rho \qquad \text{where } \xi = \frac{L}{k_{\omega} \omega_o^2}$$

where $h(B,\xi)$ is the Boyd-Kleinman focussing factor, $B = 0$ as there is no walk-off in PPLN QPM, ξ is a focussing parameter where ω_0 is the focussed beam waist, ρ is a multimode factor which varies between 1 and 2 where 1 indicates single mode operation and 2 indicates multiple modes and ;

Equation 6-7
$$d_{eff} = \frac{2}{\pi} d_{33} = \frac{2}{\pi} 27\,pmV^{-1} = 17\,pmV^{-1}$$

is the effective nonlinear coefficient of the PPLN grating [55]. In the above equation a value of 27pmV^{-1} has been assumed, however it should be noted here that a large range in nonlinear optical coefficients have been quoted. Values of d_{33} range from 3.44 [56] to 49±9 [57] $\times 10^{-12}$ pmV^{-1}.

From Equation 6-6 and taking the efficiency P_{out} / P^2_{in} as the gradient of the line in Figure 6.22 and allowing for third order QPM, d_{eff} was calculated for the experimental results to be 5.6 pmV^{-1}. This is significantly lower than the predicted value of 17 pmV^{-1} for a perfect crystal due to a combination of factors including waveguide launch, modal overlap, waveguide loss, poling errors, variation in waveguide dimensions or index, and launch efficiency. Also, the conversion efficiency equation for bulk PPLN sample was used for simplicity, however in a waveguide the conversion efficiency is more complicated.

By extrapolating Figure 6.21, the conversion efficiency was found to be 0.062 %W^{-1}cm^{-1}. In a waveguide geometry the conversion efficiency is dependent on L^2 instead of L and is therefore expressed in %W^{-1}cm^{-2}. In this experiment this gives 0.095 % W^{-1} cm^{-2}.

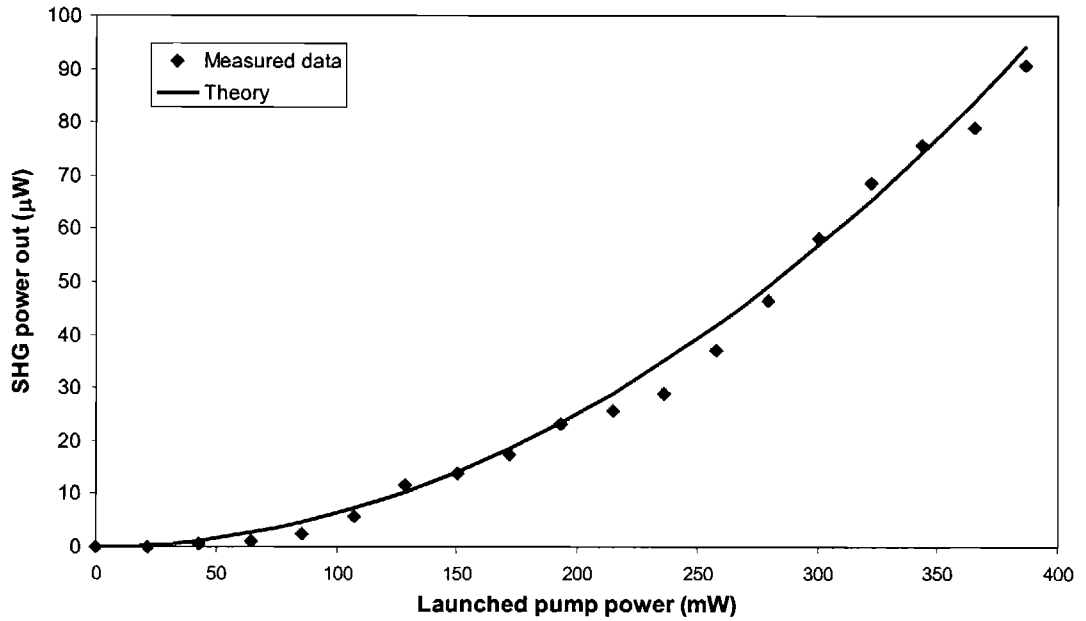

Figure 6.21 *Graph of SHG power out with pump power in*

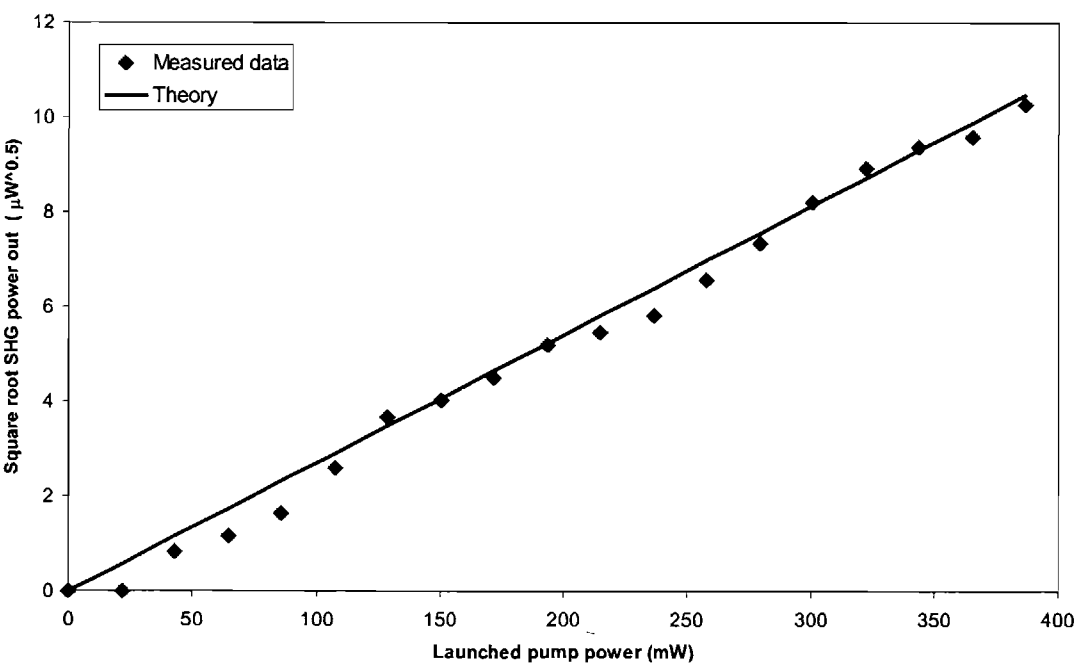

Figure 6.22 *Graph of square root SHG power out with pump power in*

A temperature tuning curve was also recorded for this waveguide. The temperature of the oven was varied from 140°C to 160°C and the output power at 416nm measured.

This is shown in Figure 6.23 with a fitted sinc^2 curve. From Chapter 2 it can be seen that one of the terms the SHG efficiency is dependant on is :

Equation 6-8

$$\left(\frac{\sin \frac{\Delta k L_{eff}}{2}}{\frac{\Delta k L_{eff}}{2}} \right)^2 = \text{sinc}^2 \left(\frac{\Delta k L_{eff}}{2} \right)$$

Using this term and the data in Figure 6.23 the effective length, L_{eff}, of the device was calculated using a Maple7 worksheet. The effective length of the device gives important information about the quality of the PPLN grating.

To calculate the effective length the temperature at the first minima is found. From Figure 6.23 it can be seen that T_{min}=*146.5, 151.5 °C.* These are then substituted into the equation for phase mismatch to find values of Δk ;

Equation 6-9

$$\Delta k = k_{2\omega} - 2k_{\omega} - K_g = \frac{2\pi \times n_{2\omega}(T, \lambda_{2\omega})}{\lambda_{2\omega}} - 2 \times \frac{2\pi \times n_{\omega}(T, \lambda_{\omega})}{\lambda_{\omega}} - K_g$$

where $K_g = \frac{2\pi}{\Lambda}$ and Λ is the grating period for first order phasematching. The effective length of the grating can then be found by substituting in the value of Δk to

Equation 6-10

$$\text{sinc}^2 \left(\frac{\Delta k \times L_{eff}}{2} \right) = 0 .$$

For the data in Figure 6.23 the effective length was calculated to be 4.7mm. This is less than the actual length of 6.5mm, which could be due to the several factors mentioned before, the most significant being the imperfect grating quality.

Another way to look at this is to compare the experimental and theoretical temperature bandwidths. The experimental temperature bandwidth can be found from Figure 6.23 to be 2.25°C. The theoretical temperature bandwidth for this device was calculated as 1.58°C from the above equations. The increase in temperature

bandwidth for the measured value compared to the theoretical value is thought to be due to the imperfect PPLN grating and possibly the effect of the titanium indiffused waveguides as the equations used were for bulk PPLN gratings.

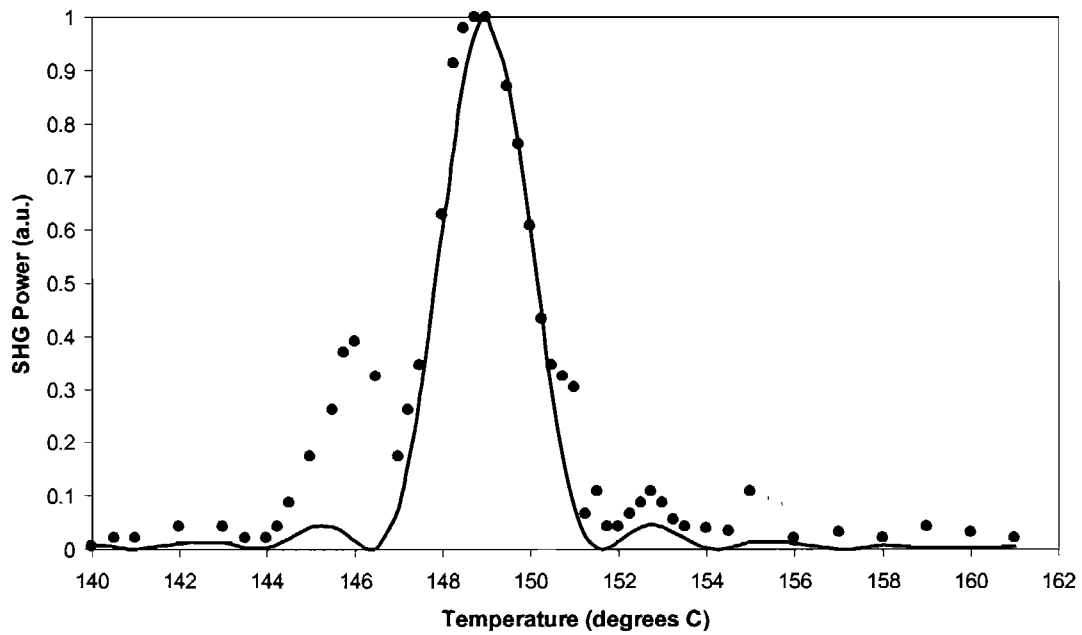

Figure 6.23 *Graph of SHG power out with temperature where the dots represent the experimental data and the solid line the fitted theoretical curve*

6.7.3 Conclusions

A successful Ti:PPLN waveguide device has been demonstrated for second harmonic generation of blue light at 416nm. Conversion efficiencies of 0.095 $\%W^{-1}cm^{-2}$ were achieved. The measured temperature bandwidth was 1.4 times larger than theoretically expected, indicating that the effective poled length was only 4.7mm rather than the full crystal length of 6.5mm. This L_{eff} can be used to work out the conversion efficiency in the properly poled regions and corresponds to 0.18% $W^{-1}cm^{-2}$ which compares favourably to previous work in the ORC on SHG in Ti:PPLN waveguides reporting efficiencies of 0.1 $\%W^{-1}cm^{-2}$ [10], but is still significantly lower than more recent work from Paderborn which achieved conversion efficiencies of 1.6 $\%W^{-1}cm^{-2}$ [11]. This is due to the poor quality PPLN grating and the high losses found in the waveguide. Future work to improve the compatibility of the titanium diffused waveguide and periodic poling procedures and to develop each of the

fabrication process will result in lower loss waveguides with better quality gratings achieving higher conversion efficiencies during SHG. Future work will need to involve optimisation of modal overlaps with the nonlinearity.

6.8 Chapter conclusions

This Chapter has reviewed nonlinear optical waveguides, concluding that titanium indiffused waveguides are the most versatile for harmonic generation applications. The actual mechanism of titanium diffusion into lithium niobate was described and a theoretical model presented which enables the resultant mode profile of a titanium waveguide to be found given the initial diffusion parameters.

Initial investigations into combining the two fabrication processes of titanium indiffusion and periodic poling were presented and an optimum fabrication procedure concluded. Following from this a Ti:PPLN waveguide device was fabricated initially with waveguides on the negative z face followed by periodic poling of a 8.7μm grating.

The Ti:PPLN waveguide was used to achieve second harmonic generation of 416nm in a 12μm wide, 6.5mm long waveguide. Conversion efficiencies of 0.095 $\%W^{-1}cm^{-2}$ were achieved. It can be seen that improved fabrication techniques are needed to produce better Ti:PPLN waveguides. The whole fabrication is a very hit and miss process and has been found to vary enormously with starting material supplier. This is a major scientific challenge which will need significant studies if these attractive devices are to see actual realisation.

6.9 References

[1] D B Anderson and J T Boyd *'Wideband CO_2 laser second harmonic generation phase matched in GaAs thin-film waveguides' Appl Phys Lett* **19** p266 (1971)

[2] G I Stegeman and C T Seaton *'Nonlinear integrated optics' J Appl Phys* **58** R57 (1985)

[3] G I Stegeman, E M Wright, N Finlayson, R Zanoni and C T Seaton *'3rd order nonlinear integrated optics' IEEE J Lightwave Tech* **6** p953 (1988)

[4] J M Dziedzic, R H Stolen and A Ashkin *'Optical Kerr effect in long fibres' Appl. Opt.* **20** p1403-1406 (1981)

[5] R H Stolen and J E Bjorkholm *'Parametric amplification and frequency conversion in optical fibres' IEEE J Quantum Electronics* **18** p1062 (1982)

[6] M M Fejer, J L Nightingale, G A Magel and R L Byer *'Laser heated miniature pedestal growth apparatus for single crystal optical fibres' J Opt Soc Am* **4** (13) p77 (1987)

[7] U Osterberg and W Margulis *'Dye-laser pumped by Nd:Yag pulses frequency doubled in a glass optical fibre' Opt Letters* **11** p516 (1986)

[8] V Pruneri and P G Kazansky *'Frequency doubling of picosecond pulses in periodically poled D-shape silica fibre' Elec Lett* **33** p318 (1997)

[9] V Pruneri, G Bonfrate, P G Kazansky, et al. *'Greater than 20% efficient frequency doubling of 1532nm nanosecond pulses in quasi-phasematching germanosilicate optical fibres' Opt Lett* **24** p208 (1999)

[10] J Amin, V Pruneri, J Webjorn, P St J Russell, D C Hanna and J S Wilkinson *'Blue light generation in a periodically poled Ti:$LiNbO_3$ channel waveguide' Opt. Comms.* **135** (1-3) p41-44 (1996)

[11] D Hofmann, G Schreiber, C Haase, H Herrmann, W Grundkotter, R Ricken, W Sohler *'Quasi-phasematched difference frequency generation in periodically poled Ti:$LiNbO_3$ channel waveguides' Opt. Letts.* **24** (13) p896-898 (1999)

[12] D Hoffman et al *'Mid-infrared difference frequency generation in periodically poled Ti:$LiNbO_3$ channel waveguides' ECIO'99 Turin*

[13] G Schreiber, R Ricken and W Scholer *'Near infrared second harmonic and difference frequency generation in periodically poled Ti:LiNbO3 waveguides' ECIO'99 Turin*

[14] C G Trevino-Palacios, G I Stegeman, P Baldi and M P de Micheli *'Wavelength shifting using cascaded second order processes for WDM applications at 1.55μm' Elec Lett* **34** (22) p2957 (1998)

[15] D C Hutchings, J S Aithison and C N Ironside *'All optical switching based on nondegenerate phase shifts from a cascaded second order nonlinearity' Optics Lett* **18** (1993) pp793

[16] M H Chou, K R Parameswaran, M M Fejer and I Brener *'Multiple-channel wavelength conversion by use of engineered quasi-phase-matching structures in $LiNbO_3$ waveguides' Optics Letters* **24** p1157 (1999) and *CLEO'99 CTuW7*

[17] P Baldi, M P De Micheli, K El Hadi, S Nouh, A C Cino, P Aschieri and D B Ostrowsky *'Proton exchange waveguides in $LiNbO_3$ and $LiTaO_3$ for integrated lasers and nonlinear frequency converters' Opt. Eng.* **37** (4) p1193 (1998)

[18] C B E Gawith, D P Shepherd, J A Abernethy, D C Hanna, G W Ross and P G R Smith *'Second-harmonic generation in a direct-bonded periodically poled $LiNbO_3$ buried waveguide' Opt. Letts.* **24** (7) p481-483 (1999)

[19] F D Nunes, J Andrade and J M Filho *'A mathematical model for Ti diffusion in $LiNbO_3$' J. Physics: Condensed Matter* **6** p4067-4076 (1994)

[20] C Buchal, S Mantl and D K Thomas *Mat. Res. Soc. Symp. Proc.* **100 p**317 (1988)

[21] K Sugji, M Fukuma and H Iwasaki *'A study on Ti diffusion into ion waveguides by electron probe analysis and X-ray diffraction methods' J. Mater. Sci* **13** p523 - 533 (1978)

[22] B Hauer, R Vianden, M F da Silva, J C Soares and A Aguillo-Lopez *'The lattice site of Ti in $LiNbO_3$' J. Phys. Condensed Matter* **6** (1) p267–274 (1994)

[23] D Kollewe, A Kling, B C Grabmaier, T Bremer, W Heiland and W Zimmerman. *'Lattice site location of titanium diffused and doped in lithium niobate' Phys. Lett.* **169A** 177 (1992)

[24] M Fukuma and J Noda *'Optical properties of titanium diffused $LiNbO_3$ strip waveguides and their coupling to a fibre characteristics' Appl. Opt.* **19** (4) p591- 597 (1980)

[25] W K Burns, P H Klien, E J West and L E Plew *'Indiffusion in Ti:$LiNbO_3$planar and channel optical waveguides' J. Appl. Phys.* **50** p6175 - 6182 (1979)

[26] R J Holmes and D M Smyth *'Titanium diffusion into $LiNbO_3$ as a function of stoichiometry' J. Appl. Phys.* **55** p3531-3535 (1984)

[27] D P Birnie *'Analysis of diffusion in lithium niobate' J. Mat. Sci.* **28** p302 (1993)

[28] I P Kaminow and J A Carruthers *Appl. Phys. Lett.* **22** p326-328 (1973)

[29] S Fouchet, A Carenco, C Daguet, R Guglielmi and L Riviere *'Wavelength dispersion of Ti induced refractive index change in $LiNbO_3$ as a function of diffusion parameters' J Lightwave Tech* **5** p700 (1987)

[30] EMIS Datareview Series No5 *'Properties of lithium niobate' INSPEC London* p26 (1989)

[31] S K Korotky, W J Minford, L L Buhl, M D Divino and R C Alferess *'Modesize and method for estimating the propagation constant of single-mode Ti:$LiNbO_3$ waveguides' IEEE Trans. Microwave Theory and Tech.* **30** (10) p1784 (1982)

[32] G P Bava, I Montrosset, W Sohler and H Suche *'Numerical modelling of Ti:$LiNbO_3$ integrated optical parametric oscillators' IEEE J. Quant. Electron.* **QE-23** (1) p42 (1987)

[33] K T Koai and P L Lui *'Modeling of Ti:$LiNbO_3$ waveguide devices: part I – directional couplers' IEEE J. Lightwave Tech.* **7** (3) p533 (1989)

[34] H F da Silva, S C Zilio and F D Nunes *'Modelling Ti indiffusion in $LiNbO_3$' J. Phys. Condens. Matter* **9** (2) p357 (1997)

[35] G B Hocker and W K Burns *'Modes in diffused optical waveguides of arbitrary index profile'* **QE11** (6) p270 (1975)

[36] J Crank *'The mathematics of diffusion' Oxford University Press* ISBN: 0198534116 2nd Edition (1979)

[37] H Ludtke *Workshop Integrated Optics* p121 (1980)

[38] E Strake, G P Bava and I Montrosset *'Guided modes of Ti:$LiNbO_3$ channel waveguides: A novel quasi-analytical technique in comparision with the scalar finite element model' J. Lightwave Tech.* **6** (6) p1126 (1988)

[39] D C Hutchings, J S Aithison, C N Ironside *'All optical switching based on nondegenerate phase shifts form a cascaded second-order nonlinearity'Optics Lett* **18** p793 (1993)

[40] L Huang and N A F Jaeger *'Discussion of domain inversion in $LiNbO_3$' Appl. Phys. Lett.* **65** (14) p1763 (1994)

[41] V Y Shur, E L Rumyantsev et al. *'Regular ferroelectric domain array in lithium niobate crystals for nonlinear optic applications' Ferroelectrics* **236** p129-144 (2000)

[42] B V Selyuk *Sov. Phys. Crystallogr.* **16** p292 (1971)

[43] A Koide, H Shimizu and T Saito *'Main cause of surface waveguide formed under $LiNbO_3$ crystal surface during thermal treatment' Japanese Journal of Applied Physics* **36** p239 (1997)

[44] C S Lau, P K Wei, C W Su, W S Wang *'Fabrication of magnesium oxide induced lithium outdiffusion waveguides' IEEE Photonics Tech. Letters* **4** p872 (1992)

[45] J L Jackel *'Suppression of outdiffusion in titanium diffused $LiNbO_3$' J Opt Comms* **3** p82 (1982)

[46] A Rasch, M Rottschalk, W Karthe *'Suppression of outdiffusion in Ti:$LiNbO_3$' ibid.* **6** p14 (1985)

[47] Y Qin, Y Zhu, A Zhu, H Shu and N Ming *'Electron probe microanalysis of periodic domain inversion in $LiNbO_3$ by Ti Diffusion' Materials Letters* **30** p231 (1997)

[48] S Miyazawa *'Ferroelectric domain inversion in Ti-diffused $LiNbO_3$ optical waveguide' J Appl Phys* **50** p4599 (1979)

[49] L W Stulz *'Titanium indiffused $LiNbO_3$ optical waveguide fabrication' Appl. Opt.* **18** p2041 (1979)

[50] G J Griffiths and R J Esdaile *'Analysis of titanium diffused planar optical waveguides in lithium niobate' IEEE J Quantum Elect* **2** p149 (1984)

[51] T Suhara and H Nishihara *'Theoretical analysis of wavelength second harmonic generation phase matched with uniform and chirped gratings' IEEE J Quantum Elec* **26** (7) p1265-1276 (1990)

[52] M L Bortz, S J Field, M M Feyer, D W Nam, R G Waarts and D F Welch *'Noncritial quasi-phasematched 2nd harmonic generation in an annealed proton exchanged $LiNbO_3$ waveguide' IEEE J. Quant. Elec.* **30** p2953-2960 (1994)

[53] R L Byer *'Parametric oscillators and nonlinear materials' Nonlinear Optics – Harper 1977*

[54] A Yariv *'Quantum Electronics' Wiley* (1989)

[55] R W Minck, R W Terhune and C C Wang *'Nonlinear Optics' Applied Optics* **5** (10) p1595-1612 (1966)

[56] A M Prokhorov and Y S Kuz'minov *'Physics and Chemistry of crystalline lithium niobate' Adam Hilger* (1990)

[57] C C Davis *'Lasers and Electro-optics' Cambridge University Press* (1996)

Chapter 7

Conclusions and future work

This thesis has reported the development of several novel periodically poled lithium niobate devices. It has been shown that a large range of devices exists which exploit the ability to create areas of inverted domains in lithium niobate, and in particular devices with applications in laser modulation and frequency conversion were described. As the fabrication techniques develop, increasing numbers of new microstructured and nanostructured devices in lithium niobate are expected to appear.

This Chapter highlights the main achievements and conclusions from the work carried out within the scope of this thesis and details directions for future improvement.

7.1 Material quality

During the initial research for this thesis it was noticed that lithium niobate material from different suppliers behaved differently and gave very different results when undergoing procedures such as domain inversion, titanium indiffusion and acid etching. A comprehensive study into the differences between material from different suppliers was undertaken and was presented in Chapter 3. The main aim of this study was to understand the causes of the inconsistent results between material obtained from different places and to introduce procedures or techniques to achieve uniform PPLN quality across all supplied material, therefore not restricting the supply to one particular company or compromising availability.

Differences in material polishing techniques, thickness uniformity, refractive index fluctuations across wafers, deviations in domain wall boundaries (and therefore crystal lattice boundaries), and structural defects in the crystals were found. These differences each contributed to the inconsistent grating quality seen between material from different suppliers. Fabrication techniques such as pre-etching samples in $HF:HNO_3$ for several minutes were found to slightly alleviate some of the inconsistencies seen, however it was concluded that the underlying limiting factor to better poling quality was the raw material from the supplier. To achieve better quality gratings better quality material with more appropriate properties for domain inversion is required from the crystal growers. As such, it is of crucial importance to further understand the material aspects of lithium niobate and the growing process. Future work will be carried out to work with crystal growers to develop more consistent material suitable for periodic domain inverted devices.

One possible solution which has recently emerged is the use of stoichiometric lithium niobate [1] instead of congruent lithium niobate. Stoichiometric lithium niobate offers several superior qualities compared to congruent lithium niobate [2,3]. It has reduced defect density, larger nonlinear and electro-optic coefficients, improved transparency in the UV, increased resistance to optic damage and most important in the fabrication of PPLN and a 5 to 10 reduction in the coercive field required for poling compared to congruent lithium niobate [4]. In 2001, 3 inch stoichiometric lithium niobate and lithium tantalate crystals became commercially available from a Japanese company called Oxide Corporation [5,6]. The quality of devices achievable using stoichiometric material and the differences compared to congruent material is currently an area of considerable international research. An initial visit has already taken place to Oxide Corporation to discuss the use of stoichiometric lithium niobate within the ORC.

Despite the problems mentioned in Chapters 3 to 6, such as domain wall meandering, fabrication issues, stitching errors, poling problems and inconsistencies between material from different suppliers, several successful periodically poled lithium niobate devices were fabricated. Bragg grating modulators of lengths from 2 to 5 cm and grating periods from 40 to 90μm were achieved in 500μm thick lithium niobate.

Conventional PPLN devices for frequency conversion were produced in the same thickness material with grating periods down to 6.58μm, and gratings of period 8.7μm were achieved in titanium indiffused waveguides.

7.2 Electro-optic Bragg grating modulators

Chapters 4 and 5 described the work done to investigate and develop an electro-optically controlled Bragg grating modulator in periodically poled lithium niobate. In Chapter 4 a review of currently available electro-optic and acousto-optic modulators, and previous work on electro-optic Bragg modulators by other authors [7,8,9] was carried out, a theoretical analysis based on Kogelnik's coupled wave theory [10] was presented, the design and fabrication process for such modulators was described and the first infrared demonstration of a Bragg modulator was reported.

From the results in Chapter 4, and from the reviewed previous work by Yamada [7,8] and Gnewuch [9] several discrepancies and anomalies were found between the experimental results and the theoretical predictions. To investigate this further an experimental investigation into operation at visible wavelengths was carried out and the results presented in Chapter 5. The second part of Chapter 5 looked at several of the discrepancies in turn and offered explanations and solutions for each. Finally an alternative theoretical model was developed which avoided some of the limiting assumptions of the Kogelnik theory, such as the sinusoidal refractive index grating assumption. This was found to give a clearer picture of higher order diffraction orders and background scatter not predicted by the Kogelnik model.

The investigations and measurements made in these two Chapters indicate that this device is very promising as a versatile modulation device for use optimally at visible wavelengths. Already work is being carried out to obtain dynamic measurements at high frequency operation by applying approximately 100 picosecond pulses. Gnewuch et al. achieved 10-90% risetimes of 1.4ns, it is hoped to confirm these risetimes for the devices presented in this thesis and show faster risetimes as the maximum capability of the fast power supply is improved.

Lithium niobate is a popular material for many integrated telecommunications devices. The ability to modulate an optical signal on and off and to independently direct it is highly desirable. Future work is planned to integrate the modulator devices described before with deflector devices on the same lithium niobate sample. A deflector device can be created using a similar technique to the grating modulator by applying an electric field to a domain inverted region to give a refractive index difference boundary. The shape of this domain can be chosen such that it will deflect the incoming optical signal, within the constraints of the naturally preferred domain boundary orientation, for example triangular or hexagonal shapes could be used. This idea was demonstrated by Yamada et al. in the form of an electro-optic deflection device which consisted of a series of 20 domain inverted prisms [7] which achieved a deflection of 2^{o} by applying 200V. Electro-optic deflection and switching in lithium niobate has also been demonstrated by Boyland et al. in the ORC, in the form of a total internal reflection device [Chapter 3, 11,12].

Further work is planned to investigate the optimal deflection device based on electro-optically controlled deflection and to fabricate such devices. The ultimate aim is to integrate a Bragg grating modulator and a deflection device onto the same sample.

Another piece of future work is to combine the Bragg grating modulators with planar waveguides, in particular with titanium indiffused waveguides, thus removing any focussing effects and improving integration with other devices. Other types of materials could also be investigated such as KTP or poled polymers.

7.3 Ti:PPLN waveguides

Chapter 6 described work carried out to integrate titanium indiffused waveguides and PPLN for use in harmonic frequency conversion. The mechanisms controlling titanium diffusion in lithium niobate were discussed, and a theoretical model developed to enable the mode profile of a diffused waveguide to be calculated for any set of initial diffusion variables. Titanium waveguide fabrication and characterisation

were described, including investigations into fabrication issues such as spontaneous poling and lithium outdiffusion. Work was presented on the development of the titanium waveguide fabrication process, however it was seen that there is still future development to be done. Further investigations into alternative methods of fabrication or the addition of extra fabrication processes will be carried out to produce lower loss, 'cleaner' waveguides.

The extensive research carried out to investigate the integration of titanium indiffused waveguides and periodically poled lithium niobate was described and results achieved in a successful Ti:PPLN device for third order second harmonic generation of 416nm light in a 12μm wide titanium waveguide running through an 8.7μm period PPLN grating were presented. However this device gave poor performance compared to previously published work [13,14] due to the poor quality PPLN grating in the titanium waveguide. This was due to fundamental incompatibility problems with the two fabrication processes – the high temperatures and times involved in the diffusion process annealed out the PPLN gratings and the presence of titanium atoms in the lithium niobate crystal produced non-uniform gratings. The presence of a Ti-Li-O compound on the surface, crystal surface 'swelling' due to the indiffused titanium atoms and lithium outdiffusion were found to inhibit or produce inconsistent poling. The fabrication process will be re-examined and developed to minimise these effects resulting in better quality gratings in the waveguides.

As highlighted earlier one of the main limiting factors in device development and improvement is the quality and suitability of the available material for periodic domain inversion devices. It is hoped that the quality of devices achievable will improved as more suitable material is found.

As well as improving the existing fabrication techniques, several new devices are being investigated. One option is to combine the titanium indiffused channel waveguides with a direct bonding technique. Direct bonding [15,16] is a fabrication technique which uses the Van der Waals forces present when two suitably flat materials are brought into contact to create low-loss, seamless, vacuum-tight interfaces between explicit material layers. Such a bond can be formed irrespective of

the lattice constants and the orientation of the materials concerned and involves no deleterious modification [17] of the crystalline microstructure of either material. When applied to PPLN-based waveguide devices this becomes particularly important, as the nonlinearity and domain characteristics of bulk PPLN should remain completely unchanged when bonded to another material. Direct bonding has been successfully demonstrated in the ORC by Gawith et al. [18] to produce a buried periodically poled lithium niobate waveguide for second harmonic generation of 532nm with conversion efficiency of 4.3 % W^{-1}, a 40 % improvement in SHG conversion efficiency compared to bulk material. Single mode waveguiding was observed in the PPLN grating with less than 1.7 $dBcm^{-1}$ loss. The device fabricated for frequency conversion is shown in Figure 7.1 with a planar PPLN layer and lithium tantalate cladding and substrates.

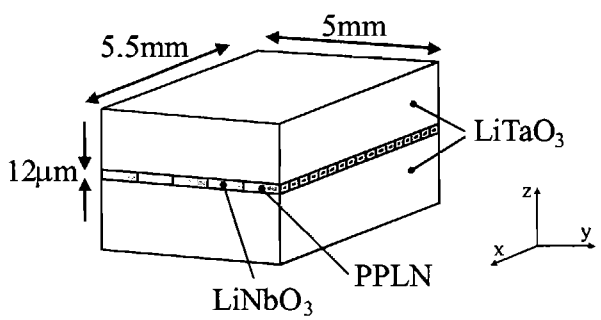

Figure 7.1 *Schematic end-face diagram of buried $LiNbO_3$ waveguide, incorporating three PPLN gratings (fabricated before bonding), each 1mm wide.*

This existing device only provides waveguiding in one dimension, future work will include combining the channel titanium indiffused waveguides with direct bonding to create buried channel periodically poled waveguides. After titanium diffusion the samples will be polished and direct bonded with a lithium niobate cladding before periodic poling, as shown in Figure 7.2. By burying the titanium diffused channels it is hoped that some of the problems encountered in Chapter 6 will be prevented as the 'defects' caused by the titanium atoms are removed from the surface and so will have less influence on inverted domain nucleation. It is hoped that more uniform nucleation and therefore more uniform domain inversion will occur.

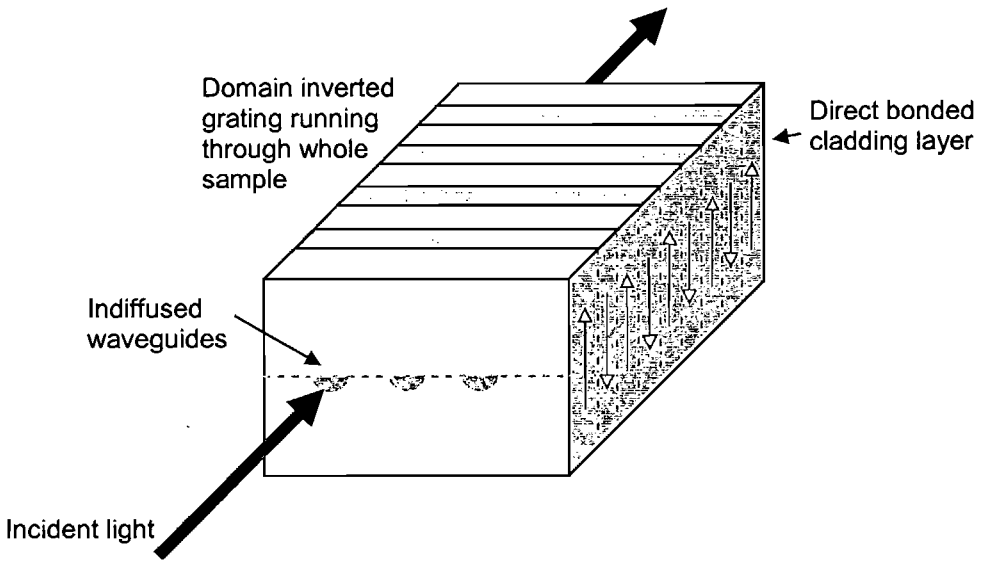

Figure 7.2 Direct bonded buried titanium indiffused channel waveguides in PPLN

Other future possibilities may include investigating waveguides diffused with metals other than titanium. Titanium indiffused waveguides are by far the most extensively used metal indiffused waveguide technology due to their use in integrated optics, telecommunications, SAW devices, etc. However indiffused waveguides in lithium niobate have been reported using other transition metals such as zinc [19,20,21,22], nickel [23,24] and vanadium [24]. Schmidt and Kaminov also report that gold, silver, iron, cobalt, niobium and germanium all yield good waveguides when diffused into lithium niobate. The most attractive out of these is zinc indiffused waveguides as they offer several superior qualities over the more widely used titanium indiffused and proton exchange waveguides. The disadvantages of titanium waveguides are the formation of an outdiffused layer near the lithium niobate surface [Chapter 6,25], the decrease in bulk electro-optic coefficients when the diffusion temperature is above 950°C [26] and the increased photorefractive damage at visible wavelengths [27]. Although proton exchange waveguides are much more resistant to photorefractive damage, they only guide extraordinary polarised light. In comparison zinc indiffused waveguides support propagation of both polarisations, and next to magnesium, zinc is the second most damage resistant impurity in lithium niobate. It has been reported that the damage resistance of lithium niobate is increased by a factor of 10^2 when the crystals are heavily doped with Zn [28] and increases in refractive index are twice those obtained via titanium indiffusion [19]. Future work will investigate zinc

indiffused waveguides and their possible integration with the devices described in this thesis.

Finally, as mentioned before the other future work in the area of titanium indiffused waveguide in PPLN will involve investigating the combination of planar waveguides with Bragg grating modulators and with HexLN.

7.4 Other periodically poled lithium niobate devices

The fabrication process used for all periodically poled lithium niobate devices in this research was described in Chapter 3. The fabrication process is continually being developed and improved as the material aspects of lithium niobate are better understood. New methods such as reverse poling and backswitching, were investigated and led to the conclusion that the forward poling liquid gel electrode electric poling technique used still gave the better and more consistent results.

The ORC has a very large research group working on novel devices in lithium niobate based on periodic poling. The last Section in Chapter 3 described several different pieces of research carried out in collaboration with other group members; The fabrication of surface relief gratings combining titanium indiffused waveguides and preferential etching of lithium niobate carried out in association with Mailis et al. [29] for applications such as wavelength filtering, wavelength division multiplexing and distributed feedback, was described.

Work with Broderick et al. [30] on the development of two-dimensional photonics crystals (or HexLN), which allow simultaneous frequency generation of several harmonics, was reported. Future work has already been planned to investigate the fabrication of HexLN waveguides which will combine HexLN frequency generation with benefits of waveguide geometry such as higher efficiencies and lower operational thresholds. One possibility is to use a direct bonding technique [18] as outlined in Section 7.3 to bury a HexLN layer in lithium tantalate to create a planar waveguide.

An alternative waveguide technique is to use titanium indiffusion to create a planar waveguide at the surface of the lithium niobate sample as described in Chapter 6. Initial work has been carried out to combine these waveguides with HexLN but was found to be unsuccessful due to similar problems seen in Chapter 6 when fabricating Ti:PPLN channel waveguides. The presence of titanium atoms in the surface layers is thought to influence the nucleation of the inverted domains, causing uneven poling and patchy gratings. Also the effect of lithium outdiffusion during the diffusion process suppresses nucleation and prevents domain inversion. These effects are currently being investigated. One possible solution may be to bury the titanium indiffused layer, for example by direct bonding, thus taking the titanium 'impurities' away from the surface. Future investigations will look at this.

7.5 References

[1] S Furukawa, K Kitamura, S Takekawa, K Niwa and H Hatano *'Improved properties of stoichiometric $LiNbO_3$ for electro-optic applications'* *J. Intel. Mat. Syst. Str.* **10** (6) p470-475 (1999)

[2] K Kitamura, S Takekawa, M Nakamura and Y Furukawa *'Commercialisation of stoichiometric $LiNbO_3$ and $LiTaO_3$ for optical devices'* *CLEO/PR July 2001* WH2-1

[3] Y-L Chen, J-J Xu, X-J Chen, Y-F Kong and G-Y Zhang *'Domain reversion process in near-stoichiometric $LiNbO_3$ crystals'* *Optics Comms.* **188** p359-364 (2001)

[4] V Gopalan, T E Mitchell, K Kitamura and Y Furukawa *'The role of nonstoichiometry in 180 degrees domain switching of $LiNbO_3$ crystals'* *Appl. Phys. Lett.* **72** p1981 (1998)

[5] www.opt-oxide.com

[6] Newsbreak *Laser Focus World* p11 (May 2001)

[7] M Yamada, M Saitoh and H Ooki *'Electric-field induced cylindrical lens, switching and deflection devices composed of the inverted domains in $LiNbO_3$ crystals'* *Appl Phys Lett* **69** p3659-3661 (1996)

[8] M Yamada *'Electrically induced Bragg-diffraction grating composed of periodically inverted domains in lithium niobate crystals and its application devices'* *Rev. Sci. Inst.* **71** no.11 p4010-4016 (2000)

[9] H Gnewuch, C N Pannell, G W Ross, P G R Smith and H Geiger *'Nanosecond response of Bragg deflectors in periodically poled $LiNbO_3$' IEEE Photonics Tech Lett* **10** p1730-1732 (1998)

[10] H Kogelnik *'Coupled wave theory for thick hologram gratings' The Bell System Technical Journal* **48** no.9 p2909-2947 (1969)

[11] A J Boyland, S Mailis, J M Hendricks, P G R Smith and R W Eason *'Electro-optically controlled beam switching via total internal reflection at a domain engineered interface in $LiNbO_3$' Opt. Comms.* **197** p193-200 (2001)

[12] R W Eason, A J Boyland, S Mailis, P G R Smith *'Electro-optically controlled beam deflection for grazing incidence geometry on a domain engineered interface in $LiNbO_3$' Opt. Comms.* **197** p201-207 (2001)

[13] J Amin, V Pruneri, J Webjorn, P St J Russell, D C Hanna and J S Wilkinson *'Blue light generation in a periodically poled Ti:LiNbO3 channel waveguide' Opt. Comms.* **135** (1-3) p41-44 (1996)

[14] D Hofmann, G Schreiber, C Haase, H Herrmann, W Grundkotter, R Ricken, W Sohler *'Quasi-phasematched difference frequency generation in periodically poled Ti:$LiNbO_3$ channel waveguides' Opt. Letts.* **24** (13) p896-898 (1999)

[15] J Haisma, G A C M Spierings, U K P Biermann and A A van Gorkum *'Diversity and feasibility of direct bonding: a survey of a dedicated optical technology' Appl. Opt.* **33** p1154 (1994)

[16] A Plößl and G Kräuter *'Wafer direct bonding: tailoring adhesion between brittle materials' Mat. Sci. Eng.* **R25** p1 (1999)

[17] K Eda, M Sugimoto and Y Tomita *'Direct heterobonding of lithium niobate onto lithium tantalate' Appl. Phys. Lett.* **66** p827 (1995)

[18] C B E Gawith, D P Shepherd, J A Abernethy, D C Hanna, G W Ross and P G R Smith *'Second-harmonic generation in a direct-bonded periodically poled $LiNbO_3$ buried waveguide' Opt. Letts.* **24** (7) p481-483 (1999)

[19] V A Fedorov, Y N Korkishko, F Vereda, G Lifanate and F Cusso *'Structural characterisation of vapour Zn-difffused waveguides in lithium niobate' J. Crystal Growth* **194** p94-100 (1998)

[20] V A Fedorov, Y N Korkishko, G Lifant and F Cusso *'Optical and structural characterisation of ainc vapour diffused waveguides in $LiNbO_3$ crystals' J. Eur. Ceramic Soc.* **19** p1563-1567 (1999)

[21] W M Young, M M Fejer, M J F Digonnet, A F Marshall and R S Feigelson *'Fabrication, characterisation and index profile modelling of high-damage resistance Zn-*

diffused waveguides in congruent and MgO: lithium niobate' J. Light. Tech. **10** (9) p1238 (1992)

[22] R Nevado, C Sada, F Segeto, F Caccavale, A Kling, J C Soares, E Cantelar, F Cusso and G Lifante *'Compositional characterisation of Zn-diffused lithium niobate waveguides' Appl. Phys. B: Lasers* **73** (5-6) p555-558 (2001)

[23] P-K Wei and W-S Wang *'Fabrication of lithium niobate optical channel waveguides by nickel indiffusion' Micr. Opt. Tech. Letts.* **7** (5) p219 (1994)

[24] R V Schmidt and I P Kaminov *'Metal-diffused optical waveguides in $LiNbO_3$' Appl. Phys. Lett.* **25** (8) p458 (1974)

[25] I P Kaminow and and J C Carruthers *'Optical waveguiding layers in $LiNbO_3$ and $LiTaO_3$' Appl. Phys. Lett.* **22** p326-328 (1973)

[26] J Noda, N Uchida, S Saito, T Saku and M Minakata *'Electro-optic amplitude modulation using three dimensional waveguide $LiNbO_3$ fabricated by TiO_2diffusion' Appl.Phys. Lett.* **27** p19-21 (1979)

[27] R A Becker 'Thermal fixing of Ti-indiffused $LiNbO_3$ channel waveguides for reduced photorefractive susceptibility' Appl. Phys. Letts. **45** (2) p21-123 (1984)

[28] T Volk, N Rubinina and V Pryalkin *'Optical damage resistant $LiNbO_3$-Zn crystal' Opt. Lett.* **15** p996 (1990)

[29] S Mailis, G W Ross, L Reekie, J A Abernethy and R W Eason *'Fabrication of surface relief gratings on lithium niobate by combined UV laser and wet etching' Electronics Letters* **36** (21) p1801-1803 (2000)

[30] N G R Broderick, G W Ross, H L Offerhaus, D J Richardson and D C Hanna *'Hexagonally poled lithium niobate: a two-dimensional nonlinear photonic crystal' Phys. Rev. Lett.* **84** p4345-4348 (2000)

Appendix I

Theoretical model of titanium indiffused waveguides

It is assumed that titanium diffusion in lithium niobate is isotropic with diffusion coefficient, D, independent of concentration. Therefore, the equation which describes three dimensional diffusion is given by :

Equation 1
$$\frac{1}{D}\frac{\partial C(x,y,z,t)}{\partial t} = \frac{\partial^2 C(x,y,z,t)}{\partial x^2} + \frac{\partial^2 C(x,y,z,t)}{\partial y^2} + \frac{\partial^2 C(x,y,z,t)}{\partial z^2}$$

where $C(x,y,z,t)$ is the concentration profile of titanium.

By assuming that the solution of this equation is independent in x,y and z, a solution can be obtained by separation of variables and using Fourier transforms. Fourier transform theory states that if ;

Equation 2
$$F(\xi) = \frac{1}{\sqrt{2\pi}}\int_{-\infty}^{\infty} e^{i\xi x'} f(x')dx' \qquad \text{then} \qquad f(x') = \frac{1}{\sqrt{2\pi}}\int_{-\infty}^{\infty} e^{-i\xi x} F(\xi)d\xi$$

For example, consider one dimensional diffusion in the x direction. The diffusion equation is given by :

Equation 3
$$\frac{1}{D}\frac{\partial C(x,t)}{\partial t} = \frac{\partial^2 C(x,t)}{\partial x^2} \qquad \text{where } -\infty < x < \infty \text{ for } t > 0.$$

The general Fourier solution is given by :

Equation 4 $$C(x,t) = \frac{Ti_o}{\sqrt{2\pi}} \int_{-\infty}^{\infty} e^{-i\xi x - D\xi^2 t} \phi(\xi) d\xi$$ where Ti_o is the amount of titanium deposited. At $t = 0$, the initial concentration profile is given by :

Equation 5 $$C(x,0) = f(x') = \frac{Ti_o}{\sqrt{2\pi}} \int_{-\infty}^{\infty} e^{-i\xi x} \phi(\xi) d\xi$$ which is the above Fourier integral. Then it follows that ;

Equation 6 $$\phi(\xi) = \frac{1}{\sqrt{2\pi}} \int_{-\infty}^{\infty} e^{i\xi x'} f(x') dx'$$

And by substitution ;

Equation 7 $$C(x,t) = \frac{Ti_o}{\sqrt{2\pi}} \int_{-\infty}^{\infty} e^{-i\xi x - D\xi^2 t} d\xi \int_{-\infty}^{\infty} e^{-i\xi x'} f(x') dx'$$

$$= \frac{Ti_o}{\sqrt{2\pi}} \int_{-\infty}^{\infty} f(x') dx' \int_{-\infty}^{\infty} e^{-D\xi^2 t - i\xi(x-x')} d\xi$$

$$= \frac{Ti_o}{2\sqrt{\pi Dt}} \int_{-\infty}^{\infty} f(x') e^{\frac{-(x-x')^2}{4Dt}} dx'$$

This is the one dimensional solution for an instantaneous point source, amount Ti_o of titanium, at $x = x`$, with initial concentration profile $f(x`)$.

Similarly in y and z, giving us a general three dimensional solution for the concentration profile of an instantaneous point source at $(x`,y`,z`)$ with initial concentration profile $f(x`,y`,z`)$, into an infinite solid:

Equation 8 $$C(x,y,z,t) = \frac{Ti_o}{\left(2\sqrt{\pi Dt}\right)^3} \int_{-\infty}^{\infty}\int_{-\infty}^{\infty}\int_{-\infty}^{\infty} f(x',y',z') e^{\frac{-\{(x-x')^2+(y-y')^2+(z-z')^2\}}{4Dt}} dx'dy'dz'$$

From this equation it can be seen that as $t \to 0$, $C(x,y,z,t) \to 0$ at all points except $(x`,y`,z`)$, where it tends to infinity. Also, the total quantity of titanium in the infinite region is obtained by integrating the concentration over all space for $t > 0$. As expected, we get Ti_o :

Equation 9 $$\int_{-\infty}^{\infty}\int_{-\infty}^{\infty}\int_{-\infty}^{\infty} C(x,y,z,t) dxdydz = Ti_o$$

since

Equation 10
$$\frac{1}{2\sqrt{\pi Dt}}\int_{-\infty}^{\infty} e^{\frac{-(x-x')^2}{4Dt}}dx' = \frac{1}{2\sqrt{\pi Dt}}\int_{-\infty}^{\infty} e^{\frac{-(y-y')^2}{4Dt}}dy' = \frac{1}{2\sqrt{\pi Dt}}\int_{-\infty}^{\infty} e^{\frac{-(z-z')^2}{4Dt}}dz' = 1$$

This general solution can now be applied to the particular diffusion problem in this work.

From Chapter 6 the assumption can be made that the titanium strip is infinite in the $\pm x$ direction, as $l >> w >> d$, thus reducing the problem to a two dimensional one. Therefore the instantaneous point source can be extended to an instantaneous line source parallel to y and passing through the point $(y`,z`)$, by considering a distribution of point sources of strength $Ti_o dx`$ along the line $x`$ and integrating :

Equation 11
$$C(y,z,t) = \frac{Ti_o}{\left(2\sqrt{\pi Dt}\right)^3}\int_{-\infty}^{\infty} e^{\frac{-\{(x-x')^2+(y-y')^2+(z-z')^2\}}{4Dt}}dx' = \frac{Ti_o}{4\pi Dt}e^{\frac{-\{(y-y')^2+(z-z')^2\}}{4Dt}}$$

where Ti_o is now the quantity of titanium deposited per unit length of the line.

However, it can be seen that the problem consists of a strip source, width $2w$ in the y direction, and not a line source. This can be modelled by considering a distribution of line sources of strength $Ti_o dy`$ along the line $z = z`$ and integrating in the range $-w < y` < w$:

Equation 12
$$C(y,z,t) = \frac{Ti_o}{4\pi Dt}\int_{-w}^{w} e^{\frac{-\{(y-y'-\xi)^2+(z-z')^2\}}{4Dt}}d\xi$$

$$= \frac{Ti_o}{4\pi Dt}e^{-\frac{(z-z')^2}{4Dt}}\int_{\frac{y-y'+w}{\sqrt{4Dt}}}^{\frac{y-y'-w}{\sqrt{4Dt}}} e^{-u^2}(-\sqrt{4Dt}du) \qquad \text{where } u = \frac{y-y'-\xi}{\sqrt{4Dt}}$$

$$= -\frac{Ti_o}{\pi\sqrt{Dt}}e^{\frac{-(z-z')^2}{4Dt}}\frac{\sqrt{\pi}}{2}\left[\frac{2}{\sqrt{\pi}}\int_0^{\frac{y-y'+w}{\sqrt{4Dt}}} e^{-u^2}du - \frac{2}{\sqrt{\pi}}\int_0^{\frac{y-y'-w}{\sqrt{4Dt}}} e^{-u^2}du\right]$$

$$= -\frac{Ti_o}{\sqrt{4\pi Dt}}e^{\frac{-(z-z')^2}{4Dt}}\left[erf\left(\frac{y-y'+w}{\sqrt{4Dt}}\right) - erf\left(\frac{y-y'-w}{\sqrt{4Dt}}\right)\right]$$

$$= \frac{Ti_o}{\sqrt{4\pi Dt}}e^{\frac{-(z-z')^2}{4Dt}}\left[erf\left(\frac{y-y'-w}{\sqrt{4Dt}}\right) - erf\left(\frac{y-y'+w}{\sqrt{4Dt}}\right)\right]$$

This is now the solution for an instantaneous strip source of titanium, centred on $(x`,y`,z`)$, amount Ti_o per unit area. This solution was graphed for different values of time as shown in Figure 1. It can be seen that this solution gives a realistic concentration model. For simplicity, the variables were chosen as follows ; $x' = 0$, $y' = 0$, $D = 3.6\mu m^2$ / hour, $w = 5\mu m$, and $Ti_o = 10$.

Although the above equation is a very good model, it still does not fully describe the actual diffusion problem in this research. The titanium deposited has thickness d, and therefore is not an instantaneous source, but acts as a continuous line source until a time t_{dep}, when the deposited titanium has been depleted, and then acts as an instant line source with initial concentration $f(x`,y`,z`)$. To take this into account the diffusion can be modelled in two parts; Part I - For $0 < t < t_{dep}$, treating the diffusion as a continuous strip source, found by integrating the above equation with time. Part II - For $t > t_{dep}$, treating the diffusion as an instantaneous line source with initial concentration found from the solution of Part I evaluated at t_{dep}.

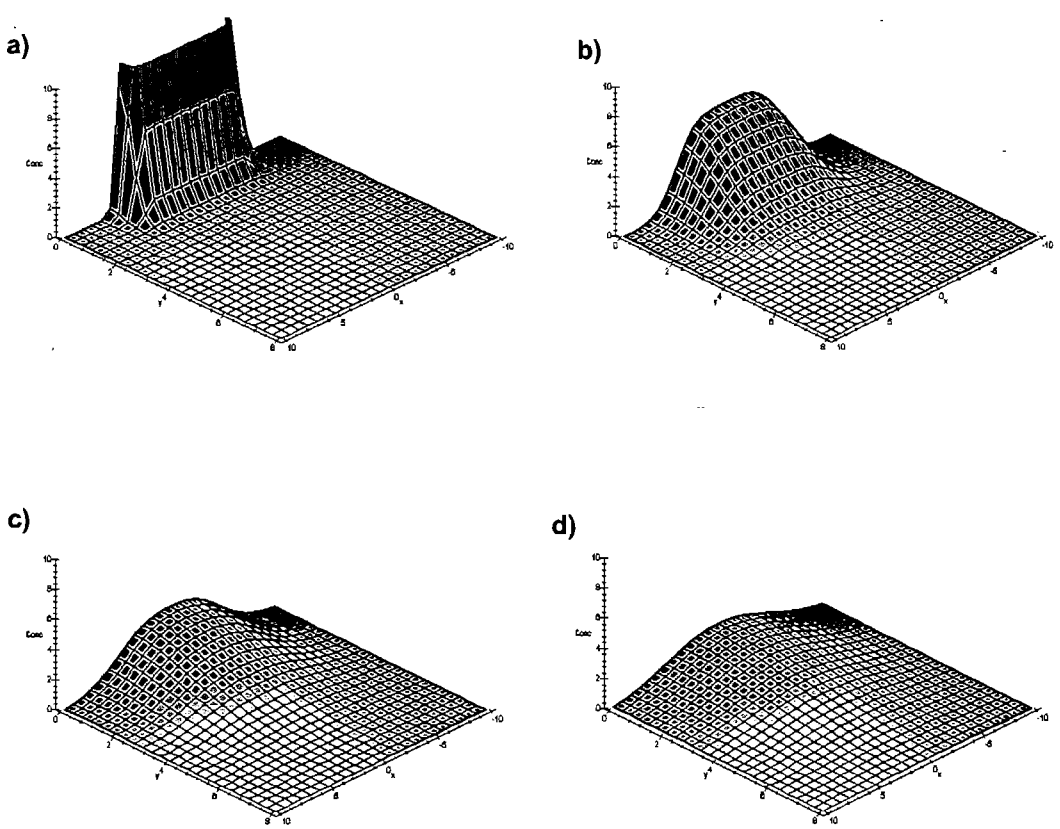

Figure 1 *Diffusion profile of an instantaneous strip source with time after a) 0.1 hours, b) 1 hour, c) 2.5 hours and d) 5 hours*

Part I : Integrate the instantaneous strip source with time ;

Equation 13

$$C(y,z,t<t_{dep}) = \int_0^t \frac{Ti_o}{\sqrt{4\pi D(t-t')}} e^{\frac{-(z-z')^2}{4D(t-t')}} \left[erf\left(\frac{y-y'-w}{\sqrt{4D(t-t')}} \right) - erf\left(\frac{y-y'+w}{\sqrt{4D(t-t')}} \right) \right] dt'$$

$$= \int_0^t \frac{Ti_o}{\sqrt{4\pi D(t-t')}} e^{\frac{-(z-z')^2}{4D(t-t')}} erf\left(\frac{y-y'-w}{\sqrt{4D(t-t')}} \right) dt' - \int_0^t \frac{Ti_o}{\sqrt{4\pi D(t-t')}} e^{\frac{-(z-z')^2}{4D(t-t')}} erf\left(\frac{y-y'+w}{\sqrt{4D(t-t')}} \right) dt'$$

where Ti_o is the amount of titanium per unit area per unit time. This integral cannot be evaluated easily using analytical methods and a numerical solution must be sought.

Part II : The numerical solution from Part I, evaluated at t_{dep}, is substituted into the diffusion equation for an instantaneous line source giving ;

Equation 14
$$C(y,z,t>t_{dep}) = \frac{Ti_o}{\left(2\sqrt{\pi Dt}\right)^3} \int_{-\infty}^{\infty}\int_{-\infty}^{\infty} C(y',z',t_{dep}) e^{\frac{-\{(y-y')^2+(z-z')^2\}}{4Dt}} dy'\,dz'$$

where $t > t_{dep}$, and the initial concentration distribution is centred on the point $(y`,z`)$ and Ti_o is now the amount of titanium per unit area deposited in time t_{dep}.

Using the model above, the concentration profile of the diffused titanium can be calculated for a depleted or non-depleted source for any set of initial variables.

The author would like to acknowledge the help of Dr Geoff Daniell, Physics and Astronomy, University of Southampton.

Appendix II

Matlab Code

```
function [results_opol, results_epol] = angspec(fname)

%to run type " angspec('filename'); "

%this function is the top level one which plots the diffracted intensity with
output angle

%define all the variables :

%grating period, W=width of grating, d=length of grating, t=thickness of
grating, all in metres
period = 40e-6;
W = 1e-3;
d = 0.03;
t = 0.5e-3;

%refractive index & wavelength of light (in air) in metres
no = 2.24;
ne = 2.16;
lambda_air = 633e-9;
lambda_e = lambda_air / ne;
lambda_o = lambda_air / no;

%calculates the internal Bragg Angle for these variables in degrees
%(note that Bragg angle is the angle between grating plane and incident light)
bragg = asin(lambda_air / (2 * ne * period));
bragg_degrees = 180 * bragg / pi;


%Applied Voltage in Volts and resultant Electric field :
V = 200;
E = V / t;

% r is electro-optic coefficient in metres per Volt
%for o-polarised light (light polarised perpendicular to optic axis)
r_opol = 8.6e-12;
%therefore the change in refractive index induced by the applied field is :
delta_n_opol = no^3 * r_opol * E / 2;

%and similarly for e-polarised light (light polarised parallel to optic axis)
r_epol = 32.2e-12;
delta_n_epol = ne^3 * r_epol * E / 2;
```

```
%all in degrees - INTERNAL input angle (equal to Bragg),
%starting value of output angle, finishing value of output angle & stepsize of
output angle
%all measured as angle between grating plane to light
theta_in = bragg_degrees;
phistartd = 0;
phiendd = 0.5;
phistepd = 0.001;

% we need to re-express the input and output angles as the angles from the
grating plane normal and convert them to radians
phistart = (90 - phiendd) * pi / 180;
phiend = (90 - phistartd) * pi / 180;
phistep = phistepd * pi / 180;
theta = (90 - theta_in) * pi / 180;


% first the case of O-POLARISED light :

%assuming that you are already in a lower refractive index part of the grating
when you start...
%calculate the angle of light in the high and low refractive index parts of the
grating measured from the normal to the grating to the light (all still in
degrees)
theta_low_d = 90 - theta_in;
theta_high_d = asin(sin(theta_low_d * (no - delta_n_opol) / (no +
delta_n_opol)));

%As Matlab does its calculations in radians, we need to convert the angles from
degrees into radians :
theta_low = theta_low_d * pi / 180;
theta_high = theta_high_d * pi / 180;

%this is the main bit of the program which plots the output intensity for a
given input angle over a range or output angles
%this is the calculation loop

%first define the list of output angles you want to calculate over
phiv = phistart:phistep:phiend;
results_opol = zeros(2, size(phiv, 2));
count = 0;

%the raw data is written to a .dat file
fid2 = fopen(strcat(fname, '_opol.dat'), 'w');

%this is the FOR loop which loops through a range of output angles and
calculates the output intensity at each one

for phi = phiv

    count = count + 1;

    %this calculates the amplitude reflection coefficients for opol light using
    the Fresnel Equations
    % A_up is the reflection from lower to higher refractive index interface
    % A_down is the reflection from a higher to lower refractive index interface

    A_up = tan(theta_low - theta_high) / tan(theta_low + theta_high);
    A_down = tan(theta_high - theta_low) / tan(theta_high - theta_low);
```

```
    %the next line calls the function DIFFRACT which calculates the output
intensity
    number = diffract(theta, phi, period, W, d, no, lambda_o, A_up, A_down);

    %put the results into an array called RESULTS_OPOL in two columns - the
output angle and the diffracted intensity at that angle
    %remembering to convert the output angle back into the angle
    results_opol(1, count) = phi;
    results_opol(2, count) = number;

    %this prints the output angle, the real part of the diffracted intensity and
the imaginary part
    fprintf(fid2, '%e, %e, %e\n', phi, real(results_opol(2, count)),
imag(results_opol(2, count)));
end


% second the case of E-POLARISED light :

%assuming that you start in a lower refractive index part of the grating...
%calculate the angle of light in the high and low refractive index parts of the
grating measured from the normal to the grating to the light (all still in
degrees)
theta_low_d = 90 - theta_in;
theta_high_d = asin(sin(theta_low_d * (ne - delta_n_epol) / (ne +
delta_n_epol)));

%As Matlab does its calculations in radians, we need to convert the angles from
degrees into radians :
theta_low = theta_low_d * pi / 180;
theta_high = theta_high_d * pi / 180;

%this is the main bit of the program which plots the output intensity for a
given input angle over a range or output angles
%this is the calculation loop

%first define the list of output angles you want to calculate over
phiv = phistart:phistep:phiend;
results_epol = zeros(2, size(phiv, 2));
count = 0;

%the raw data is written to a .dat file
fid3 = fopen(strcat(fname, '_epol.dat'), 'w');

%this is the FOR loop which loops through a range of output angles and
calculates the output intensity at each one

for phi = phiv

    count = count + 1;

    %this calculates the amplitude reflection coefficients for epol light using
the Fresnel Equations
    % A_up is the reflection from lower to higher refractive index interface
    % A_down is the reflection from a higher to lower refractive index interface

    A_up = -sin(theta_low - theta_high) / sin(theta_low + theta_high);
    A_down = -sin(theta_high - theta_low) / sin(theta_high - theta_low);

    %the next line calls the function DIFFRACT which calculates the output
intensity
```

```
    number = diffract(theta, phi, period, W, d, ne, lambda_e, A_up, A_down);

    %put the results into an array called RESULTS_EPOL in two columns - the
output angle and the diffracted intensity at that angle
    results_epol(1, count) = phi;
    results_epol(2, count) = number;

    %this prints the output angle, the real part of the diffracted intensity and
the imaginary part
    fprintf(fid3, '%e, %e, %e\n', phi, real(results_epol(2, count)),
imag(results_epol(2, count)));
end


%information about the calculation is stored in a text file which is defined as
follows :
fid = fopen(strcat(fname, '.doc'), 'w');

%this is what the file will contain, it lists all the variables used

fprintf(fid, 'Specifications data file\n');
fprintf(fid, '................\n');
fprintf(fid, 'filename                        %s     \n', fname);
fprintf(fid, '\n');
fprintf(fid, 'Width Grating, W                %f    mm\n', W*1e3);
fprintf(fid, 'Length Grating, d               %f    cm\n', d*1e2);
fprintf(fid, 'Applied voltage, V              %f    V\n', V);
fprintf(fid, 'Wavelength in air               %f    nm\n', lambda_air*1e9);
fprintf(fid, 'Grating Period                  %f    microns\n', period*1e6);
fprintf(fid, 'Ordinary refractive index     %f\n', no);
fprintf(fid, 'Extraordinary refractive index %f\n', ne);
fprintf(fid, '\n');
fprintf(fid, 'Phi start                       %f    degrees\n', phistartd);
fprintf(fid, 'Phi end                         %f    degrees\n', phiendd);
fprintf(fid, 'Phi Step                        %f    degrees\n', phistepd);
fprintf(fid, '\n');
fprintf(fid, 'Internal incident angle         %f    degrees\n', theta_in);
fprintf(fid, '\n');
fprintf(fid, 'The calculated internal Bragg Angle for these variables is   %f
degrees\n', bragg_degrees);

fclose (fid2);
fclose (fid);

%this next line plots the modulus of the intensity with output angle for o
polarised light
figure (1)
plot(90 - (results_opol(1,:)*180/pi), abs(results_opol(2,:)));
set(gca, 'Yscale', 'log')
title('Plot of intensity with internal output angle for o-polarised light');
xlabel('Internal output angle (degrees) ');
ylabel('Intensity (a.u)');

%this next line plots the modulus of the intensity with output angle for e
polarised light
figure (2)
plot(90 - (results_epol(1,:)*180/pi), abs(results_epol(2,:)));
set(gca, 'Yscale', 'log')
title('Plot of intensity with internal output angle for e-polarised light');
xlabel('Internal output angle (degrees) ');
ylabel('Intensity (a.u)');
```

```
function total = diffract(theta, phi, period, W, d, n, lambda, A_up, A_down)

%this function calculates the intensity of the diffracted light for a given
input
%and output angle and a defined set of variables
%according to -
%A * exp ( i 2 Pi n x {sin theta + sin phi} / lambda ) * ( lambda * ( exp { i 2
Pi n (cos theta - cos phi) d / lambda } - 1 ) / i 2 Pi n (cos theta - cos phi) )

%we can split this up into its different parts to calculate :

%to save computational time, values which don't change are calculated first:
costerm = (cos(theta) - cos(phi));
sinterm = (sin(theta) + sin(phi));

constant1 = ( i * 2 * pi * n / lambda);

part1 = (exp (constant1 * costerm * d) - 1) / (constant1 * costerm);


%set the total to zero
total = 0;
total_up = 0;
total_down = 0;
part2_up = 0;
part2_down = 0;

%this FOR loop steps up the grating planes over the width of the grating
%and calculates the diffracted component from low to high refractive index
for x = 0:period:W

        result_up = exp ( constant1 *  x * sinterm);

        part2_up = part2_up + result_up;
end

total_up = A_up * part1 * part2_up;


%this FOR loop steps up the grating planes - half over the width of the grating
%and calculates the diffracted component from high to low refractive index
for x = period:(period - period / 2):W

        result_down = exp ( constant1 *  x * sinterm);

        part2_down = part2_down + result_down;
end

total_down = A_down * part1 * part2_down;

%and then calculate the total diffraction for this set of variables

total = total_up + total_down;
```

Appendix III

Publications, refereed journal and international conference papers

Journal Papers

I. J A Abernethy, C B E Gawith, R W Eason and P G R Smith *'Demonstration and optical characteristics of electro-optic Bragg modulators in periodically poled lithium niobate in the near infrared'* Applied Physics Letters Vol.81 (14) 30th September 2002

II. S Mailis, G W Ross, L Reekie, J A Abernethy and R W Eason *'Fabrication of surface relief gratings on lithium niobate by combined UV laser and wet etching'* Electronics Letters Vol.36 (21) p1801-1803 12th October 2000

III. C B E Gawith, D P Shepherd, J A Abernethy, D C Hanna, G W Ross and P G R Smith *'Second-harmonic generation in a direct-bonded periodically-poled-$LiNbO_3$ buried waveguide'* Optics Letters Vol.24 (7) p481-483 1st April 1999

International Conferences

I. J A Abernethy, R W Eason and P G R Smith *'Bulk optical Bragg deflectors at 1.064μm based on an electro-optically induced grating in periodically poled lithium niobate'* CLEO/Pacific Rim Chiba 15-19 Jul 2001 ME2-3 pp.102-3

II. J A Abernethy, R W Eason and P G R Smith *'Investigation into bulk optical Bragg deflectors based on an electro-optically induced grating in periodically poled lithium niobate'* International Workshop on Periodically Microstructured Nonlinear Optical Materials Madrid 10-13 Jun 2001

III. P G R Smith, P E Britton, D Taverner, N G Broderick, D J Richardson, G W Ross, C B E Gawith, J A Abernethy, H L Offerhaus and D C Hanna *'Review of erbium fibre laser based nonlinear optics in periodically poled lithium niobate (PPLN)'* International Workshop on Periodically Microstructured Nonlinear Optical Materials Madrid 10-13 Jun 2001

IV. P G R Smith, C B E Gawith, J A Abernethy, R W Eason, I E Barry, S Mailis, N G R Broderick, D J Richardson, D C Hanna *'Material aspects of periodically poled lithium niobate'* BACG (British Assoc for Crystal Growth) Manchester 17-19 Sep 2000

V. S Mailis, G W Ross, L Reekie, J A Abernethy, I E Barry, R.W.Eason, I Nee, M Muller and K Buse *'Optically assisted chemical surface microstructuring of $LiNbO_3$'* CLEO/Europe 2000 Nice 10-15 Sep 2000 CTuO7

VI. S Mailis, G W Ross, L Reekie, J A Abernethy and R W Eason *'New technique for fabrication of surface relief Ti-indiffused $LiNbO_3$ waveguides'* CLEO 2000 San Francisco 7-12 May 2000 CWK46

VII. C B E Gawith, D P Shepherd, J A Abernethy, D C Hanna, G W Ross and P G R Smith *'Efficient second-harmonic generation in a directly-bonded, buried, periodically-poled $LiNbO_3$, planar waveguide'* Proc. CLEO/Europe '98 Glasgow Scotland 13-18 Sep 1998 CPD2.7 (Postdeadline)

Books

J A Abernethy, R W Eason and P G R Smith *'Investigation into bulk optical Bragg deflectors based on an electro-optically induced grating in periodically poled lithium niobate'* Chapter in *'The state of the art periodically microstructured nonlinear optical materials' World Scientific* March 2003